

---

# Probing Bloch band geometry with ultracold atoms in optical lattices

Tracy Li

---



München 2016



---

# **Probing Bloch band geometry with ultracold atoms in optical lattices**

**Tracy Li**

---

Dissertation  
an der Fakultät für Physik  
der Ludwig-Maximilians-Universität  
München

vorgelegt von  
Tracy Li  
aus Nanjing, China

München, Mai 2016

Erstgutachter: Prof. I. Bloch

Zweitgutachter: Prof. E. Demler

Weitere Prüfungskommissionsmitglieder: Prof. A. Högele, Prof. U. Schollwöck

Tag der mündlichen Prüfung: 13. Juli 2016

## Zusammenfassung

Ultrakalte Atome in optischen Gittern haben sich unlängst als vielversprechendes Mittel zur Untersuchung geometrischer und topologischer Aspekte von Bandstrukturen erwiesen. In dieser Arbeit werden wir das hohe Maß an Kontrolle, das diese Systeme ermöglichen, ausnutzen, um die Bandgeometrie eines hexagonalen optischen Gitters zu untersuchen. In der ersten Reihe von Experimenten realisieren wir ein Atominterferometer im Quasiimpulsraum, um den singulären Berryfluss zu messen, der mit einem Dirakpunkt assoziiert ist. Diese Technik erlaubt es uns, die Verteilung der Berrykrümmung in der Brillouinzone mit sehr hoher Quasiimpulsauflösung zu bestimmen. Als Nächstes realisieren wir Dynamiken, die durch sehr starke Kräfte erzeugt werden und die mithilfe von Wilsonlinien beschrieben werden können. Diese Wilsonlinien werden durch Matrizen dargestellt und sind eine Verallgemeinerung der Berryphase für entartete Systeme. Wir zeigen, dass aus der Entwicklung der Bandpopulationen in diesem Regime direkt die Bandgeometrie abgeleitet werden kann. Diese Methode ermöglicht die Rekonstruktion der zellenperiodischen Blochzustände für alle Quasiimpulse sowie der Eigenwerte der Wilson-Zak-Schleifen. Unsere Techniken können genutzt werden, um topologische Invarianten zu bestimmen, die die Bandstruktur charakterisieren, wie zum Beispiel die Chernnummer und die  $\mathbb{Z}_2$  Nummer. Aufbauend auf diesen Ergebnissen präsentieren wir abschließend vorläufige Experimente zur Manipulation von Bandstrukturen.

## Abstract

Ultracold atoms in optical lattices have recently emerged as promising candidates for investigating the geometric and topological aspects of band structures. In this thesis, we exploit the high degree of control available in these systems to directly probe the band geometry of an optical honeycomb lattice. In the first series of experiments, we realize an atomic interferometer in quasimomentum space to measure the singular Berry flux associated with a Dirac point. This technique enables us to determine the distribution of Berry curvature in the Brillouin zone with high quasimomentum resolution. Next, we realize strong-force dynamics that are described by matrix-valued Wilson lines, which are generalizations of the Berry phase to degenerate systems. In this strong-force regime, we show that the evolution in the band populations directly reveals the band geometry. This method enables the reconstruction of both the cell-periodic Bloch states at every quasimomentum and the eigenvalues of Wilson-Zak loops. Our techniques can be used to determine the topological invariants, such as the Chern and  $\mathbb{Z}_2$  numbers, that characterize the band structure. Lastly, having established our ability to detect the band geometry, we present preliminary experiments on engineering band structures.



# Contents

<b>1. Introduction</b>	<b>1</b>
<b>2. Geometric quantities in Bloch bands</b>	<b>7</b>
2.1. Geometric phases in brief	7
2.2. Accessing geometric properties in Bloch bands	10
2.2.1. Preliminaries	10
2.2.2. Derivation of the equations of motion	12
2.2.3. Adiabatic motion: the Berry phase	13
2.2.4. Diabatic motion: the Wilson line	15
2.3. Gauge invariance: which quantities are measurable?	16
2.3.1. Single-band geometric quantities	16
2.3.2. Multi-band geometric quantities	17
2.3.3. A summary	18
2.4. A blueprint for the experiments	19
<b>3. The optical honeycomb lattice</b>	<b>21</b>
3.1. The tight-binding model	21
3.1.1. $\Delta = 0$ : Dirac points and Berry phases	24
3.1.2. $\Delta \neq 0$ : Effect of the Semenoff mass and the Bloch sphere picture	26
3.2. The <i>ab-initio</i> calculation	30
3.2.1. Setting up the problem	30
3.2.2. Application to the optical honeycomb potential	31
3.2.3. Energy bands from the <i>ab-initio</i> calculation	33
<b>4. An overview of the experimental setup</b>	<b>37</b>
4.1. Creation of the optical honeycomb lattice	38
4.1.1. The optical dipole potential	38
4.1.2. The ideal optical honeycomb lattice	39
4.1.3. Modifications on the ideal: non-isotropic tunneling and adding a Semenoff mass	41
4.2. State preparation: creating a BEC	44
4.3. State evolution: creating a gradient	45
4.3.1. Magnetic field	46
4.3.2. Lattice acceleration	46

4.4.	State detection: absorption imaging . . . . .	48
4.4.1.	Sudden shut-off of the lattice: plane-wave decomposition . . . . .	49
4.4.2.	Ramp-down of the lattice: band mapping . . . . .	51
4.5.	Applications: Bloch oscillations and lattice depth calibration . . . . .	54
4.5.1.	Bloch oscillations . . . . .	54
4.5.2.	Lattice calibration . . . . .	56
<b>5.</b>	<b>Measuring the Berry phase</b>	<b>59</b>
5.1.	An analogy with the Aharonov-Bohm effect . . . . .	59
5.2.	The experimental procedure . . . . .	60
5.2.1.	The sequence . . . . .	61
5.2.2.	Experimental parameters . . . . .	63
5.2.3.	Experimental caveats . . . . .	64
5.3.	Experimental results . . . . .	66
5.3.1.	Detecting the Berry flux . . . . .	67
5.3.2.	Self-referenced interferometry near the Dirac point . . . . .	68
5.3.3.	Moving and annihilating Dirac cones . . . . .	69
<b>6.</b>	<b>Bloch state tomography with Wilson lines</b>	<b>73</b>
6.1.	Wilson lines in the $s$ -bands of the honeycomb lattice . . . . .	74
6.1.1.	Wilson-Zak loop eigenvalues . . . . .	74
6.1.2.	Bloch state tomography . . . . .	74
6.2.	Reconstructing eigenstates: the Bloch sphere picture . . . . .	76
6.2.1.	Extracting the polar angle $\theta_{\mathbf{q}}$ . . . . .	77
6.2.2.	Extracting the azimuthal angle $\phi_{\mathbf{q}}$ . . . . .	77
6.2.3.	Gauge-invariance of $\phi_{\mathbf{q}}$ and $\theta_{\mathbf{q}}$ . . . . .	79
6.3.	Experimental details . . . . .	80
6.3.1.	Experimental parameters . . . . .	80
6.3.2.	Reaching the strong gradient regime . . . . .	81
6.3.3.	The effect of higher bands . . . . .	83
6.3.4.	Data analysis . . . . .	83
6.4.	Experimental results . . . . .	85
6.4.1.	Measuring $\theta_{\mathbf{q}}$ . . . . .	85
6.4.2.	The real-space picture . . . . .	85
6.4.3.	Measuring $\phi_{\mathbf{q}}$ . . . . .	88
6.5.	Determining the Wilson-Zak loop eigenvalues . . . . .	89
6.5.1.	Decomposition of the Wilson line into $U(1)$ and $SU(2)$ . . . . .	89
6.5.2.	The back-tracking condition . . . . .	91
6.5.3.	Wilson-Zak loop eigenvalues with and without inversion symmetry . . . . .	92
6.5.4.	Wilson-Zak loop eigenvalues and the real-space embedding . . . . .	93

<b>7. Conclusion and Outlook</b>	<b>95</b>
7.1. Outlook . . . . .	96
7.1.1. Preliminary experiments . . . . .	98
7.1.2. Next steps . . . . .	101
7.1.3. Future endeavors . . . . .	102
<b>A. Experimental details</b>	<b>105</b>
A.1. The vacuum setup . . . . .	105
A.1.1. The magnetic transport coils and the experiment cell . . . . .	107
A.2. The laser setup . . . . .	110
A.2.1. Cooling in the $2D^+$ -MOT and 3D-MOT . . . . .	110
A.2.2. Optical dipole trap and lattice lasers . . . . .	111
A.3. The experimental sequence . . . . .	112
<b>B. Numerical calculation of the Wilson line</b>	<b>119</b>
<b>Bibliography</b>	<b>121</b>
<b>Acknowledgements</b>	<b>137</b>



# Chapter 1.

## Introduction

In condensed matter physics, band theory describes the approximation of the complex many-body problem of electrons in a solid by that of a single-particle in a periodic potential [1]. At first glance, this approximation may seem unreasonably extreme, as it neglects all interaction effects and the inevitable impurities and deformations present in any real solid. However, band theory has been remarkably successful in describing a wide range of condensed matter phenomena and forms the foundation for our understanding of material properties. For example, the eigenvalues of the single-particle Schroedinger equation are discretely spaced for a given quasimomentum, forming bands of allowed energies. The collection of these bands forms a band structure and explains the difference between metals, insulators, and semiconductors. Although many insights can be derived from the energy bands alone, they are, however, not the complete story. In 1980, the experimental discovery of the integer quantum Hall effect [2] propelled band theory in a new direction where the band eigenstates and their geometric structure take center stage.

In the integer quantum Hall effect, the Hall conductivity of a 2D semiconductor at low temperatures and high magnetic fields is quantized in integer units of  $e^2/h$ . Moreover, this quantization is remarkably robust to variations in the details of the device, such as its precise shape, material, or fabrication process [3]. In fact, already in 1987, measurements in four different samples yielded the same results within  $5 \times 10^{-9}$  [4]. Presently, the Hall conductivity is particularly relevant for metrological applications [3]: it has been measured to better than one part in a billion and is used to define the standard of resistance [5].

The robust quantization in the integer quantum Hall effect is a hallmark of phenomena with topological underpinnings. In mathematics, the branch of topology aims to group geometric objects into broad classes based on their global properties. For example, 2D surfaces are topologically classified by their genus, which counts the number of holes. The genus can be expressed in terms of a topological invariant that is given by the integral of the local curvature of the surface [6]. While the local curvature depends on the geometry, the total integral is independent of these details and reflects the topology of the object.

In condensed matter physics, there exist analogous topological invariants that de-

scribe the topology of the band eigenstates. For example, the integer quantum Hall effect is characterized by the TKNN invariant, which remarkably relates the Hall response to the topology of the band eigenstates [7]. Similar to the genus, the TKNN invariant is obtained by integrating a local geometric quantity over the Brillouin zone; as before, while the integrand depends on details of the geometry, the final integral does not. The TKNN invariant, originally named after the authors Thouless, Kohmoto, Nightingale, and den Nijs who first formulated it, is also commonly called the Chern number.

The description of the integer quantum Hall effect in topological terms was more than just a particularly convenient formulation. It heralded a fundamentally new classification scheme for phases of matter [8–11]. Prior to the discovery of the integer quantum Hall effect, phases were solely classified according to the Landau-Ginzburg theory of spontaneous symmetry breaking [12]. For example, the transition from a paramagnet to a ferromagnet is accompanied by the breaking of rotational symmetry. Other examples include the broken translational symmetry of crystalline solids or the broken gauge symmetry of superfluids. The quantum Hall state, however, does not fit into this paradigm. Instead, the distinction between a quantum Hall state and, for example, a standard band insulating state is topological.

Practically, topological classification amounts to asking whether one gapped state can be transformed into another gapped state through a continuous deformation of the Hamiltonian, where a continuous deformation is defined as one that preserves the energy gaps of the system [8–11]. If so, these two states are topologically equivalent. If not, these two states are topologically distinct and a quantum phase transition must occur where the system becomes gapless. Topologically distinct states are characterized by different topological invariants. For example, the standard insulating state is said to be topologically trivial because its Chern number is zero, while the quantum Hall state is said to be topological because its Chern number is non-zero [8–11].

For many years after the discovery of the integer quantum Hall effect, there was the misconception that the conditions under which it appears, namely, broken time-reversal symmetry in a 2D system at low temperatures, were necessary for the existence of topological quantum states [9, 13]. Although it was clear by the early 90's that topological classification should be applicable beyond the quantum Hall states, not until 2005 was there a concrete physical model of a system both exhibiting topological order and preserving time-reversal symmetry [14]. Such systems are characterized by a  $\mathbb{Z}_2$  invariant and are now termed time-reversal invariant topological insulators, or, equivalently, quantum spin Hall insulators in 2D. The original model of a time-reversal invariant topological insulator required spin-orbit coupling on a graphene-like honeycomb lattice but was difficult to experimentally test due to the weak spin-orbit coupling in material graphene [15]. An alternative scheme using HgTe-CdTe semiconductor quantum wells was soon proposed in 2006 [16] and experimentally realized only one year later [17]. Around the same time, time-reversal invariant topological insulators were also theoretically predicted in 3D systems [18–20], with the first experimental

---

confirmation in 2008 [21].

The extended band theory that takes into account the geometric aspects of the band eigenstates is termed topological band theory and, like its predecessor, is formulated in a single-particle framework [9, 22]. Although rooted in the mathematical theory of fiber bundles, many aspects of topological band theory can be derived from considering the adiabatic evolution of quantum mechanical systems. This very general problem was first examined by Berry in 1984, separate from considerations of band structures [23]. Berry's main result was that a non-degenerate eigenstate accumulates a geometric phase, in addition to the standard dynamical phase, as the parameters of its Hamiltonian are adiabatically varied. This geometric phase is physically significant and, as its name suggests, depends only on the geometric aspects of the evolution, such as the shape of the evolution path, and not on the time taken for the evolution (provided that the adiabaticity condition is fulfilled). The geometric phase is also commonly termed the Berry phase, or, in a 2D system, the Berry flux.

Berry's ideas were particularly important because they encapsulated abstract mathematical notions in a very physical problem. The link between adiabatic quantum evolution and holonomies in fiber bundles, first noted by Simon in 1983<sup>1</sup>, was crucial to connecting Berry's phase to the quantization of the Hall conductivity in the integer quantum Hall effect [25]. Presently, topological band theory is routinely couched in terms of Berry's phases, their generalizations, and associated quantities [22]. For example, the Chern number can be formulated in terms of a quantity called the Berry curvature [8, 9, 26]. Beyond providing an accessible formulation, the physical intuition behind Berry's work hints at how we might ultimately probe the geometric aspects of band structures: applied to condensed matter systems, the Berry phase results from integrating a quantity determined by the geometric structure of the band eigenstates over the reciprocal space. This suggests that an evolution of the quasimomentum might be required, which is precisely the route we take in our experiments.

## Ultracold atoms in optical lattices

Inspired by the advances in solid state systems, there has been intense interest and rapid progress within the last decade in exploring the geometric and topological aspects of band structures using ultracold atoms in optical lattices. In comparison to real materials, ultracold atom systems offer exceptionally clean and tunable environments [27]. A variety of lattice geometries can be created [27–32], disorder can be added at will [33–36], fermions or bosons or mixtures of both can be used [37], and the interactions between particles can be tuned via Feshbach resonances [38]. Furthermore, high resolution imaging at the single-atom level is now possible for both

---

<sup>1</sup> It was Simon who first coined the term "Berry's phase." Simon's paper actually preceded Berry's paper, which took almost a year to be published after it was received by the journal. Apparently, one of the referees eventually confessed to having lost the manuscript [24].

bosons [39–42] and fermions [43–46], promising access to new observables. Detailed reviews on the attributes and applications of optical lattice systems as quantum simulators for general condensed matter phenomena can be found in Refs. [27, 37, 47–49]. Closer to the contents of this thesis, Refs. [50–52] review progress on mimicking the effects of electromagnetic fields with neutral atoms. More recently, there has also been growing interest in using ultracold atoms to explore high-energy physics [53, 54].

Although they have emerged as promising candidates for the study of geometric and topological phenomena that might otherwise be hindered by the complexity of real solids, ultracold atom systems also come with their own set of challenges. One such challenge concerns the detection of geometric quantities. For example, geometric features in 2D solid state materials are probed by transport measurements [15]. While analogous measurements have been made in ultracold atom experiments [55–58], they do not match the quantitative level of precision achievable in solid state systems. Therefore, new detection techniques are needed both to better adapt condensed matter methods and (perhaps more) to exploit the opportunity to access observables without condensed matter analogues. Next, many of the basic effects that give rise to topological insulators or quantum Hall effects, such as spin-orbit coupling or even the electronic charge necessary for the Lorentz force, are naturally found in real solids but absent from our neutral atoms in optical lattices. Hence, in addition to questions of detection, a second primary goal of the field is to engineer systems with interesting geometric or topological features.

Significant advances have already been made on both fronts. Since many topological phenomena in solid state systems occur in the presence of magnetic fields, one main direction has been to simulate this behavior by creating artificial magnetic fields for neutral atoms. In continuum systems, pioneering experiments exploited Raman couplings between internal and motional atomic states to create both synthetic electric [59] and magnetic fields [60]. Soon afterwards, by implementing an early proposal based on imprinting Peierls phases via laser-assisted tunneling [61], strong effective magnetic fields were created in a lattice system [62]. Although the fields in this experiment were staggered, the same approach was then extended to engineer a strong uniform magnetic field [63], thereby realizing the Harper-Hofstadter Hamiltonian [64]. Alternatively, there has also been significant interest in using periodically driven optical lattice systems to directly modify the band structure [65–67]. In particular, periodic modulation of the phase or frequency of the lattice beams, colloquially termed “shaking” the lattice, has been used to alter the dispersion of a 1D lattice [68] and both the dispersion and topological structure of a 2D hexagonal lattice [55]. In the latter experiment, the shaking modified next-nearest neighbor tunnelings to realize the Haldane model, a Hamiltonian which exhibits topologically distinct phases with broken time-reversal symmetry but, in contrast to the integer quantum Hall effect, in the absence of a magnetic field [69].

In parallel to the advances in creating topological systems, there has also been steady progress in developing novel detection methods by combining adaptations of tradi-

---

tional solid state techniques with the newly available possibilities in optical lattice systems. For example, measurements analogous to the edge state detection methods commonly used in solid state materials have also been made in a synthetic 2D lattice of an ultracold atom system [57]. Other transport-based techniques have relied on the anomalous velocity acquired by particles probing areas of non-zero Berry curvature [26, 70]. This deflection of the atomic cloud was used to qualitatively map out the Haldane phase diagram [55] and quantitatively measure the Chern number [56]. Thus far, these experiments have all probed indirect signatures of band topology. However, the control afforded by ultracold atom systems also offers the unique opportunity for a direct investigation [71–73], which can often be more straightforward: instead of first identifying and then measuring responses to the band geometry, we simply measure the band geometry itself. This is especially beneficial in increasingly complex systems, where multiple effects might manifest in similar ways and it becomes difficult to identify the appropriate observables.

In this thesis, we present two methods to directly map the band geometry using a Bose-Einstein condensate (BEC) in a graphene-like optical honeycomb lattice [31, 74]. Although its band structure is not topological, several features of the honeycomb lattice make it an ideal testing ground for our detection methods. Notably, as a consequence of its two-site unit cell, the lowest band of the honeycomb lattice splits into two bands with Dirac points at the corners of the Brillouin zone [22, 75]. These Dirac points carry a  $\pi$  Berry flux, corresponding to a perfectly localized Berry curvature, and are stable against small perturbations in the presence of both time-reversal and inversion symmetry [22]. In the first set of experiments (Chapter 5), we employ an interferometric technique to directly locate and measure this  $\pi$  Berry flux. Furthermore, we are able to detect its eventual annihilation when perturbations of the system are sufficiently large. Although our experiments probe the Berry curvature only in a part of the Brillouin zone, this method can in principle be extended to map the Berry curvature over the entire Brillouin zone, thereby obtaining the Chern number of the system.

In the second set of experiments (Chapter 6), we exploit the large energy separation between the lowest two bands and higher bands of the honeycomb lattice to realize dynamics that are described by Wilson lines, which are matrix-valued generalizations of the Berry phase to degenerate bands [76]. The motivation is two-fold. First, the eigenvalues of Wilson lines can be used to formulate the  $\mathbb{Z}_2$  invariant, which characterizes time-reversal invariant topological insulators [77]. Second, in systems such as ours or the Haldane model, where the  $\mathbb{Z}_2$  invariant is zero, the Wilson line simplifies to enable a comparison between band eigenstates at any quasimomentum. Consequently, by comparing all other band eigenstates to those at a reference quasimomentum, we can perform a complete tomographic reconstruction of the band eigenstates as an alternative method for mapping out band structures.

## Thesis contents

In the next chapter, we briefly review the basics of geometric phases, before examining the problem of a single particle in a periodic potential subjected to a constant force. We show that both experiments can be understood within this framework: the Berry phase can be measured when using a small force, while the Wilson line measurement requires a large force. While our calculations in this chapter are general and can be applied to any lattice, we then specifically examine the case of a honeycomb lattice in Chapter 3. We first look at the tight-binding model to gain some intuition for the system. We derive important geometric quantities and use a Bloch sphere representation to illustrate the behavior of the band eigenstates under various lattice parameters. The experiment, however, does not necessarily take place in the tight-binding regime. Therefore, the tight-binding discussion is followed by a numerical *ab-initio* calculation, which can be compared with experimental data.

In Chapter 4, we present the experimental setup, beginning with the creation of the optical honeycomb lattice. We note the parameters required for an ideal honeycomb lattice, a honeycomb lattice with non-isotropic tunneling, and a honeycomb lattice with an energy offset between sublattice sites. Next, we discuss the preparation of a BEC, its evolution in reciprocal space, and its detection. We conclude the chapter by combining these three steps for use in some applications: we first examine both adiabatic and non-adiabatic Bloch oscillations and then perform Stückelberg interferometry to calibrate the lattice depth.

Next, the main experiments are described. In Chapter 5, we employ spin-echo interferometry to directly measure the  $\pi$ -phase shift acquired by a particle encircling a Dirac cone in reciprocal space. In Chapter 6, we use a strong gradient to effectively “collapse” the two lowest bands of the honeycomb lattice to realize a two-fold degenerate system with dynamics described by Wilson lines. Lastly, we conclude this thesis in Chapter 7 and discuss possible extensions of our work.

We note that a more detailed discussion of the experiments in Chapter 5 can be found in Ref. [78].

## Publications

- **Bloch state tomography using Wilson lines.**

Tracy Li, Lucia Duca, Martin Reitter, Fabian Grusdt, Eugene Demler, Manuel Endres, Monika Schleier-Smith, Immanuel Bloch, Ulrich Schneider.

[Science 352, 1094-1097 \(2016\).](#)

- **An Aharonov-Bohm interferometer for determining Bloch band topology.**

Lucia Duca, Tracy Li, Martin Reitter, Immanuel Bloch, Monika Schleier-Smith, Ulrich Schneider.

[Science 347, 288-292 \(2015\).](#)

## Chapter 2.

# Geometric quantities in Bloch bands

The (relatively) recent realization that material properties are determined not only by the dispersion but also the geometric structure of the Bloch bands has been one of the most fruitful and exciting developments in band theory. In this chapter, by considering the evolution of a quantum mechanical system, we define the quantities that describe the band geometry and examine how they can be measured.

To gain some physical intuition, we begin with the classical transport of a vector on a manifold. At the end of a cycle, the vector may have rotated compared to its initial orientation. This difference in angle is analogous to the Berry phase acquired by a quantum state [79, 80]. Here, we simply state the form of Berry's phase and its related quantities. We have omitted a detailed derivation, as there already exist many excellent discussions in literature. A pedagogical introduction can be found in most contemporary quantum mechanics texts, such as Refs. [81, 82]. There are also numerous more specialized resources, such as Refs. [15, 24, 26, 79, 80, 83], that include experimental confirmations and discuss applications in specific fields.

Following the overview of the Berry's phase, we specifically consider geometric quantities in band structures. We examine the scenario of a particle confined in a periodic potential in the presence of a constant, external force and find that a geometric quantity termed the Berry connection arises in the equations of motion. To gain some intuition for this system, we examine two limiting cases of a very small and very large force. While the former case leads to the Berry phase, the latter case yields the Wilson line, which is a generalization of the Berry phase to degenerate systems [76].

Next, having discussed how various geometric quantities arise in band structures, we examine their gauge-invariance (or lack thereof). This helps us understand which quantities are actually measurable and which quantities are merely useful mathematical tools. To conclude the chapter, we give a general overview of how the Berry phase and Wilson line will be measured in our system.

## 2.1. Geometric phases in brief

An intuitive understanding of the geometric quantities associated with Bloch bands can be derived from considering the parallel transport of a vector on a manifold. Par-

allel transport means that a vector should be moved such that its length and direction are constant [79]. Imagine that the vector lies on a plane tangent to some manifold at a given point along our transport path. Next, we define a coordinate system on this tangent plane. Parallel transport means our vector remains the same length in the tangent plane at a fixed orientation relative to this coordinate system (i.e., it should not rotate) for every point along the transport path.

Let us first consider the case of transport along a closed path on a plane, as illustrated in Fig. 2.1a. Here, the tangent plane is simply the plane itself at every point along the path. When the vector returns to its initial position, its orientation is the same as its initial orientation. In contrast, as illustrated in Fig. 2.1b, transport along a closed path on a sphere results in a rotation of the vector compared to its initial orientation. The difference in angle between the vector at the start and end of its cycle is known as the holonomy or anholonomy and is a consequence of the curvature of the sphere [79, 80, 83].

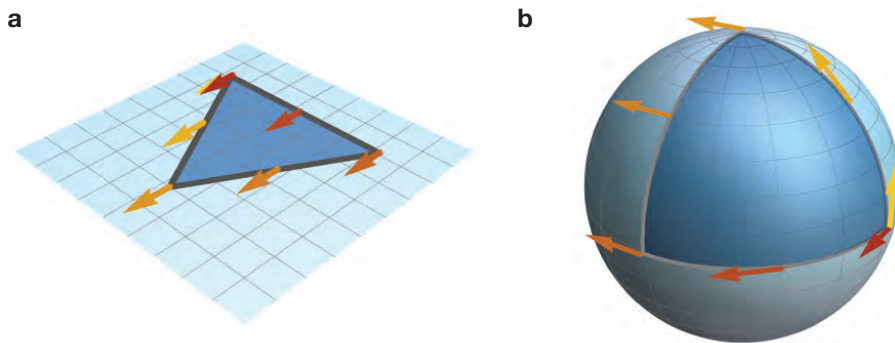


Figure 2.1.: **Parallel transport of vectors on manifolds.** The cyclic and adiabatic evolution of a quantum state is analogous to the cyclic transport of a vector on the surface of a manifold. If the surface is flat (**a**), the vector remains unchanged while traveling (red to yellow vectors) and, at the end of the cycle, points along its initial orientation. In contrast, if the surface is curved—such as the surface of a sphere (**b**)—the vector rotates during transport and, at the end of the cycle, does not return to its initial orientation. This rotation angle is a direct measure of the curvature of the surface within the closed path and depends only on the geometry of the loop and the surface, but not on the speed of the movement. Just as cyclic transport of a vector on a manifold can lead to non-zero rotation, the cyclic and adiabatic transport of a quantum state in some parameter of the Hilbert space can yield a non-zero Berry phase.

A similar phenomenon occurs in the evolution of quantum mechanical systems, where the quantum state plays the role of the vector and the Hilbert space is analogous to the manifold. A particularly important case of quantum evolution is the *adiabatic and cyclic* evolution of a quantum state, which was delineated by M. Berry in 1984 [23]. In his seminal paper, Berry considered the evolution of an eigenstate as the parameters of its Hamiltonian are adiabatically and cyclically varied. At the end of the evolution, when the Hamiltonian parameters form a closed path in parameter space, the eigen-

state returns to itself but has picked up a phase factor. This phase factor is comprised of a dynamical part which depends on the time taken en-route, and a geometric part given by

$$\oint_{\mathcal{C}} i \langle \Psi | \nabla_{\mathbf{x}} | \Psi \rangle \cdot d\mathbf{x}, \quad (2.1)$$

where  $|\Psi\rangle$  is the state,  $\nabla_{\mathbf{x}}$  takes partial derivatives with respect to the variable  $\mathbf{x}$ ,  $\mathbf{x}$  parametrizes the change in the Hamiltonian, and the contour  $\mathcal{C}$  forms a closed path in parameter space. Notably, this geometric phase, now commonly called Berry's phase, depends only on the geometry of the path.

Returning to our example above, the Berry's phase acquired in the cyclic evolution of a quantum state in the Hilbert space is analogous to the holonomy acquired in the cyclic evolution of a vector on a manifold. Two important quantities associated with the Berry phase are the Berry connection and the Berry curvature. The Berry connection specifies the conditions for parallel transport of the quantum state [79], in analogy to our rules for parallel transport of the vector, i.e., that it does not change direction or length. In Eq. 2.1, the Berry connection is the integrand. The Berry curvature, as its name suggests, influences the Berry phase of the quantum state as the curvature of the manifold influences the holonomy of the vector. By Stokes' theorem, the Berry curvature is curl of the Berry connection [84]. We shall later examine these terms in more detail.

Since their inception, Berry's ideas have found widespread applications in physics and inspired a multitude of work [83]. A particularly important generalization of Berry's phase was made by Wilczek and Zee in 1984 when they considered adiabatic evolution in degenerate systems, where adiabatic now means that the evolution always stays in the subspace of degenerate states [76]. In this case, the initial state is transformed by a matrix called the Wilson line, a term which originally comes from the field of quantum chromodynamics [85]. In fact, in their paper, Wilczek and Zee were not considering questions of band structures but rather noting the remarkable fact that the same mathematical structures arise in both the adiabatic evolution of simple quantum mechanical systems and the more complex gauge theories of fundamental interactions [76].

Since it is a matrix, the Wilson line can result in population changes between the degenerate states, in contrast to Berry phases which result only in the acquisition of a phase factor. Furthermore, Wilson lines can be non-commuting. For example, imagine taking two closed paths in parameter space. When the evolution is described by the Berry phase, the order in which the paths are taken does not matter because phase factors always commute. However, if the evolution is in a degenerate system, the final state could differ depending on which closed path is first traversed. This non-commuting or non-abelian property is central to proposals on geometric quantum computing [86, 87].

Paralleling the relationship between the Berry phase and Berry connection, the Wilson line is obtained by integrating a Berry connection matrix. Similar to the standard Berry connection, the Berry connection matrix specifies the rules for parallel transport, with the only difference being that the parallel transport now occurs in a more complex, degenerate subspace. Likewise, there is a quantity called the non-abelian Berry curvature that is analogous to the standard Berry curvature. However, in defining it from the Berry connection matrix, the curl is replaced by the covariant derivative [88]. Furthermore, in contrast to the standard, non-degenerate system, Stokes' theorem does not apply here, so there is no analogous formulation of the Wilson line in terms of the non-abelian Berry curvature [80]. In essence, there are related geometric quantities in degenerate and non-degenerate systems. However, in the case of the latter, the mathematics are often more involved and a physical picture less accessible.

## 2.2. Accessing geometric properties in Bloch bands

Having discussed geometric quantities arising from the evolution of general quantum systems, we now turn our attention to the specific case of band structures. We begin this section by defining some key quantities that will be used in calculating the equations of motion for a single particle in a periodic potential subject to a constant external force. We will see that the equations of motion will contain both dynamical factors that depend on the time taken for the evolution and geometric factors that are determined solely by the band geometry. Furthermore, we examine the two limiting cases of a very small and a very large force and find that the unitary evolution operator is the Berry phase factor and the Wilson line, respectively.

### 2.2.1. Preliminaries

The solutions to the Schroedinger equation of a single-particle in a periodic potential are given by the Bloch states  $\Phi_{\mathbf{q}}^n(\mathbf{r})$  and the energies  $E_{\mathbf{q}}^n$  [1]. The index  $\mathbf{q}$  is the quasi-momentum or crystal momentum. Since the Brillouin zones are periodic, the quasi-momentum can always be confined to the first Brillouin zone. At every  $\mathbf{q}$ , there are an infinite number of discretely spaced eigenenergies, which are labeled with the band index  $n$ . From Bloch's theorem, the Bloch state of band  $n$  at quasimomentum  $\mathbf{q}$  can be written as:

$$\Phi_{\mathbf{q}}^n(\mathbf{r}) = e^{i\mathbf{q}\cdot\mathbf{r}} u_{\mathbf{q}}^n(\mathbf{r}), \quad (2.2)$$

where  $e^{i\mathbf{q}\cdot\mathbf{r}}$  is a plane-wave and  $u_{\mathbf{q}}^n(\mathbf{r})$  is called the cell-periodic Bloch function because it has the same periodicity as the potential. That is, if  $\mathbf{R}$  is a direct lattice vector such that the potential  $V(\mathbf{r}) = V(\mathbf{r} + \mathbf{R})$ , then  $u_{\mathbf{q}}^n(\mathbf{r}) = u_{\mathbf{q}}^n(\mathbf{r} + \mathbf{R})$ . For simplicity, we will hence-

forth work in Dirac notation and set  $\hbar = 1$ . In Dirac notation, the Bloch state is

$$|\Phi_{\mathbf{q}}^n\rangle = e^{i\mathbf{q}\cdot\hat{\mathbf{r}}}|u_{\mathbf{q}}^n\rangle, \quad (2.3)$$

where  $\hat{\mathbf{r}}$  is the position operator.<sup>1</sup>

When a constant force is applied to this periodic system, the quasimomentum becomes time-dependent and the Bloch states are no longer the eigenstates of the (new) Hamiltonian [1]. For a force  $\mathbf{F}$ , the quasimomentum evolves as [1, 89]:

$$\mathbf{q}(t) = \mathbf{q}(0) + \mathbf{F}t. \quad (2.4)$$

The quasimomentum is now the time-dependent parameter of the Hamiltonian, yielding a system analogous to the one originally considered by Berry. In our subsequent derivation, we will similarly see the Berry connection naturally arises in the equations of motion.

In the Bloch bands, the Berry connection is defined by the cell-periodic Bloch functions as [26]:

$$\mathbf{A}_{\mathbf{q}}^{n,n'} = i\langle u_{\mathbf{q}}^n | \nabla_{\mathbf{q}} | u_{\mathbf{q}}^{n'} \rangle. \quad (2.5)$$

When  $n \neq n'$ , this quantity is often called the non-abelian Berry connection to distinguish it from the standard Berry connection, where  $n = n'$ . The Berry phase, as defined in Eq. 2.1, is the line-integral of the standard Berry connection (where  $n = n'$ ) in reciprocal space. There is no equivalent definition of a Berry phase for the non-abelian Berry connection. However, as we will later see, the non-abelian Berry connection is part of the matrix-valued Wilson line.

---

<sup>1</sup>The equivalence of Eqs. 2.3 and 2.2 can be shown by projecting Eq. 2.2 into the position-basis:

$$\begin{aligned} \langle \mathbf{r} | \Phi_{\mathbf{q}}^n \rangle &= \langle \mathbf{r} | e^{i\mathbf{q}\cdot\hat{\mathbf{r}}} | u_{\mathbf{q}}^n \rangle \\ &= \langle \mathbf{r} | (i\mathbf{q}\cdot\hat{\mathbf{r}} + \frac{(i\mathbf{q}\cdot\hat{\mathbf{r}})^2}{2!} + \dots) | u_{\mathbf{q}}^n \rangle \\ &= \langle \mathbf{r} | (i\mathbf{q}\cdot\mathbf{r} + \frac{(i\mathbf{q}\cdot\mathbf{r})^2}{2!} + \dots) | u_{\mathbf{q}}^n \rangle \\ &= \langle \mathbf{r} | e^{i\mathbf{q}\cdot\mathbf{r}} | u_{\mathbf{q}}^n \rangle \\ &= e^{i\mathbf{q}\cdot\mathbf{r}} \langle \mathbf{r} | u_{\mathbf{q}}^n \rangle \\ &\rightarrow \Phi_{\mathbf{q}}^n(\mathbf{r}) = e^{i\mathbf{q}\cdot\mathbf{r}} u_{\mathbf{q}}^n(\mathbf{r}) \end{aligned}$$

where we have expanded the exponential as  $(i\mathbf{q}\cdot\hat{\mathbf{r}} + \frac{(i\mathbf{q}\cdot\hat{\mathbf{r}})^2}{2!} + \dots)$  in the second line and used that the state  $|\mathbf{r}\rangle$  is an eigenstate of the position operator  $\hat{\mathbf{r}}$  as  $\hat{\mathbf{r}}|\mathbf{r}\rangle = \mathbf{r}|\mathbf{r}\rangle$  in the third line. We put the power series back as an exponential in the fourth line and, in the fifth line, used that  $e^{i\mathbf{q}\cdot\mathbf{r}}$  commutes with  $\langle \mathbf{r} |$ . This gives the Bloch state in Dirac notation projected onto the position-basis.

### 2.2.2. Derivation of the equations of motion

In the basis of the Bloch states, the Hamiltonian of the lattice is

$$\hat{H} = \sum_{\mathbf{q}, n} E_{\mathbf{q}}^n |\Phi_{\mathbf{q}}^n\rangle \langle \Phi_{\mathbf{q}}^n|. \quad (2.6)$$

where  $E_{\mathbf{q}}^n$  is the energy of the  $n$ th band at quasimomentum  $\mathbf{q}$ .

Adding a constant force  $\mathbf{F}$  to the system results in a Schroedinger equation

$$i\partial_t |\psi(t)\rangle = (\hat{H} - \mathbf{F} \cdot \hat{\mathbf{r}}) |\psi(t)\rangle. \quad (2.7)$$

We assume the initial state at  $t = 0$  is localized in reciprocal space at quasimomentum  $\mathbf{q}_0$  such that

$$|\psi(0)\rangle = \sum_n \alpha^n(0) |\Phi_{\mathbf{q}_0}^n\rangle \quad (2.8)$$

where  $|\alpha^n(0)|^2$  gives the population in the  $n$ th band at time  $t = 0$ . To solve Eq. 2.7, we express the time-evolved state  $|\psi(t)\rangle$  as a superposition of Bloch states:

$$|\psi(t)\rangle = \sum_n \alpha^n(t) |\Phi_{\mathbf{q}(t)}^n\rangle \quad (2.9)$$

Substituting Eqs. 2.9 and the time-dependence of the quasimomentum (Eq. 2.4 with  $\hbar = 1$ ) into Eq. 2.7 yields the following equation of motion for coefficient  $\alpha^n$ :

$$i\partial_t \alpha^n(t) = E_{\mathbf{q}(t)}^n \alpha^n(t) - \sum_{n'} \mathbf{A}_{\mathbf{q}(t)}^{n, n'} \cdot \mathbf{F} \alpha^{n'}(t) \quad (2.10)$$

where

$$\mathbf{A}_{\mathbf{q}(t)}^{n, n'} = i \langle u_{\mathbf{q}}^n | \nabla_{\mathbf{q}} | u_{\mathbf{q}}^{n'} \rangle |_{\mathbf{q}=\mathbf{q}(t)}. \quad (2.11)$$

This is precisely the Berry connection defined in Eq. 2.5. Therefore, from Eq. 2.10, we see that the evolution depends on the energies  $E_{\mathbf{q}(t)}^n$  and the Berry connections  $\mathbf{A}_{\mathbf{q}(t)}^{n, n'}$ . In the case of a single band, Eq. 2.5 reduces to an acquisition of the familiar dynamical and Berry phase factors.

Although these equations apply to any number of bands, we will focus on two-band systems, which is the most relevant for the experiments in this thesis. For a two-band system, the equations of motion in matrix-form are

$$i\partial_t \begin{pmatrix} \alpha^1(t) \\ \alpha^2(t) \end{pmatrix} = \begin{pmatrix} E_{\mathbf{q}(t)}^1 - A_{\mathbf{q}(t)}^{11} \cdot \mathbf{F} & -A_{\mathbf{q}(t)}^{12} \cdot \mathbf{F} \\ -A_{\mathbf{q}(t)}^{21} \cdot \mathbf{F} & E_{\mathbf{q}(t)}^2 - A_{\mathbf{q}(t)}^{22} \cdot \mathbf{F} \end{pmatrix} \begin{pmatrix} \alpha^1(t) \\ \alpha^2(t) \end{pmatrix} \quad (2.12)$$

Generally, Eq. 2.12 must be numerically solved. However, we can nonetheless gain some intuition by examining some qualitative features. To this end, it is useful to employ an analogy to the familiar quantum optics problem of a two-level atom in a laser field. Recall that, after making the rotating-wave approximation, the diagonal terms specify the detuning of the laser field to the atomic transition and the off-diagonal elements give the Rabi frequency, which parametrizes the coupling strength between the two levels.

In our system, the time-dependent Rabi frequency is

$$-2A_{\mathbf{q}(t)}^{12} \cdot \mathbf{F}. \quad (2.13)$$

Hence, we see that the non-abelian Berry connection is responsible for interband transitions. Similarly, the time-dependent detuning is

$$E_{\mathbf{q}(t)}^1 - A_{\mathbf{q}(t)}^{11} \cdot \mathbf{F} - (E_{\mathbf{q}(t)}^2 - A_{\mathbf{q}(t)}^{22} \cdot \mathbf{F}). \quad (2.14)$$

Here, the dispersion and the standard Berry connections play the role of the detuning.

In the case of a two-level atom interacting with a light-field, if the detuning is much larger than the Rabi frequency, interband transitions are suppressed. Conversely, if the Rabi frequency is much larger than the detuning, full population transfer can occur between the ground and excited states. In our system, the "knob" for tuning the strength of the Rabi frequency relative to the detuning is the magnitude of the force. Using a very small force enables us to neglect interband transitions, while using a very large force enables us to neglect the dispersion relation  $E_{\mathbf{q}}^n$ . Next, we more closely examine these two limiting cases.

### 2.2.3. Adiabatic motion: the Berry phase

We define using a "very small force" to mean that the atoms move in the Bloch bands but do not make transitions to other bands, i.e., the motion is adiabatic. Hence, the final distribution of the atomic population at the end of the evolution will be identical to that of the initial distribution of the atomic population. Consequently, the coefficients of the Bloch states only pick up (individual) phase factors during the course of the evolution and Eq. 2.12 reduces to

$$i\partial_t \begin{pmatrix} \alpha^1(t) \\ \alpha^2(t) \end{pmatrix} = \begin{pmatrix} E_{\mathbf{q}(t)}^1 - A_{\mathbf{q}(t)}^{11} \cdot \mathbf{F} & 0 \\ 0 & E_{\mathbf{q}(t)}^2 - A_{\mathbf{q}(t)}^{22} \cdot \mathbf{F} \end{pmatrix} \begin{pmatrix} \alpha^1(t) \\ \alpha^2(t) \end{pmatrix} \quad (2.15)$$

The unitary time-evolution operator governing the evolution of an initial state  $|\psi(0)\rangle$

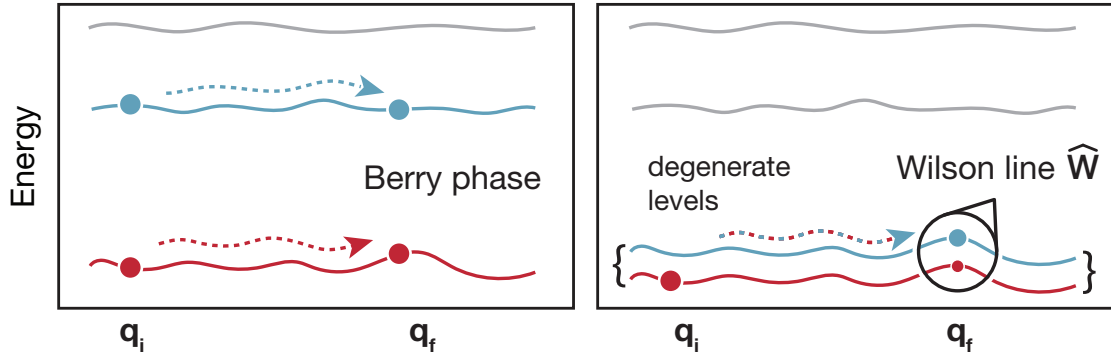


Figure 2.2.: **Berry phases and Wilson lines.** **a**, When the motion is adiabatic with respect to the energy differences between each occupied band in the system, the initial population distribution does not change. The evolution is equivalent to that of  $n$  independent bands, where  $n$  refers to the number of occupied bands. Here,  $n=2$  (blue and red bands). In each band, the state picks up a phase factor comprised of the dynamical phase and the (geometric) Berry's phase. **b**, When the force is sufficiently large, the effect of the dispersion relation in a given subset of bands can be neglected and the system becomes effectively degenerate. Instead of acquiring independent phase factors in each band, the initial state is transformed by the Wilson line matrix which can mix state populations. For example, atoms initially entirely in one band (red) may, at the end of the evolution, predominantly occupy the second band (larger blue circle).

to final state  $|\psi(t)\rangle$  is simply

$$|\psi(t)\rangle = \exp\left[-i \int dt \hat{\mathbf{E}}_{\mathbf{q}(t)}\right] \exp\left[i \int_{\mathcal{C}} d\mathbf{q} \hat{\mathbf{A}}_{\mathbf{q}}\right] |\psi(0)\rangle, \quad (2.16)$$

where the dispersion matrix  $\hat{\mathbf{E}}_{\mathbf{q}(t)}$  is a diagonal  $2 \times 2$  matrix with entries  $E_{\mathbf{q}(t)}^1$  and  $E_{\mathbf{q}(t)}^2$ . Likewise, the Berry connection matrix  $\hat{\mathbf{A}}_{\mathbf{q}}$  is a diagonal  $2 \times 2$  matrix with entries  $\mathbf{A}_{\mathbf{q}}^{11}$  and  $\mathbf{A}_{\mathbf{q}}^{22}$ . To write the integration of the Berry connection in terms of  $\mathbf{q}$  rather than time  $t$ , we made a change-of-variables using Eq. 2.4. The dispersion and Berry connection matrix separate because both are diagonal and therefore commute at every quasimomentum. For the same reason, path-ordering (or time-ordering) of the integration is not necessary.

From Eq. 2.16, we see that the population in each band simply acquires a phase factor during adiabatic evolution. This phase factor is comprised of a dynamical phase due to the band energy and a geometric phase due to the Berry connection. This geometric phase is no other than the Berry phase. Again, we see that the Berry phase depends only on the geometry of the path and not on the time taken to traverse the path.

### 2.2.4. Diabatic motion: the Wilson line

We define a “very large” force to mean that  $\mathbf{F}$  is large enough such that the Berry connection terms  $\mathbf{A}_{\mathbf{q}(t)}^{n,n'} \cdot \mathbf{F}$  are much greater than the dispersion  $E_{\mathbf{q}(t)}^n$ . Neglecting the energy term, Eq. 2.12 is

$$i\partial_t \begin{pmatrix} \alpha^1(t) \\ \alpha^2(t) \end{pmatrix} = \begin{pmatrix} -A_{\mathbf{q}(t)}^{11} \cdot \mathbf{F} & -A_{\mathbf{q}(t)}^{12} \cdot \mathbf{F} \\ -A_{\mathbf{q}(t)}^{21} \cdot \mathbf{F} & -A_{\mathbf{q}(t)}^{22} \cdot \mathbf{F} \end{pmatrix} \begin{pmatrix} \alpha^1(t) \\ \alpha^2(t) \end{pmatrix} \quad (2.17)$$

Accordingly, the evolution of a state  $|\psi(0)\rangle$  to  $|\psi(t)\rangle$  is given by

$$\begin{aligned} |\psi(t)\rangle &= \mathcal{T} \exp \left[ i \int dt \hat{\mathbf{A}}_{\mathbf{q}(t)} \cdot \mathbf{F} \right] |\psi(0)\rangle \\ &= \mathcal{P} \exp \left[ i \int_{\mathcal{C}} d\mathbf{q} \hat{\mathbf{A}}_{\mathbf{q}} \right] |\psi(0)\rangle \\ &\equiv \hat{\mathbf{W}}_{\mathbf{q}_i \rightarrow \mathbf{q}_f} |\psi(0)\rangle \end{aligned} \quad (2.18)$$

where  $\mathcal{C}$  is the path taken from initial quasimomentum  $\mathbf{q}_i$  to the final quasimomentum  $\mathbf{q}_f$ , and  $\mathcal{P}$  ( $\mathcal{T}$ ) is the path (time)-ordering operator. In contrast to the adiabatic case, path (time)-ordering is necessary because matrices  $\hat{\mathbf{A}}_{\mathbf{q}(t)}$ , which are generally not diagonal, may not commute at all integration points.

In contrast to the case of adiabatic evolution, which amounts to the independent acquisition of dynamical and geometric phase factors in each band, the unitary evolution operator here is not diagonal and can therefore mix state populations. This matrix  $\hat{\mathbf{W}}_{\mathbf{q}_i \rightarrow \mathbf{q}_f}$  is called the Wilson loop or Wilson line, depending on whether the evolution path is a closed loop or an open line [85]. For generality, we shall most commonly use the term Wilson line.

In our analysis, by neglecting the band energies, we effectively solved for the evolution of a degenerate system. That is, by moving very fast in a non-degenerate system, we can reach a regime where the dynamics are equivalent to moving adiabatically in a degenerate system. Furthermore, in contrast to adiabatic evolution in the bands which probes both the dispersion and the Berry connection, the strong-gradient evolution accesses only the geometric quantities of the bands. As a concrete example, consider a system containing only a single band. In this case, the Berry connection matrix has size  $1 \times 1$ . Integrating this Berry connection “matrix” yields the standard Berry phase of Sec. 2.2.3. Hence, Wilson lines are simply a generalization of the Berry phase factor to multiple, degenerate bands. In analogy, the eigenvalues of Wilson lines are known as the non-abelian Berry phases [90].

## 2.3. Gauge invariance: which quantities are measurable?

In quantum mechanics, transforming a state  $|\Psi\rangle \rightarrow |\Psi'\rangle = e^{i\gamma}|\Psi\rangle$  by a phase factor is termed a gauge-transformation [81, 82]. Quantities that are not affected by this gauge-transformation are termed gauge-invariant. For example, the mean position  $\langle\Psi|\hat{\mathbf{r}}|\Psi\rangle$  of the state  $|\Psi\rangle$  is a gauge-invariant quantity because the gauge-transformed quantity  $\langle\Psi'|\hat{\mathbf{r}}|\Psi'\rangle$  is equivalent to the original quantity. In fact, physical observables are always gauge-invariant, i.e., independent of basis choice.

In this section, we examine which geometric quantities are gauge-invariant and thereby measurable in the single- and multi-band case. Our analysis will show the importance of taking closed paths in parameter space.

### 2.3.1. Single-band geometric quantities

We begin by checking if the standard Berry connections are gauge-invariant by making the gauge-transformation

$$|u_{\mathbf{q}}^n\rangle \rightarrow e^{i\gamma_{\mathbf{q}}^n}|u_{\mathbf{q}}^n\rangle \quad (2.19)$$

The Berry connection ( $n = n'$ ) transforms as

$$\mathbf{A}_{\mathbf{q}}^{n,n} \rightarrow \mathbf{A}_{\mathbf{q}}^{n,n} + \nabla_{\mathbf{q}}\gamma_{\mathbf{q}}^n \quad (2.20)$$

Our analysis shows that the Berry connection is not gauge-invariant and is therefore not a measurable quantity.

Integrating the (standard) Berry connection over some path  $\mathcal{C}$  in reciprocal space yields the Berry phase. Under the same transformation given in Eq. 2.19, the Berry phase transforms as:

$$\begin{aligned} \int_{\mathcal{C}} d\mathbf{q}\mathbf{A}_{\mathbf{q}}^{n,n} &\rightarrow \int_{\mathcal{C}} d\mathbf{q}(\mathbf{A}_{\mathbf{q}}^{n,n} + \nabla_{\mathbf{q}}\gamma_{\mathbf{q}}^n) \\ &= \int_{\mathcal{C}} d\mathbf{q}\mathbf{A}_{\mathbf{q}}^{n,n} + (\gamma_{\mathbf{q}_f}^n - \gamma_{\mathbf{q}_i}^n), \end{aligned} \quad (2.21)$$

where  $\mathbf{q}_f$  and  $\mathbf{q}_i$  specify the final and initial points of the path  $\mathcal{C}$ . Here, we see that the Berry phase is, in general, not gauge-invariant. However, for a closed path where  $\mathbf{q}_f = \mathbf{q}_i$ , the term  $(\gamma_{\mathbf{q}_f}^n - \gamma_{\mathbf{q}_i}^n) = 0$ . Therefore, we see that for closed paths, the Berry phase is indeed gauge-invariant and measurable.

Another way of formulating the Berry phase is to use Stokes' theorem to relate the line-integral over a closed contour to an area integral [84]. Doing so gives an equivalent

expression of the Berry phase as

$$\int_{\mathcal{C}} d\mathbf{q} \mathbf{A}_{\mathbf{q}}^{n,n} = \int_S d^2\mathbf{q} \nabla \times \mathbf{A}_{\mathbf{q}}^{n,n} \quad (2.22)$$

where  $S$  is the surface enclosed by the path  $\mathcal{C} = \partial S$ . The quantity

$$\Omega_{\mathbf{q}}^n = \nabla \times \mathbf{A}_{\mathbf{q}}^{n,n} \quad (2.23)$$

is called the Berry curvature and gauge-transforms as:

$$\nabla \times \mathbf{A}_{\mathbf{q}}^{n,n} \rightarrow \nabla \times (\mathbf{A}_{\mathbf{q}}^{n,n} + \nabla_{\mathbf{q}} \gamma_{\mathbf{q}}^n) = \nabla \times \mathbf{A}_{\mathbf{q}}^{n,n} \quad (2.24)$$

Hence, the Berry curvature is gauge-invariant and therefore measurable. Since the Berry phase can be formulated in terms of an area integral, it is also sometimes called the Berry flux.

The gauge-invariance of the Berry curvature is particularly useful when we actually want to compute the Berry phase. This is because calculating the Berry connection requires the cell-periodic Bloch functions to be smooth and continuous because we need to take derivatives. However, numerical calculations generally assign random phase factors to each cell-periodic Bloch function. Although there are some prescriptions on how to then modify the gauge to obtain differentiable cell-periodic Bloch functions [91], it is often easier to avoid this gauge-choice issue altogether and use the Berry curvature to calculate the Berry phase [26].

### 2.3.2. Multi-band geometric quantities

Before examining the matrix-valued quantities, we first take a look at the non-abelian Berry connection  $\mathbf{A}_{\mathbf{q}}^{n,n'}$ , where  $n \neq n'$ . Although the (standard) Berry connection of a single band was gauge-dependent, under the same gauge-transformation of Eq. 2.19, the non-abelian Berry connection becomes

$$\mathbf{A}_{\mathbf{q}}^{n,n'} \rightarrow e^{i(\gamma_{\mathbf{q}}^n - \gamma_{\mathbf{q}}^{n'})} \mathbf{A}_{\mathbf{q}}^{n,n'} \quad \text{for } n \neq n' \quad (2.25)$$

Since it is transformed only by a phase factor, the absolute value of the non-abelian Berry connection is gauge-invariant and therefore a physical observable. Recall in the discussion near the end of Sec. 2.2.2 that the non-abelian Berry connection is responsible for coupling the bands. Therefore, the absolute value of the non-abelian Berry connection corresponds to a Rabi frequency, which we will later measure in Sec. 7.1.1.

When writing a state in terms of  $n$  basis states, the system has  $U(n)$  gauge-freedom. For example, in the single-band case, we had  $U(1)$  gauge-freedom, meaning that we were able to change the state by an arbitrary phase-factor. In the multi-band case, the

state  $|\Psi_{\mathbf{q}}\rangle = \begin{pmatrix} \alpha_{\mathbf{q}}^1 \\ \alpha_{\mathbf{q}}^2 \end{pmatrix}$  written in the basis of the Bloch states of the first and second band at quasimomentum  $\mathbf{q}$  transforms as

$$|\Psi_{\mathbf{q}}\rangle \rightarrow \hat{U}_{\mathbf{q}}|\Psi_{\mathbf{q}}\rangle, \quad (2.26)$$

where  $\hat{U}_{\mathbf{q}}$  is a quasimomentum-dependent  $U(2)$  matrix.

Under such a gauge-transformation, the Berry connection matrix  $\hat{\mathbf{A}}_{\mathbf{q}}$  becomes

$$\hat{\mathbf{A}}_{\mathbf{q}} \rightarrow \hat{U}_{\mathbf{q}}\hat{\mathbf{A}}_{\mathbf{q}}\hat{U}_{\mathbf{q}}^\dagger - i(\nabla_{\mathbf{q}}\hat{U}_{\mathbf{q}})\hat{U}_{\mathbf{q}}^\dagger. \quad (2.27)$$

Just like the standard Berry connection, the Berry connection matrix is gauge-dependent.

The Wilson line transforms as

$$\hat{\mathbf{W}}_{\mathbf{q}_i \rightarrow \mathbf{q}_f} \rightarrow \hat{U}_{\mathbf{q}_f}\hat{\mathbf{W}}_{\mathbf{q}_i \rightarrow \mathbf{q}_f}\hat{U}_{\mathbf{q}_i}^\dagger \quad (2.28)$$

and is also gauge-dependent. However, in analogy with the Berry phase, the eigenvalues of a Wilson loop, i.e., the Wilson line of a closed path, are gauge-invariant. If a state  $|\Psi_{\mathbf{q}_i}\rangle$  is an eigenstate of the Wilson line operator  $\hat{\mathbf{W}}_{\mathbf{q}_i \rightarrow \mathbf{q}_f}$  with eigenvalue  $\lambda$ , then a gauge transformation yields:

$$\begin{aligned} \hat{\mathbf{W}}'_{\mathbf{q}_i \rightarrow \mathbf{q}_f}|\Psi'_{\mathbf{q}_i}\rangle &= \hat{U}_{\mathbf{q}_f}\hat{\mathbf{W}}_{\mathbf{q}_i \rightarrow \mathbf{q}_f}\hat{U}_{\mathbf{q}_i}^\dagger\hat{U}_{\mathbf{q}_i}|\Psi_{\mathbf{q}_i}\rangle \\ &= \hat{U}_{\mathbf{q}_f}\lambda|\Psi_{\mathbf{q}_i}\rangle \\ &= \lambda|\Psi'_{\mathbf{q}_i}\rangle \quad \text{if } \mathbf{q}_f = \mathbf{q}_i \end{aligned} \quad (2.29)$$

The eigenvalues of a Wilson loop are often called the non-abelian Berry phases.

Finally, for completeness, we note that the non-abelian Berry curvature is defined as [26]

$$\mathcal{F}_{\mathbf{q}} = \nabla \times \mathbf{A}_{\mathbf{q}} - i\mathbf{A}_{\mathbf{q}} \times \mathbf{A}_{\mathbf{q}} \quad (2.30)$$

and gauge transforms as

$$\mathcal{F}_{\mathbf{q}} \rightarrow \hat{U}_{\mathbf{q}}\mathcal{F}_{\mathbf{q}}\hat{U}_{\mathbf{q}}^\dagger \quad (2.31)$$

Unlike the standard Berry curvature, the non-abelian Berry curvature is not gauge-invariant and therefore not an observable quantity.

### 2.3.3. A summary

We summarize the results of our gauge-invariance discussion in Table 2.1, where gauge-invariant quantities for a closed loop are denoted with an asterisk.. The most

relevant quantities for the experiments in this thesis are the Berry phase, Berry curvature, Wilson line, and the Wilson loop eigenvalues, i.e, the non-abelian Berry phases.

Single-band	Gauge-invariant?	Multi-band	Gauge-invariant?
Berry connection	No	Berry connection matrix	No
Berry phase factor	Yes	Wilson line	No
Berry phase	Yes	Wilson line eigenvalues	Yes
Berry curvature	Yes	Non-abelian Berry curvature	No
–	–	Non-abelian Berry connection	Only absolute value*

Table 2.1.: A summary of the geometric quantities in the single- and multi-band case. "Berry phase" refers to the phase itself, while "Berry phase factor" refers to the exponentiated Berry phase. The "gauge-invariant?" column answers whether the quantity is gauge-invariant when the path is closed. In the case of the non-abelian Berry connection, there is no single-band analog and the asterisk denotes that the absolute value is gauge-invariant even for non-closed paths.

## 2.4. A blueprint for the experiments

As we previously saw, by tuning the magnitude of the force, we can measure either the Berry phase or the Wilson line. In our experiments, the magnitude of the force is compared to the energy spacing between the two lowest bands of the honeycomb lattice. In the first experiment (Chapter 5), the gradient due to the force is small compared to this energy spacing, enabling us to measure the Berry phase associated with evolution in the lowest band. When the evolution encircles a Dirac cone, we observe a Berry phase of  $\approx \pi$ .

In contrast, in the second experiment (Chapter 6), the gradient due to the force is large compared to the energy spacing between the two lowest bands, enabling us to neglect the dispersion relations. Hence, we have an effectively two-fold degenerate system and the evolution is determined by the matrix-valued Wilson line. We then measure the elements of these Wilson lines in the basis of the band eigenstates, which enables us to directly reveal the geometric structure of the cell-periodic Bloch functions. Furthermore, we also access the gauge-invariant eigenvalues of Wilson loops closed by a reciprocal lattice vector.

For both experiments, the three main ingredients required are similar. We must<sup>2</sup>:

1. Prepare a quantum state at an initial quasimomentum  $\mathbf{q}_i$ :  $|\Psi_{\mathbf{q}_i}\rangle$
2. Evolve the state to final quasimomentum  $\mathbf{q}_f$ :  $\hat{\mathbf{W}}_{\mathbf{q}_i \rightarrow \mathbf{q}_f} |\Psi_{\mathbf{q}_i}\rangle$
3. Detect the new state  $\hat{\mathbf{W}}_{\mathbf{q}_i \rightarrow \mathbf{q}_f} |\Psi_{\mathbf{q}_i}\rangle$

These three ingredients are readily available in our cold-atom toolbox and detailed in our discussion of the experimental setup in Chapter 4. First, in the next chapter, we introduce the honeycomb lattice and examine its geometric attributes.

---

<sup>2</sup> Here, we have used the Wilson line as the evolution operator for generality. Recall that in the case of a single band, the Wilson line is simply the Berry phase factor.

## Chapter 3.

# The optical honeycomb lattice

We begin this chapter by deriving the single-particle tight-binding model for the honeycomb lattice, which contains two sites, A and B, in its unit cell. We examine the dispersion and eigenstates when A and B sites are degenerate and find a degeneracy in the energy spectrum (sec. 3.1.1). In the vicinity of this degeneracy, the dispersion is linear and resembles that of the massless Dirac equation. Appropriately, this degeneracy point is called the Dirac point. We show that taking even an infinitesimal loop around the Dirac point yields a Berry phase of  $\pi$ .

Next, we consider the dispersion and eigenstates when there is an energy offset between A and B sites (sec. 3.1.2). To more conveniently analyze the scenario, we introduce the Bloch sphere picture, where the evolution of an eigenstate in reciprocal space is visualized as a rotation of a vector of unit length. We illustrate the difference between evolutions in a lattice with degenerate and non-degenerate A and B sites. Furthermore, we show that paths that encircle a Dirac point enclose a non-zero solid angle on the Bloch sphere. We derive the relation between this solid angle and the Berry phase.

In the second part of this chapter, we introduce an *ab-initio* single-particle calculation for the optical honeycomb potential (Sec. 3.2). We compare the *ab-initio* and tight-binding dispersions and find that, although a minimum lattice depth is required before the *ab-initio* dispersion begins to closely resemble the tight-binding dispersion, the Dirac points are always present even at very low lattice depths (Sec. 3.2.3). Lastly, in order to better understand the appearance of multiple sets of bands in the *ab-initio* calculation, we consider the limiting cases of a vanishing and very deep lattice, where the system is that of a free-particle and a harmonic oscillator, respectively.

### 3.1. The tight-binding model

The honeycomb lattice is not a monoatomic Bravais lattice, but rather a Bravais lattice with a two-site unit cell. It can be decomposed into two triangular sublattices composed of A and B sites (see Fig. 3.1a). The primitive direct lattice vectors spanning the

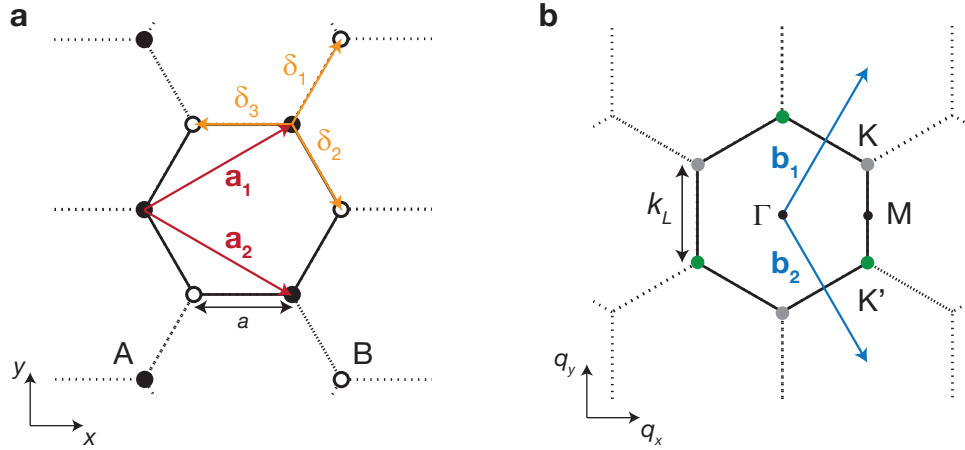


Figure 3.1.: **Real-space lattice and reciprocal space Brillouin zones.** **a**, The honeycomb lattice is comprised of two triangular Bravais sublattices, A and B. The triangular A sublattice is spanned by primitive direct lattice vectors  $\mathbf{a}_1$  and  $\mathbf{a}_2$ . Hopping from an A site (solid circles) to B sites (open circles) occurs along three directions  $\delta_1, \delta_2$ , and  $\delta_3$ . The distance between nearest-neighbor A and B sites is  $a$ . **b**, The Brillouin zone is spanned by primitive reciprocal lattice vectors  $\mathbf{b}_1$  and  $\mathbf{b}_2$ . It contains high-symmetry points  $\Gamma$ , at the center, M at the edge, and K and K' at the corners of the Brillouin zone. The corner points K and K' are non-equivalent as they are not related by a reciprocal lattice vector. This is emphasized by the different gray and green coloring of the K and K' points, respectively.

A-sublattice can be chosen to be

$$\begin{aligned}\mathbf{a}_1 &= \frac{a}{2}(3, \sqrt{3}) \\ \mathbf{a}_2 &= \frac{a}{2}(3, -\sqrt{3}),\end{aligned}\quad (3.1)$$

where  $a$  is the distance between neighboring A and B sites. The A (B) sublattice is defined by points with position vectors  $\mathbf{r}_{A(B)}$  that are linear combinations of the primitive direct lattice vectors. For integers  $m_1, m_2, n_1$  and  $n_2$  ranging from  $-\infty$  to  $+\infty$ ,

$$\begin{aligned}\mathbf{r}_A &= m_1 \mathbf{a}_1 + m_2 \mathbf{a}_2 \\ \mathbf{r}_B &= n_1 \mathbf{a}_1 + n_2 \mathbf{a}_2 + \delta_3,\end{aligned}\quad (3.2)$$

The A and B sublattice sites are coupled via nearest-neighbour lattice vectors  $\delta_i$ , where

$$\begin{aligned}\delta_1 &= \frac{a}{2}(1, \sqrt{3}) \\ \delta_2 &= \frac{a}{2}(1, -\sqrt{3}) \\ \delta_3 &= a(-1, 0)\end{aligned}\quad (3.3)$$

Associated with the real-space lattice is a reciprocal lattice. The primitive reciprocal lattice vectors  $\mathbf{b}_i$  ( $i = 1, 2$ ) that fulfill the condition  $\mathbf{a}_i \cdot \mathbf{b}_i = 2\pi\delta_{ij}$  [1], where  $\delta_{ij}$  is the Kronecker delta, are

$$\begin{aligned}\mathbf{b}_1 &= \frac{2\pi}{3a}(1, \sqrt{3}) = k_L\left(\frac{\sqrt{3}}{2}, \frac{3}{2}\right) \\ \mathbf{b}_2 &= \frac{2\pi}{3a}(1, -\sqrt{3}) = k_L\left(\frac{\sqrt{3}}{2}, -\frac{3}{2}\right),\end{aligned}\quad (3.4)$$

where we have defined  $k_L = \frac{4\pi}{3\sqrt{3}a}$ .

The reciprocal lattice, like the direct lattice, has a honeycomb structure. High-symmetry points  $\Gamma$ , located at the center of the Brillouin zone, M, located at the edge of the Brillouin zone, and K ( $K'$ ), located at the corners of the Brillouin zone are illustrated in Fig. 3.1b. We emphasize that points K and  $K'$  are inequivalent, as a K point cannot be reached from a  $K'$  point by a reciprocal lattice vector. The importance of these points, known as Dirac points, will become apparent in the next sections.

The single-particle Hamiltonian describing nearest-neighbor hopping between A and B sites with hopping amplitude  $J$  and an energy difference  $\Delta$  between A and B sites can be written as

$$\begin{aligned}\hat{H}_{tb} &= -J \sum_{\langle \mathbf{R}_B, \mathbf{R}_A \rangle} |w_{\mathbf{R}_B}\rangle \langle w_{\mathbf{R}_A}| + c.c \\ &+ \frac{\Delta}{2} \sum_{\langle \mathbf{R}_A, \mathbf{R}_A \rangle} (|w_{\mathbf{R}_A}\rangle \langle w_{\mathbf{R}_A}| - |w_{\mathbf{R}_B}\rangle \langle w_{\mathbf{R}_B}|),\end{aligned}\quad (3.5)$$

where  $|w_{\mathbf{R}_{A(B)}}\rangle$  are the Wannier states localized on the A (B) sites.

Furthermore, in analogy to the Bloch states, we define quasimomentum-dependent states  $|\Phi_{\mathbf{q}}^{A(B)}\rangle$  of the A (B) sites as

$$|\Phi_{\mathbf{q}}^A\rangle = \frac{1}{\sqrt{N}} \sum_{\mathbf{r}_A} e^{i\mathbf{q}\cdot\mathbf{r}_A} |w_{\mathbf{r}_A}\rangle = e^{i\mathbf{q}\cdot\hat{\mathbf{r}}} |u_{\mathbf{q}}^A\rangle \quad (3.6)$$

$$|\Phi_{\mathbf{q}}^B\rangle = \frac{1}{\sqrt{N}} \sum_{\mathbf{r}_B} e^{i\mathbf{q}\cdot\mathbf{r}_B} |w_{\mathbf{r}_B}\rangle = e^{i\mathbf{q}\cdot\hat{\mathbf{r}}} |u_{\mathbf{q}}^B\rangle, \quad (3.7)$$

where  $N$  denotes the number of lattice sites and  $|u_{\mathbf{q}}^{A(B)}\rangle$  are the analogous cell-periodic Bloch functions of the A (B) sites.

In the basis of  $|\Phi_{\mathbf{q}}^A\rangle$  and  $|\Phi_{\mathbf{q}}^B\rangle$ , the Hamiltonian describing the two lowest bands of the honeycomb lattice is

$$\hat{H}_{\mathbf{q}}^{\text{tb}} = \begin{pmatrix} \Delta/2 & t_{\mathbf{q}} \\ t_{\mathbf{q}}^* & -\Delta/2 \end{pmatrix}, \quad (3.8)$$

where

$$t_{\mathbf{q}} = |t_{\mathbf{q}}| e^{i\vartheta_{\mathbf{q}}} = J \sum_{i=1}^3 e^{-i\mathbf{q} \cdot \delta_i} \quad (3.9)$$

This Hamiltonian is diagonalized by eigenstates

$$|\Phi_{\mathbf{q}}^{1(2)}\rangle = \frac{1}{\sqrt{|f_{\mathbf{q}}^{1(2)}|^2 + 1}} \left( f_{\mathbf{q}}^{1(2)} e^{i\vartheta_{\mathbf{q}}} |\Phi_{\mathbf{q}}^A\rangle - |\Phi_{\mathbf{q}}^B\rangle \right), \quad (3.10)$$

where  $f_{\mathbf{q}}^{1(2)} = \frac{\Delta - (+)\sqrt{\Delta^2 + 4|t_{\mathbf{q}}|^2}}{2|t_{\mathbf{q}}|}$ .

The corresponding eigenenergies are

$$E_{\mathbf{q}}^{1(2)} = \frac{-(+)\sqrt{\Delta^2 + 4|t_{\mathbf{q}}|^2}}{2}. \quad (3.11)$$

### 3.1.1. $\Delta = 0$ : Dirac points and Berry phases

When  $\Delta = 0$ ,  $f_{\mathbf{q}}^{1(2)} = -(+)1$  and the expression of the eigenstates in Eq. 3.10 reduces to

$$|\Phi_{\mathbf{q}}^{1(2)}\rangle = \frac{1}{\sqrt{2}} \left( -(+) e^{i\vartheta_{\mathbf{q}}} |\Phi_{\mathbf{q}}^A\rangle - |\Phi_{\mathbf{q}}^B\rangle \right). \quad (3.12)$$

That is, when the A and B sites are at the same energy, the eigenstates are in an equal superposition of the Bloch states of the A and B sites at every quasimomentum. Using Eq. 3.12, the standard Berry connections of the first and second band are

$$\mathbf{A}_{\mathbf{q}}^{11} = \mathbf{A}_{\mathbf{q}}^{22} = \frac{1}{2} \nabla_{\mathbf{q}} \vartheta_{\mathbf{q}} \quad (3.13)$$

and the off-diagonal or non-Abelian Berry connections are

$$\mathbf{A}_{\mathbf{q}}^{12} = \mathbf{A}_{\mathbf{q}}^{21} = -\frac{1}{2} \nabla_{\mathbf{q}} \vartheta_{\mathbf{q}} \quad (3.14)$$

The dispersion (see Fig. 3.2a) at  $\Gamma \equiv (q_x = 0, q_y = 0)$  has an energy gap of  $6J$ . At  $M \equiv k_L(q_x = \sqrt{3}/2, q_y = 0)$ , the gap is  $2J$ . At  $K \equiv k_L(q_x = \sqrt{3}/2, q_y = 1/2)$ , however, the bands are degenerate. Furthermore, in the vicinity of the K point, the dispersion looks linear. To quantitatively examine the behavior of the dispersion and eigenstates in the vicinity of the K point, we expand in  $\mathbf{q}$  at quasimomentum  $K - \mathbf{q}$ . This yields a

Hamiltonian

$$\hat{H}_{\mathbf{q}}^K = v_F \begin{pmatrix} 0 & q_x + iq_y \\ q_x - iq_y & 0 \end{pmatrix} = v_F |q| \begin{pmatrix} 0 & e^{i\phi} \\ e^{-i\phi} & 0 \end{pmatrix}, \quad (3.15)$$

where  $v_F = 3Ja/2$ . In the second equality, we have expressed the matrix in polar coordinates such that  $\mathbf{q} = |q| e^{i\phi}$ . This change of coordinates enables us to more conveniently analyze the problem.

The eigenenergies are

$$\pm v_F |q|. \quad (3.16)$$

Here, we see that the eigenenergies are indeed linear in the distance  $|q|$  to the K point. This dispersion resembles the massless Dirac equation, for which the K point is named, with the exception that the speed of light is replaced by  $v_F$ , commonly referred to as the Fermi velocity. In material graphene, where  $v_F$  is about 300 times smaller than the speed of light, this linear dispersion relation results in novel transport phenomena that are of great interest both fundamentally and for technological applications [75, 92].

Next, we examine the Berry phase acquired by a particle traversing an infinitesimal loop around the Dirac point in the lowest band. Doing so requires the cell-periodic part of the eigenvectors of the Hamiltonian, which, expressed in the basis of  $|u_{\mathbf{q}}^A\rangle$  and  $|u_{\mathbf{q}}^B\rangle$ , are

$$|u_{\phi}^{1(2)}\rangle = \frac{1}{\sqrt{2}} \begin{pmatrix} -(+)e^{i\phi} \\ 1 \end{pmatrix}. \quad (3.17)$$

In polar coordinates, the Berry connection of the lowest band is

$$\mathbf{A}_{\mathbf{q}}^{11} = i \langle u_{\mathbf{q}}^1 | \nabla_{\mathbf{q}} | u_{\mathbf{q}}^1 \rangle \rightarrow \left( i \langle u_{\phi}^1 | \partial_{|q|} | u_{\phi}^1 \rangle, i |q| \langle u_{\phi}^1 | \partial_{\phi} | u_{\phi}^1 \rangle \right), \quad (3.18)$$

where we have split the Berry connection into its  $|q|$  and  $\phi$  components. There is no dependence of  $|q|$  in the eigenstate, so the  $|q|$  component is zero. The  $\phi$  component is

$$\mathbf{A}_{\phi}^{11} = \frac{1}{2|q|} \quad (3.19)$$

The Berry phase can then be expressed as

$$\int_{\mathcal{C}} \mathbf{A}_{\mathbf{q}}^{11} d\mathbf{q} = \int_0^{2\pi} \mathbf{A}_{\phi}^{11} |q| d\phi = \int_0^{2\pi} \frac{1}{2} d\phi = \pi, \quad (3.20)$$

where  $\mathcal{C}$  refers to the closed loop around the K point. Therefore, an infinitesimal loop

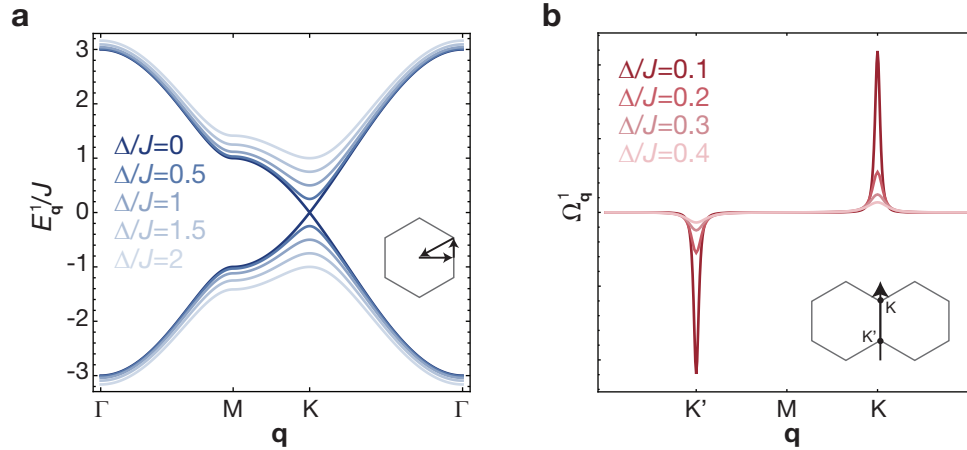


Figure 3.2.: **The tight-binding dispersion and Berry curvature with varying Semenoff mass.** **a**, The dispersion along the high-symmetry path  $\Gamma$ -M-K- $\Gamma$  for hopping strength  $J = 1$ . When A and B sites are degenerate ( $\Delta = 0$ ), there is a Dirac point at the K (and  $K'$ ) point. At finite energy offset between A and B sites, an energy gap opens at the K (and  $K'$ ) point, breaking the degeneracy between the first and second bands. This energy gap increases as the energy offset between A and B sites increases. **b**, The Berry curvature  $\Omega_{\mathbf{q}}^1$  of the first band at K and  $K'$  points for increasing values of  $\Delta$  (decreasing shades of red). As the Semenoff mass is increased, the HWHM of the Berry curvature increases. In the massless case, the Berry curvature is a delta function [93, 94].

around the K point results in a Berry phase (or flux) of  $\pi$ . The same analysis holds for the other two K points (at  $k_L(0, -1)$  and  $k_L(-\sqrt{3}/2, 1/2)$ ). Performing the same calculation around  $K'$  points (located at  $k_L(0, 1)$ ,  $k_L(\sqrt{3}/2, -1/2)$ , or  $k_L(-\sqrt{3}/2, -1/2)$ ) results in a Berry phase of  $-\pi$ . Hence, when  $\Delta = 0$ , we cannot distinguish between encircling the K or  $K'$  point—both yield a phase of  $\pi = -\pi$ . In contrast, we will later see that these two scenarios are distinguishable when  $\Delta \neq 0$ .

### 3.1.2. $\Delta \neq 0$ : Effect of the Semenoff mass and the Bloch sphere picture

We now examine what happens when there is an energy offset between A and B sublattice sites. Introducing this energy offset is commonly called adding a Semenoff mass [95]. We see from Eqs. 3.11 and 3.10 that the Semenoff mass influences the form of both the eigenstates and the eigenenergies. At the Dirac point, for example, the energy difference between the two bands is given by  $\Delta$ . Hence, the larger the Semenoff mass, the larger the energy splitting at the Dirac points, as illustrated in Fig. 3.2a.

In terms of the eigenstates, the Semenoff mass imbalances their composition of A and B sites. When  $\Delta = 0$ , the eigenstate at every quasimomentum is an equal superposition of the A and B site states. In contrast, when  $\Delta$  is non-zero, the A and B site composition of the eigenstates becomes dependent on the quasimomentum, sign of  $\Delta$ , and the band. For example, let us specifically consider the lowest eigenstates. When

A and B sites are at the same energy, atoms favor both sites equally. In contrast, when there is an energy offset such that, for example, A sites are lower in energy than B sites, atoms will be preferentially located on A sites.

To visualize this effect, it is convenient to examine the eigenstates on a Bloch sphere, where the north and south poles are  $|u_{\mathbf{q}}^A\rangle$  and  $|u_{\mathbf{q}}^B\rangle$ , respectively, as shown in Fig. 3.3. For simplicity, we shall draw only the eigenstate of the lower band.<sup>1</sup> In its most general form, the lower eigenstate at quasimomentum  $\mathbf{q}$  is

$$|u_{\mathbf{q}}^1\rangle = \cos \frac{\theta_{\mathbf{q}}}{2} e^{i\varphi_{\mathbf{q}}} |u_{\mathbf{q}}^A\rangle + \sin \frac{\theta_{\mathbf{q}}}{2} |u_{\mathbf{q}}^B\rangle, \quad (3.21)$$

where  $\theta_{\mathbf{q}}$  parametrizes the composition of and  $\varphi_{\mathbf{q}}$  parametrizes the phase between the A and B site states<sup>2</sup>.

For  $\Delta = 0$ , the eigenstate is constrained along the equatorial plane at  $\theta_{\mathbf{q}} = \pi/2$  as an equal superposition of A and B site states for every quasimomentum  $\mathbf{q}$ . The rotation of the eigenstate for two closed paths, one around the  $\Gamma$  point and the other around a Dirac cone, is shown Fig. 3.3. In contrast, the rotation of the eigenstate for  $\Delta = J$  for the same two paths occurs in lower hemisphere. Since the A sites are at energy  $\Delta/2$  while the B sites are at energy  $-\Delta/2$ , the eigenstate is now mostly comprised of the B site states.

### Acquired Berry phase as the enclosed solid angle

Lastly, we highlight the difference between paths that enclose and do not enclose a Dirac cone. In the former case, the evolution of the eigenstate encloses a solid angle on the Bloch sphere, while in the latter case, it does not (see Fig. 3.3). This is directly related to whether the state acquires a non-trivial Berry phase along its evolution path. In more suggestive language, it is directly related to whether the evolution path encloses some Berry flux, which requires a non-zero area element.

To understand this link, we first write down the solid angle subtended by a surface in spherical coordinates, where  $r$ ,  $\theta$ , and  $\varphi$  parametrize the distance to the origin, the polar angle, and the azimuthal angle, respectively:

$$\mathcal{S} = \int d\mathcal{S} = \int \int \sin\theta d\theta d\varphi. \quad (3.22)$$

In our case, the relevant surface is the surface of the Bloch sphere enclosed by the evo-

<sup>1</sup> Since the eigenstates of the lower and upper band are orthogonal, their orientations are not independent. Namely, if the eigenstate of the lower band has coordinates  $(\varphi, \theta)$ , where  $\varphi$  is the azimuthal angle and  $\theta$  is the polar angle, the eigenstate of the upper band has coordinates  $(\varphi + \pi, \pi - \theta)$ . That is, they point in opposite direction on the Bloch sphere.

<sup>2</sup> Note that the Bloch sphere representation neglects global phases. That is, we can not distinguish  $|u_{\mathbf{q}}^1\rangle$  from  $e^{i\gamma}|u_{\mathbf{q}}^1\rangle$ , where  $\gamma$  is a constant.

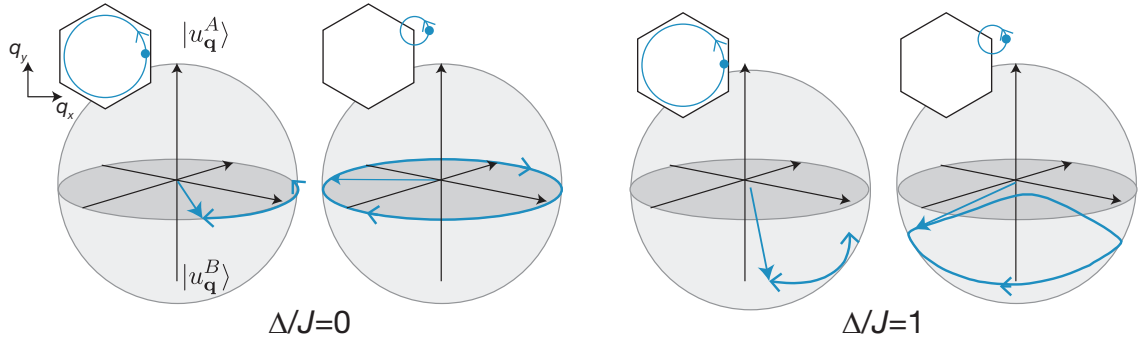


Figure 3.3.: **Visualizing the effect of the Semenoff mass with Bloch spheres.** For each quasi-momentum  $\mathbf{q}$ , the eigenstates can be represented on a Bloch sphere where the north and south poles are states  $|u_{\mathbf{q}}^A\rangle$  and  $|u_{\mathbf{q}}^B\rangle$ , respectively. The initial and final position of the eigenstate is shown as the blue vector for circular paths around  $\Gamma$  and around the K (insets). In the case of  $\Delta/J = 0$ , the eigenstate is constrained to rotate along the equatorial plane because it is always in an equal superposition of A and B site states. However, for  $\Delta/J = 1$ , the eigenstate is comprised mostly of B site states and consequently rotates primarily in the lower hemisphere of the Bloch sphere. For both  $\Delta$  parameters, moving around the Gamma point corresponds to the eigenstate rotating forwards and backwards along the same path on the Bloch sphere. In contrast, a path around a Dirac point moves the eigenstate in a loop on the Bloch sphere that encloses a finite solid angle. The enclosed solid angle is twice the Berry phase acquired by the state in the course of its evolution.

lution of the eigenstate. We have already conveniently written the eigenstate in spherical coordinates in Eq. 3.21 and can now calculate the Berry curvature in spherical coordinates. Component-wise, the Berry connections are

$$\mathbf{A}_r^{11} = \langle u_{\mathbf{q}}^1 | \partial_r | u_{\mathbf{q}}^1 \rangle = 0 \quad (3.23)$$

$$\mathbf{A}_\theta^{11} = \langle u_{\mathbf{q}}^1 | \partial_\theta | u_{\mathbf{q}}^1 \rangle = 0 \quad (3.24)$$

$$\mathbf{A}_\varphi^{11} = \langle u_{\mathbf{q}}^1 | \partial_\varphi | u_{\mathbf{q}}^1 \rangle = -\frac{\cos^2 \theta / 2}{r \sin \theta / 2} \quad (3.25)$$

The Berry curvature of the Berry connection in spherical coordinates  $\mathbf{A}_{r,\theta,\varphi}^{11}$  is only non-zero for the  $\hat{r}$  term

$$\nabla \times \mathbf{A}_{r,\theta,\varphi}^{11} = \frac{\cos \theta / 2 \sin \theta / 2}{r^2 \sin \theta} \hat{r} \quad (3.26)$$

The  $\hat{r}$  component of the differential area element in spherical coordinates is

$$d\mathbf{a} = r^2 \sin \theta d\theta d\varphi \hat{r}, \quad (3.27)$$

giving

$$\begin{aligned}\nabla \times \mathbf{A}_{\mathbf{r},\theta,\varphi}^{\text{II}} \cdot d\mathbf{a} &= \frac{1}{2} \sin\theta d\theta d\varphi \\ &= \frac{1}{2} d\mathcal{S},\end{aligned}\tag{3.28}$$

where we have related the Berry curvature in a differential area to the solid angle from Eq. 3.22. Performing an area integral of the Berry curvature for the Berry phase gives

$$\begin{aligned}\phi_{\text{Berry}} &= \int \nabla \times \mathbf{A}_{\mathbf{r},\theta,\varphi}^{\text{II}} d\mathbf{a} \\ &= \frac{1}{2} \int \int \sin\theta d\theta d\varphi \\ &= \frac{1}{2} \mathcal{S}\end{aligned}\tag{3.29}$$

We find that the Berry phase a state acquires is simply half of the solid-angle enclosed by the evolution of the state on the Bloch sphere. From this, we can immediately conclude that only the path enclosing a Dirac point yields a non-trivial Berry phase. Moreover, the  $\pi$  Berry phase that we analytically worked out in Sec. 3.1.1 can be understood here as resulting from a path that encloses half of the Bloch sphere (since the eigenstate is constrained on the equatorial plane). The solid angle of half a sphere is  $2\pi$ , yielding a Berry phase of  $\pi$ .

In the presence of a Semenoff mass, the winding of the eigenstate is displaced from the equatorial plane. Consequently, the acquired Berry phase will be less than  $\pi$ , due to the decreased enclosure of solid angle. Moreover, if we acquire a phase of  $\phi_{\text{Berry}}$  (that is less than  $\pi$ ) when encircling a K point, we will acquire a phase of  $-\phi_{\text{Berry}}$  when encircling a K' point. Hence, in contrast to the massless ( $\Delta = 0$ ) case, we would indeed be able to distinguish between encircling a K or K' point. Visualized on the Bloch sphere, the eigenstates in these two scenarios would wind along the same path but in opposite directions. For example, in Fig. 3.3, the eigenstate currently winds clockwise when encircling a K point. When encircling a K' point, it would instead wind counter-clockwise.

Lastly, as another way of understanding the effect of the Semenoff mass on the acquired Berry phase, we plot the Berry curvature of the first band as a function of quasi-momentum in Fig. 3.2b. When  $\Delta = 0$ , the Berry curvature is a delta function localized at the K and K' points [93, 94]. As  $\Delta$  is increased, the Berry curvature "spreads out" in the sense that its half-width-half-max (HWHM) increases. Therefore, the Berry phase acquired by encircling a K or K' point decreases with increasing  $\Delta$ , due to the decreased Berry flux in the enclosed area of the path. Furthermore, the opposite signs of the Berry curvature at K and K' yields Berry phases with opposite signs; this was previously understood in the Bloch sphere picture as opposite winding directions of the eigenstates. The sign of the Berry curvature at the K and K' points is determined by the symmetries

of the Hamiltonian and has important implications for the topological character of the bands [22]. For example, since the Berry curvature at the K and K' points have opposite sign in our case, we know that the Chern number, which is given by the integral of the Berry curvature over the whole Brillouin zone [8, 26], must be zero. Correspondingly, in, for example, the Haldane model, where the Chern number is finite, the Berry curvature at K and K' have the same sign.

## 3.2. The *ab-initio* calculation

Having derived a tight-binding model of the honeycomb lattice, we now provide an *ab-initio* calculation for a single particle confined in an optical honeycomb potential. This is necessary for the comparison of our actual experimental parameters to the tight-binding model.

### 3.2.1. Setting up the problem

We begin by writing down the Schroedinger equation of a single particle in a periodic potential in the position basis:

$$\hat{\mathbf{H}}\Psi_{\mathbf{q}}^n(\mathbf{r}) = \left( \frac{\hat{\mathbf{p}}^2}{2m} + V(\mathbf{r}) \right) \Psi_{\mathbf{q}}^n(\mathbf{r}) = E_{\mathbf{q}}^n \Psi_{\mathbf{q}}^n(\mathbf{r}), \quad (3.30)$$

where  $\hat{\mathbf{p}} = -i\hbar\nabla$  is the momentum operator and the potential  $V(\mathbf{r})$  is periodic such that  $V(\mathbf{r}+\mathbf{R}) = V(\mathbf{r})$  for all Bravais lattice vectors  $\mathbf{R}$ . This is a canonical problem in solid state theory and can be found in any introductory solid state book (see e.g, Ref. [1]). From Bloch's theorem, we know the Bloch functions  $\Psi_{\mathbf{q}}^n(\mathbf{r})$  are plane waves multiplied by the cell-periodic Bloch functions which have the same periodicity as the potential:

$$\Psi_{\mathbf{q}}^n(\mathbf{r}) = e^{i\mathbf{q}\cdot\mathbf{r}} u_{\mathbf{q}}^n(\mathbf{r}). \quad (3.31)$$

Substituting Eq. 3.31 into Eq. 3.30 yields an eigenvalue equation for the cell-periodic functions  $u_{\mathbf{q}}^n(\mathbf{r})$ :

$$\hat{\mathbf{H}}_B u_{\mathbf{q}}^n(\mathbf{r}) = \left( \frac{(\hat{\mathbf{p}} + \mathbf{q})^2}{2m} + V(\mathbf{r}) \right) u_{\mathbf{q}}^n(\mathbf{r}) = E_{\mathbf{q}}^n u_{\mathbf{q}}^n(\mathbf{r}) \quad (3.32)$$

Our goal now is to find the elements of the Hamiltonian  $\hat{\mathbf{H}}_B$  such that we can numerically diagonalize  $\hat{\mathbf{H}}_B$  to obtain  $E_{\mathbf{q}}^n$  and  $u_{\mathbf{q}}^n(\mathbf{r})$ . To this end, we expand  $u_{\mathbf{q}}^n(\mathbf{r})$  in the plane wave basis. Since  $u_{\mathbf{q}}^n(\mathbf{r})$  has the same periodicity of the lattice, its plane wave expansion also contains only plane waves with the same periodicity of the lattice, i.e., its

plane wave expansion is comprised of the reciprocal lattice vectors  $\mathbf{K}$ :

$$u_{\mathbf{q}}^n(\mathbf{r}) = \sum_{\mathbf{K}} c_{\mathbf{K}}^{(n,\mathbf{q})} e^{i\mathbf{K}\cdot\mathbf{r}}, \quad (3.33)$$

where summation over  $\mathbf{K}$  is to be understood as running over all reciprocal lattice vectors. Similarly, the potential  $V(\mathbf{r})$  can also be expanded as plane waves of the reciprocal lattice vectors

$$V(\mathbf{r}) = \sum_{\mathbf{K}'} V_{\mathbf{K}'} e^{i\mathbf{K}'\cdot\mathbf{r}} \quad (3.34)$$

Substituting the plane wave expansions of Eq. 3.33 and Eq. 3.34 into Eq. 3.32 yields

$$\sum_{\mathbf{K}} \left( \frac{(\mathbf{q} + \mathbf{K})^2}{2m} c_{\mathbf{K}}^{(n,\mathbf{q})} e^{i\mathbf{K}\cdot\mathbf{r}} + \sum_{\mathbf{K}'} V_{\mathbf{K}'} c_{\mathbf{K}}^{(n,\mathbf{q})} e^{i(\mathbf{K}+\mathbf{K}')\cdot\mathbf{r}} = E_{\mathbf{q}}^n c_{\mathbf{K}}^{(n,\mathbf{q})} e^{i\mathbf{K}\cdot\mathbf{r}} \right) \quad (3.35)$$

To select a particular plane wave coefficient  $c_{\bar{\mathbf{K}}}^{(n,\mathbf{q})}$  with momentum  $\bar{\mathbf{K}}$ , we multiply both sides of the equation by  $C e^{-i\bar{\mathbf{K}}\cdot\mathbf{r}}$  and integrate over all space, where  $C$  is a constant chosen to appropriately cancel out pre-factors in the integration. The resulting equation can be written in matrix form as

$$\sum_{\mathbf{K}} H_{\mathbf{K}\bar{\mathbf{K}}} c_{\mathbf{K}}^{(n,\mathbf{q})} = E_{\mathbf{q}}^n c_{\bar{\mathbf{K}}}^{(n,\mathbf{q})} \quad (3.36)$$

where we have evaluated the Kronecker delta on the right-hand-side and

$$H_{\mathbf{K}\bar{\mathbf{K}}} = \frac{(\mathbf{q} + \mathbf{K})^2}{2m} \delta_{\mathbf{K},\bar{\mathbf{K}}} + \sum_{\mathbf{K}'} V_{\mathbf{K}'} \delta_{\mathbf{K}+\mathbf{K}',\bar{\mathbf{K}}} \quad (3.37)$$

### 3.2.2. Application to the optical honeycomb potential

Thus far, our analysis has been generic and applicable to any periodic potential. To proceed further, we need to substitute in the reciprocal lattice vectors of the honeycomb potential. Although we already know what these vectors are from our tight-binding analysis, we would like to determine them using basic information on the setup of the honeycomb optical lattice in the lab. Details on the experimental realization of the optical lattice are in Sec. 4.1; for now, we need only to know that the lattice is created by interfering three running-wave laser beams at  $120^\circ$  angles, as depicted in

Fig. 3.4a. The wave-vector  $\mathbf{k}_i$  of beam  $i$  is

$$\mathbf{k}_1 = k_L(0, 1) \quad (3.38)$$

$$\mathbf{k}_2 = k_L\left(-\frac{\sqrt{3}}{2}, -\frac{1}{2}\right) \quad (3.39)$$

$$\mathbf{k}_3 = k_L\left(\frac{\sqrt{3}}{2}, -\frac{1}{2}\right), \quad (3.40)$$

where  $k_L = 2\pi/\lambda_L$  and  $\lambda_L$  is the wavelength of the beam. In contrast to the tight-binding approach where we found the primitive reciprocal lattice vectors by first defining a direct lattice, we now find the primitive reciprocal lattice vectors by taking the difference between the wave-vectors of the lattice beams [96]:

$$\mathbf{b}_1 = \mathbf{k}_{12} = k_L\left(\frac{\sqrt{3}}{2}, \frac{3}{2}\right) \quad (3.41)$$

$$\mathbf{b}_2 = \mathbf{k}_{31} = k_L\left(\frac{\sqrt{3}}{2}, -\frac{3}{2}\right), \quad (3.42)$$

where  $\mathbf{k}_{ij} \equiv \mathbf{k}_i - \mathbf{k}_j$ . As usual, we can now write each reciprocal lattice vector  $\mathbf{K}$  as a linear combination of primitive reciprocal lattice vectors  $\mathbf{b}_1$  and  $\mathbf{b}_2$ :

$$\mathbf{K} = l_1\mathbf{b}_1 + l_2\mathbf{b}_2, \quad (3.43)$$

where  $l_1$  and  $l_2$  are integers. Hence, a summation over  $\mathbf{K}$  is, more explicitly, a summation over integers  $l_1$  and  $l_2$ . In the expansion of the honeycomb potential  $V(\mathbf{r})$  in reciprocal lattice vectors  $\mathbf{K}'$  in Eq. 3.34, only a few combinations of  $l'_1$  and  $l'_2$  give non-zero coefficients  $V_{\mathbf{K}'}$ . They are

$$(l'_1, l'_2) = \{(0, 0), (0, \pm 1), (\pm 1, 0), (-1, -1), (1, 1)\} \quad (3.44)$$

Using this information, we can now simplify Eq. 3.37 by evaluating the summation over  $\mathbf{K}'$ . For an ideal honeycomb potential, the Hamiltonian becomes

$$H_{\mathbf{K}, \bar{\mathbf{K}}} = \begin{cases} (\mathbf{q}/(\hbar k_L) + l_1\mathbf{b}_1 + l_2\mathbf{b}_2)^2 E_r + 3V_0, & l_1 = \bar{l}_1 \text{ and } l_2 = \bar{l}_2 \\ V_0, & |l_1 - \bar{l}_1| = 1 \text{ and } l_2 = \bar{l}_2 \\ V_0, & |l_2 - \bar{l}_2| = 1 \text{ and } l_1 = \bar{l}_1 \\ V_0, & l_1 - \bar{l}_1 = 1 \text{ and } l_2 - \bar{l}_2 = 1 \\ V_0, & l_1 - \bar{l}_1 = -1 \text{ and } l_2 - \bar{l}_2 = -1 \\ 0, & \text{otherwise} \end{cases} \quad (3.45)$$

Here,  $E_r = \hbar^2/(2m\lambda_L)$  is the lattice recoil energy, where  $m$  is the atomic mass and

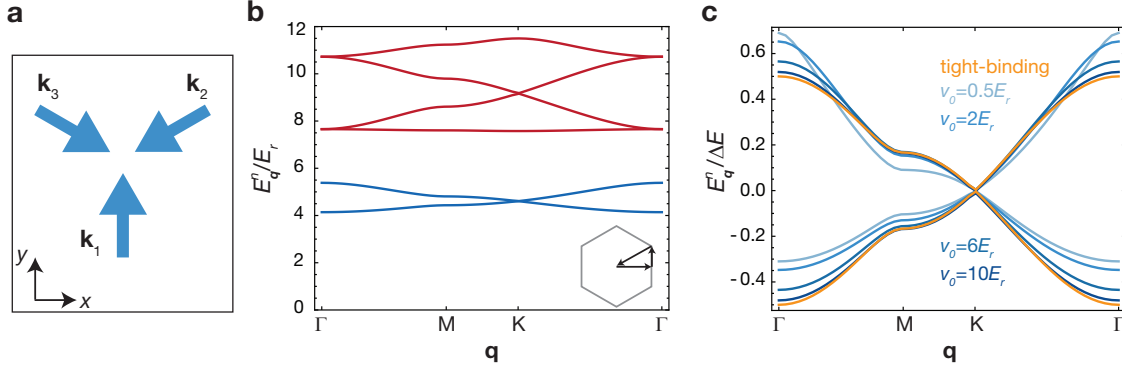


Figure 3.4.: **Creating the optical honeycomb potential and the *ab-initio* dispersion.** **a**, In the lab, the optical honeycomb lattice is created by interfering three running-wave beams at  $120^\circ$  angles. The wave-vector of each beam  $i$  is denoted  $\mathbf{k}_i$ . **b**, The energies of the first six bands as a function of quasimomentum  $\mathbf{q}$  along the high-symmetry line  $\Gamma$ -M-K- $\Gamma$  (inset) for lattice depth  $V_0 = 3E_r$ . Dirac points occur in the two lowest bands and the fourth and fifth bands at the K-point. **c**, The dispersion of the two lowest bands along  $\Gamma$ -M-K- $\Gamma$  for increasing lattice depth (darker shades of blue) with an energy offset such the Dirac point occurs at zero energy. Starting around  $V_0 = 6E_r$ , the dispersion begins to be well-approximated by the tight-binding dispersion (orange line). Energies are plotted in units of  $\Delta E$ , the energy difference between the two bands at  $\Gamma$ . The Dirac points are present even at low lattice depths when the dispersion does not match the tight-binding dispersion well.

$h$  is Planck's constant, and  $V_0$  is the single-beam light shift<sup>3</sup> parametrizing the lattice depth. Furthermore, we have explicitly written the dependence of the matrix elements on  $\mathbf{K}$  and  $\bar{\mathbf{K}}$  as a dependence on integers  $l_1, l_2$  and  $\bar{l}_1, \bar{l}_2$ , respectively.

To numerically find the eigenvectors and eigenvalues of the matrix in Eq. 3.45, we must of course truncate the sum at some finite  $l_{max}$  such that  $l_1$  and  $l_2$  range from  $-l_{max}$  to  $+l_{max}$ . This results in a matrix of size  $(2l_{max} + 1)^2 \times (2l_{max} + 1)^2$  and yields the eigenenergies of the first  $(2l_{max} + 1)^2$  bands. As the lattice depth increases,  $l_{max}$  must also be increased to account for the increasing population in higher order coefficients. For our lattice depths of  $\approx 1 - 5 E_r$ , we typically use  $l_{max}=6$ .

### 3.2.3. Energy bands from the *ab-initio* calculation

The energies of the first six bands obtained from diagonalizing the matrix in Eq. 3.45 are plotted along high symmetry lines  $\Gamma$ -M-K- $\Gamma$  for a lattice depth of  $V_0 = 3E_r$  in Fig. 3.4b. Notably, there are two "sets" of bands comprised of the lowest two bands (blue) and the highest four bands (red). The two lowest bands correspond to the  $s$ -bands previously derived in the tight-binding model.

To compare these two lowest bands to the tight-binding model, we plot the dispersion along the high-symmetry path for increasing lattice depth in Fig. 3.4c. By a lattice

<sup>3</sup>A brief explanation on the origin of the light-shift, i.e. the dipole potential, can be found in Sec. 4.1.1.

depth of  $V_0 = 6E_r$ , the *ab-initio* bands match the tight-binding bands quite well. At low lattice depths, the deviation is due to non-negligible next-nearest-neighbor tunneling, which was not included in our tight-binding model. However, even at low lattice depths, the Dirac points are still present. This is due to the symmetries of the lattice, which constrain the form of the Bloch Hamiltonian at  $\mathbf{q}$  and  $-\mathbf{q}$ . When the system has time-reversal, inversion, and  $C_3$  symmetry, Dirac points must occur at the corners of the Brillouin zone, i.e., at the K and K' points [22, 97, 98]. In other words, these three symmetries guarantee the local stability of the Dirac points regardless of the details of the system, such as lattice depth. When  $C_3$  symmetry is broken but time-reversal and inversion symmetry remain, the Dirac points can shift away from the K and K' points and eventually annihilate at a finite time-reversal invariant quasimomentum, i.e, where  $\mathbf{q} = -\mathbf{q}$  [22]. We will experimentally probe the annihilation of the Dirac points in Sec. 5.3.3 by breaking the  $C_3$  symmetry. Lastly, if time-reversal or inversion symmetry is broken (which also breaks  $C_3$  symmetry), the Dirac points will gap. For example, adding a Semenoff mass opens the Dirac points via a broken inversion symmetry.

In Fig. 3.4b, the lowest two bands corresponding to the tight-binding bands are commonly referred to as "s-bands" and the highest four bands are called the "p-bands." To understand this terminology and the separation between these sets of bands, we examine the dispersion relation for increasing lattice depth, which is plotted along M- $\Gamma$ -M in Fig. 3.5 for maximally twelve bands.

In the case of vanishing lattice depth, the problem reduces to that of a free-particle. Hence, the dispersion is a free-particle parabola reduced to the first Brillouin zone. As lattice depth is increased, band gaps appear and increase while band widths decrease. For deeper and deeper lattices, the lattice wells become more and more decoupled, and the problem approaches that of a single harmonic oscillator potential. Consequently, we obtain bands that appear independent of quasimomentum and are separated by quantized gaps,  $\hbar\omega_{ho}$ , where  $\omega_{ho}$  is the harmonic oscillator frequency. By expanding the ideal honeycomb potential on a lattice site and assuming an isotropic 2D harmonic potential, we obtain

$$\omega_{ho}^2 = \frac{9k_L^2 V_0}{2m}. \quad (3.46)$$

In an isotropic 2D harmonic oscillator, the first band is not degenerate, the second band is two-fold degenerate, the third band is three-fold degenerate, and so on [81]. In analogy with atomic orbitals, the non-degenerate ground state is commonly called the *s*-band, the doubly degenerate first-excited state is called the *p*-band, and the triply degenerate second-excited state is called the *d*-band. Hence, in a monoatomic lattice, there is one *s*-band, two *p*-bands, and three *d*-bands. However, since the honeycomb lattice has two sites per unit cell, the lowest band is split into two bands, corresponding to the A and B sublattice sites. Hence, there are instead two *s*-bands, four *p*-bands and six *d*-bands.

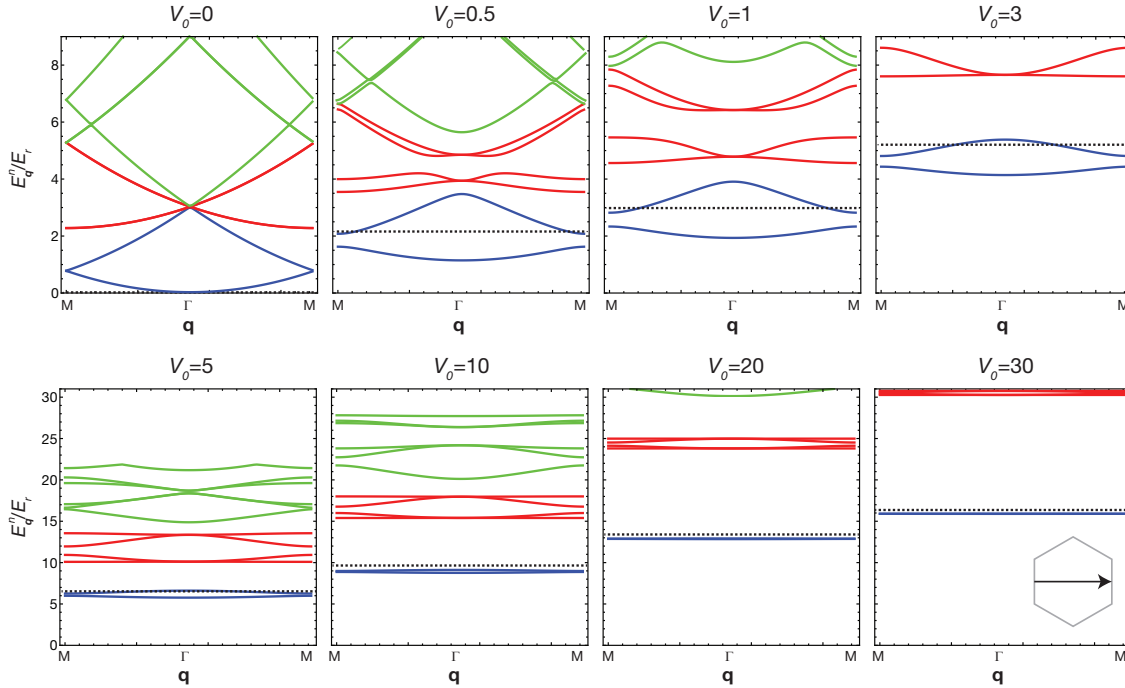


Figure 3.5.: **Band structure of the honeycomb lattice.** We show the eigenenergies  $E_{\mathbf{q}}^n$  of maximally twelve bands with increasing lattice depth along the path  $\mathbf{q} = \text{M}-\Gamma\text{-M}$  (inset of  $V_0 = 30E_r$  plot). In a lattice of vanishing depth, the dispersion is that of the free-particle. As lattice depth is increased, individual lattice wells decouple from each other, and the potential can be simply approximated as an isotropic 2D harmonic oscillator. The grouping of the bands can be understood by considering the two-site unit cell of the honeycomb lattice and the excitation levels of the harmonic oscillator. In analogy with atomic orbitals, the two lowest bands are the *s*-bands (blue), the third through sixth bands are the *p*-bands (red), and the seventh through twelfth bands are the *d*-bands (green). The zero-point energy of the 2D harmonic oscillator  $\hbar\omega_{ho}$  is shown as a dashed line.



# Chapter 4.

## An overview of the experimental setup

In this chapter, we overview the most relevant technical aspects of the experiments. After a brief review of how laser light traps atoms via interaction with their light-induced dipole moment, we describe the experimental realization of the optical honeycomb potential in Sec. 4.1. In particular, we exploit the high degree of control offered by optical potentials to examine how the intensity and polarization of the beams can introduce non-isotropic tunnelings and a Semenoff mass, respectively. These two (controlled) deformations of the ideal honeycomb lattice are most relevant for the experiments in this thesis.

Directly paralleling the tools needed to probe geometric effects on the evolution of a quantum state, the next three sections are divided as the preparation, evolution, and detection of the state. In the first section (Sec. 4.2), we briefly introduce our experimental apparatus and the procedure for achieving BECs. A more detailed description with references can be found in Appendix A.

Next, in Sec. 4.3, we describe how to experimentally create a constant force to induce evolution of the state. We use either a magnetic field gradient from a single coil or accelerate the lattice. While the former method creates a gradient in the lab frame, the latter method creates a gradient in the lattice frame. Although the physics are certainly the same in all reference frames, this difference is nonetheless important when interpreting our absorption images.

Absorption imaging of the atoms is our method of state detection (Sec. 4.4). We always image the atoms after a certain time-of-flight (TOF), during which they freely expand after all confining optical potentials have been switched off. Depending on whether the lattice potential is suddenly switched off or gradually ramped down, we procure different types of reciprocal-space information. The former method is used to probe the similarity in the intensity of the three lattice beams as a quality-check before all experiments. The latter method, termed band mapping, is used in the experiments to detect the relevant observable, which is the distribution of atoms in the bands at a specific quasimomentum.

We conclude the chapter by putting these tools together to demonstrate some applications in Sec. 4.5. We show adiabatic Bloch oscillations induced by the magnetic field gradient and by lattice acceleration to emphasize the difference in the absorption im-

ages due to the different frames of reference. Furthermore, we show non-adiabatic Bloch oscillations, where atoms in the first and second band can be clearly distinguished. Finally, we describe how the lattice depth can be calibrated through a procedure called Stueckelberg interferometry, whereby the energy difference between the first and second bands is encoded in an oscillation of the band populations.

## 4.1. Creation of the optical honeycomb lattice

The honeycomb lattice is created by interfering three running-wave, coplanar laser beams at  $120^\circ$  angles, as depicted in Fig. 4.1a. The wavelength of our laser is  $\lambda_L = 755$  nm when working with  $^{87}\text{Rb}$  atoms and  $\lambda_L = 740$  nm when working with  $^{39}\text{K}$  atoms. Since the laser light is far-detuned from the ground- to excited- state resonance frequencies of 780 nm for  $^{87}\text{Rb}$  [99] and 767 nm for  $^{39}\text{K}$  [100], spontaneous emission processes can be neglected and the interaction between the light-induced electric dipole moment of the atoms and laser light results in an energy shift of the atomic levels [101]. This energy shift is known as the ac Stark effect and depends on the intensity of the laser light. Due to the Gaussian profile of the laser beams, the atoms experience a spatially-dependent trapping potential that is the basis for the formation of optical traps, such as those used to cool atoms to quantum degeneracy or optical lattices. We begin with a brief overview of the optical dipole potential before moving on to specific configurations of the honeycomb lattice.

### 4.1.1. The optical dipole potential

For alkali atoms, if the laser detuning from the D1 and D2 lines is large compared to the hyperfine splitting of the excited states, the hyperfine splitting is not resolved. In this case, the dipole potential is given by [101]

$$\begin{aligned} V(\mathbf{r}) &= V_d I(\mathbf{r}) \\ &= \frac{\pi c^2}{2} \left( \frac{\Gamma_{D2}}{\omega_{D2}^3} \frac{2 + \mathcal{P} g_F m_F}{\Delta_{D2}} + \frac{\Gamma_{D1}}{\omega_{D1}^3} \frac{1 - \mathcal{P} g_F m_F}{\Delta_{D1}} \right) I(\mathbf{r}), \end{aligned} \quad (4.1)$$

where  $I(\mathbf{r})$  is the intensity of the interference pattern,  $c$  is the speed of light,  $\Gamma_{D2(D1)}$  is the spontaneous decay rate of the D2 (D1) line of the alkali atom,  $\omega_{D2(D1)}$  is the transition frequency from the ground state to the center of the D2 (D1) line,  $g_F$  is the Landé factor,  $m_F$  is the magnetic quantum number, and  $\mathcal{P}$  is 0 for  $\pi$ -polarized light and  $\pm 1$  for  $\sigma^\pm$ -polarized light. The effective detuning of the laser frequency  $\omega_L$  from the the D1 (D2) line is given by

$$\frac{1}{\Delta_{D1(D2)}} = \frac{1}{\omega_L - \omega_{D1(D2)}} + \frac{1}{\omega_L + \omega_{D1(D2)}} \quad (4.2)$$

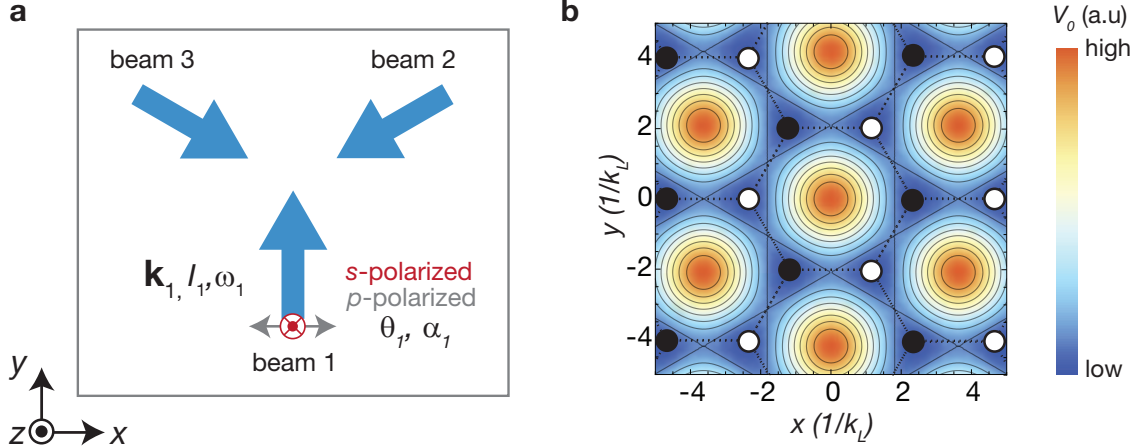


Figure 4.1.: **Creating the optical honeycomb lattice.** **a**, The honeycomb lattice is created by three blue-detuned beams at  $120^\circ$  angles. The quantization axis is defined to be the  $z$ -axis and the plane-of-incidence is the  $xy$ -plane. We express the polarization of each beam in terms of  $s$ - and  $p$ -polarizations, which, as depicted for beam 1, oscillates along the  $z$ -axis (red) and in the  $xy$ -plane (gray), respectively. The proportion of  $s$ - to  $p$ -polarization is parametrized for beam  $n$  by angle  $\theta_n$ , where  $\theta_n = 0$  refers to pure  $s$ -polarizations and  $\theta_n = \pi/2$  refers to pure  $p$ -polarization. The phase between  $s$ - and  $p$ -polarizations is given by  $\alpha_n$ . Each beam is also characterized by its intensity  $I_n$ , frequency  $\omega_n$  and wave-vector  $\mathbf{k}_n$ . **b**, The potential obtained when all beams have the same intensity and are purely  $s$ -polarized, i.e.,  $\theta_1 = \theta_2 = \theta_3 = 0$ . Since the laser is blue-detuned to the atomic resonance, atoms are trapped at intensity minima. Dashed lines emphasize the honeycomb structure, which contains non-equivalent sites A (solid circles) and B (open circles) in its unit cell

Note that the pre-factor  $V_d$  is positive when the detuning is blue, i.e.,  $\omega_L$  is greater than the transition frequency. Consequently, since the intensity is always positive, the minima of  $V(\mathbf{r})$  correspond to the intensity minima. Conversely, the pre-factor  $V_d$  is negative when the detuning is red, i.e.,  $\omega_L$  is less than the transition frequency. In this case, the minima of  $V(\mathbf{r})$  correspond to the intensity maxima. This means that atoms are trapped in intensity minima when the light is blue-detuned and in intensity maxima when the light is red-detuned.

### 4.1.2. The ideal optical honeycomb lattice

To find the parameters to create an ideal honeycomb lattice, we begin with some definitions and general comments. Our coordinate axes are defined such that the quantization axis is the  $z$ -axis and the plane-of-incidence along which the beams propagate is the  $xy$ -plane (see Fig. 4.1a). Each beam  $n$  is characterized by its wave-vector  $\mathbf{k}_n$ , an intensity  $I_n$ , and frequency  $\omega_n$ . The polarization of beam  $n$  is parametrized by the phase  $\alpha_n$  and the ratio  $\theta_n$  between  $s$ - and  $p$ -polarizations. For example, if  $\theta=0$ , the light is purely  $s$ -polarized and oscillates along the  $z$ -axis while if  $\theta = \pi/2$ , the light is purely

$p$ -polarized and oscillates in the  $xy$ -plane.

In the  $z$ -direction, there is no lattice structure and the trapping potential is only due to the Gaussian profile of the lattice and dipole beams. Since the frequency of the trapping potential in the  $z$ -direction is on the order of one hundred Hz, while the on-site potential of the lattice in the  $xy$ -plane is on the order of many kHz for typical experimental parameters, the system has "tubes" along the  $z$ -direction. Henceforth, when writing the total potential  $V(\mathbf{r})$ , we consider the potential in the  $xy$ -plane, i.e.,  $\mathbf{r} \equiv (x, y)$ .<sup>1</sup>

It is convenient to express the lattice potential  $V(\mathbf{r})$  as a sum of the  $s$ -polarized component  $V^s(\mathbf{r}) = V_d I^s(\mathbf{r})$  and the  $p$ -polarized component  $V^p(\mathbf{r}) = V_d I^p(\mathbf{r})$  resulting from the  $s(p)$ -polarized component of the intensity  $I^{s(p)}(\mathbf{r})$ :

$$\begin{aligned} V(\mathbf{r}) &= V^s(\mathbf{r}) + V^p(\mathbf{r}) \\ &= \left| \sum_{n=1}^3 \sqrt{V_n^s} e^{-i\mathbf{k}_n \cdot \mathbf{r}} \right|^2 + \left| \sum_{n=1}^3 \sqrt{V_n^p} e^{-i(\mathbf{k}_n \cdot \mathbf{r} - \alpha_n)} \right|^2. \end{aligned} \quad (4.3)$$

The wave-vectors  $\mathbf{k}_n$  of beam  $n$  are

$$\mathbf{k}_1 = k_L(0, 1) \quad (4.4)$$

$$\mathbf{k}_2 = k_L\left(-\frac{\sqrt{3}}{2}, -\frac{1}{2}\right) \quad (4.5)$$

$$\mathbf{k}_3 = k_L\left(\frac{\sqrt{3}}{2}, -\frac{1}{2}\right), \quad (4.6)$$

where  $k_L = 2\pi/\lambda_L$ . When all three beams have equal intensity and are purely  $s$ -polarized, the expression for the total potential reduces to

$$V(\mathbf{r}) = V_0 \left( 3 + 2 \cos(\mathbf{k}_{12} \cdot \mathbf{r}) + 2 \cos(\mathbf{k}_{13} \cdot \mathbf{r}) + 2 \cos(\mathbf{k}_{23} \cdot \mathbf{r}) \right) \quad (4.7)$$

where  $V_0 \equiv V_1^s = V_2^s = V_3^s$  and  $\mathbf{k}_{ij} \equiv \mathbf{k}_i - \mathbf{k}_j$ . The term  $V_0$  gives the full lattice depth and is typically expressed in units of the lattice recoil energy,  $E_r = \hbar^2/(2m\lambda_L^2)$ , where  $m$  is the atomic mass and  $\hbar$  is Planck's constant. For  $^{87}\text{Rb}$ ,  $E_r/\hbar \approx 4$  kHz and for  $^{39}\text{K}$ ,  $E_r/\hbar \approx 9$  kHz.

The ideal honeycomb potential given by Eq. 4.7 is illustrated in Fig. 4.1b.

---

<sup>1</sup> The potential in the  $xy$ -plane is comprised of the interference pattern of the blue-detuned lattice beams and their Gaussian profile and the Gaussian profile of the dipole beams. The overall confinement due to the blue-detuned anti-confining lattice beams and the red-detuned confining dipole beams has a frequency on the order of  $2\pi \times 10$  Hz. This is sufficiently small to be neglected for our experiments which occur near the center of the trap but becomes more relevant as the atoms are further displaced from the center.

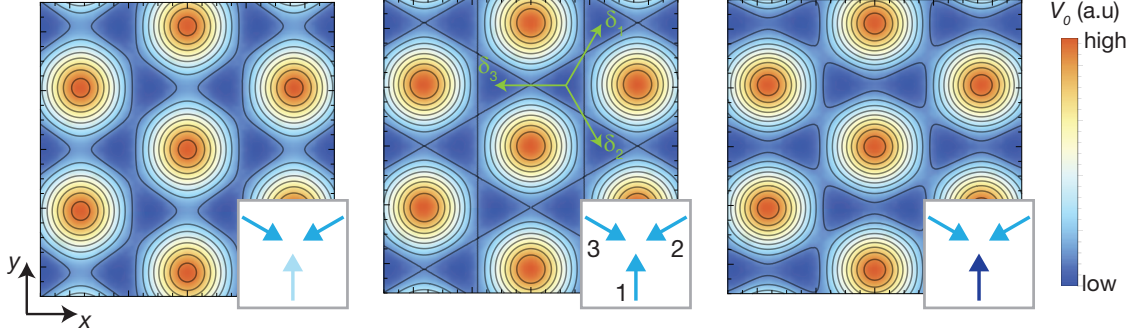


Figure 4.2.: **Realizing non-isotropic tunneling.** When all beams have equal intensities, the hopping amplitudes along directions  $\delta_1, \delta_2$ , and  $\delta_3$  are equivalent (center). Non-isotropic tunneling occurs when the intensity of, e.g., beam 1 is changed. When the intensity of beam 1 is decreased (light blue arrow, left panel), the tunneling amplitude along  $\delta_3$  decreases compared to the tunneling amplitude along  $\delta_1$  and  $\delta_2$ . When the intensity of beam is increased (dark blue arrow, right panel), the tunneling amplitude along  $\delta_3$  increases.

### 4.1.3. Modifications on the ideal: non-isotropic tunneling and adding a Semenoff mass

Control over both the intensity and polarization of each beam affords the optical honeycomb lattice a high degree of tunability. For example, by changing the intensity of a single beam, both the real-space and reciprocal-space structure of the honeycomb lattice can be modified [31, 78, 102]. By changing the polarization of the beams, the honeycomb lattice can become state-dependent [28, 103] or tuned into a triangular lattice [28]. In this section, we focus on experimentally implementing two methods of  $C_3$ -symmetry breaking: non-isotropic tunneling and the Semenoff mass.

#### Realizing non-isotropic tunneling

In the ideal honeycomb lattice, the magnitude of the hopping is equivalent in all three directions,  $\delta_1, \delta_2$ , and  $\delta_3$ . The simplest way to break this equivalence is to change the intensity of the beams. For a purely  $s$ -polarized potential where the beams have inequivalent intensities and contribute a potential  $V_1, V_2$ , and  $V_3$ , where  $V_j$  refers to the potential due to beam  $j$ , the total potential is

$$V(\mathbf{r}) = V_1 + V_2 + V_3 + 2\sqrt{V_1 V_2} \cos(\mathbf{k}_{12} \cdot \mathbf{r}) + 2\sqrt{V_1 V_3} \cos(\mathbf{k}_{13} \cdot \mathbf{r}) + 2\sqrt{V_2 V_3} \cos(\mathbf{k}_{23} \cdot \mathbf{r}) \quad (4.8)$$

By changing the intensity of a single beam, we obtain a different potential barrier along one hopping direction and have therefore broken  $C_3$  symmetry. The effect of this real-space change in reciprocal space is to shift the positions of the Dirac points, as was discussed in Sec. 3.2.3.

### Realizing a Semenov mass

To realize a Semenov mass, we constrain the polarizations of each beam to have the same (non-zero) composition of  $s$ - and  $p$ -polarizations, i.e.,  $\theta_1 = \theta_2 = \theta_3 \equiv \theta$ . The potentials arising from the interference of the  $s$ - and  $p$ - components of the three beams, which are shown separately in Fig. 4.3, have the form

$$V^s(\mathbf{r}) = V_0 \cos^2 \theta \left( 3 + 2 \cos(\mathbf{k}_{12} \cdot \mathbf{r}) + 2 \cos(\mathbf{k}_{13} \cdot \mathbf{r}) + 2 \cos(\mathbf{k}_{23} \cdot \mathbf{r}) \right) \quad (4.9)$$

and

$$V^p(\mathbf{r}) = V_0 \sin^2 \theta \left( 3 - \cos(\mathbf{k}_{12} \cdot \mathbf{r} + \alpha_{12}) - \cos(\mathbf{k}_{13} \cdot \mathbf{r} + \alpha_{13}) - \cos(\mathbf{k}_{23} \cdot \mathbf{r} + \alpha_{23}) \right) \quad (4.10)$$

where  $\alpha_{ij} \equiv \alpha_i - \alpha_j$ . Note that in defining the same  $V_0$  for the  $s$ - and  $p$ -polarizations, we have neglected the state-dependence of the dipole potential, which is valid in our case of far-detuned light<sup>2</sup>.

By choosing the phase  $\alpha_n$  of each beam, we can shift the  $p$ -polarized potential rela-

---

<sup>2</sup>As a rough justification of this approximation, we note that Eq. 4.1 can be written as

$$V(\mathbf{r}) = (2V_{D2} + V_{D1} + \Delta V \mathcal{P} m_F g_F) I(\mathbf{r}),$$

where we have defined

$$V_{D1(D2)} = \frac{\pi c^2 \Gamma_{D1(D2)}}{2\omega_{D1(D2)}^3} \frac{1}{\Delta_{D1(D2)}}$$

$$\Delta V = V_{D2} - V_{D1}.$$

The intensity can be separated into its polarization components as  $I(\mathbf{r}) = I^s(\mathbf{r}) + I^p(\mathbf{r})$ . Furthermore, we note that in our coordinate system,  $I^s(\mathbf{r}) = I^\pi(\mathbf{r})$  and  $I^p(\mathbf{r}) = I^{\sigma^+}(\mathbf{r}) + I^{\sigma^-}(\mathbf{r})$ . By substituting the polarization-separated intensity into the expression for  $I(\mathbf{r})$ , we clearly see that the potential is comprised of a state-independent and a state-dependent part:

$$V(\mathbf{r}) = (2V_{D2} + V_{D1} + \Delta V \mathcal{P} m_F g_F) (I^\pi(\mathbf{r}) + I^{\sigma^+}(\mathbf{r}) + I^{\sigma^-}(\mathbf{r}))$$

$$= (2V_{D2} + V_{D1}) I(\mathbf{r}) + \Delta V m_F g_F (I^{\sigma^+}(\mathbf{r}) - I^{\sigma^-}(\mathbf{r})),$$

where we have used that  $\mathcal{P} = 0, \pm 1$  for  $\pi$  and  $\sigma^\pm$  light in the second line. In neglecting the state independent part, our assumption is that

$$\frac{\Delta V m_F g_F (I^{\sigma^+}(\mathbf{r}) - I^{\sigma^-}(\mathbf{r}))}{(2V_{D2} + V_{D1}) I(\mathbf{r})} \ll 1 \quad (4.11)$$

Due to our large detuning  $\omega - \omega_L$ , the term  $\Delta V m_F g_F / (2V_{D2} + V_{D1})$  is on the order 15%. Furthermore, the term  $(I^{\sigma^+}(\mathbf{r}) - I^{\sigma^-}(\mathbf{r})) / I(\mathbf{r})$  is maximally 1, but is, for experimentally relevant values of  $\theta$ , on the order of 10%. The product of these two terms yields that the state-dependent part of the potential contributes only on the percent level to the total potential. Hence, our approximation to neglect the state-dependent part is valid. Ref. [78] contains a detailed derivation of the potential in terms of its polarization components.

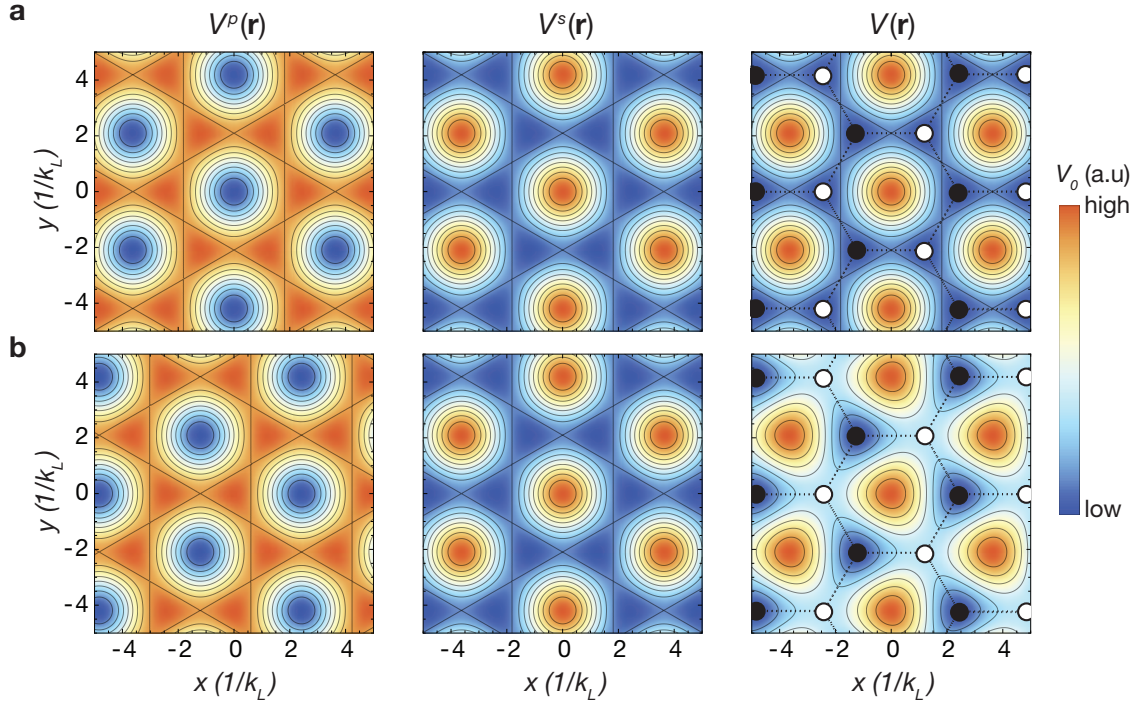


Figure 4.3.: **Realizing the Semenoff mass.** We add an energy offset between A and B sublattice sites while maintaining isotropic tunneling by tuning the proportion of and phase between the  $s$ - and  $p$ -polarizations of each beam. The  $p$ -polarized (left),  $s$ -polarized (center), and total potential (right) are shown for  $\theta = \pi/4$ . The lattice structure is outlined in dashed gray lines with black (white) dots representing A (B) sites in the total potential. In **a**, both polarization components are in-phase, i.e.,  $\alpha_1 = \alpha_2 = \alpha_3 = 0$ . Note that for the  $p$ -polarized potential, the minima form a triangular lattice. In **b**,  $\alpha_1 = 0, \alpha_2 = 2\pi/3$ , and  $\alpha_3 = 4\pi/3$ . With these parameters, the potential minima of the  $s$ -polarized potential coincide with the minima of the  $p$ -polarized potential on A sites and the maxima of the  $p$ -polarized potential on B sites. Hence, there is an energy difference between A and B sites in the total potential.

tive to the  $s$ -polarized potential. When  $\alpha_1 = \alpha_2 = \alpha_3 = 0$ , the minima of the  $p$ -polarized potential and the maxima of the  $s$ -polarized potential coincide with the A and B sites (Fig. 4.3a). Consequently, atoms experience the same ac Stark shift on either an A or B site. However, by setting  $\alpha_{12} = \alpha_{23} = 4\pi/3$  and  $\alpha_{13} = 2\pi/3$ , the  $s$ -polarized potential is shifted such that the potential maxima occur on B sites while the potential minima occur on A sites (Fig. 4.3b). Consequently, the potential on A sites is lower than the potential on B sites, as illustrated in the right-most column of Fig. 4.3b.

## 4.2. State preparation: creating a BEC

The starting point of all experiments described in this thesis is the adiabatic loading of a BEC of either  $^{87}\text{Rb}$  or  $^{39}\text{K}$  into an optical honeycomb lattice. To obtain a BEC, we cool an atomic vapor of  $^{87}\text{Rb}$  and/or  $^{39}\text{K}$ . When a  $^{87}\text{Rb}$  BEC is desired, only  $^{87}\text{Rb}$  is cooled. When a  $^{39}\text{K}$  BEC is desired, we cool both  $^{39}\text{K}$  and  $^{87}\text{Rb}$  atoms for later use in sympathetic cooling. The cooling process begins in a two-species 2D+MOT [104–110], as shown in Fig. 4.4. From the 2D+MOT, the atoms enter the 3D-MOT [111], where further cooling occurs. At the end of the 3D-MOT, the magnetic fields are switched off and the atoms are again cooled by an optical molasses [111]. Next, both  $^{39}\text{K}$  and  $^{87}\text{Rb}$  atoms are spin-polarized into their  $|F=2, m_F=2\rangle$  state in preparation for magnetic transport. The atoms are then transported by a 100 G/cm magnetic quadrupole trap formed by pairs of overlapping coils [112]. We ramp the current through each pair of coils such that a magnetic quadrupole potential smoothly moves the atoms a total distance of 58cm from the 3D-MOT to the science cell.

Once the atoms reach the science cell, we begin microwave evaporation in a plugged quadrupole trap. The center of the quadrupole trap is plugged with a tightly-focused, blue-detuned beam in order to avoid Majorana losses [113–115]. Next, as the quadrupole gradient is being ramped down to zero, the intensity of a pair of crossed dipole beams is ramped up to initiate further evaporative cooling in the crossed-dipole trap until condensation. Soon after the crossed-dipole trap has been ramped up, we perform an RF-sweep to transfer both  $^{87}\text{Rb}$  and  $^{39}\text{K}$  into their  $F=1$  ground state manifold and blow away residual  $F=2$  atoms via a resonant light-pulse. Evaporative cooling then proceeds with only  $F=1$  atoms, thereby avoiding possible spin-changing collisions.

When cooling only  $^{87}\text{Rb}$ , we simply lower the intensity of the dipole beams. The crossed-beam dipole trap is formed from light of wavelength 1064 nm and is therefore red-detuned from the atomic transition. Hence, based on Eq. 4.1, a lower intensity means a lower trapping potential, from which hot atoms can escape. The remaining atoms efficiently thermalize to a lower temperature and eventually condense.

Condensation of  $^{39}\text{K}$  is achieved using the same principle, but we must additionally utilize Feshbach resonances, which allow us to tune the scattering length between atoms via a magnetic offset field [38] for efficient thermalization. We first utilize a Fes-

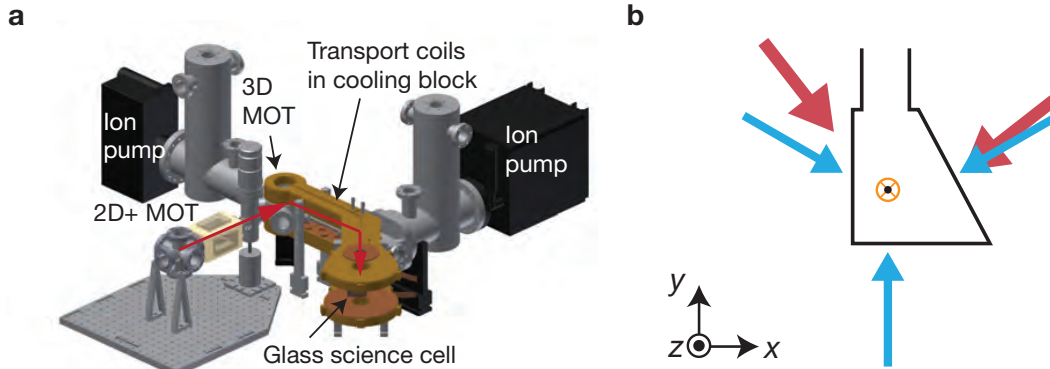


Figure 4.4.: **Experimental setup for preparing a BEC.** **a**, An overview of the vacuum setup with the path of the atoms shown in red. Atoms begin in the 2D+MOT, where they are pre-cooled before traveling into the 3D-MOT chamber for further cooling. Next, the atoms are magnetically transported to the science cell, where they are evaporatively cooled to quantum degeneracy before the experiments occur. **b**, The glass science cell has an asymmetric shape (black outline) to avoid back-reflections of beams onto the atoms (black dot) from the inner surface of the glass. The lattice beams (blue) propagate at  $120^\circ$  degree angles onto the atoms. The dipole beams (red) propagate perpendicular to each other, forming the crossed-dipole trap. One dipole beam propagates nearly on the same axis as one of the lattice beams. The main imaging beam (orange circle with cross) is centered on the atoms and travels vertically into the plane.

hbach resonance between  $^{39}\text{K}$  and  $^{87}\text{Rb}$  atoms, sympathetically cooling the  $^{39}\text{K}$  atoms with the microwave-evaporated  $^{87}\text{Rb}$  atoms [116, 117]. During this time, we continuously lower the dipole trap depth. Once the  $^{87}\text{Rb}$  atoms have dropped out of the trap due to their larger mass, we use another Feshbach resonance between  $^{39}\text{K}$  atoms and continue evaporation until condensation [118]. We then decrease the scattering length to avoid losses before ramping the field to the desired scattering length for the experiments. Further details can be found in Appendix A.

After condensation has occurred, the atoms are held in the low-intensity dipole trap as the intensity of the lattice beams is adiabatically ramped up. When the lattice is stationary with respect to the atomic cloud, the BEC macroscopically occupies the ground state of the lattice, given by the Bloch state  $|\Psi_\Gamma^1\rangle$  at quasimomentum  $\Gamma$  in the first band.

### 4.3. State evolution: creating a gradient

In the presence of a constant external force, the quasimomentum of a Bloch state becomes time-dependent [89]. In this section, we review how this force is realized using either a magnetic field or by accelerating the lattice. While the force due to the magnetic field gradient is spin-dependent, the force due to the lattice acceleration is spin-independent. As we will later explain in Chapter 5, both a spin-dependent and a

spin-independent force is required to measure the Berry phase. Measuring elements of the Wilson line requires only a spin-independent force.

### 4.3.1. Magnetic field

To create a magnetic field gradient, we use a single coil oriented along the  $x$ -axis, as shown in Fig. 4.5a. The positioning and geometry of the coil was chosen to maximize the force felt by the atoms. The coil is conically shaped in order to fit as close as possible to the experimental cell without obstructing the dipole and lattice beams. Since the magnetic field is proportional to the current, we could try to compensate for the distance between the coil and the atoms by sending more current. However, this would result in excess heating of the coil.

Near the position of the atoms, the magnitude of the magnetic field created by the coil is, to first order,  $B_a(\mathbf{r}) = B_0 + \nabla\mathbf{B} \cdot \mathbf{r}$ , where  $\nabla\mathbf{B}$  is the magnetic field gradient created by the coil evaluated at the position of the atoms. Due to the Zeeman effect, the magnetic field breaks the energy degeneracy between the magnetic sublevels  $m_F$  of the hyperfine level  $F$  as

$$E(\mathbf{r}) = \mu_B m_F g_F B_a(\mathbf{r}), \quad (4.12)$$

where  $\mu_B$  is the Bohr magneton and  $g_F$  is the Landé  $g$ -factor. Since the coil is oriented along the  $x$ -axis, the linear gradient  $E(\mathbf{r})$  is predominantly in the  $x$ -direction. Furthermore, this gradient is associated with a force

$$\mathbf{F} = \nabla E(\mathbf{r}) = \mu_B m_F g_F \nabla\mathbf{B} \quad (4.13)$$

Due to the dependence on  $g_F$  and  $m_F$ , the force will be different for different hyperfine states.

### 4.3.2. Lattice acceleration

#### How do we accelerate the lattice?

To understand the acceleration of the lattice, it is instructive to first consider the interference pattern formed by two counterpropagating beams along the  $x$ -direction. If the frequencies of the beams are the same, the resulting interference pattern is a standing wave. If, however, there is a frequency difference between the counterpropagating beams, the total interference pattern now moves with a velocity proportional to the frequency difference. Accordingly, if the frequency difference is time-dependent, then the total interference pattern moves with a time-dependent velocity. In this case, we say that the lattice is accelerating.

The same reasoning applies to the honeycomb lattice. Changing the frequency of, for example, beam 1 propagating along the  $y$ -direction, moves the entire interference

pattern along the  $y$ -direction, as illustrated in Fig. 4.5b. The velocity with which the lattice potential moves is

$$v_y(t) = \frac{2}{3}\lambda\delta\nu, \quad (4.14)$$

where  $\delta\nu$  is the frequency difference between beam 1 and the other two beams. It follows that the acceleration of the lattice in the  $y$ -direction is given by

$$a_y(t) = dv(t)/dt = \frac{2}{3}\lambda\frac{d}{dt}\delta\nu. \quad (4.15)$$

Generally, sweeping the frequency of beam  $i$  results in acceleration along the propagation direction of beam  $i$ . The acceleration due to a frequency sweep of two beams is the vector sum of the accelerations from each individual beam. By tuning the parameter  $\frac{d}{dt}\delta\nu$ , which parametrizes the rate of the frequency sweep, we can tune the magnitude of the acceleration of the lattice. Hence, by independently controlling the frequencies of two beams, we can accelerate the lattice along arbitrary paths. In our experiments, we choose the frequency sweep rate  $\frac{d}{dt}\delta\nu$  to be constant to obtain a constant acceleration.

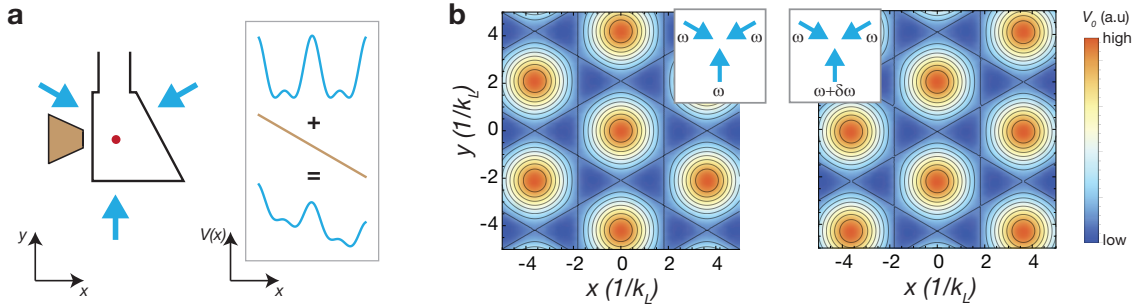


Figure 4.5.: **Methods of creating a force for state-evolution: magnetic field gradient and lattice acceleration.** **a**, A (not-to-scale) schematic showing the relative positions of the lattice beams (blue arrows), atoms (red dot), and coil (brown conical shape). The single coil is centered along the position of the atoms and creates a magnetic field gradient along the  $x$ -axis. The resulting potential along the  $x$ -direction (bottom blue in the inset box) is the sum of the original lattice potential (top blue) and the gradient potential (brown). **b**, By changing the frequency of beam  $n$  by  $\delta\omega$  while keeping the frequency of the other two beams fixed, the entire potential shifts along the propagation direction of beam  $n$ . We show the position of the potential at two different times for a constant frequency shift in beam 1, which moves the lattice potential along the  $y$ -axis.

### How does lattice acceleration create a gradient?

The lattice acceleration is equivalent to a gradient in the frame co-moving with the lattice. This can be seen by first writing the time-dependent Hamiltonian for a lattice potential with varying position  $\mathbf{R}(t)$ :

$$H(t) = \frac{\hat{\mathbf{p}}^2}{2m} + V(\hat{\mathbf{r}} - \mathbf{R}(t)), \quad (4.16)$$

where  $\hat{\mathbf{p}}$  and  $\hat{\mathbf{r}}$  are the momentum and position operators, respectively. To enter a frame co-moving with the lattice we use the a unitary transformation

$$U(t) = e^{-im\dot{\mathbf{R}}(t)\cdot\hat{\mathbf{r}}} e^{i\mathbf{R}(t)\cdot\hat{\mathbf{p}}}, \quad (4.17)$$

where  $\hbar = 1$  and  $m$  is the atomic mass. These are translation operators of real and momentum space. Hence, the unitary transformation takes into account both the varying position and momentum of the atoms. The time-dependent Schrödinger equation  $i\dot{\Psi} = H(t)\Psi$  can then equivalently be expressed as  $i\dot{\tilde{\Psi}} = \tilde{H}\tilde{\Psi}$ , where  $\tilde{\Psi} = U\Psi$  and

$$\tilde{H} = UHU^\dagger + i\dot{U}U^\dagger \quad (4.18)$$

Noting that

$$\begin{aligned} UHU^\dagger &= \frac{(\hat{\mathbf{p}}^2 + m\dot{\mathbf{R}}(t))^2}{2m} + V(\hat{\mathbf{r}}), \\ i\dot{U}U^\dagger &= m\ddot{\mathbf{R}}(t)\cdot\hat{\mathbf{r}} - \dot{\mathbf{R}}(t)\cdot(\hat{\mathbf{p}} + m\dot{\mathbf{R}}(t)), \end{aligned} \quad (4.19)$$

we arrive at

$$\tilde{H} = \frac{\hat{\mathbf{p}}^2}{2m} + V(\hat{\mathbf{r}}) + m\ddot{\mathbf{R}}(t)\cdot\hat{\mathbf{r}} - \frac{m\dot{\mathbf{R}}(t)^2}{2} \quad (4.20)$$

In the co-moving frame, the atoms experience a force  $\mathbf{F} = -m\ddot{\mathbf{R}}(t)$ , i.e., in the opposite direction of the lattice movement. The term  $\frac{m\dot{\mathbf{R}}(t)^2}{2}$  is an energy offset associated with the momentum  $m\dot{\mathbf{R}}(t)$  imparted by the moving lattice.

## 4.4. State detection: absorption imaging

Information about our atoms are attained through absorption imaging, one of the most standard techniques in ultracold atom experiments [119]. In absorption imaging, we shine a collimated beam of resonant light onto the atoms. The density-dependent intensity profile  $I(x, y)$  is then imaged onto a charge-coupled-device (CCD) camera. According to the Beer-Lambert law, an imaging beam propagating in the  $z$ -direction

through an atomic sample with density  $n(x, y, z)$  has resultant intensity[120]

$$\begin{aligned} I(x, y) &= I_0 e^{\sigma \int n(x, y, z) dz} \\ &= I_0 e^{\sigma n_{col}(x, y)}, \end{aligned} \quad (4.21)$$

where  $n_{col}(x, y)$  is called the local column density and  $\sigma$  is the scattering cross-section of the atoms, which takes into account details of the atomic level structure and the intensity and polarization of the imaging beam. Solving for the local column density, which is the quantity of interest, we obtain

$$n_{col}(x, y) = -\frac{1}{\sigma} \ln \frac{I(x, y)}{I_0(x, y)} \quad (4.22)$$

Experimentally, we obtain  $n_{col}(x, y)$  by taking four images: 1) one image with the atoms and the imaging beam, 2) one image with only the imaging beam, and 3) and 4) two dark images with neither atoms nor imaging beam to account for stray light hitting the CCD chip. Image 3 is then subtracted from image 1, to give  $I(x, y)$ , and image 4 is subtracted from image 2, to give  $I_0(x, y)$ .

In these experiments, we image the atoms after they have been released from all confining potentials and have undergone free-flight expansion for a given time. These time-of-flight (TOF) images reveal different aspects of the momentum composition of the atoms, depending on whether we suddenly shut off or gradually ramp down the lattice potential. The former method is primarily used to ensure that all three beams have equal intensity at the position of the atoms, such that the lattice is as ideal as possible. The latter method is used for state-detection in the experiments.

#### 4.4.1. Sudden shut-off of the lattice: plane-wave decomposition

Assume we have adiabatically loaded the BEC into the lattice at  $\mathbf{q} = \Gamma$  in the first band. When the lattice is suddenly shut off, the Bloch state  $|\Psi_{\Gamma}^1\rangle$  is projected onto the real space momentum states. In other words, a sudden shut-off of the lattice probes the (modulus-squared) coefficients of the plane wave expansion of the Bloch state. Recall from Eq. 3.33 that the plane wave expansion of  $u_{\mathbf{q}}^n(\mathbf{r})$  is comprised only of reciprocal lattice vectors. Consequently, as shown in Fig. 4.6a, only momenta that are a linear combination of the primitive reciprocal lattice vectors  $\mathbf{b}_1$  and  $\mathbf{b}_2$  are occupied. In other words, a sudden shut-off of the real-space lattice images the reciprocal lattice points. These plane wave components are commonly called Bragg peaks or coherence peaks.

However, the Bloch state is of course not an equal superposition of all plane waves. This can be understood intuitively by noting that the BEC occupies a single plane wave state without a lattice. As the lattice depth is increased, the potential deviates more from the free-space potential. Consequently, we require more plane waves to con-

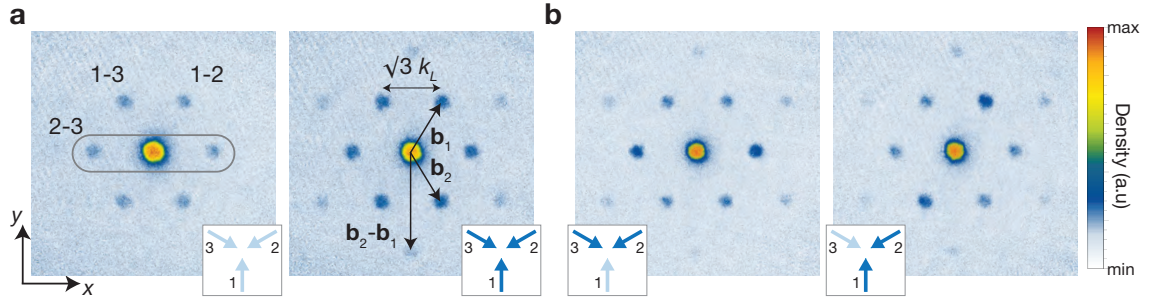


Figure 4.6.: **TOF images: sudden-shutoff.** **a**, When all confining potentials are abruptly shut off, the Bloch states are projected onto the real-space momentum states. In a weak lattice, we see only first-order coherence peaks (left image with light-blue arrows in the inset), while a stronger lattice also reveals second-order coherence peaks (right image with dark-blue arrows in the inset). In the left image, we label the coherence peak resulting from the interference of the beams  $i$  and  $j$  as  $i - j$ . As an example, the coherence peaks due to beams 2-3 are boxed. In the right image, we show how each coherence peak can be understood as a point in the reciprocal lattice by labeling a few peaks in terms of a linear combination of the primitive reciprocal lattice vectors  $\mathbf{b}_1$  and  $\mathbf{b}_2$ . **b**, An imbalance in the intensity of the beams reveals itself as an imbalance in the intensities of the coherence peaks. In the left image, beam 1 is too weak (lighter blue arrow) such that the coherence peak resulting from beams 2 and 3 is stronger than the coherence peaks resulting from beams 1 and 2 and 1 and 3. Likewise, when beam 3 is too weak, the coherence peak from beams 1 and 2 is stronger (right image).

struct the appropriate eigenstate.<sup>3</sup> A more accurate description takes into account the real-space size of the BEC in the lattice and the real-space wavefunction, i.e., Wannier function, on each lattice site.<sup>4</sup>

For our purposes, the simplistic picture will suffice. From it, we can conclude that higher order plane-wave components (i.e., larger  $l_1$  and  $l_2$ ) become more populated as the lattice depth is increased. If we furthermore know the plane wave component that results from a particular pair of beams, we can use the atoms to fine tune the intensities of the beams to obtain the desired potential. For example, if beam 1 is weaker than beams 2 and 3, then the plane wave components resulting from the potential created by interference of beams 1 and 2 and beams 1 and 3 will be weaker than those due to the potential from beams 2 and 3, as shown in Fig. 4.6b.

We primarily use this sudden shut-off method to ensure our beam intensities are equal. It is necessary to use the atoms themselves as probes of the beam intensity

<sup>3</sup> Indeed, the plane wave expansion is simply a Fourier expansion and the plane wave coefficients are simply the Fourier coefficients.

<sup>4</sup> The sudden shut-off images essentially probes the Fourier transform of the real-space wavefunction. The largest feature in real-space then becomes the smallest feature in momentum-space and vice versa. Consequently, the broad envelope of the TOF image is given by the real-space extent of the Wannier functions and the size of individual momentum peaks is given by the size of the entire BEC. For more details, see Refs. [121, 122].

since technical imperfections such as the inhomogeneity of beam sizes, differences in the positioning of the beams onto the atoms, or angle-dependent reflectivity of light on the glass of the experiment cell preclude accurate measurements of intensity using power meters or photodiodes.

Lastly, we note that the appearance of coherence peaks is specific for a superfluid state because it relies on the macroscopic occupation of a single Bloch state. Such a system is said to be phase coherent. In contrast, for large enough lattice depths, the phase coherence between lattice sites is lost and sudden shut-off TOF images result in a broad background. These images were used to probe the superfluid to Mott insulator transition [123] and are a routine observable in investigating phase coherence in optical lattice systems [122, 124, 125]. In our experiment, we always work in the superfluid regime.

#### 4.4.2. Ramp-down of the lattice: band mapping

In a technique called band mapping, we gradually ramp down the lattice depth to zero to map both the band population and the quasimomentum distribution onto real space momentum components [121, 125, 126], as schematically shown in Fig. 4.7a. As the band structure is adiabatically deformed into the free-space dispersion (top to bottom panel in Fig. 4.7a), the time-scale of the ramp-down must be adiabatic compared to the energy gaps between bands to preserve the original population distribution in the bands. Fulfilling this adiabaticity condition is easiest near the center of the Brillouin zone, where the gap between the first and second band is largest, and becomes more difficult closer to the band-edge. At exactly the band-edge, the first and second bands become degenerate for vanishing lattice depths, and the ramp-down can never be adiabatic. Accordingly, it is impossible to distinguish between first and second band atoms at the band-edge, since there, they are mapped to the same point.

In addition to respecting the adiabaticity condition, the time-scale of the ramp-down must also be fast enough to avoid redistribution of the quasimomentum within each occupied band. When both conditions are fulfilled, Atoms located in the  $n^{\text{th}}$  band at quasimomentum  $\mathbf{q}$  are mapped onto real space momentum  $\mathbf{p} = \mathbf{q} + \hbar\mathbf{K}(n - 1)$  in the  $n^{\text{th}}$  Brillouin zone, where  $\mathbf{K}$  is a reciprocal lattice vector. The extended-zone scheme for the honeycomb lattice is shown in Fig. 4.7b and illustrates the mapping of the first, second, and third bands. For example, consistent with our reasoning above, atoms located on the band-edges in the first and second bands are mapped to the same point. In contrast, atoms located at  $\Gamma$  in the first and second bands are clearly distinguishable: they appear at the center of the Brillouin zone in the first band, but are split into the six tips of the star-shape in the second band. However, second and third band atoms at  $\Gamma$  are not distinguishable. Since our experiments mostly involve detecting atoms in the first and second band, we primarily band map at  $\Gamma$ .

We show two examples of band mapped images in Fig. 4.7c and Fig. 4.7d. In the former, condensed, higher band atoms are band-mapped at  $\Gamma$ . While it is clear that

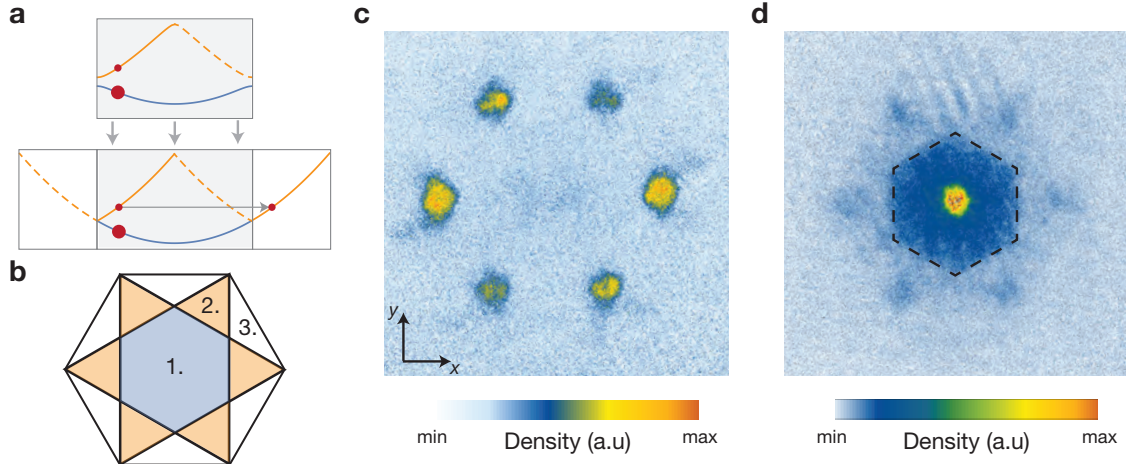
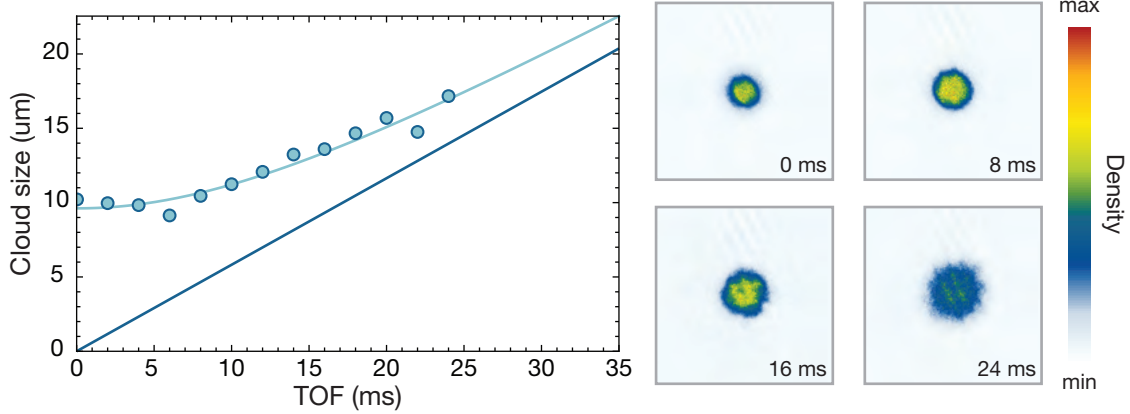


Figure 4.7.: **Band mapping schematics and example images.** **a**, Atoms (red circles) are initially primarily in the first band (blue) with some population (smaller red circle) in the second band (orange). Assuming that the band mapping time-scales are fulfilled, the lattice dispersion is adiabatically deformed into the free-particle dispersion (top to bottom panel). We simultaneously show the reduced and extended zone scheme for the free-particle dispersion. The first band remains in the first Brillouin zone (shaded region) in both reduced and extended zone schemes. However, the second band is mapped into the second Brillouin zone in the extended zone scheme. The solid orange branch is mapped to the right and the dashed orange branch of the second band is mapped to the left. Hence, we can clearly distinguish between first and second band atoms. **b**, Band mapping schematic for the honeycomb lattice showing the first (blue), second (orange) and third (white) Brillouin zones, corresponding to the first, second, and third bands. **c**, Absorption image of higher band  $^{39}\text{K}$  atoms band mapped at  $\Gamma$  after 3.5 ms TOF. Although we clearly see that there are no atoms in the first band, we do not know whether the atoms are in the second through sixth bands. Band mapping at a different quasimomentum revealed that these atoms are in fact in the fifth band. **d**, Absorption image of primarily first band  $^{87}\text{Rb}$  atoms band mapped at  $\Gamma$  after 6 ms TOF. The first Brillouin zone is indicated by the dashed hexagon. After loading, the atoms were held in the lattice for an extended period of time. This induces heating such that the condensate is depleted and hot atoms occupy other quasimomenta in the first Brillouin zone, clearly illustrating its hexagonal structure.

there are no atoms in the first band, we cannot determine whether the atoms are in the second or third band (or the fourth, fifth, or sixth band, for that matter). In Fig. 4.7d, the band mapping again occurs at  $\Gamma$ , but the atoms are heated and primarily in the first band. Although most of the condensed atoms are located at  $\Gamma$ , there is a hot background extending throughout the Brillouin zone, clearly showing its hexagonal structure.

In both images, the band mapped atoms have some finite width, suggesting that they are spread out in reciprocal space. This is especially clear in Fig. 4.7d, where the condensed atoms are visible against a background of heated atoms and occupy a sizeable

portion of the first Brillouin zone. While the atoms are indeed slightly distributed in reciprocal space, the actual width we see in the images is a convolution of the *in-situ* size of the atomic cloud with the momentum distribution. At our typical TOFs of 3-10 ms, the *in-situ* size of the cloud dominates. Therefore, our band mapped images are not a reliable way of determining the quasimomentum spread of the BEC in reciprocal space. Instead, we measure the quasimomentum spread by observing the expansion in the BEC width after release from all confining potentials at different TOFs, as shown in Fig. 4.8. We find that, assuming an initial Gaussian distribution in the Brillouin zone, the standard deviation of the BEC is approximately  $0.1 k_L$ .



**Figure 4.8.: Measuring the quasimomentum distribution.** We measure the standard deviation of the  $^{87}\text{Rb}$  cloud width after release from all optical potentials at different TOFs. Assuming a Gaussian distribution in both momentum and real space, we expect the standard deviation of the cloud width in our convolved images to scale as  $\sqrt{\sigma_0^2 + (t\sigma_{\mathbf{q}}/m)^2}$ , where  $\sigma_0$  is the *in-situ* standard deviation of the cloud width,  $\sigma_{\mathbf{q}}$  is the standard deviations of the quasimomentum distribution, and  $m$  is the mass of  $^{87}\text{Rb}$ . Fitting the data above yields  $\sigma_0 = 9.6(3) \mu\text{m}$  and  $\sigma_{\mathbf{q}} = 0.095(3) k_L$ . Light blue line is the fit and dark blue line shows the expected expansion of the cloud neglecting the *in-situ* width, i.e., with  $\sigma_0$  set to zero. At very long TOFs, the *in-situ* width becomes negligible. However, for our TOFs of  $<10$  ms, the *in-situ* width is dominant.

## 4.5. Applications: Bloch oscillations and lattice depth calibration

We conclude this chapter by applying the tools described in previous sections to examine Bloch oscillations and calibrate the lattice depth. We show the difference in Bloch oscillations between applying a small force, such that the evolution is adiabatic, and a large force, such that the second band is also populated. Next, we utilize our ability to move along arbitrary paths in the Brillouin zone with a non-adiabatic force to calibrate the lattice depth through a technique called Stueckelberg interferometry.

### 4.5.1. Bloch oscillations

Bloch oscillations originate from solid state physics and describe the response of an electron in a perfect crystal to a constant electric field [1]. In contrast to a free-particle which accelerates uniformly along the field, Bloch electrons oscillate in real space. When we refer to Bloch oscillations here, we refer to the motion of the atoms in reciprocal space, where the quasimomentum scans the Brillouin zone at a rate linearly proportional to the applied force. When the atoms have moved by one reciprocal lattice vector, we say that it has undergone a single Bloch oscillation. Although the movement in reciprocal space is related to the movement in real space, we cannot resolve the real space movement in our experiment and restrict ourselves to looking at Bloch oscillations in reciprocal space. The connection between real space Bloch oscillations and reciprocal space movement in the context of cold atoms is detailed in Refs. [89, 127, 128].

In Fig. 4.9, we show bandmapped images of atoms undergoing adiabatic Bloch oscillations due to a magnetic gradient and accelerating the lattice along the  $\Gamma$ -M direction. In the case of the gradient (Fig. 4.9a), the atoms move as they scan the Brillouin zone, which remains fixed in the lab frame. Here, the real space momentum we see directly gives the quasimomentum. In contrast, in the case of lattice acceleration (Fig. 4.9b), the atoms seem stationary. This is because their real space momentum consists of both the quasimomentum and the momentum imparted by the lattice, which is given by the last term of Eq. 4.20. Furthermore, recall that the force the atoms experience is in the opposite direction as the movement of the lattice. Hence, for a lattice moving with speed  $|\nu| = |\mathbf{F}| t / m$  at time  $t$ , where  $\mathbf{F}$  is the applied force and  $m$  is the atomic mass, the real space momentum is given by the difference between the quasimomentum,  $|\mathbf{F}| t$  and the lattice momentum  $m|\nu| = |\mathbf{F}| t$ . This difference is zero until the atoms reach the edge of the Brillouin zone and suddenly Bragg-reflect to the opposite edge of the Brillouin zone. In the bottom row of Fig. 4.9b, we show band mapped images of atoms undergoing non-adiabatic Bloch oscillations due to lattice acceleration. The population in the second band is clearly visible after the atoms traverse the Brillouin zone edge.

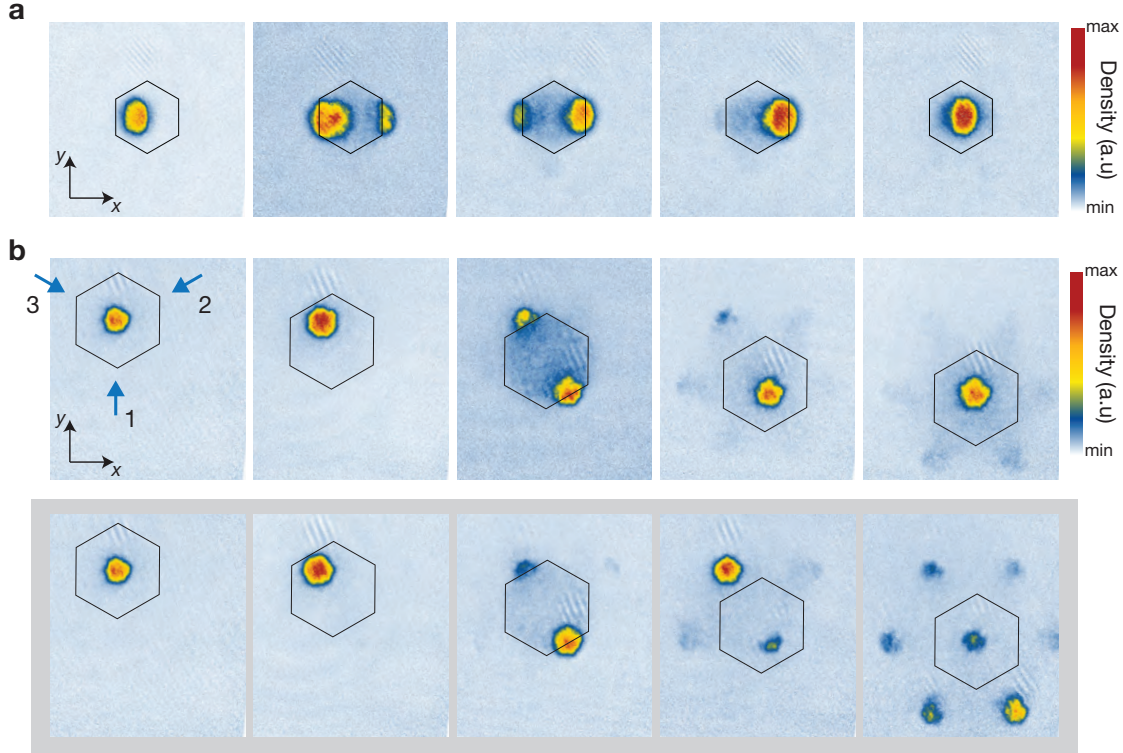


Figure 4.9.: **Bloch oscillations overlaid with the first Brillouin zone.** **a**, Band mapped images of  $^{87}\text{Rb}$  after 9 ms TOF showing adiabatic Bloch oscillations due to a magnetic field gradient. As the atoms scan the Brillouin zone, we directly image their change in quasimomentum  $\mathbf{q}$  onto real-space momenta. In the first image, the atoms are at a finite  $\mathbf{q}$  displaced from  $\Gamma$ . As they approach the band-edge, their finite distribution in reciprocal-space results in some atoms crossing the band-edge before others (second and third images). In the fourth image, all atoms have crossed the band-edge and in the fifth image, they have completed one Bloch oscillation and returned to  $\Gamma$ . **b**, Band mapped images of  $^{87}\text{Rb}$  after 12 ms TOF showing adiabatic (top row) and non-adiabatic (shaded bottom row) Bloch oscillations with lattice acceleration of beams 1 and 3. Lattice beams are shown as blue arrows in the first image. Top row: We begin with atoms at  $\Gamma$  and, in contrast to using a magnetic field gradient, Bloch oscillations with lattice acceleration moves the Brillouin zone. Atoms appear stationary in the lab frame until they Bragg-reflect at the band-edge (third image). After crossing the band-edge, atoms again appear stationary as the Brillouin zone continuously moves. In the last image, we have completed slightly more than one Bloch oscillation. There is slight but negligible population in the second band. Bottom row: When using a large enough force, we have clearly populated the second band after completing a single Bloch oscillation.

### 4.5.2. Lattice calibration

In order to calibrate our lattice depth, we use a process called Stueckelberg interferometry, which has been previously used to calibrate the depth of 1D lattices [129, 130]. The basic idea is to measure the energy difference between two bands at various quasi-momenta and match them with calculations in order to infer the lattice depth. The process is illustrated in Fig.4.10a and is as follows:

1. We begin with the adiabatic loading of a BEC into the honeycomb lattice. The BEC is in the state:

$$|\psi\rangle = |\Psi_{\Gamma}^1\rangle \quad (4.23)$$

2. We move the state to the quasimomentum at which we would like to measure the energy difference,  $\mathbf{Q}$ . It is important to move the state quickly enough such that atoms also populate the second band at  $\mathbf{Q}$ . For simplicity, we will assume an equal splitting between the first and second band at  $\mathbf{Q}$ . The state is given by

$$|\psi\rangle = \frac{1}{\sqrt{2}}(|\Psi_{\mathbf{Q}}^1\rangle + |\Psi_{\mathbf{Q}}^2\rangle) \quad (4.24)$$

3. We hold the atoms at  $\mathbf{Q}$ , during which they acquire a dynamical phase. Atoms in the first (second) band acquire a phase  $e^{iE_{\mathbf{Q}}^{1(2)}\tau/\hbar}$  for hold time  $\tau$ , where  $E_{\mathbf{Q}}^{1(2)}$  gives the energy of the first (second) band at  $\mathbf{Q}$ :

$$|\psi\rangle = \frac{1}{\sqrt{2}}(e^{iE_{\mathbf{Q}}^1\tau/\hbar}|\Psi_{\mathbf{Q}}^1\rangle + e^{iE_{\mathbf{Q}}^2\tau/\hbar}|\Psi_{\mathbf{Q}}^2\rangle) \quad (4.25)$$

4. We move the state back to  $\Gamma$ . If this second segment is again non-adiabatic (in practice, we always use the same force as in the first segment), atoms originally in the first band split into first and second band atoms and likewise for second band atoms:

$$|\psi\rangle = \frac{1}{2}e^{iE_{\mathbf{Q}}^1\tau/\hbar}(|\Psi_{\Gamma}^1\rangle + |\Psi_{\Gamma}^2\rangle) + \frac{1}{2}e^{iE_{\mathbf{Q}}^2\tau/\hbar}(|\Psi_{\Gamma}^1\rangle - |\Psi_{\Gamma}^2\rangle) \quad (4.26)$$

5. By bandmapping at  $\Gamma$  to measure the population of the first band atoms, we obtain information about the energy difference between the first and second band.

$$|\langle\Psi_{\Gamma}^1|\psi\rangle|^2 = \left| \frac{1}{2}(e^{iE_{\mathbf{Q}}^1\tau/\hbar} + e^{iE_{\mathbf{Q}}^2\tau/\hbar}) \right|^2 \propto 1 + \cos(\Delta\omega\tau), \quad (4.27)$$

where  $\Delta\omega = (E_{\mathbf{Q}}^2 - E_{\mathbf{Q}}^1)/\hbar$ .

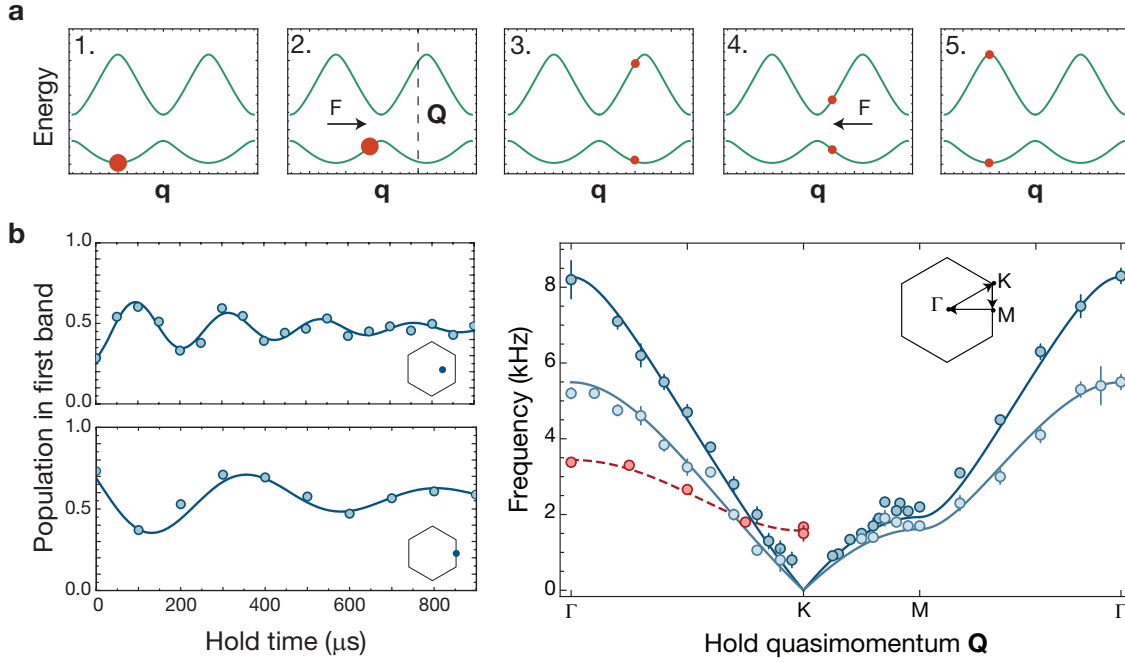


Figure 4.10.: **Lattice calibration using Stueckelberg interferometry.** **a**, Atoms (orange circles) are initiated at  $\Gamma$  (1.) and then accelerated with a non-adiabatic force  $F$  toward the desired quasimomentum  $Q$  (2.). After a hold time at  $Q$  (3.), atoms are accelerated back toward  $\Gamma$  with the same force  $F$  (4.). Finally, atoms are band mapped at  $\Gamma$  for the population in the first band (5.). As a function of hold time at  $Q$ , the population in the first band oscillates with a frequency  $\Delta\omega$  given by the energy difference between the first and second band. **b**, Left: Two examples of population oscillations in a lattice of depth  $V_0 = 0.8E_r$  taken between  $\Gamma$  and M (top) and at M (bottom). Right: The dispersion relation along the high-symmetry line  $\Gamma$ -M-K- $\Gamma$  for a lattice with degenerate A and B sites and depths of  $V_0 = 0.8E_r$  (dark blue) and  $V_0 = 3.2E_r$  (light) blue. Solid lines are theory from the *ab-initio* calculation. Red data map the dispersion for a lattice with an energy offset between A and B sites. A best-fit tight-binding calculation (red dashed line) gives an offset of  $\Delta/J = 3.1$  and lattice depth of  $V_0 = 5.2E_r$ . The two data points at K denote a measurement at K and K' which, in accordance with theory, yield the same energy splitting.

Hence, as illustrated in the left panel Fig. 4.10b, by changing the hold time  $\tau$ , we obtain an oscillation in the population of the first band. The contrast of the oscillation depends on the splitting between bands, with a 50/50 splitting yielding the maximum contrast. We, however, are more interested in the frequency of the oscillation, which reveals the energy difference between the first and second bands. By repeating this measurement sequence at various  $\mathbf{Q}$ , we obtain a map of the dispersion relation over the entire Brillouin zone (right panel of Fig. 4.10b). We can then calculate the dispersion at various lattice depths, choose the dispersion that best fits our data, and therefore, find our lattice depth. The solid theory lines in Fig. 4.10b are *ab-initio* calculations at lattice depths that match our data the best by eye. In practice, when calibrating our lattice each day before experimental runs, we measure only the  $\Gamma$  point.

Due to the vanishing energy gap at the Dirac point, it becomes progressively more difficult to measure the energy difference in the vicinity of the K point. The problem is two-fold: the period of the oscillations becomes longer, necessitating longer hold times near K, while dynamical instabilities due to our weakly-interacting BEC limit the lifetime of the condensate [131–133]. We can, however, open a gap at the Dirac point by adding an energy-offset between A and B sites of the lattice. This allows us to measure the energy difference between first and second bands at K (red data in Fig. 4.10b). By fitting our data to a tight-binding model, we obtain an energy-offset of  $\Delta/J = 3.1$ .

# Chapter 5.

## Measuring the Berry phase

In this chapter, we measure the geometric phase acquired by a particle adiabatically encircling a Dirac point. We begin by drawing an analogy between our experiment and the Aharonov-Bohm effect [134], in which electrons encircle an infinitely long solenoid of magnetic flux and experience a phase shift in their interference pattern despite always traversing a region of zero magnetic field. We then present the spin-echo interferometry used to perform our measurements in Sec. 5.2.1, followed by a brief description of experimental parameters in Sec. 5.2.2. Although the interferometric sequence ideally yields only the geometric phase, technical imperfections preclude complete cancellation of dynamical phases and contribute to our experimental uncertainty; these issues are discussed in Sec. 5.2.3. Finally, we conclude with experimental results in Sec. 5.3. A more thorough account of the contents of this chapter can be found in Ref. [78].

### 5.1. An analogy with the Aharonov-Bohm effect

The Aharonov-Bohm effect clearly demonstrated the importance of electromagnetic potentials. Previously, in classical mechanics, these potentials were mainly considered as convenient tools for formulating electromagnetic fields, with no physically meaningful consequences due to their gauge-dependence [134]. However, as we saw in Sec. 2.3, a gauge-dependent quantity, such as the Berry connection, can yield gauge-invariant quantities under certain circumstances, such as the Berry phase. In fact, the Aharonov-Bohm effect, which preceded Berry's paper by more than two decades, can be elegantly formulated in terms of Berry connections, phases, and curvatures [23, 135].

In the Aharonov-Bohm effect, the particle encircling a confined magnetic field acquires a phase shift due to the electromagnetic vector potential. In Berry-terms, the vector potential is analogous to the Berry connection. Accordingly, the phase acquired by the particles when traversing a closed path is simply the line-integral of the Berry connection, i.e., the Berry phase. Just as the magnetic field is the curl of the electromagnetic vector potential, the Berry curvature is the curl of the Berry connection. Since the Berry phase can be equivalently expressed as an area integral of the Berry curva-

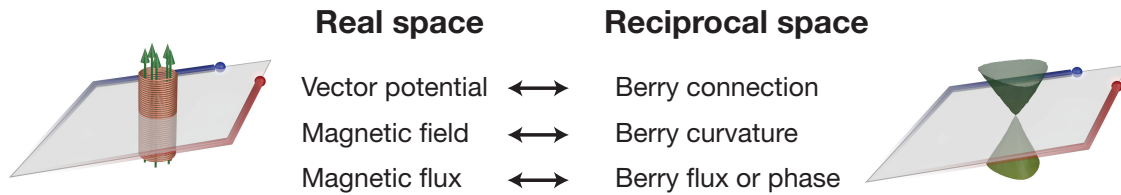


Figure 5.1.: **An analogy with the Aharonov-Bohm effect.** In the Aharonov-Bohm effect (left), electrons encircle a localized magnetic field in real space and are influenced by the associated electromagnetic vector potential, while in our interferometer (right), the particles encircle the localized Berry curvature of a Dirac point in reciprocal space and are influenced by the associated Berry connection. In both cases, flux through the interferometer loop gives rise to a measurable phase.

ture, this Berry flux is analogous to the magnetic flux arising from an area integral of the magnetic field. Hence, in terms of more physical quantities, the phase acquired by the particles is the effect of the magnetic flux through the enclosed path. The relation between the electromagnetic quantities of the Aharonov-Bohm effect and the geometric quantities of Berry is summarized in Fig. 5.1.

The experiment presented in this chapter can be considered as an Aharonov-Bohm effect in reciprocal space, where the Dirac cones of the honeycomb lattice act as the infinitely long solenoid (see Fig. 5.1). By performing interferometry with two particles around the Dirac cone, we detect the associated  $\pi$ -Berry flux (see Sec. 3.1.1) in an ideal honeycomb lattice via a  $\pi$ -phase shift in the interference fringe. Furthermore, although the Berry curvature of the Dirac cones is in principle perfectly localized in reciprocal space, in reality, it will have a finite spread due to imperfection of the lattice. We quantify the HWHM spread  $\delta q_\Omega$  of the Berry curvature to simultaneously quality-check our lattice and benchmark the resolution of our interferometer<sup>1</sup>. Lastly, we detect the motion and eventual annihilation of the Dirac cones when the  $C_3$  symmetry is broken through non-isotropic tunnelings.

## 5.2. The experimental procedure

We begin this section by outlining our interferometric sequence. The geometric Berry phase is encoded in the phase of the resulting oscillation. After understanding the theoretical procedure, we briefly review our experimental parameters and discuss technical imperfections that contribute to our experimental uncertainty.

<sup>1</sup> See Sec. 3.1.2 for a brief discussion on the spread in Berry curvature and acquired Berry phase and Ref. [78] for more details.

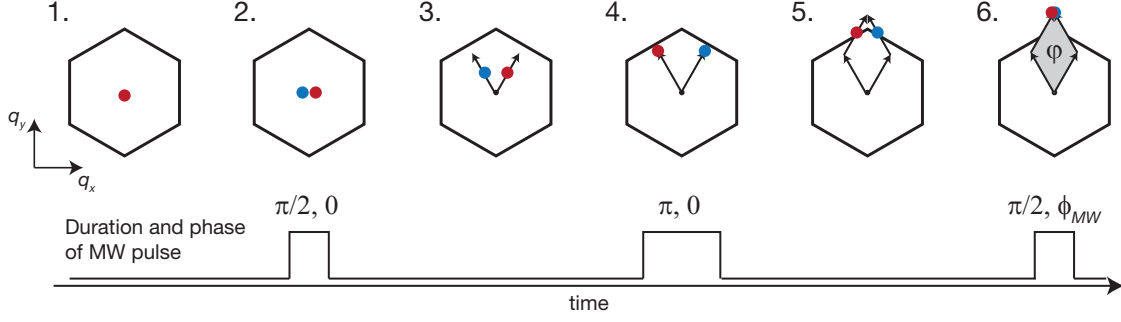


Figure 5.2.: **The interferometric procedure.** The hexagons indicate the first Brillouin zone and the spin state  $|\uparrow\rangle$  ( $|\downarrow\rangle$ ) is denoted by the red (blue) circle. After initializing the atoms in  $|\uparrow\rangle$  (1), a  $\pi/2$ -pulse is applied to create a superposition of states  $|\uparrow\rangle$  and  $|\downarrow\rangle$  (2). This is followed by an evolution time of  $\tau = 0.8$  ms (3). Next, a  $\pi$ -pulse is applied to swap the spin-states (4). After another evolution segment of time  $\tau$  (5), a  $\pi/2$ -pulse is applied with variable phase  $\phi_{MW}$  to close the interferometer.

### 5.2.1. The sequence

To measure the geometric phase acquired by two states encircling the Dirac cone, we perform a spin-echo sequence inspired by Ref. [136]. We utilize hyperfine states with opposite magnetic moment as spin states  $|\uparrow\rangle$  and  $|\downarrow\rangle$ . The procedure is as follows (see Fig. 5.2):

1. The sequence begins with a BEC of  $^{87}\text{Rb}$  in state  $|\psi\rangle = |\uparrow\rangle$  at the center of the Brillouin zone.
2. We apply a  $\pi/2$  microwave-pulse to create an equal superposition of  $|\uparrow\rangle$  and  $|\downarrow\rangle$ . In general, the rotation matrix in the basis of the  $|\uparrow\rangle$  and  $|\downarrow\rangle$  states can be expressed as

$$R(\theta, \phi) = \begin{pmatrix} \cos(\theta/2) & -e^{i\phi} \sin(\theta/2) \\ e^{-i\phi} \sin(\theta/2) & \cos(\theta/2) \end{pmatrix} \quad (5.1)$$

where  $\theta$  is the rotation angle and  $\phi$  is the phase of the microwave pulse. The state is now

$$|\psi\rangle = \frac{1}{\sqrt{2}}(|\uparrow\rangle + |\downarrow\rangle) \quad (5.2)$$

3. We allow  $|\psi\rangle$  to evolve for a time  $\tau$  in the presence of a lattice acceleration and a magnetic field gradient. These hyperfine states have opposite magnetic moment and therefore experience a force in opposite directions along the  $x$ -axis due to the magnetic field gradient. In combination with the spin-independent lattice

acceleration in the  $y$ -direction, the spin-states move in a v-shaped path. After time  $\tau$ , the state is

$$|\psi\rangle = \frac{1}{\sqrt{2}}(D_{\uparrow}G_{\uparrow}|\uparrow\rangle + D_{\downarrow}G_{\downarrow}|\downarrow\rangle), \quad (5.3)$$

where  $D_{\uparrow(\downarrow)}$  and  $G_{\uparrow(\downarrow)}$  are the dynamical and geometric phases acquired during the evolution for state  $|\uparrow\rangle$  ( $|\downarrow\rangle$ ). Explicitly,  $D_{\uparrow(\downarrow)}$  is given by  $e^{i\int_0^{\tau} dt E^{\uparrow(\downarrow)}(\mathbf{q}(t))}$ , where  $E^{\uparrow(\downarrow)}(\mathbf{q}(t))$  is the dispersion of the band on the path of the state  $|\uparrow\rangle$  ( $|\downarrow\rangle$ ). The geometric phase  $G_{\uparrow(\downarrow)}$  is given by  $e^{i\int_{C_{\uparrow(\downarrow)}} d\mathbf{q}\mathbf{A}_{\mathbf{q}}}$ , where  $\mathbf{A}_{\mathbf{q}}$  is the Berry connection of the band and  $C_{\uparrow(\downarrow)}$  denotes the path taken by the state  $|\uparrow\rangle$  ( $|\downarrow\rangle$ ). In separating the dynamical and geometric contributions, we have used the fact that they are simply phase factors and therefore commute at all quasimomenta. Furthermore, note that at this point, the geometric phase is gauge-dependent.

4. We apply a  $\pi$ -pulse, i.e.,  $R(\pi, 0)$ , to swap  $|\uparrow\rangle$  and  $|\downarrow\rangle$  states, giving

$$|\psi\rangle = \frac{1}{\sqrt{2}}(D_{\uparrow}G_{\uparrow}|\downarrow\rangle - D_{\downarrow}G_{\downarrow}|\uparrow\rangle) \quad (5.4)$$

5. After another evolution period  $\tau$ , the states  $|\uparrow\rangle$  and  $|\downarrow\rangle$  are at the same quasimomentum at the tip of the diamond-shaped interferometer path. Each arm of the interferometer has acquired additional dynamical and geometric phases, such that the total state is now

$$\begin{aligned} |\psi\rangle &= \frac{1}{\sqrt{2}}(\tilde{D}_{\downarrow}\tilde{G}_{\downarrow}D_{\uparrow}G_{\uparrow}|\downarrow\rangle - \tilde{D}_{\uparrow}\tilde{G}_{\uparrow}D_{\downarrow}G_{\downarrow}|\uparrow\rangle) \\ &= \frac{1}{\sqrt{2}}(\tilde{D}_{\downarrow}D_{\uparrow}\tilde{G}_{\downarrow}G_{\uparrow}|\downarrow\rangle - \tilde{D}_{\uparrow}D_{\downarrow}\tilde{G}_{\uparrow}G_{\downarrow}|\uparrow\rangle) \end{aligned} \quad (5.5)$$

where  $\tilde{D}_{\uparrow(\downarrow)}$  and  $\tilde{G}_{\uparrow(\downarrow)}$  are the dynamical and geometric phases acquired during this second portion of the evolution for state  $|\uparrow\rangle$  ( $|\downarrow\rangle$ ), respectively.

6. We perform  $R(\pi/2, \phi_{MW})$ , a  $\pi/2$ -pulse with variable phase  $\phi_{MW}$ , to close the interferometer. The final state is

$$|\psi\rangle = \frac{1}{2}\tilde{D}_{\downarrow}D_{\uparrow}\tilde{G}_{\downarrow}G_{\uparrow}\left(|\downarrow\rangle - e^{i\phi_{MW}}|\uparrow\rangle\right) - \frac{1}{2}\tilde{D}_{\uparrow}D_{\downarrow}\tilde{G}_{\uparrow}G_{\downarrow}\left(e^{-i\phi_{MW}}|\downarrow\rangle + |\uparrow\rangle\right) \quad (5.6)$$

Our observable is the population of atoms in each spin state. For concreteness, let us take the spin-down state. The population is

$$\begin{aligned}
 |\langle \downarrow | \psi \rangle|^2 &= \frac{1}{4} \left| \tilde{D}_\downarrow D_\uparrow \tilde{G}_\downarrow G_\uparrow - \tilde{D}_\uparrow D_\downarrow \tilde{G}_\uparrow G_\downarrow e^{-i\phi_{MW}} \right|^2 \\
 &= \frac{1}{4} \left| \tilde{D}_\downarrow D_\uparrow (\tilde{G}_\downarrow G_\uparrow - \tilde{G}_\uparrow G_\downarrow e^{-i\phi_{MW}}) \right|^2 \\
 &= \frac{1}{4} \left| \tilde{G}_\downarrow G_\uparrow - \tilde{G}_\uparrow G_\downarrow e^{-i\phi_{MW}} \right|^2, \tag{5.7}
 \end{aligned}$$

where we have used that  $\tilde{D}_\downarrow D_\uparrow = \tilde{D}_\uparrow D_\downarrow$  and  $|\tilde{D}_\downarrow D_\uparrow|^2 = 1$ . This is based on the assumption that the dispersion, and consequently, the acquired dynamical phase, is the same for the left and right path since interferometer loop and the Brillouin zone share the same symmetry axis (See Fig. 5.3). In Sec. 5.2.3, we discuss the experimental validity of this assumption, in addition to other experimental concerns, such as, for example, the different Zeeman phases acquired by the spin states.

Accepting our assumptions on the cancellation of dynamical phases, we see that the spin-echo sequence contains information only on the geometric phase. Evaluating the equation above gives

$$|\langle \downarrow | \psi \rangle|^2 = \frac{1}{2} \left( 1 - \cos(\phi_{MW} + \varphi) \right), \tag{5.8}$$

where  $\varphi = \tilde{G}_\downarrow G_\uparrow \tilde{G}_\uparrow^* G_\downarrow^*$  is the geometric phase of interest (see Fig. 5.3). The phase  $\varphi$  is gauge-invariant because it results from the line-integral of the Berry connection over a closed-path. The population in the  $|\downarrow\rangle$  state oscillates as a function of  $\phi_{MW}$ , and the phase of this oscillation is precisely the Berry phase.

## 5.2.2. Experimental parameters

We begin by creating a  $^{87}\text{Rb}$  BEC of  $\approx 4 \times 10^4$  atoms in the  $|F=1, m_F=1\rangle$  state. Before turning on the magnetic field gradient, we use a 100ms RF sweep to transfer the BEC into the  $|F=1, m_F=0\rangle$  state, which is magnetically-insensitive. This is necessary because it takes around 2 s for the current in the gradient coil to stabilize. Once the current has stabilized, we adiabatically load the  $|F=1, m_F=0\rangle$  atoms into the lowest band of a lattice of depth  $V_0 = 1.0(1)E_r$ . We then use a 15  $\mu\text{s}$  microwave  $\pi$ -pulse to transfer all the atoms into the  $|F=2, m_F=1\rangle = |\uparrow\rangle$  state. This is the starting point of the experiment. We then apply a  $\pi/2$  pulse in 14  $\mu\text{s}$  to flip half of the  $|\uparrow\rangle$  atoms into  $|\downarrow\rangle = |F=1, m_F=1\rangle$ , thereby preparing the superposition  $\frac{1}{\sqrt{2}}(|\uparrow\rangle + |\downarrow\rangle)$ . Immediately after this  $\pi/2$  pulse, we begin accelerating the lattice.

The total duration of the interferometer sequence is kept constant at  $2\tau = 1.6$  ms. The magnitude of the magnetic field gradient is 9.0(1) G/cm, resulting in an acceleration of  $\pm 2.9(1)$  m/s<sup>2</sup> in the  $x$ -direction. The magnitude of the lattice acceleration varies

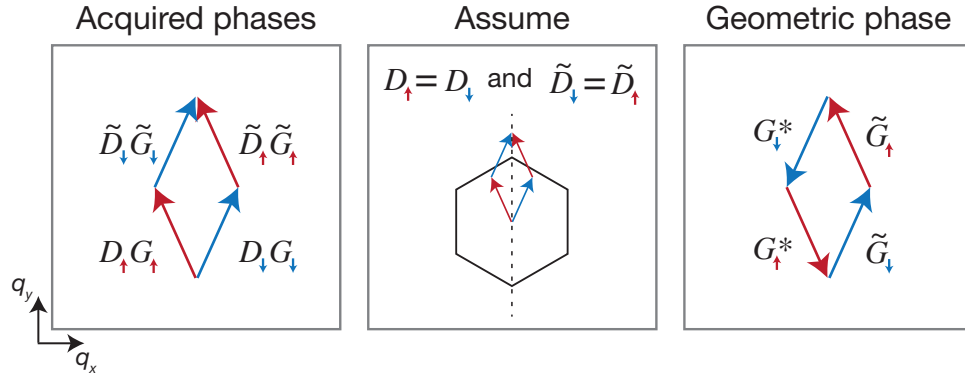


Figure 5.3.: **Visual aid for the calculations.** Left: During the interferometric sequence, each state acquires a dynamical and geometric phase  $D_{|\uparrow\rangle(|\downarrow\rangle)}$  and  $G_{|\uparrow\rangle(|\downarrow\rangle)}$ . Similarly, during the second half of the evolution, each state acquires a dynamical and geometric phase  $\tilde{D}_{|\uparrow\rangle(|\downarrow\rangle)}$  and  $\tilde{G}_{|\uparrow\rangle(|\downarrow\rangle)}$ . Center: When calculating the population of atoms in, e.g., the  $|\downarrow\rangle$  state on completion of the interferometric sequence, we assume the dynamical phases acquired on the left and right sides of the path are equivalent. This assumption is valid if the symmetry axis (dashed line) of the path and the Brillouin zone coincide. Right: With this assumption, we obtain a geometric phase  $\varphi = \tilde{G}_{\downarrow} G_{\uparrow} \tilde{G}_{\uparrow}^* G_{\downarrow}^*$ , which corresponds to the geometric phase acquired when traveling in a closed path. We have not included the effect of the Zeeman energies of the two spin states in our analysis.

from 1 to 11 m/s<sup>2</sup>, depending on the size of the interferometer loop. A sketch of the experimental setup is shown in Fig. 5.4a.

Once the interferometer loop is closed, we stop the lattice acceleration and turn off the magnetic field gradient. We ramp down the lattice in 410  $\mu$ s to band map the atoms, after which we switch off the dipole trap so the atoms undergo TOF. After 0.5 ms of TOF, we switch on the magnetic field gradient again. In free-space, the direction of the force experienced by the atoms depends on the sign of their magnetic moment. This spatially separates the  $|\uparrow\rangle$  and  $|\downarrow\rangle$  atoms such that we can distinguish them when imaging at 10 ms TOF, as shown in Fig. 5.4b. The use of a magnetic field gradient to spatially separate spin components before imaging is termed Stern-Gerlach imaging.

### 5.2.3. Experimental caveats

Here, we briefly examine several technical imperfections in the experiment that affect our measurements.<sup>2</sup> We have made two main assumptions in describing the experimental sequence:

1. The evolution is always adiabatic
2. The sequence cancels dynamical phases

<sup>2</sup> A detailed discussion can be found in Ref. [78].

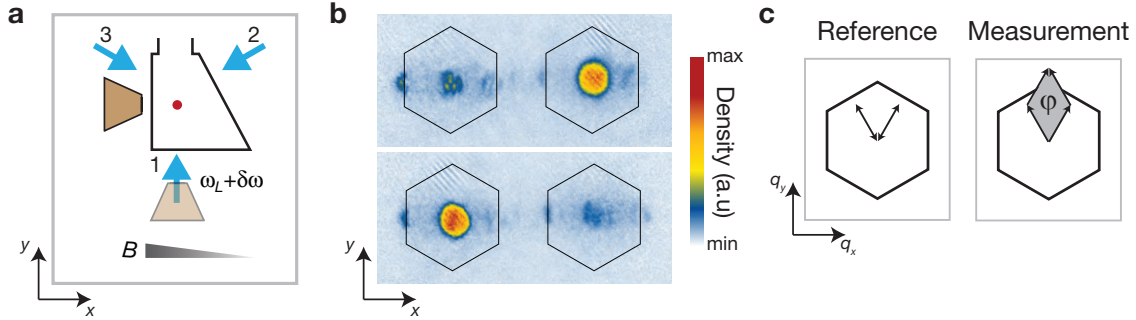


Figure 5.4.: **The experimental setup, Stern-Gerlach imaging, and a schematic of two interferometer types.** **a**, Changing the frequency of beam 1 creates a spin-independent force along  $y$  while a single coil (opaque brown) oriented along  $x$  creates a spin-dependent force along  $x$ . To fine-tune the direction of the magnetic field gradient, we add a secondary coil (translucent brown) along the  $y$ -axis. The position of the atoms (red circle) is shown in the glass cell (black outline). **b**, Applying a field gradient during TOF spatially separates the two spin-components for imaging. Atoms are mainly in the state  $|\uparrow\rangle$  ( $|\downarrow\rangle$ ) in the upper (lower) image. **c**, We employ two different types of interferometer loops: a reference (left) and measurement (right) interferometer. Phases acquired using the reference interferometer are purely dynamical.

The first assumption of adiabaticity can be ascertained by band mapping after the interferometry and checking for occupation in the second band. Note that the condition for adiabatic movement depends on the quasimomentum. It is easiest to be adiabatic near the center of the Brillouin zone, where the first and second bands are maximally separated, and more care must be taken as the band separation decreases. The condition for adiabaticity is most stringent in the vicinity of the Dirac cones, where the bands are degenerate. Here, for our range of accelerations, we obtain maximally 20% occupation in the second band. However, we find that our data is nonetheless well-described by a single-band model.

The validity of the second assumption rests on the quality of our lattice and the alignment between the magnetic field gradient and lattice acceleration directions. Before each experimental run, we ensure that each lattice beam has equal intensity by examining the coherence peaks from the sudden shut-off of confining potentials. Furthermore, we have checked the alignment of the beams and estimate the angles between the beams to be  $120(1)^\circ$ .

Regarding the alignment of the magnetic field gradient and the lattice acceleration, we first position the gradient coil perpendicular to lattice beam 1 to the best of our abilities by hand. We add a secondary gradient coil on the same axis as beam 1 (and orthogonal to the primary coil) to fine tune the alignment of the gradient, as illustrated in Fig. 5.4a. We check the precision of the alignment by performing the spin-echo sequence described above with a slight modification—after the  $\pi$ -pulse, the direction of the lattice acceleration is reversed. This yields an open, v-shaped interferometer that

we refer to as our reference interferometer. As illustrated in Fig. 5.4c, the reference path does not enclose any area, in contrast to the measurement loop. Hence, phases acquired with the reference interferometer are purely due to dynamical effects.

When the gradient force is not perpendicular to the lattice force, the interferometer arms are of different lengths and the axis of the opening angle between the interferometer arms is tilted with respect to the  $y$ -axis. Hence, the interferometer arms acquire different dynamical phases. To align the gradient force, we measure the phase of the reference interferometer as we change the current through the secondary coil. The current setting that yields a gradient force most perpendicular to the lattice acceleration is the one that results in minimum phase. After optimization, our measurements suggest a residual gradient misalignment of approximately  $2^\circ$ .

In addition to the dynamical phase due to the dispersion relation, another possible contribution that we have not yet included in our analysis is the difference in Zeeman energy acquired by the two spin states. The magnitude of the magnetic field at the position of the atoms is  $B_0 + \nabla\mathbf{B} \cdot \mathbf{R}(t)$ , where  $\mathbf{R}(t)$  gives the position of the lattice (and hence of the atoms). The Zeeman energy of atoms with magnetic moment  $\mu$  is then  $\mu(B_0 + \nabla\mathbf{B} \cdot \mathbf{R}(t))$ . The offset term  $\mu B_0$  is canceled by the spin-echo sequence—in each arm of the interferometer, atoms spend an equal amount of time in the  $|\uparrow\rangle$  and  $|\downarrow\rangle$  state, which have opposite magnetic moments. The position dependent term  $\nabla\mathbf{B} \cdot \mathbf{R}(t)$  is canceled when the magnetic field gradient is orthogonal to the lattice acceleration; we have already discussed this alignment procedure above.

Lastly, we note that even a perfectly aligned spin-echo sequence in the ideal honeycomb lattice cannot compensate for additional dynamical phases due to time-dependent fluctuations of the magnetic field. To minimize this source of uncertainty, we use a stable (but slow) current source. Furthermore, we keep the duration of the interferometry fixed and sync the entire experimental sequence to the mains line such that the interferometry always probes the same segment of the 50 Hz cycle.

### 5.3. Experimental results

We perform the spin-echo interferometry in three different scenarios. First, we compare the phase difference between measurement and reference interferometers in an ideal honeycomb lattice as the size of the loop is changed. The two interferometers are in-phase until the measurement loop encloses a Dirac cone, at which point the phase of the measurement loop jumps by  $\pi$ . When two Dirac points are enclosed, the phase contributions from each Dirac point cancel, and the reference and measurement interferometers are once again in-phase.

Next, we examine the phase-shift in the immediate vicinity of a Dirac point by exploiting the finite momentum spread  $\sigma_{\mathbf{k}}$  of the BEC in reciprocal space. Near the Dirac point, we can band map to distinguish regions of the condensate that have and have not encircled the Dirac point. By directly comparing the phases of these regions, a sin-

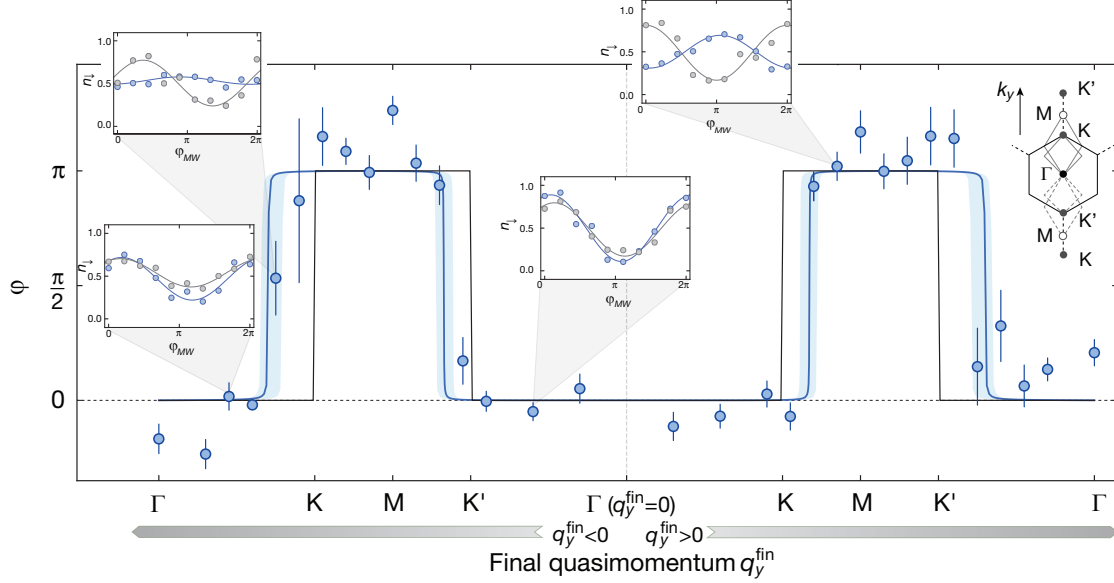


Figure 5.5.: **Detecting the Berry flux at the Dirac points.** Summary of phase differences between measurement and reference loop for different final quasimomenta  $q_y^{\text{fin}}$ . Error bars denote fit uncertainties or standard deviations in case of averages. Lines are *ab initio* theory using a full band structure calculation with: no momentum spread  $\sigma_{\mathbf{q}} = 0$  and perfectly localized Berry curvature (black)  $\delta q_{\Omega} = 0$ ; or  $\sigma_{\mathbf{q}} = 0.21 k_L$  and  $\delta q_{\Omega} \approx 10^{-4} k_L$  (blue). The shaded area accounts for an experimental uncertainty of  $\sigma_{\mathbf{q}} = 0.14\text{--}0.28 k_L$ . Insets show the fraction of atoms  $n_l$  measured as a function of the phase  $\varphi_{MW}$  for selected quasimomenta. Measurement loop data are shown in blue and reference loop data are shown in gray with corresponding sinusoidal fits.

gle image provides both the measurement and reference phases. This self-referenced interferometry enables us to quantify the spread in Berry curvature  $\delta q_{\Omega}$  to gauge the imperfections of our lattice.

Finally, we use a measurement loop of fixed size to detect the motion of the Dirac points as the intensity of two beams is changed relative to the third. We clearly observe the imbalance at which the Dirac point moves out of the loop. We then use varying measurement loop sizes at three different imbalances to detect the shift of the Dirac point. At intermediate imbalances, we observe the Dirac points move toward the M point. At a strong imbalance, the Dirac points merge and annihilate at the M point, and we do not measure a phase shift regardless of our loop size.

### 5.3.1. Detecting the Berry flux

In this first set of experiments, we perform a sequence of interferometric measurements enclosing different regions of the Brillouin zone to detect the Berry flux of the Dirac cone. This is achieved by varying the lattice acceleration at constant magnetic

field gradient to control the final quasimomentum  $q_y^{\text{fin}}$  ( $q_x^{\text{fin}} = 0$ ) of the diamond-shaped measurement loop. The resulting phase differences between measurement and reference loops are shown in Fig. 5.5. When the measurement loop does not enclose a Dirac point, measurement and reference loops are in-phase. When one Dirac point is enclosed in the measurement loop, we observe a phase difference of  $\varphi \simeq \pi$ . When two Dirac points are enclosed, the phase difference is again zero, since the  $\pi$  contribution to the phase difference from the first Dirac point is canceled by the  $-\pi$  contribution from the second Dirac point.<sup>3</sup>

In comparison to the single-particle theory line, the position of the phase jump is shifted in our measurements. This discrepancy is primarily due to the finite momentum spread  $\sigma_{\mathbf{q}}$  of our weakly-interacting BEC. When this is accounted for, we find very good agreement with theory. The position of the phase jump shifts because atoms in different parts of the cloud sample slightly different paths in reciprocal space. For instance, atoms near the top of the cloud will reach the Dirac cone before atoms near the bottom of the cloud. We measure a phase jump only once the measurement loop for at least half the atoms have enclosed the Dirac point. While the momentum spread affects the position of the phase jumps, it does not limit their sharpness. In fact, we will next exploit the momentum spread to improve the precision of our measurement in the vicinity of the Dirac point.

### 5.3.2. Self-referenced interferometry near the Dirac point

To minimize systematic errors and improve our measurement precision, we perform self-referenced interferometry close to the Dirac points. Due to the finite momentum spread, atoms near the Dirac point will be "sliced" by the Brillouin zone into sections that have or have not crossed the edge of the Brillouin zone, as illustrated in Fig. 5.6a. These three slices will be band mapped onto three different corners of the first Brillouin zone, allowing us to separately analyze the phase of each slice. Combining the phases of these three slices  $\varphi_L$ ,  $\varphi_R$  and  $\varphi_B$  to

$$\varphi = (\varphi_L + \varphi_R)/2 - \varphi_B, \quad (5.9)$$

eliminates the need for a separate reference measurement and significantly reduces the sensitivity to drifts in the experiment.

The phase  $\varphi$  exhibits a sudden jump from 0 to  $\pi$  as the atoms cross the edge of the band (see Fig. 5.6b). The position of the phase jump is in excellent agreement with a numerical calculation including an initial momentum spread of  $\sigma_{\mathbf{q}} = 0.15(1)k_L$ , consistent with an independent TOF measurement. Remarkably, the phase jump occurs within a very small quasimomentum range of  $< 0.01 k_L$ , and an arctangent fit to the ex-

---

<sup>3</sup> We know that, theoretically, the two inequivalent Dirac points contribute Berry phases of  $\pm\pi$ . However, we cannot experimentally determine whether the Dirac points have the same or opposite sign because we cannot differentiate between a phase shift of  $2\pi$  or zero.

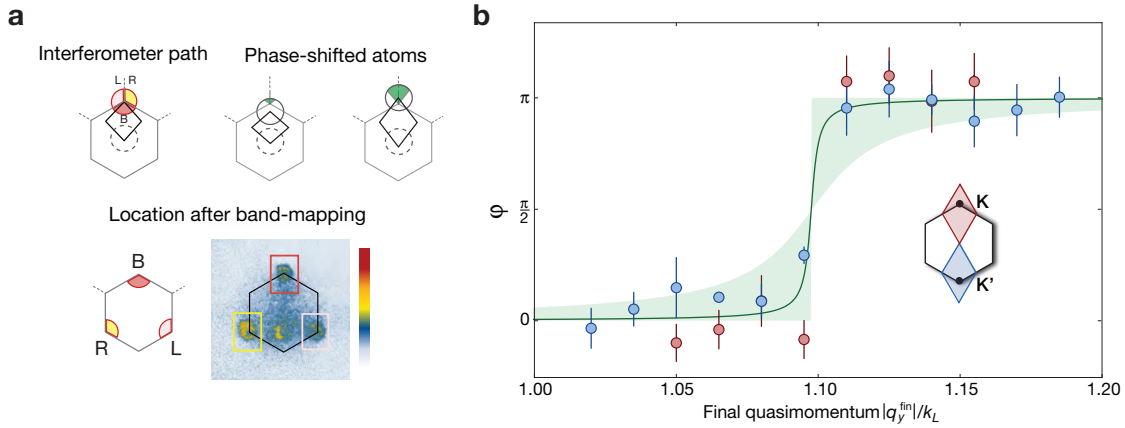


Figure 5.6.: **Self-referenced interferometry in the vicinity of the Dirac points.** Due to the initial momentum spread, the cloud (circle with colored sectors, not to scale) is split by the edges of the Brillouin zone. Atoms in the left and right sectors generally encircle the Dirac point (green shaded area) before atoms in the bottom sector. Band-mapping spatially separates the three different parts of the cloud onto three corners of the first Brillouin zone (schematic and image). The unboxed atoms near the center of the Brillouin zone are residual atoms that have not been properly addressed by all MW pulses and are not analyzed. **b**, Phase differences between atoms that crossed the band edge and the lagging (bottom) cloud versus final quasimomentum near the K (K') point in red (blue). The green shaded region indicates a range of  $\delta q_\Omega = 0 - 12 \times 10^{-4} k_L$  for the Berry curvature, while the line is calculated for  $\delta q_\Omega \simeq 10^{-4} k_L$ .

perimental data gives a phase difference of  $\varphi = 0.95(10)\pi$ . Both results are compatible with a perfectly localized and quantized  $\pi$  Berry flux; the steepness of the phase jump suggests a localization of the Berry curvature on the order of  $\delta q_\Omega \simeq 10^{-4} k_L$ .<sup>4</sup>

### 5.3.3. Moving and annihilating Dirac cones

To verify the method's sensitivity to changes in Berry flux, we performed interferometry in a modified lattice potential. Changing the power of two lattice beams ( $I_3, I_2$ ) relative to the third ( $I_1$ ) deforms the lattice structure, while preserving time-reversal and inversion symmetry (see Sec. 4.1.3 and Sec. 3.2.3). With decreasing  $I_{3,2}/I_1 < 1$ , the Dirac points and the associated fluxes move toward each other along the symmetry axis of the interferometer loop [75], as shown in Fig. 5.7a. Nonetheless, the Berry flux singularities remain protected by symmetry until the Dirac points merge and annihilate [22, 30, 97, 98].

<sup>4</sup> To further corroborate these results, we also analyzed the contrast of the interference fringes, where the location of the Dirac cone manifests itself through a pronounced minimum. These measurements provide an upper bound for the spread of the Berry curvature around the Dirac cone of  $< 6 \times 10^{-4} k_L$  (HWHM), corresponding to a maximal A-B site offset of  $\approx h \times 12$  Hz and a ratio of energy gap at the Dirac cone to bandwidth of  $< 3 \times 10^{-3}$ . Details can be found in Ref. [78].

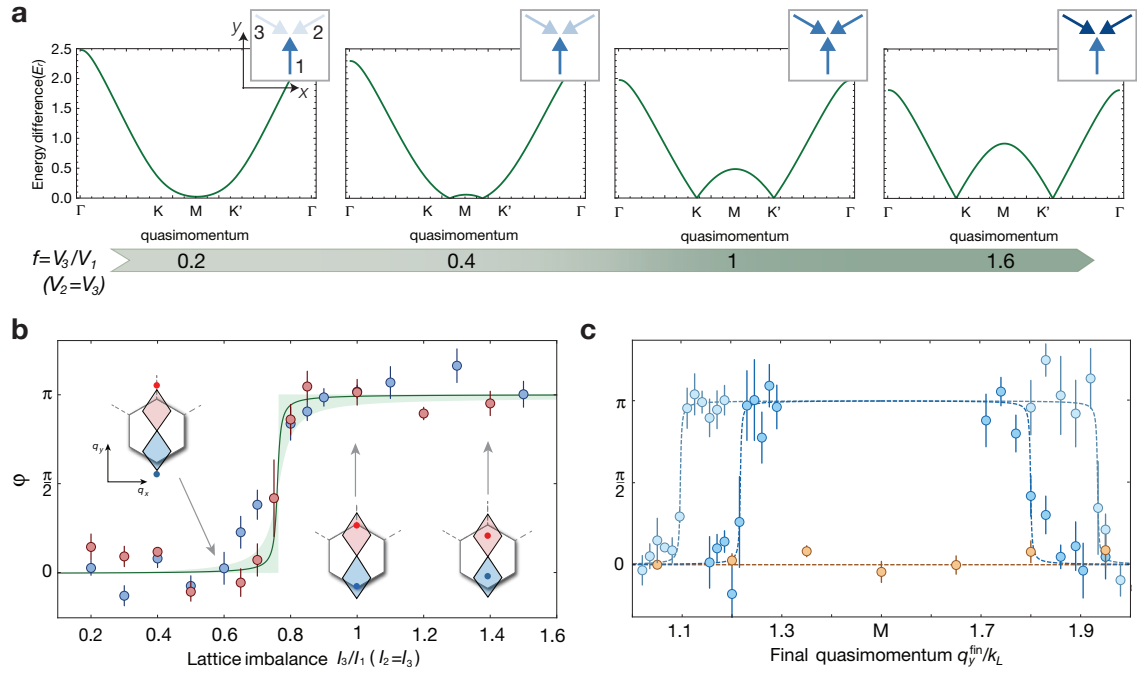


Figure 5.7.: **Detecting the motion and annihilation of Dirac cones.** **a**, The energy difference between the first and second band along  $\Gamma$ -K-M-K'- $\Gamma$  as a function of lattice intensity imbalance. As the lattice intensities are imbalanced (insets) toward  $V_3/V_1 < 1$ , the Dirac points shift away from the K and K' points toward the M point until they finally merge and annihilate. **b**, Phase difference between reference and measurement loop versus lattice imbalance around K (red) and K' (blue) for a fixed measurement loop size of  $q_y^{\text{fin}} = \pm 1.2k_L$ . Red and blue dots in the insets give the location of the Dirac points for the indicated imbalances. Theory curve is calculated for  $V_0 = 1E_r$ , momentum spread  $\sigma_{\mathbf{k}} = 0.15k_L$ , and  $\delta q_{\Omega} \approx 10^{-4}k_L$ . Shaded area corresponds to  $\delta q_{\Omega} = 0 - 12 \times 10^{-4}k_L$ . **c**, Self-referenced phase near K and K' for an imbalance  $I_{3,2}/I_1 = 1.0$  and  $I_{3,2}/I_1 = 0.7$  in light and dark blue, highlighting the shift in the location of Berry flux. Orange data are phase differences between the measurement and reference loops for an imbalance of  $I_{3,2}/I_1 = 0.2$ , where no phase shift is observed. Curves are guides to the eye.

By using a fixed measurement loop that encloses one Dirac point in the intensity-balanced case, we can measure the change of the geometric phase as we imbalance the lattice beam intensities. As shown in Fig. 5.7, the measured Berry phases drop from  $\pi$  to 0 as the Dirac point moves out of the loop, in very good agreement with *ab initio* calculations.

To precisely map the location of the Berry flux in the imbalanced lattice, we again use the self-referenced interferometry. As shown in Fig. 5.7, imbalancing the lattice by decreasing  $I_{3,2}/I_1$  narrows the range of final quasimomenta for which the interferometer encloses a single  $\pi$  flux, thereby shifting both the upward and downward phase jumps towards the M point. For a stronger imbalance ( $I_{3,2}/I_1=0.2$ ), the two Dirac points have annihilated, and hence no phase jump is observed for any loop size.



## Chapter 6.

# Bloch state tomography with Wilson lines

In this chapter, we realize strong-gradient dynamics described by Wilson lines to map out the geometric structure of the  $s$ -bands. We begin by describing the two ways in which Wilson lines can be used to characterize band structures. First, the eigenvalues of Wilson lines transporting a state by a reciprocal lattice vector  $\mathbf{G}$  can be used to formulate the  $\mathbb{Z}_2$  invariant [77, 90, 137]. Secondly, in certain situations, the form of the Wilson line can be simplified and, when measured in the basis of the band eigenstates, enables a complete map of the cell-periodic Bloch functions over the entire Brillouin zone. Although the primary focus of the chapter is on the band tomography, the same experimental techniques can also be used to obtain the eigenvalues.

In Sec. 6.2, we introduce a Bloch sphere formalism which enables us to parametrize the cell-periodic Bloch function  $|u_{\mathbf{q}}^n\rangle$  at any quasimomentum  $\mathbf{q}$  in terms of two angles,  $\theta_{\mathbf{q}}$  and  $\phi_{\mathbf{q}}$ , that are directly related to the elements of the Wilson line. After describing the experimental procedures used to measure these two angles, we move onto some experimental details in Sec. 6.3. We note the experimental parameters necessary to reach the strong-gradient regime where dynamics are described by two-band Wilson lines and consider the validity of our two-band approximation. Next, we explain our data analysis techniques before presenting our experimental results in Sec. 6.4. Unsurprisingly, in addition to mapping the cell-periodic Bloch functions, our measurements of  $\theta_{\mathbf{q}}$  and  $\phi_{\mathbf{q}}$  also reflect certain real-space attributes of the lattice.

Finally, in Sec. 6.5, we examine the situation more commonly considered in solid state theory and obtain the eigenvalues of a Wilson line transporting by a single reciprocal lattice vector. Since measuring  $\theta_{\mathbf{q}}$  and  $\phi_{\mathbf{q}}$  is equivalent to measuring the Wilson line elements in the basis of the band eigenstates, we are able to reconstruct such a Wilson line and extract its eigenvalues. We find the same eigenvalues for two different lattice configurations with different geometric attributes, corroborating the fact that these eigenvalues reflect the topological structure of the bands.

## 6.1. Wilson lines in the $s$ -bands of the honeycomb lattice

As we derived in Sec. 2.2.4, an effectively degenerate band structure can be realized by applying a large enough force such that the effect of the dispersion is negligible. The quantity that describes the evolution of such systems is the matrix-valued Wilson line. In this experiment, we use a strong gradient to probe dynamics governed by the Wilson line in the  $s$ -bands of the honeycomb lattice. In particular, our experimental technique enables the reconstruction of Wilson line elements in the basis of the Bloch states.

Recall, however, that we examined the behavior of Wilson lines in Sec. 2.3.2 under a gauge-transformation and found them to be gauge-dependent. With this in mind, one might wonder if there is any useful information to be gained from the Wilson line elements. Remarkably, it turns out the Wilson line elements provide an elegant and robust way of characterizing band structure geometry.

### 6.1.1. Wilson-Zak loop eigenvalues

First, recall again that the non-Abelian Berry phases, i.e., the eigenvalues of closed Wilson loops, are indeed gauge-invariant. In band structures, the Brillouin zones have the topology of a torus due to their periodicity, [26, 92, 138], as illustrated in Fig. 6.1a for the hexagonal Brillouin zone. On the torus, traveling one reciprocal lattice vector forms a closed loop. Associated with this particular type of closed loop is a geometric quantity termed the Zak phase [139], which is simply the line-integral of the Berry connection between points separated by a reciprocal lattice vector, i.e., the Berry phase across the Brillouin zone. Analogously, transport by one reciprocal lattice vector in multi-band systems are given by the Wilson-Zak loop, often also simply called Wilson loops [90, 137]. It was recently shown that the eigenvalues of Wilson-Zak loops can be used to formulate the  $\mathbb{Z}_2$  invariant which characterizes time-reversal invariant insulators [77] and identify topological orders protected by lattice symmetries [90, 140]. Therefore, one utility of being able to access Wilson line elements is to reconstruct a Wilson-Zak loop and obtain its eigenvalues.

### 6.1.2. Bloch state tomography

In some band structures, a simplified form of the Wilson line enables a complete map of the cell-periodic Bloch functions over the Brillouin zone. Although the Wilson line must generally be path-ordered because the Wilczek-Zee connections do not necessarily commute at all quasimomenta, in certain situations, the integration is path-independent [80, 90]. This occurs, for example, when the relevant bands span the same Hilbert space at all quasimomenta, as is the case for the  $s$ -bands of the honeycomb lattice. This can be understood by discretizing the Wilson line transporting from  $\mathbf{q}_i$  to  $\mathbf{q}_f$  into  $N$  infinitesimal Wilson lines. The elements of the Wilson line can then be written as a path-ordered product of projectors  $P(\mathbf{q}) = \sum_{n=1}^{\alpha} |u_{\mathbf{q}}^n\rangle\langle u_{\mathbf{q}}^n|$  onto  $\alpha$  bands

sandwiched between the cell-periodic states at the initial and final quasimomenta [90]:

$$W_{\mathbf{q}_1 \rightarrow \mathbf{q}_N}^{mn} = \langle u_{\mathbf{q}_N}^n | \prod_{i=1}^N P(\mathbf{q}_i) | u_{\mathbf{q}_1}^m \rangle \quad (6.1)$$

Since the projection operator reduces to identity,  $P(\mathbf{q}) = \sum_{n=1}^{\alpha} |u_{\mathbf{q}}^n\rangle \langle u_{\mathbf{q}}^n| = \mathbb{1}$ , when the bands span the same Hilbert subspace at each quasimomentum, the Wilson line reduces to

$$W_{\mathbf{q}_1 \rightarrow \mathbf{q}_N}^{mn} = \langle u_{\mathbf{q}_N}^n | u_{\mathbf{q}_1}^m \rangle. \quad (6.2)$$

Consequently, the elements of the Wilson line are simply given by the projection of the final cell-periodic Bloch state onto the initial cell-periodic Bloch state. Accordingly, if we set a reference quasimomenta  $\mathbf{Q}$  and compare the cell-periodic Bloch states at all other quasimomenta to the states at  $\mathbf{Q}$ , we can map the structure of the eigenstates over the entire Brillouin zone.

An alternative, more physical way of understanding this simplified form of the Wilson line elements is to consider the dynamics in real-space. If the gradient  $\mathbf{F} \cdot \hat{\mathbf{r}}$  is the largest energy scale of the system, it dominates the dynamics and the time-evolution operator, i.e., the Wilson line, after time  $\tau$  is simply  $e^{\frac{i}{\hbar} \tau \mathbf{F} \cdot \hat{\mathbf{r}}}$ .

Since the application of a force  $\mathbf{F}$  for period  $\tau$  results in a change in quasimomentum given by  $\mathbf{F}\tau/\hbar$  [89], the Wilson line can be equivalently written as

$$\hat{\mathbf{W}}_{\mathbf{q}_i \rightarrow \mathbf{q}_f} = e^{i\Delta\mathbf{q} \cdot \hat{\mathbf{r}}}, \quad (6.3)$$

where  $\Delta\mathbf{q} = \mathbf{q}_f - \mathbf{q}_i$  is the change in quasimomentum. Here, we see that the Wilson line is simply the quasimomentum translation operator. Measuring this Wilson line in the basis of the band eigenstates yields

$$\langle \Phi_{\mathbf{q}_f}^n | \hat{\mathbf{W}}_{\mathbf{q}_i \rightarrow \mathbf{q}_f} | \Phi_{\mathbf{q}_i}^m \rangle = \langle u_{\mathbf{q}_f}^n | e^{i\Delta\mathbf{q} \cdot \hat{\mathbf{r}}} | u_{\mathbf{q}_i}^m \rangle = \langle u_{\mathbf{q}_f}^n | u_{\mathbf{q}_i}^m \rangle, \quad (6.4)$$

since  $|\Phi_{\mathbf{q}}^m\rangle = e^{i\mathbf{q} \cdot \hat{\mathbf{r}}} |u_{\mathbf{q}}^m\rangle$ . Hence, we arrive at the same conclusion as our purely mathematical analysis above—when the relevant bands span the same Hilbert space at all quasimomenta, the Wilson line elements enable a comparison between cell-periodic Bloch states at any two quasimomenta.

In the remainder of the chapter, we primarily focus on exploiting Eq. 6.2 or Eq. 6.4 for a tomography of the cell-periodic Bloch states. It is important to note, however, that the experimental technique is applicable even in more complex scenarios when the bands do not fulfill a completeness relation. In this case, there is no obvious relation between the Wilson line elements and the cell-periodic Bloch states, but we can still obtain information about the band structure through the eigenvalues of Wilson-Zak loops. In Sec. 6.5, we reconstruct a single Wilson-Zak loop and extract its eigenval-

ues as a proof-of-principle demonstration for the feasibility of Wilson-Zak loop based characterizations of band structures in future cold atom experiments.

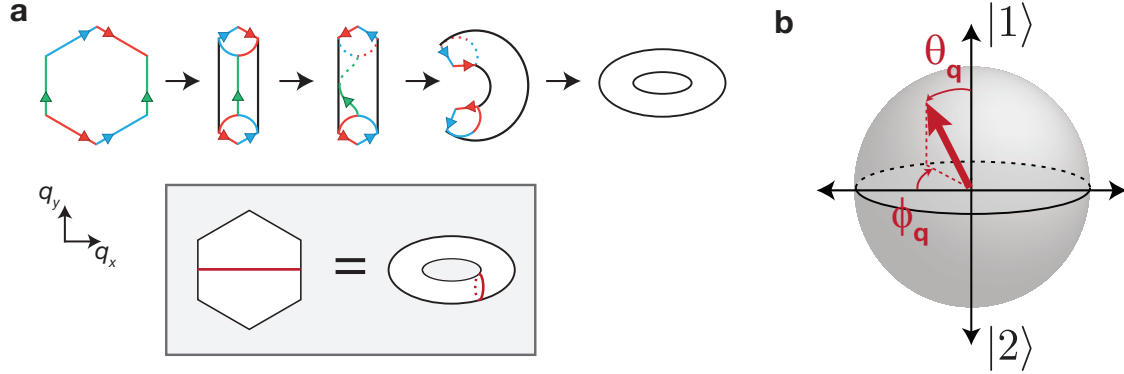


Figure 6.1.: **The toroidal Brillouin zone and the Bloch sphere.** **a**, Due to its periodicity, the Brillouin zone is topologically equivalent to a torus. Equivalent edges, i.e., those separated by a reciprocal lattice vector, are shown in matching colors with arrows as an additional reference for clarity. To continuously deform the hexagonal Brillouin zone into a torus, we first match the green edges together. Then, the upper portion of the “tube” is twisted by  $180^\circ$ . Lastly, we bend the “tube” over, color-matching the portions of the top and bottom ends to obtain a torus. Subsequently, traveling by a reciprocal lattice vector is equivalent to traveling a closed loop on the torus (red lines on Brillouin zone and torus in shaded box). **b**, The state  $|u_{\mathbf{q}}^n\rangle$  can be represented as a pseudospin on a Bloch sphere where the north and south poles are defined to be  $|1\rangle = |u_{\Gamma}^1\rangle$  and  $|2\rangle = |u_{\Gamma}^2\rangle$ . The pseudospin is parametrized by the polar angle  $\theta_{\mathbf{q}}$  and the azimuthal angle  $\phi_{\mathbf{q}}$ .

## 6.2. Reconstructing eigenstates: the Bloch sphere picture

To reconstruct the eigenstates throughout reciprocal space, it is convenient to represent the state  $|u_{\mathbf{q}}^1\rangle$  at quasimomentum  $\mathbf{q}$  in the basis of cell-periodic Bloch functions at a fixed reference quasimomentum  $\mathbf{Q}$ . In the experiment, we choose the basis states at reference point  $\mathbf{Q} = \Gamma$  such that  $|1\rangle = |u_{\Gamma}^1\rangle$  and  $|2\rangle = |u_{\Gamma}^2\rangle$  and  $|u_{\mathbf{q}}^1\rangle$  can be expressed as

$$|u_{\mathbf{q}}^1\rangle = \cos \frac{\theta_{\mathbf{q}}}{2} |1\rangle + \sin \frac{\theta_{\mathbf{q}}}{2} e^{i\phi_{\mathbf{q}}} |2\rangle. \quad (6.5)$$

In this framework, the state  $|u_{\mathbf{q}}^n\rangle$  can be visualized as a pseudospin on a Bloch sphere, where the north (south) pole represents  $|1\rangle$  ( $|2\rangle$ ), as shown in Fig. 6.1b. Mapping out the geometric structure of the lowest band amounts to obtaining  $\theta_{\mathbf{q}}$  and  $\phi_{\mathbf{q}}$ , which parametrize the amplitude and phase of the superposition between the reference Bloch states, for each quasimomentum  $\mathbf{q}$  [71, 72]. Next, we examine how to extract the angles  $\theta_{\mathbf{q}}$  and  $\phi_{\mathbf{q}}$ .

### 6.2.1. Extracting the polar angle $\theta_{\mathbf{q}}$

The polar angle can be obtained from the quantity

$$\begin{aligned} \left| \langle u_{\mathbf{q}}^1 | 1 \rangle \right| &= \left| \cos \frac{\theta_{\mathbf{q}}}{2} \right| \\ \Rightarrow \theta_{\mathbf{q}} &= 2 \arccos \left| \langle u_{\mathbf{q}}^1 | 1 \rangle \right| = 2 \arccos \left| W_{\Gamma \rightarrow \mathbf{q}}^{11} \right| \end{aligned} \quad (6.6)$$

Hence, the element  $\left| W_{\Gamma \rightarrow \mathbf{q}}^{11} \right|$  of the Wilson line directly gives  $\theta_{\mathbf{q}}$ . To experimentally measure this element, we perform the following steps:

1. Prepare the initial state as the Bloch state of the first band at quasimomentum  $\Gamma$

$$|\Phi_{\Gamma}^1\rangle \quad (6.7)$$

2. Evolve the the state to a final quasimomentum  $\mathbf{q}$  by applying a suitable force. The evolved state is given by

$$\hat{W}_{\Gamma \rightarrow \mathbf{q}} |\Phi_{\Gamma}^1\rangle \quad (6.8)$$

3. Band map at final quasimomentum  $\mathbf{q}$ . This yields the population in the first band, given by:

$$\left| \langle \Phi_{\mathbf{q}}^1 | \hat{W}_{\Gamma \rightarrow \mathbf{q}} |\Phi_{\Gamma}^1\rangle \right|^2 = \left| W_{\Gamma \rightarrow \mathbf{q}}^{11} \right|^2 \quad (6.9)$$

Taking the square-root of the population in the first band after transport yields the absolute-value of  $W_{\Gamma \rightarrow \mathbf{q}}^{11}$  and, therefore,  $\theta_{\mathbf{q}}$ .

### 6.2.2. Extracting the azimuthal angle $\phi_{\mathbf{q}}$

The relative phase  $\phi_{\mathbf{q}}$  can be expressed as<sup>1</sup>

$$\begin{aligned} \phi_{\mathbf{q}} &= \text{Arg}[\langle u_{\mathbf{q}}^1 | 1 \rangle] - \text{Arg}[\langle u_{\mathbf{q}}^1 | 2 \rangle] \\ &= \text{Arg}[W_{\Gamma \rightarrow \mathbf{q}}^{11}] - \text{Arg}[W_{\Gamma \rightarrow \mathbf{q}}^{12}] \end{aligned} \quad (6.10)$$

<sup>1</sup> From Eq. 6.5, we have

$$\begin{aligned} \text{Arg}[\langle 1 | u_{\mathbf{q}}^1 \rangle] &= \text{Arg}\left[\cos \frac{\theta_{\mathbf{q}}}{2}\right] = 0 \\ \text{Arg}[\langle 2 | u_{\mathbf{q}}^1 \rangle] &= \text{Arg}\left[e^{-i\phi_{\mathbf{q}}} \sin \frac{\theta_{\mathbf{q}}}{2}\right] = -\phi_{\mathbf{q}} \end{aligned}$$

Hence,  $\phi_{\mathbf{q}} = \text{Arg}[\langle 1 | u_{\mathbf{q}}^1 \rangle] - \text{Arg}[\langle 2 | u_{\mathbf{q}}^1 \rangle]$ .

Therefore, to access  $\phi_{\mathbf{q}}$ , we must access the phases of the Wilson line elements. This is experimentally accomplished via a process similar to Ramsey interferometry. The general idea is to first create a superposition state with a time-varying phase at quasimomentum  $\Gamma$ . In the basis of the band eigenstates at  $\Gamma$ , the superposition state is:

$$|\Psi_{\Gamma}\rangle = \begin{pmatrix} |\alpha| \\ |\beta| e^{i\Delta\omega t} \end{pmatrix}, \quad (6.11)$$

where  $|\alpha|^2$  ( $|\beta|^2$ ) denotes the population in first (second) band and  $\Delta\omega t$  is the phase-difference between the basis states at time  $t$ . We then rapidly transport this state to the desired quasimomentum  $\mathbf{q}$ . Assuming the Wilson line operator has form

$$\hat{\mathbf{W}}_{\Gamma \rightarrow \mathbf{q}} = \begin{pmatrix} W^{11} & W^{12} \\ W^{21} & W^{22} \end{pmatrix},$$

the resulting state at the desired quasimomentum  $\mathbf{q}$  is

$$|\Psi_{\mathbf{q}}\rangle = \hat{\mathbf{W}}_{\Gamma \rightarrow \mathbf{q}} |\Psi_{\Gamma}\rangle = \begin{pmatrix} |\alpha| W^{11} + |\beta| W^{12} e^{i\Delta\omega t} \\ |\alpha| W^{21} + |\beta| W^{22} e^{i\Delta\omega t} \end{pmatrix}. \quad (6.12)$$

The resulting population in the first band at  $\mathbf{q}$  is given by

$$\begin{aligned} \left| \langle \Phi_{\mathbf{q}}^1 | \Psi_{\mathbf{q}} \rangle \right|^2 &= |\alpha W^{11}| + |\beta W^{12}| \\ &+ 2 |\alpha \beta W^{11} W^{12}| \cos \left( \Delta\omega t + \text{Arg}[W^{11}] - \text{Arg}[W^{12}] \right). \end{aligned} \quad (6.13)$$

We see that the population oscillates as a function of time. The azimuthal phase  $\phi_{\mathbf{q}}$  is encoded in the phase of the oscillation.

The experimental procedure, as illustrated in Fig. 6.2a, is as follows:

1. The superposition state with time-varying phase is created by rapidly transporting atoms initialized in the first band at  $\Gamma - \mathbf{G}$  by one reciprocal lattice vector.
2. We then hold the state at  $\Gamma$  for variable time. Written in the basis of the band eigenstates at  $\Gamma$ , the state  $|\Psi_{\Gamma}\rangle$  after a hold time  $t$  is:

$$|\Psi_{\Gamma}\rangle = \frac{1}{2} \begin{pmatrix} 1 \\ \sqrt{3} e^{i\Delta\omega t} \end{pmatrix}, \quad (6.14)$$

where  $\hbar\Delta\omega = E_{\Gamma}^2 - E_{\Gamma}^1$  is the energy separation between the first and second band at  $\Gamma$ .

3. We rapidly transport this superposition state to quasimomentum  $\mathbf{q}$ , yielding the

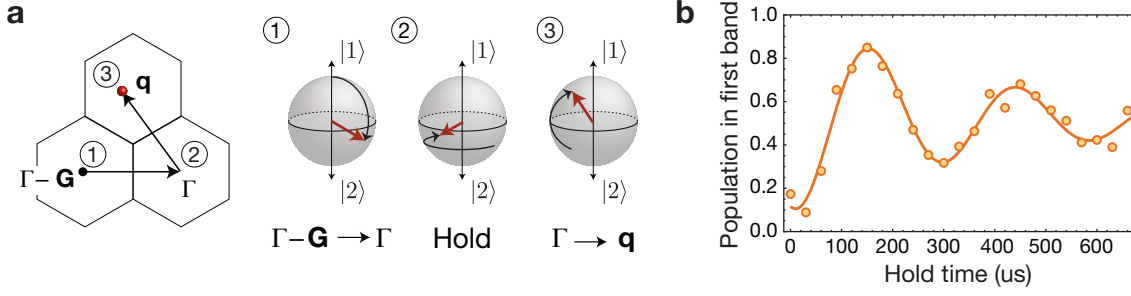


Figure 6.2.: **Interferometry for  $\phi_{\mathbf{q}}$  and a typical oscillation.** **a**, A superposition state with time-varying phase is created via steps 1) and 2). In 1), the superposition is created by rapidly accelerating atoms initialized in the first band at  $\Gamma - \mathbf{G}$  to  $\Gamma$ , which can be visualized as a rotation of the polar angle on the Bloch sphere. In 2) the time-dependent phase is created by holding for varying times at  $\Gamma$ , during which the pseudospin precesses about the  $z$ -axis. Finally, we rapidly accelerate to the desired quasimomentum  $\mathbf{q}$  and obtain the population in the first band as a function of the hold time at  $\Gamma$ . The phase of the oscillation in the first band population encodes  $\phi_{\mathbf{q}}$ . **b**, A typical dataset. By fitting the oscillation, we obtain the phase.

state  $|\Psi_{\mathbf{q}}\rangle = \hat{\mathbf{W}}_{\Gamma \rightarrow \mathbf{q}} |\Psi_{\Gamma}\rangle$ . Band mapping for the population in the first band at  $\mathbf{q}$  gives the population oscillation described by Eq. 6.13. A typical oscillation fringe is shown in Fig. 6.2b. By fitting the oscillation, we extract  $\phi_{\mathbf{q}}$ .

### 6.2.3. Gauge-invariance of $\phi_{\mathbf{q}}$ and $\theta_{\mathbf{q}}$

Since our goal now is to measure  $\theta_{\mathbf{q}}$  and  $\phi_{\mathbf{q}}$ , it is prudent to ask whether these quantities are gauge-invariant. When  $|1\rangle$ ,  $|2\rangle$ , and  $|u_{\mathbf{q}}^1\rangle$  are transformed by arbitrary phase factors, the absolute value of the overlap between these states is not affected. Hence,  $\theta_{\mathbf{q}}$  is gauge-invariant.

In contrast,  $\phi_{\mathbf{q}}$  depends on the argument of the overlap, i.e., the relative phase, between the states. Consider first a gauge change on  $|u_{\mathbf{q}}^1\rangle \rightarrow e^{i\gamma_{\mathbf{q}}} |u_{\mathbf{q}}^1\rangle$ . This transforms Eq. 6.10 to

$$\text{Arg}[e^{-i\gamma_{\mathbf{q}}} \langle u_{\mathbf{q}}^1 | 1 \rangle] - \text{Arg}[e^{-i\gamma_{\mathbf{q}}} \langle u_{\mathbf{q}}^1 | 2 \rangle] = \phi_{\mathbf{q}}. \quad (6.15)$$

Hence, a different gauge choice on  $|u_{\mathbf{q}}^1\rangle$  is cancelled out by taking the difference of the argument of Wilson line elements. In contrast, the gauge-freedom on the reference states  $|1\rangle$  and  $|2\rangle$  remains. For example, a different choice of the phase for  $|1\rangle \rightarrow e^{i\gamma_{\mathbf{q}}} |1\rangle$  yields

$$\text{Arg}[e^{i\gamma_{\mathbf{q}}} \langle u_{\mathbf{q}}^1 | 1 \rangle] - \text{Arg}[\langle u_{\mathbf{q}}^1 | 2 \rangle] = \phi_{\mathbf{q}} + \gamma_{\mathbf{q}}. \quad (6.16)$$

We obtain a similar result when choosing a different phase for  $|2\rangle$ . This problem can be surmounted by comparing two measurements of  $\phi_{\mathbf{q}}$  at different quasimomenta  $\mathbf{q}_1$  and  $\mathbf{q}_2$ . If the same reference states are used to define both  $\phi_{\mathbf{q}_1}$  and  $\phi_{\mathbf{q}_2}$ , then taking

the difference  $\phi_{\mathbf{q}_1} - \phi_{\mathbf{q}_2}$  cancels out the gauge-freedom of the reference states.

In fact, a comparison of  $\phi_{\mathbf{q}}$ 's at different quasimomenta already implicitly occurs in our measurement of  $\phi_{\mathbf{q}}$ , a detail we neglected to mention in Sec. 6.2.2. This detail occurs in the creation of the superposition state using a Wilson line  $\hat{\mathbf{W}}_{\Gamma-\mathbf{G}\rightarrow\Gamma}$  transporting a state from  $\Gamma - \mathbf{G}$  to  $\Gamma$ . A more accurate description of the superposition state in Eq. 6.11 would be

$$|\Psi_{\Gamma}\rangle = \begin{pmatrix} |\alpha| \\ |\beta| e^{i(\Delta\omega t + \phi')} \end{pmatrix}, \quad (6.17)$$

where  $|\alpha| = |W_{\Gamma-\mathbf{G}\rightarrow\Gamma}^{11}|$ ,  $|\beta| = |W_{\Gamma-\mathbf{G}\rightarrow\Gamma}^{21}|$ , and

$$\begin{aligned} \phi' &= \text{Arg}[W_{\Gamma-\mathbf{G}\rightarrow\Gamma}^{21}] - \text{Arg}[W_{\Gamma-\mathbf{G}\rightarrow\Gamma}^{11}] \\ &= \langle 2|u_{\Gamma}^1\rangle - \langle 1|u_{\Gamma}^1\rangle \\ &= -\phi_{\Gamma} \end{aligned} \quad (6.18)$$

The superposition state, by nature of its creation, already contains a gauge-dependent phase. Consequently, the phase of the oscillation in the first band population we measure is actually

$$\phi_{\mathbf{q}} - \phi_{\Gamma}, \quad (6.19)$$

which is a gauge-invariant quantity, although both  $\phi_{\mathbf{q}}$  and  $\phi_{\Gamma}$  are gauge-dependent. That we actually measure a difference between phases is of no concern since we are only interested in how  $\phi_{\mathbf{q}}$  changes as we move around the Brillouin zone. In other words,  $\phi_{\Gamma}$  can be thought of as a reference phase, just as  $|1\rangle$  and  $|2\rangle$  are reference states.

## 6.3. Experimental details

In this section, we describe the experimental parameters required to reach the regime where the dynamics are well-described by two-band Wilson lines. From Sec. 2.2.4, we know that the applied force needs to be large and here, we determine the required magnitude. Furthermore, since our band structure of course has an infinite amount of bands, we examine the validity of the two-band approximation. We conclude the section with a description of our data analysis techniques.

### 6.3.1. Experimental parameters

Each experimental sequence begins by adiabatically loading a BEC of  $^{87}\text{Rb}$  into the lowest band of a lattice of depth  $V_0 = 5.2(1)E_r$  at quasimomentum  $\mathbf{q} = \Gamma$ . At this depth, the combined width  $\epsilon \approx \hbar \times 3 \text{ kHz}$  of the lowest two bands is much smaller than the

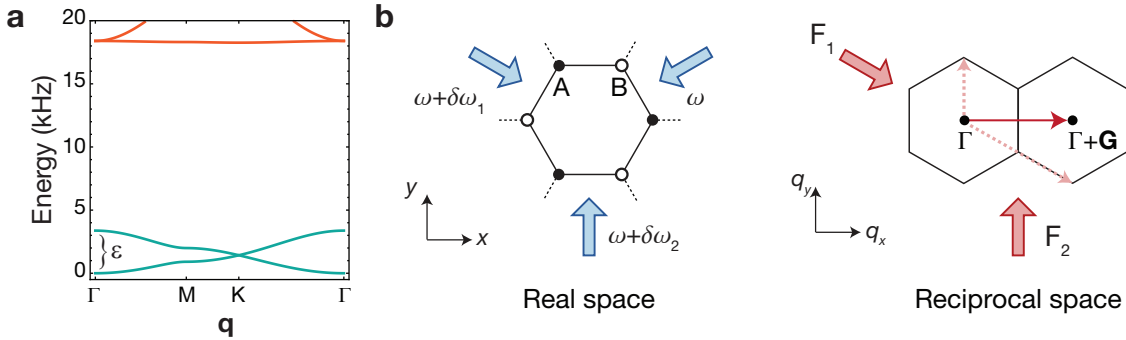


Figure 6.3.: **Experimental parameters.** **a**, Dispersion relation referenced to the energy of the first band at  $\Gamma$  at a depth of  $V_0 = 5.2E_r$ . The energy separation between the  $s$ -bands (green) at  $\Gamma$  is  $\varepsilon \approx \hbar \times 3$  kHz. There is a much larger energy gap to higher bands (red), enabling us to approximate our experiment as a two-band system. **b**, The frequency of two beams are linearly swept at independently chosen rates (left). In the lattice frame, an inertial force moves the atoms in reciprocal space (right). The total force felt by the atoms is the vector sum of the forces due to each beam. Accordingly, the total quasimomentum displacement (solid line) of the atoms is given by the vector sum of the displacement due to each beam (dashed line). In the schematic, we give an example where  $\mathbf{F}_1$  is twice as strong as  $\mathbf{F}_2$ . After a time  $|k_L| / |\mathbf{F}_1|$ , the atoms have moved by one reciprocal lattice vector.

$\hbar \times 15$  kHz gap from the second band to the third band, as shown in Fig. 6.3a. This separation in energy scales enables us to find a regime of forces that yield a gradient which is large compared to the energy gap between the first two bands but small compared to the energy gap between the second and higher bands. In this regime of forces, the dynamics are predominantly governed by the geometric structure of the lowest two bands. The experimental procedure used to find this “strong gradient regime” is detailed below.

To transport the atoms in reciprocal space, we linearly sweep the frequency of two beams, as illustrated in Fig. 6.3b. This uniformly accelerates the lattice and generates a constant inertial force in the lattice frame. The total force felt by the atoms is given by the vector sum of the forces due to each frequency-swept beam. By independently controlling the frequency sweep rate of the two beams, we can tune the magnitude and direction of the force and move the atoms along arbitrary paths in reciprocal space.

After each experimental sequence, we band map the atoms to detect the population of atoms in the first and second bands at the desired quasimomentum. The band mapping procedure consists of linearly ramping down the intensity of the lattice beams in  $800 \mu\text{s}$ , switching off the dipole trap, and then imaging after 9 ms of TOF.

### 6.3.2. Reaching the strong gradient regime

To reach the strong gradient regime, we transport the atoms from  $\Gamma$  to different final quasimomenta using a variable force  $|\mathbf{F}|$  and band map to measure the population

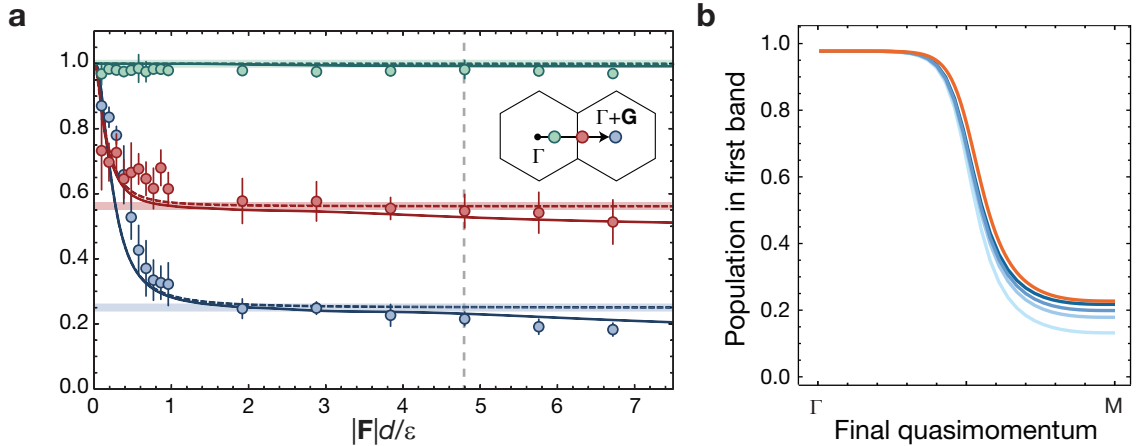


Figure 6.4.: **Reaching the strong-gradient regime and the effect of higher bands.** **a**, The population remaining in the first band for different forces after transport to  $\Gamma + 0.2\mathbf{G}$  (green),  $\Gamma + 0.55\mathbf{G}$  (red), and  $\Gamma + \mathbf{G}$  (blue). The data agree well with a two-level, tight-binding model (dashed line) which approaches the Wilson line regime (thick shaded line) at large forces. Discrepancies at larger forces result from transfer to higher bands and match well with *ab-initio* theory using a full band structure calculation including the first six bands (thin solid line). For all subsequent data, we use  $|\mathbf{F}|d/\varepsilon = 4.8$ , indicated by the dashed gray line. Error bars indicate the standard error of the mean from ten shots per data point. **b**, Comparing the population in the first band at varying quasimomenta for a two-band Wilson line using an *ab-initio* (blue) and tight-binding calculation (orange). In the former calculation, we show Wilson lines at lattice depths  $V_0 = 5.2E_r, 3E_r, 2E_r$ , and  $1E_r$  (decreasing lightness of blue). At  $V_0 = 5.2E_r$ , the results are nearly identical to the Wilson line obtained from a tight-binding calculation.

remaining in the lowest band (see Fig. 6.4a). For vanishing forces, we recover the adiabatic limit, where the population remains in the lowest band. For increasing forces, where the gradient  $|\mathbf{F}|d$  over the distance between A and B sites  $d$  is less than the combined width  $\varepsilon$ , the population continuously decreases. However, at strong forces, where  $|\mathbf{F}|d > \varepsilon$ , the population saturates at a finite value. For example, after transport by one reciprocal lattice vector (blue data in Fig. 6.4a), one quarter of the atoms remain in the first band. This is in stark contrast to typical Landau-Zener dynamics, where the population in the second band is expected to approach unity for increasing strong forces [141].

The saturation of the population transfer indicates that the dynamics depend only on the value of the final quasimomentum and no longer on the time taken to reach that quasimomentum. Here, as evidenced by the agreement of our data with the theory<sup>2</sup>, the evolution is well-described by the Wilson line formalism for a two-band model. The slight deviation from theory at higher forces is further discussed below. For all subsequent measurements, we use a (total) force of magnitude  $|\mathbf{F}| \approx 4.8\varepsilon/d$ . This cor-

<sup>2</sup>Details on the numerical calculations can be found in Appendix B.

responds to an acceleration of  $250 \text{ m/s}^2$  and a Bloch period of  $\approx 42 \mu\text{s}$ .

### 6.3.3. The effect of higher bands

Previously, we claimed that the system is well-described by a two-band model. However, we already see deviations of the data from the two-band tight-binding theory in Fig. 6.4a at larger forces. In this section, we determine whether this deviation is primarily due to the tight-binding approximation or the two-band approximation. To this end, we compare two-band Wilson lines, i.e., neglecting the dispersion of the bands, from an *ab-initio* and tight-binding calculation in Fig. 6.4b. While deviations are significant at shallow lattices, they are already small at a lattice depth of  $V_0 = 5.2E_r$ . Hence, we can conclude that it is not the tight-binding assumption, but rather the two-band assumption at fault. This conclusion is further corroborated by the excellent agreement between data and theory when six bands are taken into account (solid lines in Fig. 6.4a).

True two-band Wilson lines can only be realized by reaching the infinite gradient limit for the two lowest bands while remaining adiabatic with respect to higher bands. This is of course not experimentally possible due to the presence of higher bands. In general, the choice of gradient strength is a compromise between realizing dynamics that are fast compared to the energy scale of the lowest two bands and minimizing excitations into higher bands. We could, in principle, realize the two-band Wilson line regime more precisely by increasing the lattice depth, which decreases the combined width  $\varepsilon$  of the lowest two bands and increases the energy scale between the lowest two bands and higher bands. However, in the current work, the lattice depth was limited by the band mapping technique. As the lattice depth is increased, it becomes more difficult for the band mapping process to remain adiabatic with respect to  $\varepsilon$ .

### 6.3.4. Data analysis

#### ROI selection

To obtain the population of atoms in the first band, we identify regions of interest (ROIs) of first band and second band atoms. Example ROIs are depicted in Fig. 6.5a for atoms accelerated by approximately one reciprocal lattice vector. We count the number of atoms in the first band  $n_1$  and the atoms in the second zone  $n_2$ . Subsequently, the relative population in the first band is given by  $n_1/(n_1 + n_2)$ . Practically, "counting" the atoms means summing the pixel values within the specified regions of interest, i.e., the red circle for first band atoms ( $n_1$ ) and the six blue circles for second band atoms ( $n_2$ ).

To obtain a quantitatively accurate fraction in the first band, we subtract from  $n_1$  the mean pixel value of the region enclosed by the dashed red circles. This accounts for the hot background atoms. We do perform an additional background subtrac-

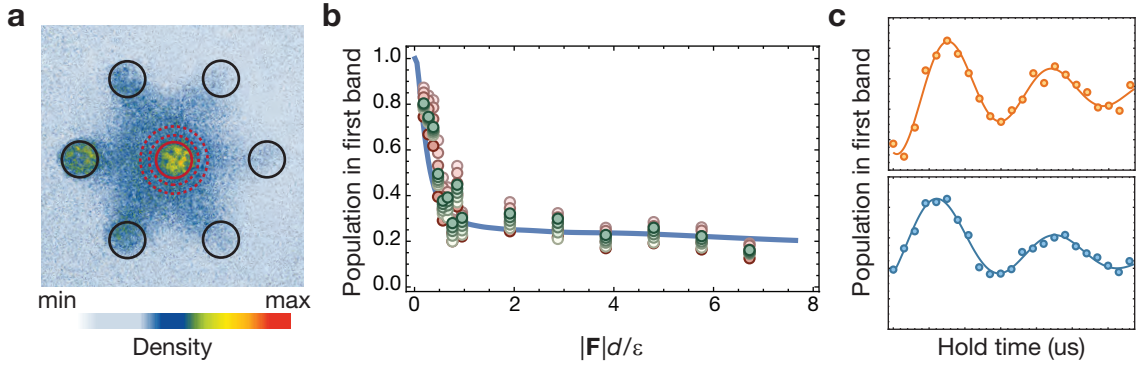


Figure 6.5.: **Data analysis.** **a**, ROIs used in data analysis. The atom number in the first (second) zone is obtained by summing the pixel values within the red (blue) circle(s). We additionally take the mean of the pixel values in the ring defined by the dashed red circles and, with the exception of the measurements for  $\phi_{\mathbf{q}}$ , subtract this value as background from the pixel sum of the first zone atoms. **b**, Checking systematic errors due to ROI selection. Green points show the effect of changing the size of the outer dashed red circle in **a**, i.e., the size of the background subtraction region. The radius ranges from 0.8 to 1.3 times the radius used in the data analysis, with deeper shades of green indicating a larger radius. Red points show the effect of changing the size of the data-analysis ROI, i.e., the size of the red and blue circles in **a**. The radius ranges from 0.1 to 1.2 times the radius used in the data analysis, with deeper shades of red indicating a larger radius. The scatter of points about the two-band, tight-binding theory (blue line) suggest systematic errors on the order of  $\pm 5\%$ . **c**, Both the maximum and minimum values of the oscillation in a lattice with AB-site offset (top) damps with increasing hold time. In contrast, for an oscillation in a lattice with AB-site degeneracy (bottom), only the maximum values damp with increasing hold time.

tion when counting second band atoms. Near  $\Gamma$ , these second band atoms are unstable due to interaction effects [142] and move to other quasimomenta. An additional background subtraction would therefore underestimate atoms in the second band by counting atoms that have decayed from  $\Gamma$  as background. All data are analyzed in this manner, with the exception of the  $\phi_{\mathbf{q}}$  measurements. For these measurements, we are interested only in the phase of the population oscillation and not in its absolute value.

To check systematic errors due to our selection of ROIs, we analyze a single data set of population transfer vs. force magnitude after transport by one reciprocal lattice vector (blue data in Fig. 6.4a) using different ROIs. We evaluate both the effect of the ROI size using a fixed background subtraction ring and the effect of the background subtraction ring using a fixed ROI size. Using the same ROI size for first and second band atoms and restricting the ROI size such that it does not overlap with the background subtraction ring yields consistent results with deviations on the order of  $\pm 5\%$ , as shown in Fig. 6.5b.

We use the same ROIs and, when applicable, background subtraction ring for all data sets.

### Fitting the population oscillation for $\phi_{\mathbf{q}}$

To obtain the phase of the oscillation in first band population, which encodes  $\phi_{\mathbf{q}}$ , we fit the oscillation to an empirically chosen function of the form:

$$A_0 e^{-t/t_0} (\cos(2\pi f t + \phi) + y_1) + y_0 \quad (6.20)$$

where  $A_0$  is the amplitude of the function,  $t_0$  parametrizes the decay of the fringe,  $f$  fits the frequency, which is in principle the energy difference  $\hbar\Delta\omega$  between the first and second band at the reference quasimomentum, and  $\phi$  is the phase. The offsets  $y_1$  and  $y_0$  interpolate between an oscillation with damping of both maximum and minimum values (Fig. 6.5c top) and an oscillation with damping of only the maximum values (Fig. 6.5c bottom).

## 6.4. Experimental results

Here, we present our measurements of  $\theta_{\mathbf{q}}$  and  $\phi_{\mathbf{q}}$ . In parametrizing the eigenstates, both angles also reflect the symmetries of the lattice. In fact, the data on  $\theta_{\mathbf{q}}$  reveals the relative positions of A and B sites, while the data on  $\phi_{\mathbf{q}}$  reveals the rotational and inversion symmetry of the honeycomb lattice.

### 6.4.1. Measuring $\theta_{\mathbf{q}}$

We measure the polar angle  $\theta_{\mathbf{q}}$  at varying quasimomenta  $\mathbf{q}$  along a straight path  $\Gamma$  to  $\Gamma + 3\mathbf{G}$ . Due to the three-fold rotational symmetry of the lattice and the rotational symmetry of the  $s$ -orbitals, which makes the path from  $\Gamma$  to  $\Gamma + 3\mathbf{G}$  equivalent to the triangular path shown in Fig. 6.6a, we expect to recover all population in the lowest band after transport by three reciprocal lattice vectors. As shown in Fig. 6.6b, our data agrees reasonably well with this prediction. Deviations from the tight-binding model are accounted for by including population transfer to higher bands.

The change in the angle  $\theta_{\mathbf{q}}$  during transport along the path  $\Gamma$  to  $\Gamma + 3\mathbf{G}$  can be visualized as rotations on the Bloch sphere (inset of Fig. 6.6b). Per reciprocal lattice vector, the pseudospin winds by  $2\pi/3$ . This is reasonable since, if transport by three reciprocal lattice vectors yields a  $2\pi$  rotation, transport by one-third that amount ought to yield one-third of the rotation. However, we can gain a deeper understanding of this behavior by considering what happens in real-space.

### 6.4.2. The real-space picture

As discussed in Sec. 3.1.1, when the A and B sites are degenerate, i.e.,  $\Delta = 0$ , the band eigenstates are equal superpositions of the ‘‘Bloch states’’ associated with the A and

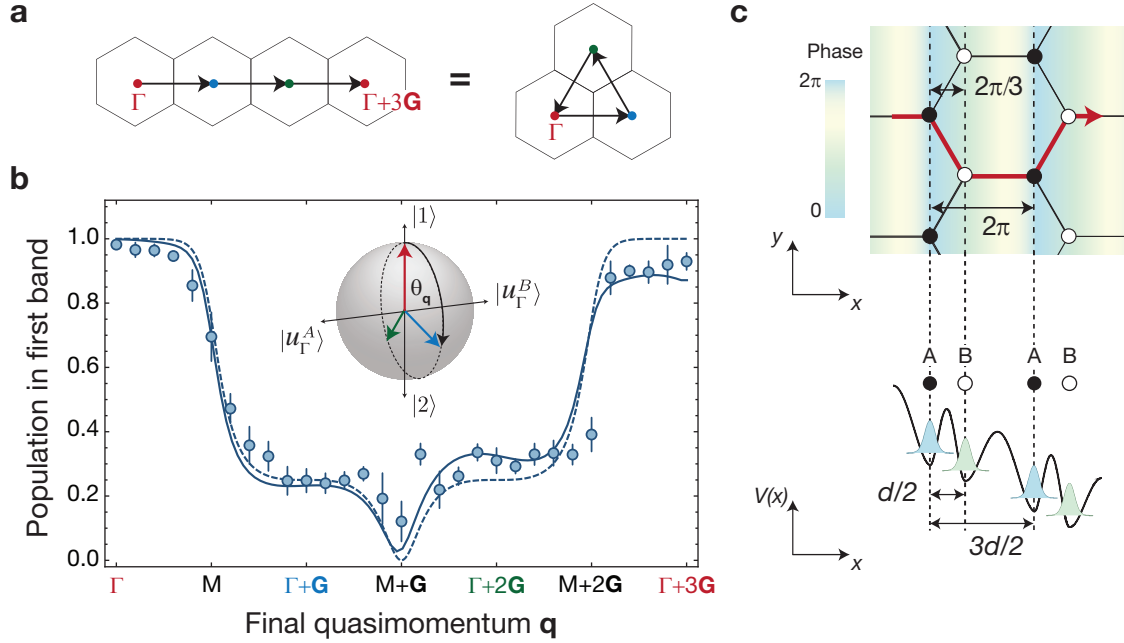


Figure 6.6.: **Measuring  $\theta_q$ .** **a**, Due to the three-fold-rotational symmetry of the honeycomb lattice, a path from  $\Gamma$  to  $\Gamma + 3\mathbf{G}$  is equivalent to a triangle-shaped path with each leg of length  $|\mathbf{G}|$ , beginning and ending at  $\Gamma$ . Coloured dots correspond to coloured quasimomentum labels in (b). **b**, The population remaining in the first band after transport to final quasimomentum  $\mathbf{q}$ . Theory lines are a single-particle solution to the dynamics using a full lattice potential and including the first six bands (solid) and a two-band, tight-binding model (dashed). The inset Bloch sphere depicts the transported state at  $\Gamma$  (red),  $\Gamma + \mathbf{G}$  (blue), and  $\Gamma + 2\mathbf{G}$  (green) in the basis of the cell-periodic Bloch functions at  $\Gamma$ . Error bars represent the standard error of the mean from averaging 9-11 shots, with the exception of  $\mathbf{q} = M + \mathbf{G}$  and  $\mathbf{q} = M + 0.9\mathbf{G}$ , which show the average of 20 shots. **c**, Transport of a Bloch state by one reciprocal lattice vector corresponds to a  $2\pi$  phase shift between real-space wavefunctions of the same sublattice site and a phase shift of  $2\pi/3$  between wavefunctions of A- and B-sites (top). Bottom: the combined lattice and gradient potential  $V(x)$  projected onto the  $x$ -axis, which is the direction of the applied force. Traveling along the path indicated by the red arrow highlights the effect of the real-space embedding of the honeycomb lattice: since the distance between A (solid circles) and B sites (open circles) is  $1/3$  the distance between sites of the same type, there is a phase difference of  $2\pi/3$  between the real-space wavefunctions of A and B sites.

B sites,  $|\Phi_{\mathbf{q}}^A\rangle$  and  $|\Phi_{\mathbf{q}}^B\rangle$ <sup>3</sup>. Accordingly, the cell-periodic Bloch functions of the first and second band at  $\Gamma$ , which are our basis states  $|1\rangle$  and  $|2\rangle$ , can also be expressed as equal superpositions of the “cell-periodic Bloch functions” associated with the A and B sites,  $|u_{\Gamma}^A\rangle$  and  $|u_{\Gamma}^B\rangle$ . These two states form an alternative set of basis states that can be represented as an equatorial axis on the Bloch sphere. Furthermore, the state  $|u_{\mathbf{q}}^n\rangle$  must rotate about this equatorial axis since  $|u_{\mathbf{q}}^n\rangle$  remains an equal superposition of  $|u_{\Gamma}^A\rangle$  and  $|u_{\Gamma}^B\rangle$  throughout the evolution. Hence, as can be seen in the inset of Fig. 6.6b, the angle  $\theta_{\mathbf{q}}$ , which parametrizes the superposition between states  $|1\rangle$  and  $|2\rangle$ , also parametrizes the phase between states  $|u_{\Gamma}^A\rangle$  and  $|u_{\Gamma}^B\rangle$ . Therefore, our aim now is to understand the  $2\pi/3$  rotation in  $\theta_{\mathbf{q}}$  by understanding why the states  $|u_{\Gamma}^A\rangle$  and  $|u_{\Gamma}^B\rangle$  accumulate a phase of  $2\pi/3$  when transporting by one reciprocal lattice vector.

In terms of states at  $\Gamma$ , the state  $|u_{\Gamma+\mathbf{G}}^1\rangle$  can be represented as

$$\begin{aligned}
 |u_{\Gamma+\mathbf{G}}^1\rangle &= e^{i\mathbf{G}\cdot\hat{\mathbf{r}}}|u_{\Gamma}^1\rangle \\
 &= e^{i\mathbf{G}\cdot\hat{\mathbf{r}}}\frac{1}{\sqrt{2}}(|u_{\Gamma}^A\rangle + |u_{\Gamma}^B\rangle) \\
 &= e^{i\mathbf{G}\cdot\hat{\mathbf{r}}}\frac{1}{\sqrt{2}}(e^{-i\Gamma\cdot\hat{\mathbf{r}}}\sum_{\mathbf{r}_A}e^{i\Gamma\cdot\mathbf{r}_A}|w_{\mathbf{r}_A}\rangle + e^{-i\Gamma\cdot\hat{\mathbf{r}}}\sum_{\mathbf{r}_B}e^{i\Gamma\cdot\mathbf{r}_B}|w_{\mathbf{r}_B}\rangle) \\
 &= e^{i\mathbf{G}\cdot\hat{\mathbf{r}}}\frac{1}{\sqrt{2}}(\sum_{\mathbf{r}_A}|w_{\mathbf{r}_A}\rangle + \sum_{\mathbf{r}_B}|w_{\mathbf{r}_B}\rangle) \tag{6.21}
 \end{aligned}$$

In the equations above, we have explicitly expressed the Wilson line transporting from  $\Gamma$  to  $\Gamma + \mathbf{G}$  in its quasimomentum-translation operator form as  $e^{i\mathbf{G}\cdot\hat{\mathbf{r}}}$ . In the second line, we write the state  $|u_{\Gamma}^1\rangle$  in the basis of  $|u_{\Gamma}^A\rangle$  and  $|u_{\Gamma}^B\rangle$ . In the third line, we write the quasimomentum-dependent state  $|u_{\Gamma}^{A(B)}\rangle$  in terms of the real-space wavefunctions  $|w_{\mathbf{r}_{A(B)}}\rangle$  localized on the A (B) sites at positions  $\mathbf{r}_{A(B)}$ . Lastly, we have used that the real-space wavefunctions are eigenstates of the position operator, i.e.,  $e^{-i\Gamma\cdot\hat{\mathbf{r}}}|w_{\mathbf{r}_{A(B)}}\rangle = e^{-i\Gamma\cdot\mathbf{r}_{A(B)}}|w_{\mathbf{r}_{A(B)}}\rangle$  [143]. From this last line, we see that the states  $|u_{\Gamma}^A\rangle$  and  $|u_{\Gamma}^B\rangle$  are superpositions of the real-space wavefunctions on the the A and B sites<sup>4</sup>.

In the particular case of transport by one reciprocal lattice vector, we know that, since  $\mathbf{r}_A$  can be written as a sum of primitive lattice vectors,  $\mathbf{G}\cdot\mathbf{r}_A = 2\pi$ . However, since the B-sites are displaced from the A-sites by  $\delta_3$  (see Sec. 3.1), we have that  $\mathbf{G}\cdot\mathbf{r}_B =$

<sup>3</sup> Recall from Sec. 3.1 that states  $|\Phi_{\mathbf{q}}^A\rangle$  and  $|\Phi_{\mathbf{q}}^B\rangle$  are Fourier transforms of the real-space wavefunctions localized on the A and B sites. We use the quotation marks because, although they are analogous to Bloch states,  $|\Phi_{\mathbf{q}}^A\rangle$  and  $|\Phi_{\mathbf{q}}^B\rangle$  are not Bloch states. By definition, Bloch states are eigenstates of the Hamiltonian.

<sup>4</sup> In fact, any  $|u_{\mathbf{q}}^A\rangle$  and  $|u_{\mathbf{q}}^B\rangle$  can be written as a superposition of the real-space wavefunctions on the A and B sites. Moreover, this superposition is quasimomentum-independent. This results from the completeness of the bands, i.e., that the bands span the same Hilbert space at all quasimomenta.

$\mathbf{G} \cdot (\mathbf{r}_A + \delta_3) = 2\pi + 2\pi/3$ . Hence,

$$\begin{aligned}
 |u_{\Gamma+\mathbf{G}}^1\rangle &= \frac{1}{\sqrt{2}} \left( \sum_{\mathbf{r}_A} e^{i\mathbf{G}\cdot\mathbf{r}_A} |w_{\mathbf{r}_A}\rangle + \sum_{\mathbf{r}_B} e^{i\mathbf{G}\cdot\mathbf{r}_B} |w_{\mathbf{r}_B}\rangle \right) \\
 &= \frac{1}{\sqrt{2}} \left( \sum_{\mathbf{r}_A} |w_{\mathbf{r}_A}\rangle + \sum_{\mathbf{r}_B} e^{i2\pi/3} |w_{\mathbf{r}_B}\rangle \right) \\
 &= \frac{1}{\sqrt{2}} (|u_{\Gamma}^A\rangle + e^{i2\pi/3} |u_{\Gamma}^B\rangle)
 \end{aligned} \tag{6.22}$$

Finally, we see that the phase factor of  $2\pi/3$  is a consequence of the real-space displacement of the B-sites from the A-sites.

In summary, although transport by one reciprocal lattice vector results in a phase difference of  $2\pi$  between the real-space wavefunctions on lattice sites of the same type due to the real-space embedding, i.e., the structure of the lattice, there is a phase difference of  $2\pi/3$  between real-space wavefunctions on the A- and B-sites, as illustrated in Fig. 6.6c. Consequently, the population transfer would be different if the same experiment were performed in a brick-wall incarnation [30] of the same tight-binding model. Furthermore, transport by three reciprocal lattice vectors results in unity overlap since  $3 \times 2\pi/3 = 2\pi$ . We emphasize now (and will further discuss in Sec. 6.5.4) that this physical picture of accumulating different phase factors between real-space wavefunctions  $|w_{\mathbf{r}_A}\rangle$  and  $|w_{\mathbf{r}_B}\rangle$  is applicable only in the strong-gradient regime.

### 6.4.3. Measuring $\phi_{\mathbf{q}}$

We measure the azimuthal angle of states that lie at the angular coordinate  $\alpha$  on a circle of radius  $\mathbf{G}$  centered at  $\Gamma$  (see Fig. 6.7a). The results are shown in Fig. 6.7b. We observe quantized jumps of  $\pi$  in the phase of the interference fringe each time  $\alpha$  is swept through a Dirac point, i.e., every  $60^\circ$  (blue circles in Fig. 6.7b). This periodicity is a consequence of the three-fold rotational symmetry of the lattice. The binary nature of the phases is due to the degeneracy between A and B sites. As previously discussed, the pseudospin  $|u_{\mathbf{q}}^n\rangle$  in a lattice with degenerate A and B sites is constrained to rotate on the meridian about an axis whose poles represent  $|u_{\Gamma}^A\rangle$  and  $|u_{\Gamma}^B\rangle$ . Therefore, the phase between states  $|1\rangle$  and  $|2\rangle$  must be zero or  $\pi$ . To remove this constraint, we introduce an energy offset between A and B sites using elliptically polarized beams. This yields smoothly varying phases that are always less than  $\pi$  (red circles in Fig. 6.7b), indicating a broken inversion symmetry. However, since the three-fold rotation symmetry of the lattice is preserved, the periodicity of the data remains.

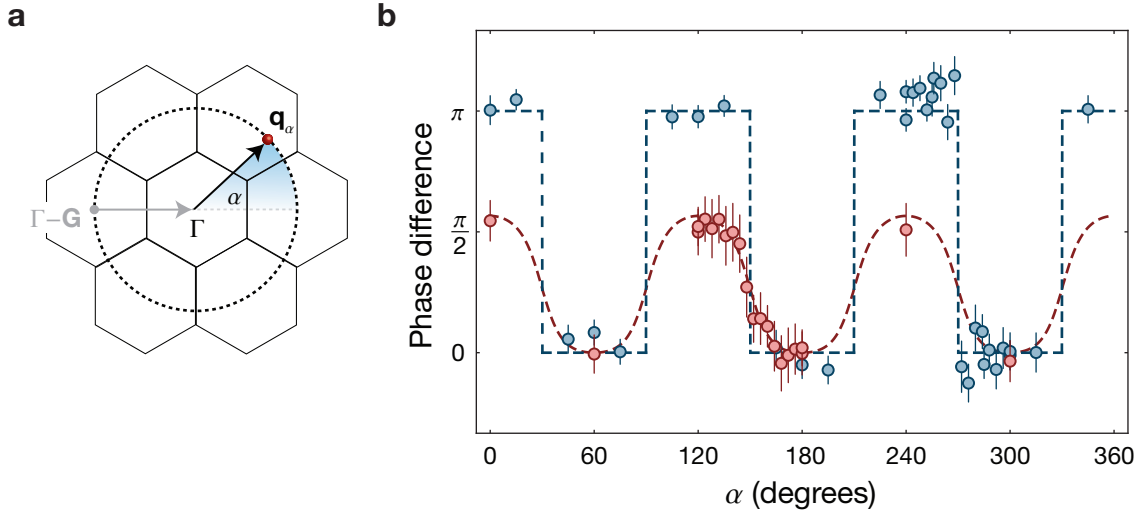


Figure 6.7.: **Measuring  $\phi_{\mathbf{q}}$ .** **a**, Schematic of the interferometric sequence in the extended Brillouin zone scheme. To create a superposition state, atoms initially in the lowest eigenstate at  $\Gamma - \mathbf{G}$  are rapidly transported to  $\Gamma$  and held for variable time. After the state preparation, the atoms are transported to the desired quasimomentum  $\mathbf{q}_{\alpha}$ , which is parametrized by the angle  $\alpha$  and lies on a circle of radius  $|\mathbf{G}|$  centered at  $\Gamma$  (iii). **b**, Phases  $\phi_{\alpha}$  referenced to  $\alpha=180^{\circ}$  for the lattice with AB-site degeneracy (blue) and AB-site offset (red). Data in blue have been offset by  $+120^{\circ}$  for visual clarity. Dashed lines are a two-band, tight-binding calculation with  $\Delta/J=0$  (blue) and  $\Delta/J=3.1$  (red), where  $J = h \times 500(10)$  Hz. Error bars indicate fit errors.

## 6.5. Determining the Wilson-Zak loop eigenvalues

Having demonstrated our ability to probe angles  $\theta_{\mathbf{q}}$  and  $\phi_{\mathbf{q}}$ , which maps the band eigenstates over the Brillouin zone if measured for all  $\mathbf{q}$ , we now turn our attention to the eigenvalues of Wilson-Zak loops, which are especially important for characterizing time-reversal invariant topological insulators [77, 137]. Although our band structure is not topological, our proof-of-principle reconstruction of the eigenvalues of a single Wilson-Zak loop is a first step toward the investigation of more complex band structures.

In order to obtain the eigenvalues, we use our previous data to reconstruct the Wilson-Zak loop operator transporting from  $\Gamma$  to  $\Gamma + \mathbf{G}$ . This requires a few properties of Wilson lines, which we discuss below, and a bit of algebra. Finally, to conclude this chapter, we return to the real-space picture and relate the Wilson-Zak loop eigenvalues to the real-space embedding.

### 6.5.1. Decomposition of the Wilson line into $U(1)$ and $SU(2)$ .

Generically, the Wilson line of a two-band system is a  $U(2)$  matrix, which can be decomposed into a global  $U(1)$  phase and an  $SU(2)$  matrix. In our experiment, we are

able to measure only the  $SU(2)$  part. Indeed, the global phase does not show up on the Bloch sphere, which represents a projected Hilbert space. That is, we obtain information only about the rotations of a vector on the Bloch sphere, which is given by the  $SU(2)$  part, while the entire Bloch sphere can be oriented in any way, which is the global gauge-freedom from the  $U(1)$  phase. Nonetheless, by examining the decomposition of the  $U(2)$  Wilson line, we can gain some insight into the quantities we are (and are not) measuring.

We begin by writing the Wilczek-Zee connection matrix  $\hat{\mathbf{A}}_{\mathbf{q}}$  in a general form as

$$\hat{\mathbf{A}}_{\mathbf{q}} = \begin{pmatrix} \mathbf{A}_{\mathbf{q}}^{1,1} & \mathbf{A}_{\mathbf{q}}^{1,2} \\ \mathbf{A}_{\mathbf{q}}^{2,1} & \mathbf{A}_{\mathbf{q}}^{2,2} \end{pmatrix} \quad (6.23)$$

To simplify notation, we henceforth suppress the  $\mathbf{q}$  subscript and note that all elements are still to be understood as being  $\mathbf{q}$ -dependent. Next, we decompose the matrix as

$$\begin{aligned} \hat{\mathbf{A}} &= \begin{pmatrix} \frac{\mathbf{A}^{1,1} + \mathbf{A}^{2,2}}{2} & 0 \\ 0 & \frac{\mathbf{A}^{1,1} + \mathbf{A}^{2,2}}{2} \end{pmatrix} + \begin{pmatrix} \frac{\mathbf{A}^{1,1} - \mathbf{A}^{2,2}}{2} & \mathbf{A}^{1,2} \\ \mathbf{A}^{2,1} & -\frac{\mathbf{A}^{1,1} - \mathbf{A}^{2,2}}{2} \end{pmatrix} \\ &:= \hat{\mathbf{A}}_{U(1)} + \hat{\mathbf{A}}_{SU(2)} \end{aligned} \quad (6.24)$$

Noting that  $\hat{\mathbf{A}}_{U(1)}$  is proportional to the identity matrix and therefore commutes with  $\hat{\mathbf{A}}_{SU(2)}$  and with itself for all quasimomenta, the Wilson line  $\hat{\mathbf{W}}_{\mathbf{Q} \rightarrow \mathbf{q}}$  transporting a state from initial quasimomentum  $\mathbf{Q}$  to final quasimomentum  $\mathbf{q}$  can be expressed as:

$$\begin{aligned} \hat{\mathbf{W}}_{\mathbf{Q} \rightarrow \mathbf{q}} &= \mathcal{P} e^{i \int_{\mathcal{C}} d\mathbf{q} \hat{\mathbf{A}}} \\ &= \mathcal{P} e^{i \int_{\mathcal{C}} d\mathbf{q} \hat{\mathbf{A}}_{U(1)} + \hat{\mathbf{A}}_{SU(2)}} \\ &= e^{i \int_{\mathcal{C}} d\mathbf{q} \hat{\mathbf{A}}_{U(1)}} \mathcal{P} e^{i \int_{\mathcal{C}} d\mathbf{q} \hat{\mathbf{A}}_{SU(2)}} \end{aligned} \quad (6.25)$$

where  $\mathcal{C}$  denotes the path taken from  $\mathbf{Q}$  to  $\mathbf{q}$ . This completes the decomposition of the  $U(2)$  Wilson line into a  $U(1)$  global phase multiplied by a path-ordered  $SU(2)$  matrix.

Notably, the global  $U(1)$  phase is given by

$$\int_{\mathcal{C}} d\mathbf{q} \frac{\mathbf{A}^{1,1} + \mathbf{A}^{2,2}}{2}, \quad (6.26)$$

which is simply the sum of the standard geometric phases acquired in the first and second band. That is, for a closed path, the  $U(1)$  phase is the sum of the Berry phases and for a closed-by-a-reciprocal-lattice-vector path, the  $U(1)$  phase is sum of the Zak phases of the first and second band. Therefore, the  $U(1)$  phase encodes the first Chern number of the system [7, 90], which, for example, characterizes the celebrated integer quantum Hall effect [2, 144].

For our purposes, we simply need to know that the experiment reconstructs an SU(2) matrix, which, in its most general form, can be written:

$$\begin{pmatrix} W^{11} & W^{12} \\ -W^{12*} & W^{11*} \end{pmatrix} \quad (6.27)$$

where  $|W^{11}|^2 + |W^{12}|^2 = 1$ . The eigenvalues  $e^{\pm i\xi}$  of this matrix are given by

$$\text{Re}[W^{11}] \pm i\sqrt{|W^{12}|^2 + \text{Im}[W^{11}]^2} \quad (6.28)$$

Our measurements of  $\theta_{\Gamma+\mathbf{G}}$  give  $|W^{11}|$  and  $|W^{12}| = \sqrt{1 - |W^{11}|^2}$ . However, to find the eigenvalues, we additionally need  $\text{Arg}[W^{11}]$  while our measurements of  $\phi_{\Gamma+\mathbf{G}}$  only give  $\text{Arg}[W^{11}] - \text{Arg}[W^{12}]$ . To find  $\text{Arg}[W^{11}]$ , we will utilize a property of Wilson lines called the back-tracking condition [145].

### 6.5.2. The back-tracking condition

For generic quasimomenta  $\mathbf{q}$  and  $\mathbf{Q}$  [145],

$$\hat{\mathbf{W}}_{\mathbf{Q}\rightarrow\mathbf{q}} = \hat{\mathbf{W}}_{\mathbf{q}\rightarrow\mathbf{Q}}^\dagger. \quad (6.29)$$

Consequently,  $\hat{\mathbf{W}}_{\mathbf{q}\rightarrow\mathbf{Q}}\hat{\mathbf{W}}_{\mathbf{Q}\rightarrow\mathbf{q}} = \mathbb{1}$ , such that going forward and back along the same path results in no transformation of the state vector. This is known as the back-tracking condition.

In the case of the Wilson-Zak loop in the experiment, the relevant relation is

$$\hat{\mathbf{W}}_{\Gamma\rightarrow\Gamma+\mathbf{G}} = \hat{\mathbf{W}}_{\Gamma\rightarrow\Gamma-\mathbf{G}}^\dagger, \quad (6.30)$$

where we have used that  $\hat{\mathbf{W}}_{\Gamma\rightarrow\Gamma-\mathbf{G}} = \hat{\mathbf{W}}_{\Gamma+\mathbf{G}\rightarrow\Gamma}$  which, assuming a periodic gauge choice, follows from the periodicity of the Brillouin zone. If the phase  $\phi_{\Gamma+\mathbf{G}}$  of the oscillation after transport from  $\Gamma$  to  $\Gamma + \mathbf{G}$  is given by

$$\phi_{\Gamma+\mathbf{G}} = \text{Arg}[W_{\Gamma\rightarrow\Gamma+\mathbf{G}}^{11}] - \text{Arg}[W_{\Gamma\rightarrow\Gamma+\mathbf{G}}^{12}], \quad (6.31)$$

then the phase  $\phi_{\Gamma-\mathbf{G}}$  of the oscillation after transport from  $\Gamma$  to  $\Gamma - \mathbf{G}$  is

$$\phi_{\Gamma-\mathbf{G}} = -\text{Arg}[W_{\Gamma\rightarrow\Gamma+\mathbf{G}}^{11}] - \text{Arg}[W_{\Gamma\rightarrow\Gamma+\mathbf{G}}^{12}] + \pi \quad (6.32)$$

Therefore, taking the difference between the two oscillation phases extracts

$\text{Arg}[W_{\Gamma \rightarrow \Gamma + \mathbf{G}}^{11}]$  as

$$\phi_{\Gamma + \mathbf{G}} - \phi_{\Gamma - \mathbf{G}} - \pi = 2\text{Arg}[W_{\Gamma \rightarrow \Gamma + \mathbf{G}}^{11}] \quad (6.33)$$

Note that there is an ambiguity in choosing  $\pm\pi$  when relating  $\phi_{\Gamma + \mathbf{G}}$  to  $\phi_{\Gamma - \mathbf{G}}$ . This results in a global  $U(1)$  phase shift of  $\pi$  in the eigenvalue phases. However, the phase difference between the eigenvalues is unaffected, which is sufficient to reconstruct, e.g., the  $\mathbb{Z}_2$  invariant.

### 6.5.3. Wilson-Zak loop eigenvalues with and without inversion symmetry

When the lattice is inversion symmetric, i.e., when A and B sites are degenerate, applying Eq.6.33 to the phase of oscillations for  $\alpha = 0$  and  $\alpha = 180$  in the interferometric sequence (Fig. 6.7b) yields  $\text{Arg}[W_{\Gamma \rightarrow \Gamma + \mathbf{G}}^{11}] = 0.03(7)$  rad. Combined with the direct transport data from  $\Gamma$  to  $\Gamma + \mathbf{G}$  (Fig. 6.6b), which gives  $|W_{\Gamma \rightarrow \Gamma + \mathbf{G}}^{11}| = 0.47(2)$  and  $|W_{\Gamma \rightarrow \Gamma + \mathbf{G}}^{12}| = \sqrt{1 - |W_{\Gamma \rightarrow \Gamma + \mathbf{G}}^{11}|^2} = 0.88(1)$ , we obtain eigenvalue phases  $\xi = 1.03(2)\pi/3$ . These values are in good agreement with the value of  $\xi = \pi/3$  predicted from the two-band model.

In a lattice with AB-site offset, data for  $\alpha = 0$  and  $\alpha = 180$  from Fig. 6.7b yields  $\text{Arg}[W_{\Gamma \rightarrow \Gamma + \mathbf{G}}^{11}] = -0.76(6)$  rad. We measure the absolute values by transporting atoms initialized at  $\Gamma$  in the lowest eigenstate to  $\Gamma + \mathbf{G}$  with increasing force. The remaining population in the first band is shown in Fig. 6.8a. At  $|\mathbf{F}|d/\varepsilon = 5$ , where the population transfer has saturated, we obtain  $|W_{\Gamma \rightarrow \Gamma + \mathbf{G}}^{11}| = 0.63(3)$  and  $|W_{\Gamma \rightarrow \Gamma + \mathbf{G}}^{12}| = \sqrt{1 - |W_{\Gamma \rightarrow \Gamma + \mathbf{G}}^{11}|^2} = 0.77(2)$ . This gives the eigenvalue phases of  $\xi = 1.04(4)\pi/3$ . Remarkably, these eigenvalues are the same (within error bars) as the eigenvalues in an inversion-symmetric lattice.

Hence, while the data in, e.g., Fig. 6.7 measures different eigenstates, indicating that the (local) geometric structure of the bands have changed, the invariance of the Wilson-Zak loop eigenvalues suggests that the (global) topological structure of the bands remains the same in lattices with and without inversion symmetry. This invariance is a direct consequence of the real-space representation of the Wilson-Zak loop,  $\hat{\mathbf{W}}_{\Gamma \rightarrow \Gamma + \mathbf{G}} = e^{i\mathbf{G} \cdot \hat{\mathbf{r}}}$ . Since the Wilson-Zak loop depends only on the position operator  $\hat{\mathbf{r}}$ , the eigenvalues are determined solely by the physical locations of the lattice sites. Consequently, any perturbation, such as an energy offset between A and B sites, that does not invalidate the completeness assumption we used to formulate the path-independent Wilson line and does not change the position of the lattice sites will yield the same Wilson-Zak loop eigenvalues.

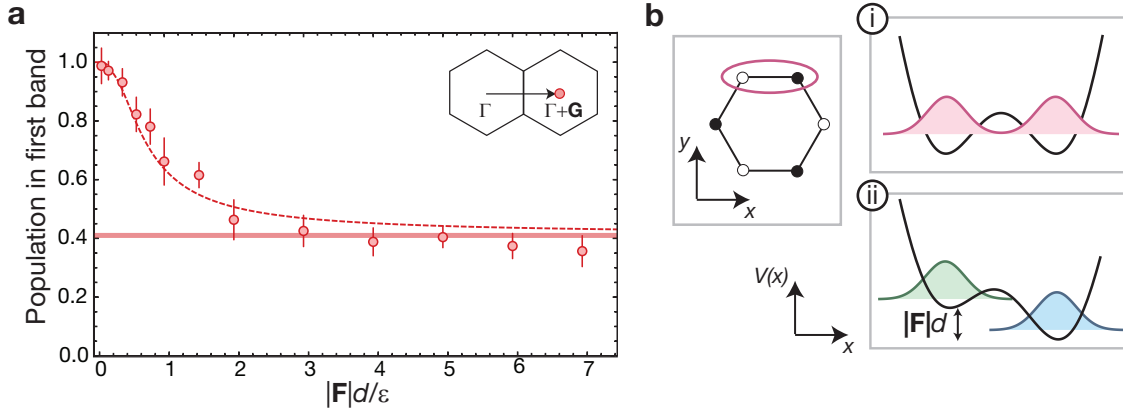


Figure 6.8.: **A-B site offset data and an intuitive picture for the strong gradient limit.** **a**, The population remaining in the first band after transport at different forces from  $\Gamma$  to  $\Gamma + \mathbf{G}$  in a lattice with broken inversion symmetry. The data agrees reasonably well with a two-level, tight-binding theory (dashed line) that approaches the Wilson line regime (thick shaded line) at large forces. We attribute the discrepancy to the two-level model at larger forces to transfer to higher bands. To calculate the  $SU(2)$  eigenvalues, we use the population at  $|F|d/\varepsilon = 5$ . The inset depicts the transport path. Error bars represent the standard error of the mean from ten shots per data point. **b**, We examine a single unit-cell of the honeycomb lattice circled in red. For a negligible gradient (i), the eigenfunction of the system is a superposition of the lattice site wavefunctions. In contrast, a strong gradient suppresses tunneling and decouples lattice sites such that the each wavefunction can independently evolve (ii).

#### 6.5.4. Wilson-Zak loop eigenvalues and the real-space embedding

The difference between the measured eigenvalue phases is ( $\approx$ )  $2\pi/3$ , which, as we saw in Sec. 6.4.2, is the same as the phase difference between the real-space wavefunctions on the A and B sites. This is not a coincidence. Since the wavefunctions localized on the A and B sites,  $|w_{\mathbf{r}_A}\rangle$  and  $|w_{\mathbf{r}_B}\rangle$  are eigenstates of position operator  $\hat{\mathbf{r}}$  [143] with eigenvalues given by the position of the lattice site  $\mathbf{r}_A$  and  $\mathbf{r}_B$ , they are also eigenstates of the real-space representation of the Wilson line  $e^{i\mathbf{q}\hat{\mathbf{r}}}$  with eigenvalues given by  $e^{i\mathbf{q}\cdot\mathbf{r}_A}$  and  $e^{i\mathbf{q}\cdot\mathbf{r}_B}$ . Hence, the phases of the Wilson-Zak loop eigenvalues are simply determined by the real-space embedding of the lattice.

Furthermore, this real-space picture gives some physical intuition for the meaning of “strong-gradient limit.” Consider a single unit-cell of the honeycomb lattice, as shown in Fig. 6.8b. When there is a negligibly weak gradient compared to the tunnel coupling, the eigenstate of the system is a superposition of wavefunctions localized on the A and B sites. The eigenstate will undergo some evolution, but the phases of the individual wavefunctions on the A and B sites are locked together. Imagine now that the two sites are decoupled such that we have two independent systems and the eigenstate of the A site is simply the wavefunction on the A site and likewise for the B site. A and B site wavefunctions can now of course independently evolve. When we add a

sufficiently strong gradient, we effectively decouple A and B sites by suppressing the tunneling, thereby enabling independent evolution of A and B site real-space wavefunctions. Consequently, in this picture, entering the strong-gradient regime depends on whether the gradient over the distance between A and B sites,  $|\mathbf{F}|d$ , is sufficiently larger than the tunneling.

# Chapter 7.

## Conclusion and Outlook

Novel detection methods are essential in the study of band structure topology using ultracold atoms in optical lattices. Although classic transport measurements from condensed matter physics [26] have been successfully used in ultracold atom setups [55–58], the ability to access new observables is a very compelling motivation for the development of techniques specific to cold atom systems [71, 146–157]. Notably, cold atom experiments offer the unique opportunity to directly probe the band geometry [72, 136, 137, 158]. In this thesis, we demonstrated two such detection methods using a BEC of  $^{87}\text{Rb}$  in the  $s$ -bands of an optical honeycomb lattice.

Both methods can be understood by considering the general problem of a single-particle confined to a periodic potential and subjected to a constant, external force. We derived the equations of motion for this problem in the basis of the band eigenstates in Chapter 2 and discovered that the non-Abelian Berry connections are responsible for interband transitions. We then proceeded to analyze the two limiting cases of a very small and very large force, where very small and very large is defined relative to the energy splitting between the bands. In the former scenario, interband transitions can be neglected and atoms in each band independently acquire Berry phases, while in the latter situation, the interband transitions dominate and the dispersion can be neglected. In this case, the unitary time evolution operator is no longer just a phase factor, but a matrix-valued quantity termed the Wilson line. Our goal then, was to measure the Berry phase and the Wilson line in order to probe the geometric structure of the bands.

In the first set of experiments (Chapter 5), we realized an atomic interferometer to measure the  $\pi$  Berry flux associated with a Dirac cone in reciprocal space, in analogy to an Aharonov-Bohm interferometer that measures the magnetic flux penetrating a given area in real space. Using a spin-echo sequence, we measured a Berry flux of  $0.95(10)\pi$  and constrained the spread in Berry curvature of a Dirac point to be smaller than  $10^{-3}k_L$ . Our results are consistent with a perfectly localized Berry curvature, indicating both the high resolution of our interferometer and the quality of our optical lattice. Furthermore, by imbalancing the lattice beams, we tracked the movement and eventual annihilation of the Dirac points.

In principle, by combining local measurements of the Berry flux in small interfer-

ometer loops, we could reconstruct the distribution of Berry curvature in the Brillouin zone and directly obtain the Chern number of the band. In practice, however, this method has a few disadvantages. First, the measurement crucially depends on the cancellation of dynamical phases. This is accomplished by the spin-echo sequence when the symmetry axis of the interferometer loop coincides with the symmetry axis of the dispersion relation. However, for off-center loops, dynamical phases are not cancelled. Second, the spin-echo sequence requires a stable magnetic field, which, depending on the level of stability, can be challenging to technically achieve. While neither issue is insurmountable, it is prudent to consider whether there exists a simpler alternative. To this end, we examined a technique for Bloch state tomography using Wilson lines in Chapter 6.

By appropriately choosing the magnitude of the force, we realized strong-gradient dynamics that are described by the Wilson line operator and measured its elements in the basis of the band eigenstates. We noted that, although Wilson lines are generally path-ordered, they are in fact path-independent in the  $s$ -bands of the honeycomb lattice, where the Hilbert subspace is the same at all quasimomenta. This simplification enabled us to relate the Wilson line elements to an overlap between cell-periodic Bloch functions and thereby map the geometric structure of the bands over the entire Brillouin zone. We noted that even in more complex band structures where the Hilbert space is quasimomentum-dependent, the same experimental techniques can be used. To characterize such bands, we would reconstruct Wilson-Zak loops (in the basis of the band eigenstates) and access the eigenvalues. As a proof-of-principle, we demonstrated the reconstruction of a single Wilson-Zak loop in our standard honeycomb lattice. We showed that, although the band eigenstates change, the Wilson-Zak loop eigenvalues remain the same when inversion symmetry is broken, corroborating the fact that these eigenvalues identify the topological nature of the bands.

The Wilson line technique is a convenient and straight-forward way to characterize band structures. It does not require a magnetic field, can be readily used to probe the entire Brillouin zone, and occurs at relatively fast time-scales which is advantageous for heating issues. However, a main limitation is the requirement of the strong-gradient condition. In other words, the technique is only applicable in band structures that contain a set of bands which are well-separated from other bands. This naturally occurs in lattices with multiple sites per unit cell, such as, for example, our familiar honeycomb lattice, the Lieb lattice, or the Kagome lattice [159]. However, in alignment with the more general goal of band structure engineering, it may also be possible to create band structures that fulfill this condition.

## 7.1. Outlook

Equipped with our new detection techniques, the next goal is to engineer band structures with the desired geometric or topological features. To this end, we have started

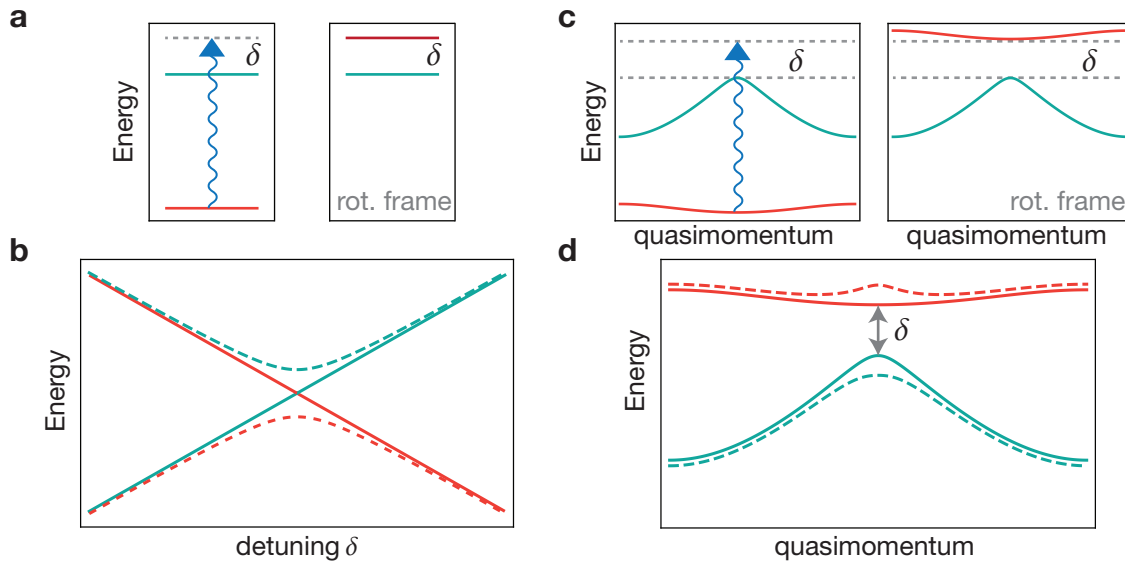


Figure 7.1.: **An analogy between coupling a two-level atom and two energy bands.** **a**, Two energy levels (red and green bars) of an atom are coupled by an electromagnetic field (blue arrow). Here, we show a field that is blue-detuned by  $\delta$  from the atomic resonance. Right: Depiction of energy levels in a frame co-rotating with the electromagnetic field, where the ground state (red) is shifted up in energy by the field frequency. **b**, Eigenenergies of the bare atomic Hamiltonian (solid lines) and coupled Hamiltonian (dashed lines) as function of detuning. **c**, Two energy bands (red and green) are coupled by a time-periodic modulation of the lattice (blue arrow). Here, we show a modulation frequency blue-detuned by  $\delta$  from the  $\Gamma$  point. Since the energy bands are quasimomentum-dependent, the modulation becomes more detuned at quasimomentum away from  $\Gamma$ . For clarity, the lowest two bands of a 1D lattice are depicted. However, the same picture applies to the more complex band structure of, e.g., a honeycomb lattice. Right: Energy bands in a frame co-rotating with the modulation. **d**, Energy bands of the static lattice (solid lines) and the modulated lattice (dashed lines) as function of quasimomentum. Note that the dashed red band exhibits two minima.

to investigate the effect of time-periodic modulations of the phase and intensity of the lattice beams. To form an intuition for how time-periodic modulations changes the band structure, we draw an analogy to the problem of a two-level atom coupled by a semi-classical electromagnetic field, as depicted in Fig. 7.1a. By applying the rotating-wave approximation and entering a frame co-rotating with the field, we obtain a time-dependent Hamiltonian parametrized only by the detuning and the coupling strength [160].

When there is no coupling, the eigenstates of this time-dependent Hamiltonian are simply the bare atomic states and, at zero detuning, the eigenenergies are degenerate (see Fig. 7.1b). When there is coupling, the new eigenstates, which are commonly called the dressed states, are superpositions of the bare atomic states. Furthermore, the degeneracy at zero detuning is broken. Hence, by coupling the ground and excited

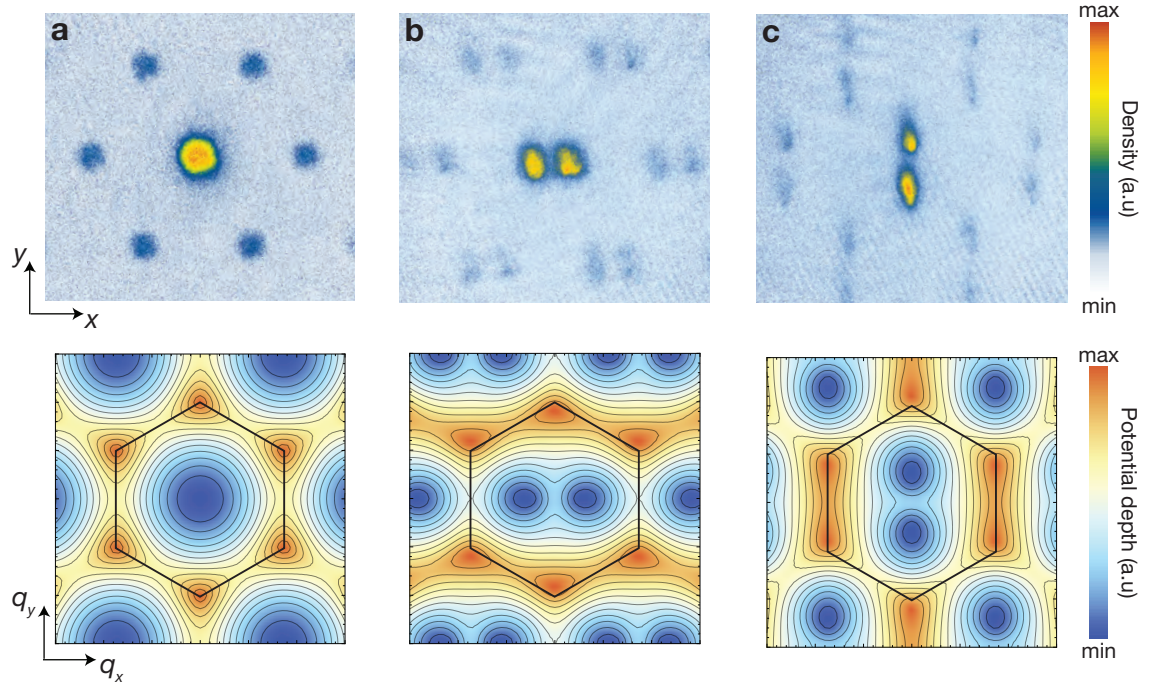


Figure 7.2.: **Modifying the energy bands with frequency modulation.** Top row: TOF images of  $^{39}\text{K}$  after sudden shut-off of optical potentials. Bottom row: Calculated dispersion of the lowest band overlaid with the first Brillouin zone (black hexagon). In the static lattice (a), atoms in the first band occupy the single dispersion minimum at  $\Gamma$ . In contrast, shaking the lattice along the  $x$ -direction (b) creates two minima along  $q_x$  and shaking along the  $y$ -direction (c) creates two minima along  $q_y$ . We observe a splitting of the atomic cloud along the corresponding directions. In both cases, the amplitude of the shaking was ramped up over several hundred cycles, with a maximum amplitude corresponding to a peak-to-peak movement of around  $0.4k_L$  in the Brillouin zone. We used a shaking frequency of 84 kHz, which is slightly blue-detuned from the first to sixth band resonance of 78 kHz in a lattice of depth  $7.4E_r$ .

states, we obtained new eigenstates with different eigenenergies. The idea for modifying our energy bands is similar: by coupling two (static) energy bands, we obtain new eigenstates with a different dispersion relation.

### 7.1.1. Preliminary experiments

In these preliminary experiments, we use both time-periodic frequency and amplitude modulation to couple the energy bands. Each experiment begins by adiabatically loading a  $^{39}\text{K}$  BEC tuned to a scattering length of  $6a_0$  into a lattice of depth  $V_0 \approx 7E_r$ . If our modulation frequency is near resonance with the energy splitting between two chosen bands and the coupling is weak, the situation is similar to the two-level atom picture (see Fig. 7.1c). However, in contrast to the case of the two-level atom where

the detuning is a tunable attribute of the applied electromagnetic field, the detuning in the band structure is parametrized by the quasimomentum. That is, due to the quasimomentum-dependence of the energy bands, a given modulation frequency naturally results in a quasimomentum-dependent detuning. In Fig. 7.1d, we schematically depict coupling two bands with a frequency slightly blue of the energy gap at  $\Gamma$  to create a "dressed state" band with two minima. This has been already been experimentally achieved in a 1D lattice [68].

In our first experiment, we modulate the frequency of the lattice beams at a frequency slightly blue-detuned of frequency gap between the first and the sixth band at  $\Gamma$ . Similar to the 1D experiment [68], this creates a dispersion with two minima. After loading the BEC, we "shake" the lattice along one direction for roughly 10 ms, which corresponds to approximately 1000 modulation cycles. Here, "shaking" the lattice means that the entire lattice potential is moving back and forth<sup>1</sup>. Next, we abruptly shut off all optical potentials and image the atoms after TOF. In contrast to TOF images from a static lattice, we see atoms occupy two distinct minima, which clearly indicates a modified dispersion relation (see top row of Fig. 7.2). The direction along which the cloud splits depends on the direction of the shaking and is in good (qualitative) agreement with theory (bottom row of Fig. 7.2).

In addition to the modified dispersion relation, a second signature of coupling between bands is the presence of Rabi oscillations. Similar to the two-level atom, where the population oscillates between the ground and the excited state, we expect the population to oscillate between the ground band and the coupled band. Indeed, we observe oscillations between bands when modulating either the frequency or the amplitude of the lattice beams. We show a typical Rabi oscillation in Fig. 7.3, where the amplitude of a single beam was modulated resonant to the energy gap between the first and third band at  $\Gamma$ . In order to selectively transfer atoms into only the third band, we imbalanced the power of one beam relative to the other two. This breaks the  $C_3$  symmetry of the lattice and lifts the degeneracy between the third and fourth bands at  $\Gamma$ . We confirmed that the atoms populated primarily the third band by band mapping.

Beyond qualitative observations, the two-level atom analogy also helps in deriving an expression for the Rabi frequency of our system. This allows us to make quantitative comparisons between theory and experiment. We begin by Taylor expanding the Hamiltonian in the time-periodic perturbation. That is, if the original Hamiltonian is  $H(V)$ , then our modulated Hamiltonian is  $H(V + \epsilon \cos(\omega t))$ , where  $V + \epsilon \cos(\omega t)$  represents the potential with a periodic modulation,  $\omega$  is the frequency of the modulation and  $\epsilon$  gives the amplitude of the modulation. Here, we have made no assumption on the type of modulation— $\epsilon \cos(\omega t)$  can refer to either frequency<sup>2</sup> or amplitude modu-

<sup>1</sup> Recall from Sec. 4.3.2 that changing the frequency of a given lattice beam shifts the entire potential along the propagation direction of that beam. Accordingly, sinusoidal modulation of the frequency of a lattice beam "shakes" the potential back and forth.

<sup>2</sup> In the specific case of frequency modulation, this formalism can be connected to the equations of motion we derived in Sec. 2.2.2. There, we saw that the coupling between bands was given by the

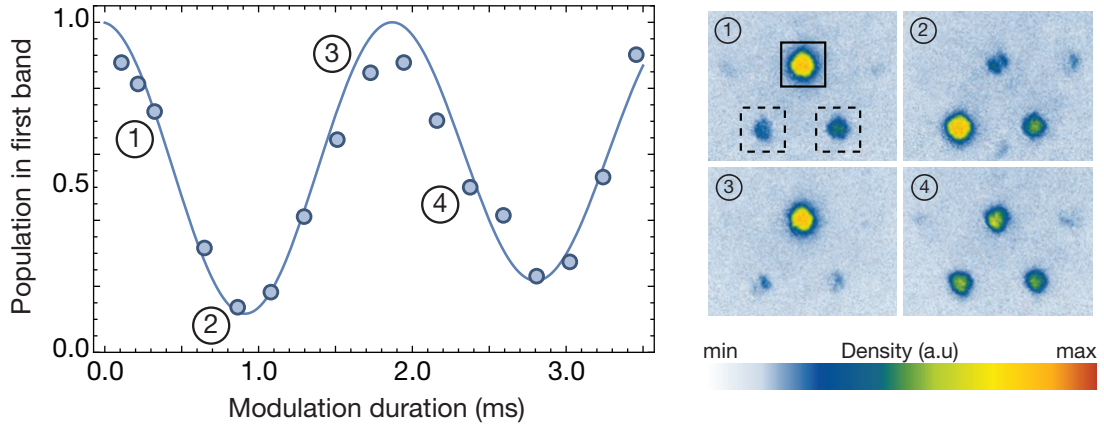


Figure 7.3.: **Rabi oscillations due to amplitude modulation.** We observe Rabi oscillations between the first and third band when resonantly modulating the amplitude of a single beam in an imbalanced lattice. Data was taken in a lattice of depth  $7.8E_r$  (when all beams are at equal intensity.) To create the imbalance, the intensity of one beam was lowered to 0.85 times the intensity of the other two beams. We fit the data and obtain a Rabi frequency of  $530(10)$  Hz, where the error is the fit error. To confirm that the atoms indeed populate only the third band, we band map along the  $q_y$  direction at  $(0, 0.4k_L)$ . This enables us to distinguish between third and fourth band atoms. In the band mapped images, the solid box denotes the position of first band atoms and the dashed box denotes the position of third band atoms.

lation. Expanding  $H(V + \epsilon \cos(\omega t))$  about  $\epsilon = 0$  yields:

$$H(V + \epsilon \cos(\omega t)) = H(V + \epsilon \cos(\omega t)) \Big|_{\epsilon=0} + \frac{\partial H}{\partial \epsilon} \Big|_{\epsilon=0} \epsilon + \frac{1}{2} \frac{\partial^2 H}{\partial \epsilon^2} \Big|_{\epsilon=0} \epsilon^2 + \dots \quad (7.1)$$

We keep only the term linear in  $\epsilon$ , which is valid when the modulation is small. Notably, this linear term is proportional to  $\cos(\omega t)$ . That is, it looks very similar to the coupling between the atomic dipole operator and the electromagnetic field. Then, using our familiarity with the two-level atom problem, we can simply write down the Rabi

---

product of the non-Abelian Berry connection and the constant applied force. When the force is instead time-periodic, the same equations apply and the coupling is instead given by

$$\mathbf{A}_{\mathbf{q}(t)}^{1,2} \cdot \mathbf{F}_0 \cos(\omega t),$$

where  $\mathbf{F}_0$  is the maximum force and  $\omega$  is the modulation frequency. Solving these equations of motion yield the same dynamics as the Taylor expansion method.

frequency  $\Omega$  coupling the two bands as<sup>3</sup>

$$\Omega = \frac{\epsilon}{\cos(\omega t)} \left. \frac{\partial H}{\partial \epsilon} \right|_{\epsilon=0}. \quad (7.3)$$

Remarkably, this simple calculation yields Rabi frequencies that are well-matched by experiment. For example, the data in Fig. 7.3 yields a Rabi frequency of 530(10) Hz, which is well within the predicted range of 465 Hz to 775 Hz for a modulation depth of 2.0(5)%.<sup>4</sup>

### 7.1.2. Next steps

Our preliminary experiments demonstrate coherent coupling between bands of the honeycomb lattice. As a next step, we would like to more thoroughly follow-up on these encouraging results. For example, it would be interesting to examine how the symmetry of the modulation influences which bands can be coupled. In a monoatomic lattice, the parity of the Bloch states determines which bands can be coupled with frequency or amplitude modulation [161]. Understanding the corresponding "selection rules" in the honeycomb lattice, which has two sites per unit cell, informs us whether to use phase or amplitude modulation or perhaps a combination of both to couple to the desired band.

This coherent control could subsequently be used to observe quantum optics phenomena, such as electromagnetically-induced transparency [162], in the bands of an optical lattice. Furthermore, coherent transfer of atoms into a higher band with nearly unit efficiency allows for the exploration of orbital physics [163]. Moreover, we could investigate flat band physics [94, 164, 165] by transferring atoms into the  $p$ -bands of the honeycomb lattice, which contain flat bands [166, 167], and adding interactions via Feshbach resonances. These directions all require first examining the lifetime of the atoms in the higher bands.

More closely related to the contents of this thesis, coherent coupling between bands may also offer a promising way to realize path-dependent and possible non-abelian Wilson lines. The experiments in this thesis took place entirely within the  $s$ -bands

<sup>3</sup> Explicitly: Let the potential and perturbation be  $f = V + \epsilon \cos \omega t$ . Then,

$$\left. \frac{\partial H}{\partial \epsilon} \right|_{\epsilon=0} \epsilon = \left. \frac{\partial H}{\partial f} \frac{\partial f}{\partial \epsilon} \right|_{\epsilon=0} \epsilon = \left. \frac{\partial H}{\partial f} \right|_{\epsilon=0} \epsilon \cos \omega t. \quad (7.2)$$

This looks very similar to the coupling  $\mathbf{d} \cdot \mathbf{E} \cos \omega' t$  between the dipole moment of an atom  $\mathbf{d}$  and the electric field  $\mathbf{E} \cos \omega' t$ , where  $\mathbf{E}$  gives the amplitude and polarization of the electric field and  $\omega'$  is its frequency.

<sup>4</sup> At the time the data was taken, our primary experimental uncertainty was the modulation depth because of some technical issues. After resolving these problems, a more recent measurement yielded a Rabi frequency of 616(6) Hz compared to the predicted value of 619 Hz.

of the honeycomb lattice, where the Hilbert subspace is the same at every quasimomentum, and, as a consequence, the Wilson lines are path-independent. To create a quasimomentum-dependent Hilbert subspace, we could couple an  $s$ -band to a  $p$ -band. This introduces a quasimomentum-dependent admixture of  $p$ -band character into the two lowest bands of the honeycomb lattice.

In addition to schemes that rely on coupling to higher orbital bands, we are also currently investigating the possibility of realizing path-dependent Wilson lines by introducing a spin degree of freedom. These experiments would require a spin-dependent lattice and coupling between both the  $s$ -bands and the spin states. The main challenge in either case of using spin states or higher orbital bands is to ensure that the strong-gradient condition can still be fulfilled in the modified band structure.

In a broader context, our investigations into time-periodic modulations of the lattice are ultimately directed toward engineering the band geometry. While our two level analogy provides some intuition on how the dispersion of the bands are modified, Floquet theory is required for a full analysis. Floquet theory encompasses our simple two-level picture and is a general framework where a time-periodic Hamiltonian is mapped onto an effective time-independent Hamiltonian, commonly called the Floquet Hamiltonian [65, 168]. It has recently been shown, both theoretically and experimentally, that Floquet Hamiltonians can have different topological properties from the original, static Hamiltonian [67, 168]. For example, in ultracold atom systems, Floquet theory underlies the recent work on the Haldane model [55] and the experiments realizing strong artificial magnetic fields in optical lattices [56, 62, 63, 169, 170]. Therefore, reinterpreted in terms of Floquet theory, our investigations into the details of amplitude and frequency modulation are directly relevant for engineering the geometry of band structures.

### 7.1.3. Future endeavors

Beyond our more immediate goals, which can all be described within a single-particle framework, lies the exciting prospect of exploring phenomena that arise from the interplay between topology and strong interactions. One such example is the paradigmatic fractional quantum Hall effect [171–173], where elementary excitations can host fractional charges and obey anyonic statistics, which are neither bosonic nor fermionic [174, 175]. An experimental observation of non-abelian anyonic statistics would be a breakthrough step toward topological quantum computing [176]. Furthermore, while the fractional quantum Hall effect, like its integer counterpart, occurs at strong magnetic fields and low temperatures, similar states, called fractional Chern insulators, are predicted to exist at zero magnetic field and room temperatures [177, 178]; they have, however, not yet been experimentally realized. Finally, another intriguing direction could be the investigation of topological Mott insulators, where interactions induce the transition into a topological phase [9, 179].

In all of these endeavors, control over the interactions between particles is central.

This requirement is fulfilled in our ultracold atom systems by Feshbach resonances, which can be used to continuously tune interactions over a wide range [38]. In concert with Floquet theory, this gives us the necessary tools with which to engineer topological systems with strong interactions. However, one primary challenge is to understand the heating rates in periodically-modulated lattice systems. Indeed, in our preliminary experiments with amplitude and phase modulation, we used  $^{39}\text{K}$  atoms tuned to a low scattering length for precisely this reason. Initial tries with  $^{87}\text{Rb}$ , which does not have an easily accessible Feshbach resonance, resulted in significant heating in the modulated lattice.

At present, the modulation-induced heating seen in experiments [62, 180] is poorly understood. However, in recent years, there have been an increasing number of theoretical investigations into the topic [181–189]. In parallel, experiments [190], including ours, have begun systematic studies into heating rates with various lattice and modulation parameters. A better understanding of the interaction effects in driven systems and the identification of optimal modulation regimes are essential to the ultimate goal of exploring strongly-interacting topological systems with ultracold atom systems.



# Appendix A.

## Experimental details

We begin this section by describing details of the vacuum setup, coil configuration, and laser system. In particular, we explain the reasoning behind several main design decisions and note the vendors from which we purchased key components.

Next, we outline our experimental sequence. Creating BECs is, by now, quite standard fare. Rather than review the mechanisms of each step here, we instead comment on the specifics of our sequence. Reviews on the preparation of BECs can be found in Refs. [111, 191, 192]. Technical details can be found in Refs. [161, 193–195]. A comprehensive overview of our setup can be also found in Ref. [78], which additionally discusses the preparation of degenerate Fermi gases of  $^{40}\text{K}$  in our setup. Refs. [196, 197] discuss the construction and characterization of our  $2\text{D}^+$ -MOT and Ref. [198] details the set-up of the laser system for our dipole trap.

### A.1. The vacuum setup

The vacuum system consists of three chambers (see Fig. A.1a): the  $2\text{D}^+$ -MOT, the 3D-MOT, and the experiment cell. Each of these chambers is connected by a differential pumping section, which enables a gradient of progressively lower pressure from the  $2\text{D}^+$ -MOT to the experiment cell. A low pressure is desirable in the science cell to limit heating due to collisions with background atoms.

In the  $2\text{D}^+$ -MOT, which is connected to our sources of rubidium (Rb) and potassium (K), the pressure is  $5 \times 10^{-5}$  mbar. Our source of Rb was purchased from Alfa Aesar and contains its two naturally occurring bosonic isotopes,  $^{85}\text{Rb}$  and  $^{87}\text{Rb}$ , in a respective relative abundance of 72.2% and 27.8% [99]. Our source of K was purchased from Trace Sciences and is enriched to contain 3% of fermionic  $^{40}\text{K}$ , 9% of bosonic  $^{41}\text{K}$ , and 88% of bosonic  $^{39}\text{K}$ . These sources are contained in heated bellows which are connected to the main  $2\text{D}^+$ -MOT chamber via a six-way cross, as shown in Fig. A.1b. The valves were opened during the initial setup of the apparatus several years ago but are currently closed.

The  $2\text{D}^+$ -MOT and its optics were built on a separate breadboard and are connected to the 3D-MOT by a valve and a flexible bellow. The idea was to be able to slightly shift the entire  $2\text{D}^+$ -MOT apparatus relative to the 3D-MOT, in case the push beam of the

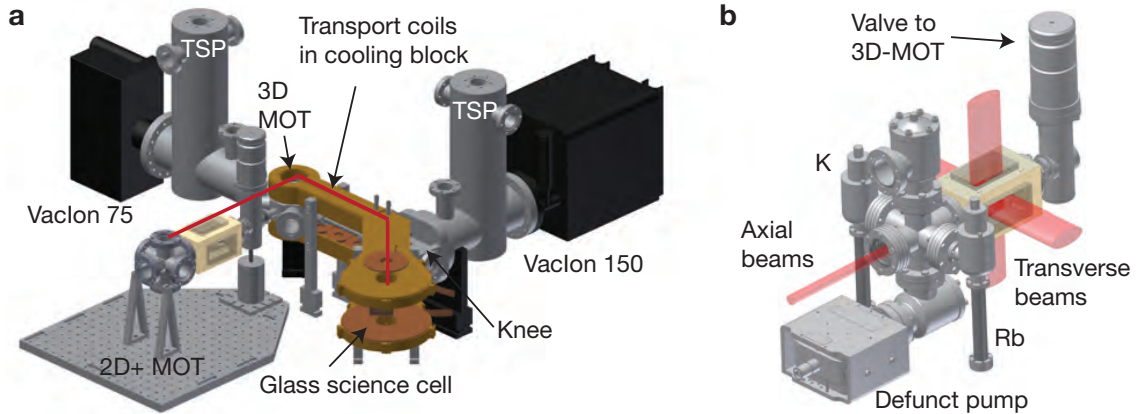


Figure A.1.: **Apparatus overview and the 2D<sup>+</sup>-MOT.** **a**, The entire experimental apparatus. Atoms begin in the 2D<sup>+</sup>-MOT (for a complete 2D<sup>+</sup>-MOT drawing, see **b**). They are pre-cooled and then travel through a short differential pumping section to the 3D-MOT chamber. There, the atoms are further cooled and then magnetically transported through a longer differential pumping section and the "knee." Finally, they end up in the experiment cell where evaporative cooling takes place. The pressure in the 3D-MOT chamber is maintained by a Vaclon 75 ion pump. After the differential pumping section, the pressure in the knee and experiment cell areas are maintained by a Vaclon 150 ion pump. We additionally use TSPs in each cylindrical chamber between the ion pumps and the main apparatus. In the drawing, the TSPs are not drawn. We show only the top opening of the cylindrical chamber into which the TSPs are inserted. **b**, A close-up of the complete 2D<sup>+</sup>-MOT with beams. Two pairs of elliptical transverse cooling beams enter the chamber windows. Axially, we send in a push beam and a third cooling beam that is retroreflected by a mirror at the end of the chamber (see Fig. A.3). The mirror has a hole drilled in its center to allow atoms and the push beam to pass through into the 3D-MOT chamber. The valve between the 2D<sup>+</sup>-MOT and 3D-MOT chambers is open. The valve between the 2D<sup>+</sup>-MOT chamber and the ion pump is now closed, as the pump is no longer operational.

2D<sup>+</sup>-MOT hit the 3D-MOT cloud. In the 3D-MOT, the pressure is  $9 \times 10^{-11}$  mbar. In the experiment cell, the pressure is  $5 \times 10^{-12}$  mbar.

The pressure in these chambers are maintained by several vacuum pumps, as labeled in Fig. A.1a. The 2D<sup>+</sup>-MOT was initially pumped by a TiTan 10S Ion Pump from Gamma Vacuum, but the pump soon started drawing overly high currents and shut down. We suspect the problem may be that Rb coated the ceramic insulators on the pump. Currently, the pump is turned off, and the valve connecting the pump to the rest of the apparatus is closed. The 3D-MOT chamber pressure is maintained by a Vaclon 75 ion pump and the knee (i.e., the piece between the differential pumping tube and the glass cell) and experiment cell pressure is maintained by a Vaclon 150 ion pump. Additionally, we insert titanium sublimation pumps (TSPs) into the cylindrical chambers.

The 3D-MOT chamber, differential pumping tube, knee, and the cylindrical pieces

housing the titanium sublimation pumps were self-designed and machined out of (non-magnetic) stainless steel by Pink GmbH Vakuumtechnik.

The main chamber of the  $2D^+$ -MOT was self-designed and machined from titanium by Vaqtec-scientific. Since the windows are directly glued onto the body of the chamber in our  $2D^+$ -MOT design, one concern was that vacuum leaks would be introduced due to material deformation when heating the apparatus. To minimize this risk, we chose titanium for the body of the chamber and BK7 glass for the windows because titanium and BK7 have similar thermal expansion coefficients.

Other vacuum components, such as bellows, valves, and flanges, were purchased from VAT Vakuumventile AG or VACOM. Flanged windows for, e.g, the 3D-MOT, were purchased from Kurt J. Lesker.

Pictures of the actual experimental apparatus are shown in Fig. A.3.

### A.1.1. The magnetic transport coils and the experiment cell

We self-wound the  $2D^+$ -MOT coils, the push coil, the experiment coils, and the bias coils around the 3D-MOT and the experiment cell. As its name suggests, the  $2D^+$ -MOT coils provide the field gradient for the  $2D^+$ -MOT. These coils were soaked in thermally conductive Electrolube ER2183 resin. The push coil is part of the magnetic transport, and the experiment coils provide the fields for the experiment cell. Each set of bias coils consist of a pair of coils along the  $x$ -,  $y$ -, and  $z$ -directions to offset, i.e., bias, the earth's magnetic field and other constant fields in the lab (from assorted metal pieces, furniture, etc.). All other coils were wound by Oswald Elektromotoren GmbH.

The main magnetic transport setup consists of a push coil, one pair of 3D-MOT coils, 15 pairs of transport coils, and one pair of experiment coils, as illustrated in Fig. A.2. The push coil is used to push the low-field seeking atoms toward the transport coils and control the aspect ratio of the atomic cloud [112, 121, 196]. This is necessary because of the relatively large distance between the centers of the 3D-MOT coils and the first set of transport coils, which results in a weak gradient along the transport direction and an elongated atomic cloud

The 3D-MOT coils and all transport coils were glued into a self-designed coil housing by Oswald Elektromotoren GmbH using Stycast FT 2850 and resined with Araldite F, which are both thermally conductive. Since we directly cool only the housing by running water through it, good thermal conductivity between the housing and the coils is crucial to keep the coils cool during experimental runs. The water flowing into the housing is temperature stabilized at  $20^\circ\text{C}$  by a Kühlmobil van der Heijden chiller. The housing was machined out of brass by the MPQ workshop.

#### The experiment coils

The design of the experiment coils required extra attention. There were certain requirements we wanted to meet: we desired a high gradient of around  $300\text{ G/cm}$  for

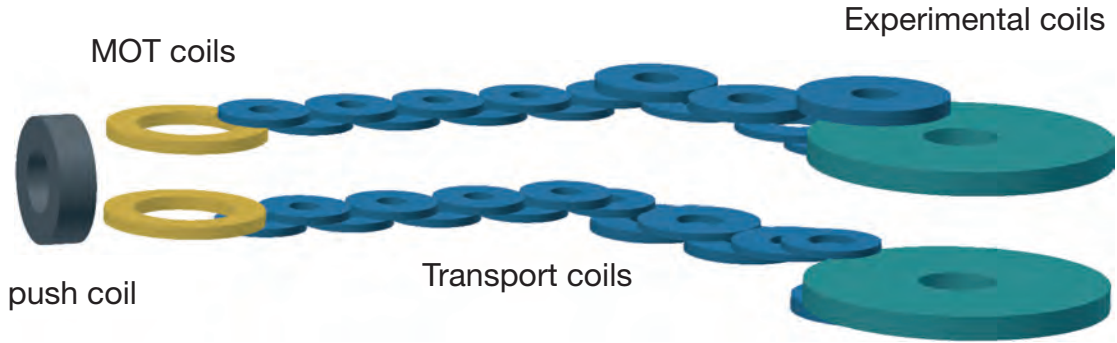


Figure A.2.: **Magnetic transport schematic.** The push coil (gray) helps to maintain the desired aspect ratio of the cloud during the initial transport between the MOT coils (yellow) and the first pair of transport coils (blue). Aptly named, the push coil creates an additional gradient that pushes the atoms toward the transport coils. Transport continues until the atoms reach the experiment cell, which is centered between the large experiment coils (green).

evaporative cooling, a homogeneous field when the coils were in the Helmholtz configuration, and a large enough inner radius such that numerical aperture of our imaging system is not limited. However, due to the shape and size of our experiment cell, the experiment coils needed to be spaced rather far apart. Since the magnitude of the magnetic field decreases with distance to the coil, reaching the desired high fields and field gradients required many windings and higher currents. Therefore, it was necessary to be particularly mindful of overheating the coils.

To optimize the thermal conductivity between the housing and the experiment coils, we created the experiment coils out of "ribbon-wire" with height 17 mm and width 0.53 mm. Although we make many radial windings, there is only a single axial winding. Therefore, every single winding is in contact with the coil housing. Furthermore, we milled the surface of the coils very flat to optimize contact with the housing and each layer of the coil was resined with Electrolube ER2183. To prevent shorts, we placed a thermally conducting foil and grease between the coil and the housing. The thermal foil was called Thermiflex TF 21209 from Dr. D Mueller Ahlhorn GmbH and the thermal grease was Duralco 134 from Polytec PT GmbH.

To hold the coils into the housing, we used clamping plates instead of glue like the other coils. Thermally conductive glue tends to be rather brittle, and we did not trust that it would hold the rather heavy coils in the long-run. We used carbon plates because they are very stiff, which ensures that even pressure is applied over the coil. Additionally, they are non-conducting, which prevents eddy currents.

### The experiment cell

The experiment cell has an angled top and side surface to avoid back-reflecting beams onto the atoms, as shown in Fig. A.3. It is made of fused quartz and terminates via a

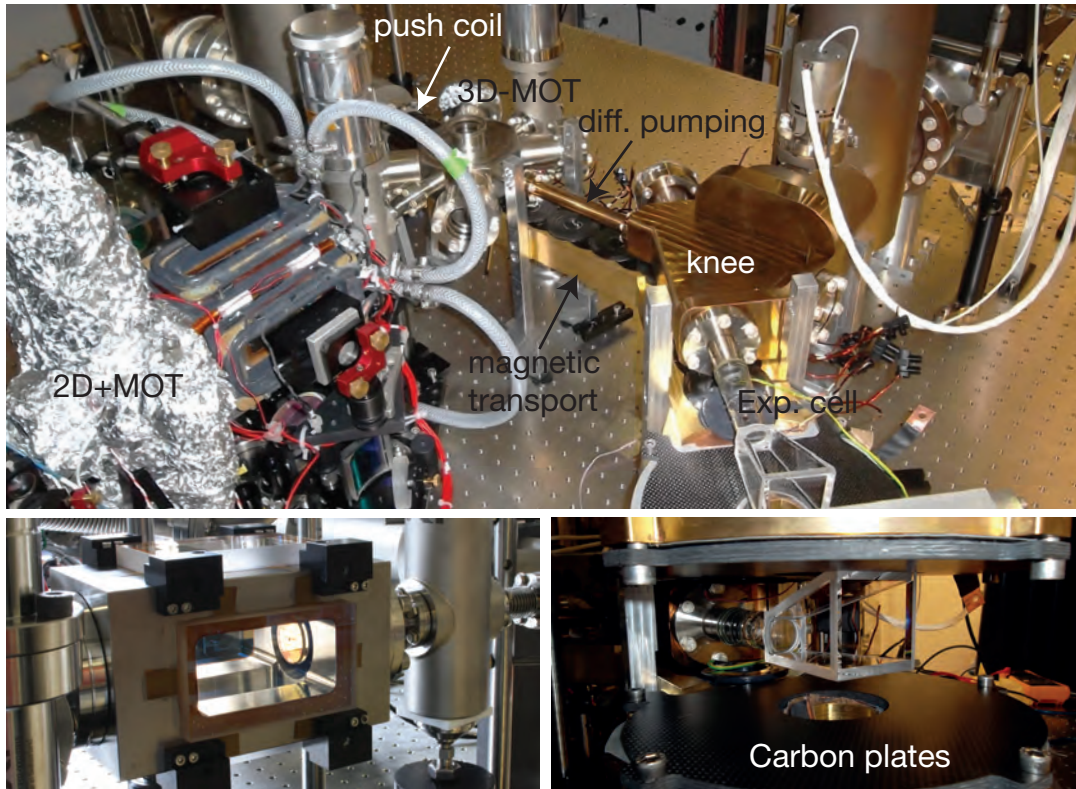


Figure A.3.: **Pictures of the experimental apparatus.** **Top:** The experimental setup without the top transport coils. The six-way cross and bellows of the  $2D^+$ -MOT are heated with heating wires and wrapped in aluminum foil. The coil holders for the  $2D^+$ -MOT coils have copper tubes soldered on top that are water-cooled. The purple-gray color is due to the resin. The push coil was wound around one "arm" of the 3D-MOT chamber. The yellowish color of the differential pumping section, knee, and cylindrical chamber is due to a high-temperature bake-out. **Bottom left:** Close-up of the  $2D^+$ -MOT chamber without the coils attached. At the end of the chamber, there is a mirror and polarizer with a hole drilled in the center. The mirror retroreflects the axial cooling beam. The hole allows atoms and the push beam to enter the 3D-MOT chamber. **Bottom right:** Close-up of the experiment cell and carbon plates, which clamp the experiment coils into the coil housing.

glass-to-metal seal in a metal flange that can be directly connected to the knee. The cell was self-designed and constructed by Hellma Analytics.

## A.2. The laser setup

### A.2.1. Cooling in the 2D<sup>+</sup>-MOT and 3D-MOT

We use a total of 11 lasers to cool <sup>87</sup>Rb and <sup>39</sup>K in the 2D<sup>+</sup>-MOT and the 3D-MOT. For cooling <sup>87</sup>Rb, we have one reference laser, two repump lasers (one for each MOT), and two cooling lasers (one for each MOT). The reference and repump lasers are Toptica DL Pros centered at 780 nm and have about 50 mW of output power. The cooling lasers are Toptica TA Pros (also centered at 780 nm) and have about 1 W of output power.

The hyperfine levels of the D2 line for <sup>87</sup>Rb are shown in Fig. A.4 and labeled with the relevant transitions. The reference laser is so-called because it is the laser to which the frequency of all the other lasers are referenced. To stabilize the frequency of the reference laser, we use Doppler-free absorption spectroscopy and a frequency-modulation lock. All other lasers are locked using a delay-line lock which stabilizes the frequency difference between a laser and the reference laser. In addition to being a frequency reference, the reference laser is also used to spin polarize the atoms into  $|F = 2, m_F = 2\rangle$  state for magnetic transport and to image the atoms in the experiment cell.

The lasers used to cool <sup>39</sup>K are very similar. We have one reference laser, two repump lasers, two cooling lasers, and one imaging laser. The reference and imaging lasers are Toptica DL Pros and the cooling and repump lasers are Toptica TA Pros. These lasers are centered at 767 nm. The reason for using tapered-amplifier (TA) lasers with greater power for the repump light can be understood by considering the hyperfine splittings for <sup>39</sup>K, as shown in Fig. A.4. Compared to the hyperfine splittings of <sup>87</sup>Rb, those of <sup>39</sup>K are around an order of magnitude smaller. In fact, the detuning of both the repump and cooling laser is roughly on the same order of magnitude as the hyperfine splitting. Consequently, the assumption of a cycling transition on the cooling line is not quite valid; compared with the cooling transition of <sup>87</sup>Rb, more atoms are being pumped into the  $|4^2S_{1/2}, F = 1\rangle$  state and a greater repump intensity is required.

The light from the reference K laser is used only for locking purposes. The light from the imaging K laser is primarily used for imaging the atoms in the experiment cell, but a few mW is also used to spin polarize the atoms for magnetic transport.

All the lasers for the 2D<sup>+</sup>-MOT and 3D-MOT are on a separate optical table from the experimental apparatus. The light is sent to the experiment via single-mode, polarization maintaining fibers made by Nufern and sold by Thorlabs.

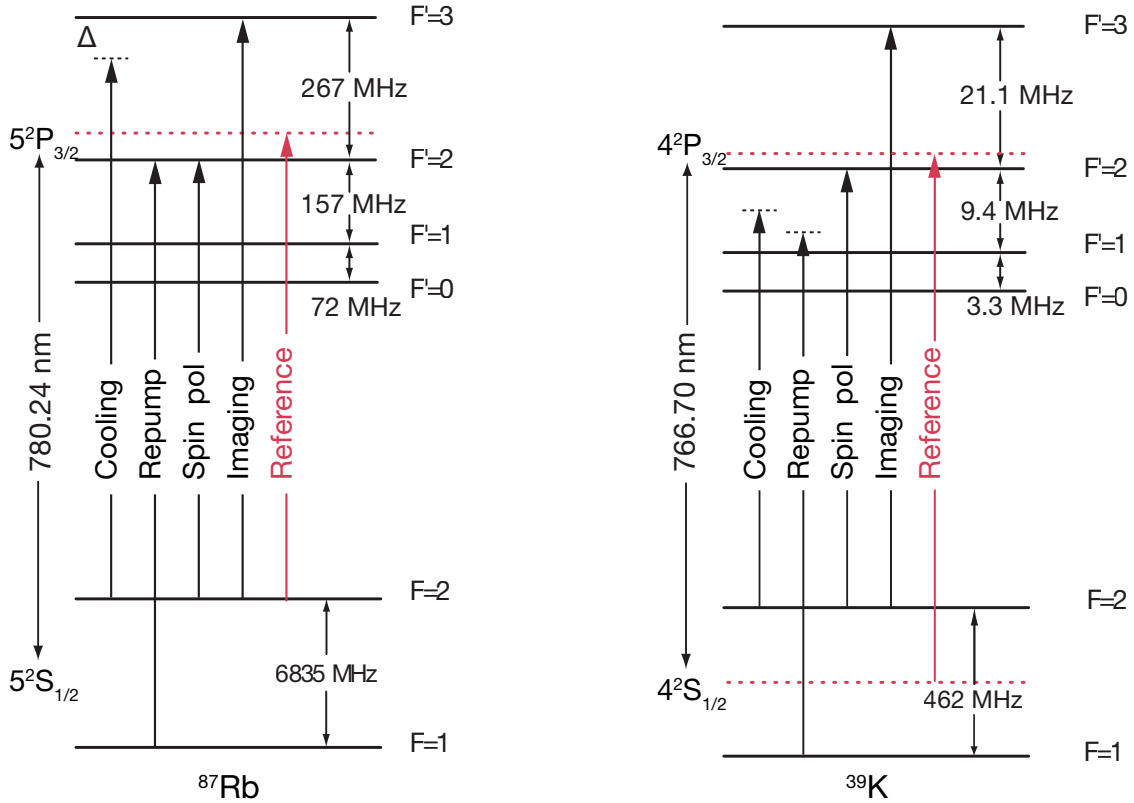


Figure A.4.: **Hyperfine structure of the D2 lines of  $^{87}\text{Rb}$  and  $^{39}\text{K}$  with experimental transitions.** Hyperfine structure from Refs. [99, 199]. Technical details on the locking and spectroscopy can be found in Ref. [193].

### A.2.2. Optical dipole trap and lattice lasers

To create the optical dipole trap at 1064 nm, we use a Nufern laser seeded by a Mephisto laser. The light is sent to experiment via high-power fibers from NKT Photonics. On the experiment table, we usually have around 2 W of dipole power.

The lattice laser used for the experiments in this thesis was an MBR110 single-frequency Ti:Sapphire laser pumped by a 10 W Verdi laser at 532 nm. Both lasers were purchased from Coherent. The total output power at 755 nm was 1.4 W. We have since replaced this laser with an MSquared Ti:Sapphire laser pumped by an 18 W Sprout laser from Lighthouse Photonics. At 740 nm, the total output power is around 6 W.

The lattice light is sent in three separate fibers to the experiment table for the three lattice beams. We use single-mode, polarization maintaining fibers from Thorlabs with a reinforced fiber tip from Diamond SA.

### A.3. The experimental sequence

We now outline the experimental sequence.

#### 2D<sup>+</sup>-MOT and 3D-MOT

MOTs combine red-detuned beams and a magnetic quadrupole trap to cool and trap the atoms. The relevant transitions used to cool <sup>39</sup>K and <sup>87</sup>Rb in the MOTs are shown in Fig. A.4. More information on MOTs can be found in, e.g., Refs. [111, 200, 201].

In our setup, thermal atoms are first pre-cooled in the 2D<sup>+</sup>-MOT. 2D<sup>+</sup>-MOTs work under the same principles as the standard 3D-MOTs, with the exception that there is a magnetic quadrupole field only along the radial directions such that the atoms are free to propagate along the axial direction into the 3D-MOT [105–108, 110, 202]. The "+" in the 2D<sup>+</sup>-MOT refers to having a cooling beam along the axial direction, in addition to the standard pair of counterpropagating cooling beams along the transverse directions [110]. The axial cooling is realized in our setup by sending in an axial beam that then reflects off a mirror, as shown in Fig. A.3. We also use a push beam in the axial direction to increase the flux into the 3D-MOT.

Our 3D-MOT is standard and consists of three pairs of counterpropagating beams and a magnetic quadrupole trap created by a pair of coils in the anti-Helmholtz configuration.

- When cooling <sup>87</sup>Rb, the duration is 1 s.
- When cooling <sup>39</sup>K, the duration of the <sup>87</sup>Rb MOT is 8 s and the duration of the <sup>39</sup>K MOT is 0.6 s. We find that our <sup>39</sup>K condensates are larger when we start first loading <sup>87</sup>Rb and then only load <sup>39</sup>K near the end of the loading time. Our neighboring lab has found the opposite to be true [194].

#### Compressed MOT

In compressed MOTs (cMOTs), both the detuning of the light and the strength of the quadrupole gradient is increased to increase the phase space density [203]. We employ a cMOT only when cooling <sup>39</sup>K. The duration of the cMOT is 5 ms. In addition to detuning the frequencies of the K and Rb lasers, the power of the K lasers for repumping and cooling in the 3D-MOT are also decreased. Our cMOT parameters were found by using a Limited Individual Lifetime Differential Evolution (LILDE) algorithm [204, 205].

#### Optical molasses

To further cool the atoms, we turn off all magnetic fields and cool only with far-detuned light. This configuration is termed an optical molasses or polarization gradient cooling and can be used to reach sub-Doppler temperatures for <sup>87</sup>Rb. However, the process is not as efficient for <sup>39</sup>K due to its small hyperfine splittings [108, 206].

- When cooling  $^{87}\text{Rb}$ , the duration is 3 ms. We increase the detuning (more red) and decrease the power of the Rb 3D-MOT cooling laser.
- When cooling  $^{39}\text{K}$ , the duration is 4.2 ms. We increase the detuning (more red) and decrease the power of the Rb 3D-MOT cooling laser, the K 3D-MOT cooling laser, and the K 3D-MOT repumping laser. We found it particularly crucial to decrease the power of the K 3D-MOT cooling laser.

### Spin polarization

In this step, we pump the atoms into their  $|F = 2, m_F = 2\rangle$  state in preparation for transport. Since only low-field seeking atoms are magnetically trappable, omitting this step would result in the loss of many atoms during magnetic transport. This procedure is also called optical pumping.

The basic idea is to use a small offset field along, in our case, the  $z$ -axis to define a quantization axis and lift the degeneracy between magnetic sublevels. We then apply  $\sigma^+$ -polarized light resonant on the  $F = 2$  to  $F' = 2$  transition to induce transitions that increase the magnetic sublevel number. We also use  $\sigma^+$ -polarized repump light address atoms that decay into the  $F = 1$  manifold. This optical pumping is quite efficient for both  $^{87}\text{Rb}$  and  $^{39}\text{K}$ . We end up with around 70% to 80% of both species in the  $|F = 2, m_F = 2\rangle$  state.

These parameters were optimized using LILDE.

- For only  $^{87}\text{Rb}$ , the optical pumping duration is 0.7 ms.
- For  $^{39}\text{K}$ , the optical pumping duration is 0.8 ms for  $^{87}\text{Rb}$  and 0.5 ms for  $^{39}\text{K}$ .

### Magnetic transport

After the spin polarization, we suddenly switch on a magnetic quadrupole field in the 3D-MOT to a gradient strength of 45 G/cm to trap the atoms. As an additional precaution to transport primarily  $|F = 2, m_F = 2\rangle$  atoms, we then ramp down the field in 150 ms and hold at a lowered gradient of 28 G/cm for 200 ms. Holding at this lowered gradient ensures that  $^{87}\text{Rb}$  atoms in  $|F = 2, m_F = 1\rangle$  leave the trap, since trapping  $^{87}\text{Rb}$  atoms in  $|F = 2, m_F = 1\rangle$  requires a gradient strength of at least 30 G/cm, while trapping  $^{87}\text{Rb}$  atoms in  $|F = 2, m_F = 2\rangle$  requires only half that strength. (The gradients required for  $^{39}\text{K}$  scale with the mass and require 13 G/cm and 6.5 G/cm. We cannot use this ramp down to remove  $|F = 2, m_F = 2\rangle$   $^{39}\text{K}$  atoms.)

Next, we ramp up the quadrupole field in 200 ms to the transport gradient of 100 G/cm and move the atoms over a distance of 58 cm into the experiment cell [112, 121, 196]. We lose about 80% of  $^{87}\text{Rb}$  atoms and 95% of  $^{39}\text{K}$  atoms once we hit the differential pumping section. This is due to both the small size of the differential pumping hole and an imperfect alignment of the transport coils relative to the center of the

differential pumping section. We could resolve this issue by using higher gradients to further compress the clouds during transport or by optimizing the cooling in the MOT and molasses phase. However, since we are still able to make sufficiently large BECs of both species despite these large losses, we have not tried to further improve the transport.

The total transport from the 3D-MOT chamber to the experiment cell takes 2 s.

### Microwave evaporation in a steep quadrupole trap

As soon as the atoms reach the knee in the transport, we turn on a tightly-focused, blue-detuned beam with a waist of  $20 \mu\text{m}$  to prepare for evaporatively cooling in a steep quadrupole trap. At the center of the quadrupole trap, the magnetic field is zero and atoms can undergo spin-flips into an untrapped state [113, 114, 207]. These Majorana losses [208] can be avoided by using a blue-detuned plug beam to add a repulsive potential at the trap center, as shown in Fig. A.5a, to prevent atoms from entering regions of low or zero magnetic field.

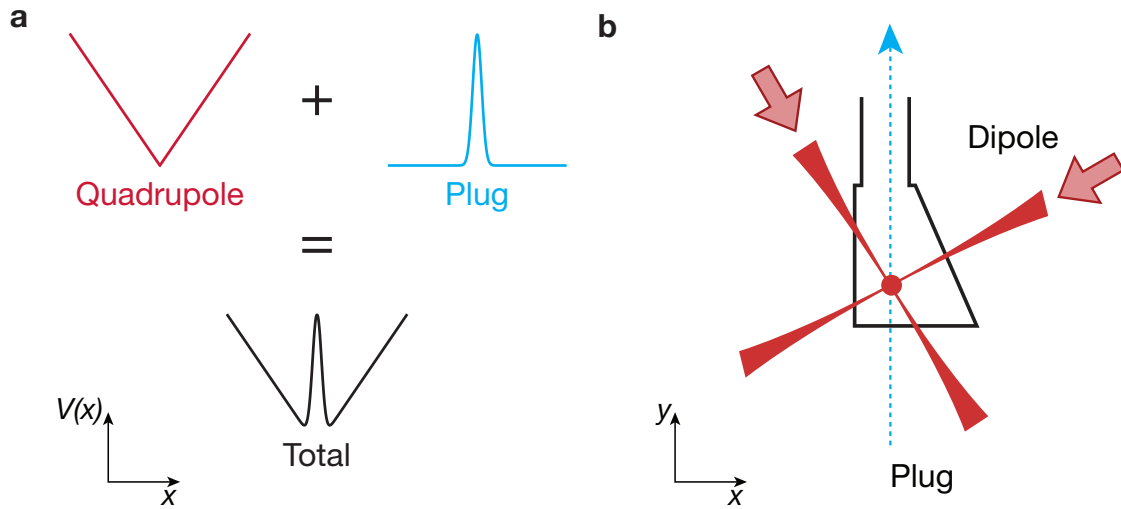


Figure A.5.: **Microwave evaporation potential and beam schematic during evaporative cooling.** **a**, At the center of the quadrupole potential (red), the magnetic field is zero. There, atoms cannot adiabatically follow the magnetic field and will undergo spin-flips to untrapped states. To resolve this issue, we add a blue-detuned plug beam (blue) such that the total potential (black) is repulsive near the trap center, thereby preventing atoms from entering regions of low magnetic field. **b**, The plug beam (blue) propagates in the same plane as the crossed dipole beams (red). The vertical dipole trap propagates into the plane of the page. Image taken from Ref. [78].

We did not find the early turn-on of this plug beam to adversely affect the transport into the experiment cell. The plug beam remains on until the magnetic quadrupole trap is turned off.

Once the atoms are in the experiment cell, we ramp up the magnetic quadrupole field to 240 G/cm in 200 ms and start microwave evaporation. In microwave evaporation, hotter atoms are selectively removed from the quadrupole trap by exploiting the position-dependent Zeeman shift due to the magnetic field gradient [209]. The microwave field induces transitions from the trapped  $|F = 2, m_F = 2\rangle$  to the untrapped  $|F = 1, m_F = 1\rangle$  state. By sweeping the microwave frequency from a high to low value, we can first address hotter atoms further away from the the trap center and then gradually address colder atoms closer to the trap center. This technique is entirely analogous to RF evaporation, which addresses magnetic sublevels within a hyperfine manifold and was used to create the first BECs [210, 211].

After the microwave evaporation, we ramp down the quadrupole trap in 470 ms. Our parameters, such as the duration and form of the microwave sweep, were optimized using LILDE.

- When cooling only  $^{87}\text{Rb}$ , the microwave evaporation takes 9 s.
- When cooling  $^{39}\text{K}$ , the microwave evaporation takes 11 s. In this case, the microwave frequencies are still tuned to address  $^{87}\text{Rb}$ , and the  $^{39}\text{K}$  atoms are cooled through thermalizing collision with  $^{87}\text{Rb}$  atoms.

### Optical evaporation

Immediately after the end of the microwave evaporation, i.e, 470 ms before the quadrupole trap ramps to zero, we ramp up the crossed dipole beams. The crossed dipole beams are highly elliptical, with a vertical waist of 35  $\mu\text{m}$  and a horizontal waist of 300  $\mu\text{m}$ . The positioning of these beams is schematically shown in Fig. A.5b. To maintain the spin-polarization, we ramp up an offset field of magnitude  $\approx 1$  G along the vertical axis in 10 ms to provide a quantization axis. The ramp-up begins 70 ms before we start ramping down the quadrupole trap.

We ramp the dipole trap to maximum power in 140 ms and then hold at maximum power for 1 s. During this hold time, 30 ms after the quadrupole trap has ramped down to zero field, we transfer the  $^{87}\text{Rb}$  atoms from the  $|F = 2, m_F = 2\rangle$  state to the  $|F = 1, m_F = 1\rangle$  state. We do this using a microwave sweep of duration 120 ms. If we are cooling  $^{39}\text{K}$ , we then similarly transfer the  $^{39}\text{K}$  atoms to the  $|F = 1, m_F = 1\rangle$  state using an RF sweep of duration 60 ms. After both species are in  $|F = 1, m_F = 1\rangle$ , we use a light pulse resonant on the  $F=2$  to  $F'=3$  transition to blow out all remaining  $|F = 2, m_F = 2\rangle$  atoms from the trap. Then, we begin the optical evaporation ramps, which are detailed below for  $^{87}\text{Rb}$  and  $^{39}\text{K}$ . In both cases, after the end of the evaporation, as the dipole trap is being ramped up to its experimental value, we additionally ramp up a vertical dipole trap in 0.4 s to provide an additional confinement in the horizontal plane. This vertical dipole trap has a waist of 180  $\mu\text{m}$ . A schematic of the optical evaporation sequence is shown in Fig. A.6.

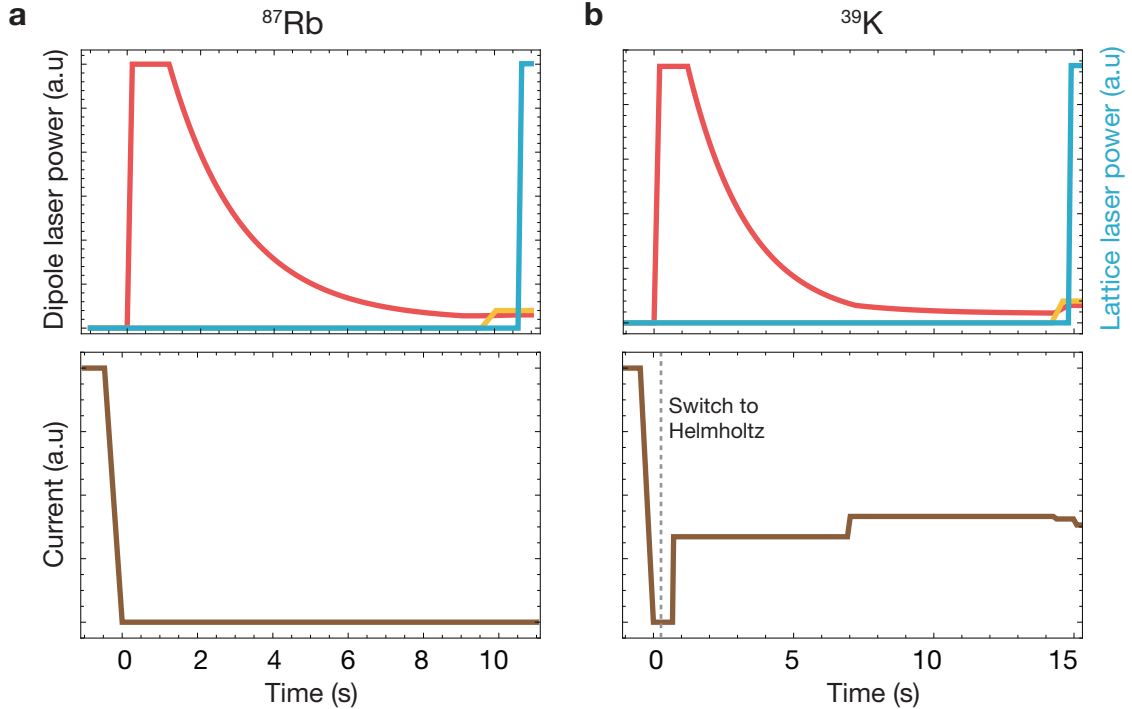


Figure A.6.: **Dipole trap intensity and current in experiment coils.** The time axis is referenced to when we begin to ramp up the power of the crossed-dipole beams (red). The schematic in **a** (**b**) details optical evaporative cooling of  $^{87}\text{Rb}$  ( $^{39}\text{K}$ ). For both atomic species, the dipole trap is ramped up immediately as the quadrupole trap current (brown) is ramped down. For  $^{87}\text{Rb}$ , after a short hold at maximum dipole power, we exponentially ramp down the power until condensation. For  $^{39}\text{K}$ , we first switch the coils into the Helmholtz configuration after the quadrupole trap ramps down (dashed line). Then, the evaporative cooling occurs in two main segments. In the first segment, we utilize a Feshbach resonance between  $^{39}\text{K}$  and  $^{87}\text{Rb}$ . In the second segment,  $^{87}\text{Rb}$  has dropped out of the dipole trap, and we ramp the Helmholtz field for an intra-species Feshbach resonance between  $^{39}\text{K}$  atoms until condensation. For both species, after a brief hold at a low power just above the trap bottom, we slightly ramp up the dipole power to its experimental value. Simultaneously, we ramp up a vertical dipole beam (yellow) to provide additional confinement in the horizontal plane. Once the horizontal and vertical dipole beams are at their experimental values, we ramp up the lattice power (blue).

Successful evaporative cooling relies on two simultaneous processes: hot atoms must leave the trap and the remaining atoms must efficiently thermalize to a lower temperature [111, 119, 212]. Thermalization occurs via collisions, which, in the low energy limit, are commonly parametrized by the  $s$ -wave scattering length  $a_s$  in units of the Bohr radius,  $a_0$ .

- When cooling only  $^{87}\text{Rb}$ , we exponentially ramp down the power of the dipole trap in 8 s, just above the trap bottom. We hold at this low power for 0.5 s during which

evaporation continues. Since the scattering length between  $^{87}\text{Rb}$  atoms is decently high at  $a_s = 100a_0$  [213, 214], the remaining atoms efficiently thermalize to a lower temperature and eventually condense. We then ramp up the dipole trap power in 1 s to the desired value for the experiments. This is usually just slightly above the trap bottom to compensate for the blue-detuned lattice.

- When cooling  $^{39}\text{K}$ , the optical evaporation requires Feshbach resonances, which utilize magnetic fields to modify the scattering lengths between particles [38] for efficient thermalization. Once the quadrupole field has been ramped down to zero, we switch the experiment coils into a Helmholtz configuration, i.e., with currents running in the same direction in both coils, to generate homogeneous fields.

After transferring both atomic species into  $|F = 1, m_F = 1\rangle$ , we turn on a field of 317 G to tune the scattering length between  $^{39}\text{K}$  and  $^{87}\text{Rb}$  atoms to  $a_s = 100a_0$  [117]. This scattering length is large enough for efficient cooling of the  $^{39}\text{K}$  atoms via thermalizing collisions with  $^{87}\text{Rb}$  atoms but still small enough to avoid excessive three-body losses [215]. At this field, we exponentially ramp down the dipole power in 6 s, ending at a trap depth where  $^{87}\text{Rb}$  atoms drop out and  $^{39}\text{K}$  atoms still remain. The  $^{87}\text{Rb}$  atoms drop out of the optical trap before the  $^{39}\text{K}$  atoms because  $^{87}\text{Rb}$  is heavier and therefore requires a higher optical potential to compensate for gravity.

Next, once the  $^{87}\text{Rb}$  atoms are gone, we utilize a second Feshbach resonance to adjust the intra-species scattering length between the  $|F = 1, m_F = 1\rangle$   $^{39}\text{K}$  atoms. We tune the field to 392 G for a scattering length of  $a_s = 110a_0$  [118] and continue to ramp down the dipole trap power for another 7 s.

In the final part of the evaporative cooling, we hold at this low dipole power, which is just above the critical trap depth for  $^{39}\text{K}$ . During this hold time, we ramp the field to 383 G for a scattering length of  $a_s = 45a_0$  because we observed atom losses at a scattering length of  $a_s = 110a_0$ .

Finally, as we ramp up the dipole trap in 0.5 s to slightly above the trap bottom to compensate for the blue-detuned lattice, we also ramp the Feshbach field to the desired interaction strength. In our experiments with  $^{39}\text{K}$ , we use a scattering length of  $a_s = 6a_0$

### Adiabatic loading into the lattice

After we have ramped up the dipole trap and the vertical dipole trap to their experimental values, we load the atoms adiabatically into the ground state of the lattice potential by ramping up lattice power in 100 ms. We then perform the experiments.

Each lattice beam has a vertical waist of 80  $\mu\text{m}$  and a horizontal waist of 350  $\mu\text{m}$ .



## Appendix B.

### Numerical calculation of the Wilson line

In our system, the equations of motion that describe the evolution of populations  $\alpha^1(t)$  and  $\alpha^2(t)$  in the first and second band in the presence of a constant external force are (see Chapter 2)

$$i\partial_t \begin{pmatrix} \alpha^1(t) \\ \alpha^2(t) \end{pmatrix} = \begin{pmatrix} E_{\mathbf{q}(t)}^1 - A_{\mathbf{q}(t)}^{11} \cdot \mathbf{F} & -A_{\mathbf{q}(t)}^{12} \cdot \mathbf{F} \\ -A_{\mathbf{q}(t)}^{21} \cdot \mathbf{F} & E_{\mathbf{q}(t)}^2 - A_{\mathbf{q}(t)}^{22} \cdot \mathbf{F} \end{pmatrix} \begin{pmatrix} \alpha^1(t) \\ \alpha^2(t) \end{pmatrix}, \quad (\text{B.1})$$

where  $\mathbf{F}$  is the applied force,  $E_{\mathbf{q}(t)}^n$  gives the energy in band  $n$  at quasimomentum  $\mathbf{q}(t)$  and  $A_{\mathbf{q}(t)}^{nm}$  gives the Berry connection between bands  $n$  and  $m$  at quasimomentum  $\mathbf{q}(t)$ .

Solving for the Wilson line transporting from quasimomentum  $\mathbf{q}(t=0)$  to quasimomentum  $\mathbf{q}(t=T)$  yields

$$\hat{\mathbf{W}}_{\mathbf{q}(0) \rightarrow \mathbf{q}(T)} = e^{-i \int_0^T \tilde{H}(t) dt}, \quad (\text{B.2})$$

where

$$\tilde{H}(t) = \begin{pmatrix} E_{\mathbf{q}(t)}^1 - A_{\mathbf{q}(t)}^{11} \cdot \mathbf{F} & -A_{\mathbf{q}(t)}^{12} \cdot \mathbf{F} \\ -A_{\mathbf{q}(t)}^{21} \cdot \mathbf{F} & E_{\mathbf{q}(t)}^2 - A_{\mathbf{q}(t)}^{22} \cdot \mathbf{F} \end{pmatrix} \quad (\text{B.3})$$

To numerically calculate the Wilson line, we compute the Trotter product of  $n$  time-independent matrices evaluated at discrete time-steps of size  $\Delta t = T/n$ :

$$\begin{aligned} \hat{\mathbf{W}}_{\mathbf{q}(0) \rightarrow \mathbf{q}(T)} &= e^{-i \int_0^T \tilde{H}(t) dt} \\ &\approx \prod_{j=1}^n e^{-i \tilde{H}(t_j) \Delta t}. \end{aligned} \quad (\text{B.4})$$

In our calculations, we use several hundred time-steps, depending on the length of the path.

In the tight-binding model, we have analytical expressions for the eigenenergies and the Berry connections (see Chapter 2); it is therefore straight-forward to calculate  $\tilde{H}(t)$

for any time  $t$ . In the *ab-initio* calculation, obtaining the Berry connections requires a particular gauge-choice to ensure that the cell-periodic Bloch functions are numerically differentiable. Similar to the approach in Ref. [91], we choose our gauge such that the Bloch functions of the  $s$ -bands are entirely real on a lattice site and the Bloch functions of the  $p$ -bands are entirely imaginary midway between neighboring lattice sites. This gauge-choice allows us to numerically differentiate the cell-periodic Bloch functions along the  $q_x$  direction, which is sufficient for our experiments.

# Bibliography

- [1] N. D. M. Neil W. Ashcroft, *Solid State Physics* (Holt, Rinehart, and Winston, 1976) (cit. on pp. 1, 10, 11, 23, 30, 54).
- [2] K. v. Klitzing, G. Dorda, and M. Pepper, “New Method for High-Accuracy Determination of the Fine-Structure Constant Based on Quantized Hall Resistance”, *Phys. Rev. Lett.* **45**, 494–497 (1980) (cit. on pp. 1, 90).
- [3] B. Jeckelmann and B. Jeanneret, “The quantum Hall effect as an electrical resistance standard”, *Rep. Prog. Phys.* **64**, 1603 (2001) (cit. on p. 1).
- [4] F. Delahaye and D. Dominguez, “Precise comparisons of quantized Hall resistances”, *IEEE Trans. Instrum. Meas.* **IM-36**, 226–229 (1987) (cit. on p. 1).
- [5] P. J. Mohr, B. N. Taylor, and D. B. Newell, “CODATA recommended values of the fundamental physical constants: 2010\*”, *Rev. Mod. Phys.* **84**, 1527–1605 (2012) (cit. on p. 1).
- [6] M. Nakahara, *Geometry, topology, and physics* (Institute of Physics Publishing, 2004) (cit. on p. 1).
- [7] D. J. Thouless, M. Kohmoto, M. P. Nightingale, and M. den Nijs, “Quantized hall conductance in a two-dimensional periodic potential”, *Phys. Rev. Lett.* **49**, 405–408 (1982) (cit. on pp. 2, 90).
- [8] M. Z. Hasan and C. L. Kane, “Colloquium: Topological Insulators”, *Rev. Mod. Phys.* **82**, 3045–3067 (2010) (cit. on pp. 2, 3, 30).
- [9] X.-L. Qi and S.-C. Zhang, “Topological insulators and superconductors”, *Rev. Mod. Phys.* **83**, 1057–1110 (2011) (cit. on pp. 2, 3, 102).
- [10] M. Z. Hasan and J. E. Moore, “Three-dimensional topological insulators”, *Annual Review of Condensed Matter Physics* **2**, 55–78 (2011) (cit. on p. 2).
- [11] J. E. Moore, “The birth of topological insulators”, *Nature* **464**, 194–198 (2010) (cit. on p. 2).
- [12] P. W. Anderson, *Basic notions of condensed matter physics* (Westview Press, 1997) (cit. on p. 2).
- [13] J. Moore, “Topological insulators: the next generation”, *Nat. Phys.* **5**, 378–380 (2009) (cit. on p. 2).
- [14] C. L. Kane and E. J. Mele, “ $Z_2$  Topological Order and the Quantum Spin Hall Effect”, *Phys. Rev. Lett.* **95**, 146802 (2005) (cit. on p. 2).

- [15] Y. Ando, “Topological Insulator Materials”, *Journal of the Physical Society of Japan* **82**, 102001 (2013) (cit. on pp. 2, 4, 7).
- [16] B. A. Bernevig, T. L. Hughes, and S.-C. Zhang, “Quantum Spin Hall Effect and Topological Phase Transition in HgTe Quantum Wells”, *Science* **314**, 1757–1761 (2006) (cit. on p. 2).
- [17] M. König, S. Wiedmann, C. Brüne, A. Roth, H. Buhmann, L. W. Molenkamp, X.-L. Qi, and S.-C. Zhang, “Quantum Spin Hall Insulator State in HgTe Quantum Wells”, *Science* **318**, 766–770 (2007) (cit. on p. 2).
- [18] J. E. Moore and L. Balents, “Topological invariants of time-reversal-invariant band structures”, *Phys. Rev. B* **75**, 121306 (2007) (cit. on p. 2).
- [19] L. Fu, C. L. Kane, and E. J. Mele, “Topological insulators in three dimensions”, *Phys. Rev. Lett.* **98**, 106803 (2007) (cit. on p. 2).
- [20] L. Fu and C. L. Kane, “Topological insulators with inversion symmetry”, *Phys. Rev. B* **76**, 045302 (2007) (cit. on p. 2).
- [21] D Hsieh, D Qian, L Wray, Y Xia, Y. S. Hor, R. J. Cava, and M. Z. Hasan, “A topological Dirac insulator in a quantum spin Hall phase.”, *Nature* **452**, 970–4 (2008) (cit. on p. 3).
- [22] B. Bernevig and T. Hughes, *Topological Insulators and Topological Superconductors* (Princeton University Press, 2013) (cit. on pp. 3, 5, 30, 34, 69).
- [23] M. V. Berry, “Quantal phase factors accompanying adiabatic changes”, *Proc. R. Soc. Lond. A* **392**, 45–57 (1984) (cit. on pp. 3, 8, 59).
- [24] M. Berry, “Geometric phase memories”, *Nat. Phys.* **6**, 148–150 (2010) (cit. on pp. 3, 7).
- [25] B. Simon, “Holonomy, the Quantum Adiabatic Theorem, and Berry’s Phase”, *Phys. Rev. Lett.* **51**, 2167–2170 (1983) (cit. on p. 3).
- [26] D. Xiao, M.-C. Chang, and Q. Niu, “Berry phase effects on electronic properties”, *Rev. Mod. Phys.* **82**, 1959–2007 (2010) (cit. on pp. 3, 5, 7, 11, 17, 18, 30, 74, 95).
- [27] I. Bloch, “Ultracold quantum gases in optical lattices”, *Nat. Phys.* **1**, 23–30 (2005) (cit. on pp. 3, 4).
- [28] C Becker, P Soltan-Panahi, J Kronjäger, S Dörscher, K Bongs, and K Sengstock, “Ultracold quantum gases in triangular optical lattices”, *New Journal of Physics* **12**, 065025 (2010) (cit. on pp. 3, 41).
- [29] G.-B. Jo, J. Guzman, C. K. Thomas, P. Hosur, A. Vishwanath, and D. M. Stamper-Kurn, “Ultracold atoms in a tunable optical kagome lattice”, *Phys. Rev. Lett.* **108**, 045305 (2012) (cit. on p. 3).

- 
- [30] L. Tarruell, D. Greif, T. Uehlinger, G. Jotzu, and T. Esslinger, “Creating, moving and merging Dirac points with a Fermi gas in a tunable honeycomb lattice.”, *Nature* **483**, 302–5 (2012) (cit. on pp. 3, 69, 88).
- [31] L. Duca, T. Li, M. Reitter, I. Bloch, M. Schleier-Smith, and U. Schneider, “An Aharonov-Bohm interferometer for determining Bloch band topology”, *Science* **347**, 288–292 (2015) (cit. on pp. 3, 5, 41).
- [32] S. Taie, H. Ozawa, T. Ichinose, T. Nishio, S. Nakajima, and Y. Takahashi, “Coherent driving and freezing of bosonic matter wave in an optical Lieb lattice”, *Sci. Adv.* **1** (2015) 10.1126/sciadv.1500854 (cit. on p. 3).
- [33] M. Pasienski, D. McKay, M. White, and B. DeMarco, “A disordered insulator in an optical lattice”, *Nat. Phys.* **6**, 677–680 (2010) (cit. on p. 3).
- [34] G. Roati, C. D’Errico, L. Fallani, M. Fattori, C. Fort, M. Zaccanti, G. Modugno, M. Modugno, and M. Inguscio, “Anderson localization of a non-interacting bose-einstein condensate”, *Nature* **453**, 895–898 (2008) (cit. on p. 3).
- [35] M. White, M. Pasienski, D. McKay, S. Q. Zhou, D. Ceperley, and B. DeMarco, “Strongly interacting bosons in a disordered optical lattice”, *Phys. Rev. Lett.* **102**, 055301 (2009) (cit. on p. 3).
- [36] M. Schreiber, S. S. Hodgman, P. Bordia, H. P. Lüschen, M. H. Fischer, R. Vosk, E. Altman, U. Schneider, and I. Bloch, “Observation of many-body localization of interacting fermions in a quasi-random optical lattice”, *Science* (2015) 10.1126/science.aaa7432 (cit. on p. 3).
- [37] M. Lewenstein, A. Sanpera, V. Ahufinger, B. Damski, A. Sen(De), and U. Sen, “Ultracold atomic gases in optical lattices: mimicking condensed matter physics and beyond”, *Adv. Phys.* **56**, 243–379 (2007) (cit. on pp. 3, 4).
- [38] C. Chin, R. Grimm, P. Julienne, and E. Tiesinga, “Feshbach resonances in ultracold gases”, *Rev. Mod. Phys.* **82**, 1225–1286 (2010) (cit. on pp. 3, 44, 103, 117).
- [39] W. S. Bakr, J. I. Gillen, A. Peng, S. Folling, and M. Greiner, “A quantum gas microscope for detecting single atoms in a Hubbard-regime optical lattice”, *Nature* **462**, 74–77 (2009) (cit. on p. 4).
- [40] J. F. Sherson, C. Weitenberg, M. Endres, M. Cheneau, I. Bloch, and S. Kuhr, “Single-atom-resolved fluorescence imaging of an atomic Mott insulator”, *Nature* **467**, 68–72 (2010) (cit. on p. 4).
- [41] R. Yamamoto, J. Kobayashi, T. Kuno, K. Kato, and Y. Takahashi, “An ytterbium quantum gas microscope with narrow-line laser cooling”, *New Journal of Physics* **18**, 023016 (2016) (cit. on p. 4).
- [42] M. Miranda, R. Inoue, Y. Okuyama, A. Nakamoto, and M. Kozuma, “Site-resolved imaging of ytterbium atoms in a two-dimensional optical lattice”, *Phys. Rev. A* **91**, 063414 (2015) (cit. on p. 4).

- [43] E. Haller, J. Hudson, A. Kelly, D. A. Cotta, B. Peaudecerf, G. D. Bruce, and S. Kuhr, “Single-atom imaging of fermions in a quantum-gas microscope”, *Nat. Phys.* **11**, Letter, 738–742 (2015) (cit. on p. 4).
- [44] M. F. Parsons, F. Huber, A. Mazurenko, C. S. Chiu, W. Setiawan, K. Wooley-Brown, S. Blatt, and M. Greiner, “Site-Resolved Imaging of Fermionic  $^6\text{Li}$  in an Optical Lattice”, *Phys. Rev. Lett.* **114**, 213002 (2015) (cit. on p. 4).
- [45] G. J. A. Edge, R. Anderson, D. Jervis, D. C. McKay, R. Day, S. Trotzky, and J. H. Thywissen, “Imaging and addressing of individual fermionic atoms in an optical lattice”, *Phys. Rev. A* **92**, 063406 (2015) (cit. on p. 4).
- [46] A. Omran, M. Boll, T. A. Hilker, K. Kleinlein, G. Salomon, I. Bloch, and C. Gross, “Microscopic Observation of Pauli Blocking in Degenerate Fermionic Lattice Gases”, *Phys. Rev. Lett.* **115**, 263001 (2015) (cit. on p. 4).
- [47] I. Bloch, J. Dalibard, and W. Zwerger, “Many-body physics with ultracold gases”, *Rev. Mod. Phys.* **80**, 885–964 (2008) (cit. on p. 4).
- [48] I. Bloch, J. Dalibard, and S. Nascimbene, “Quantum simulations with ultracold quantum gases”, *Nat. Phys.* **8**, 267–276 (2012) (cit. on p. 4).
- [49] T. Esslinger, “Fermi-Hubbard Physics with Atoms in an Optical Lattice”, *Annu. Rev. Condens. Matter Phys.* **1**, 129–152 (2010) (cit. on p. 4).
- [50] I. B. Spielman, “Detection of topological matter with quantum gases”, *Ann. Phys. (Berlin)* **525**, 797–807 (2013) (cit. on p. 4).
- [51] N. Goldman, G. Juzeliūnas, P. Ūhberg, and I. B. Spielman, “Light-induced gauge fields for ultracold atoms”, *Rep. Prog. Phys.* **77**, 126401 (2014) (cit. on p. 4).
- [52] J. Dalibard, F. Gerbier, G. Juzeliūnas, and P. Ūhberg, “*Colloquium* : artificial gauge potentials for neutral atoms”, *Rev. Mod. Phys.* **83**, 1523–1543 (2011) (cit. on p. 4).
- [53] U.-J. Wiese, “Ultracold quantum gases and lattice systems: quantum simulation of lattice gauge theories”, *Ann. Phys. (Berlin)* **525**, 777–796 (2013) (cit. on p. 4).
- [54] E. Zohar, J. I. Cirac, and B. Reznik, “Quantum simulations of lattice gauge theories using ultracold atoms in optical lattices”, *Reports on Progress in Physics* **79**, 014401 (2016) (cit. on p. 4).
- [55] G. Jotzu, M. Messer, R. Desbuquois, M. Lebrat, T. Uehlinger, D. Greif, and T. Esslinger, “Experimental realization of the topological Haldane model with ultracold fermions”, *Nature* **515**, 237–240 (2014) (cit. on pp. 4, 5, 95, 102).
- [56] M. Aidelsburger, M. Lohse, C. Schweizer, M. Atala, J. T. Barreiro, S. Nascimbène, N. R. Cooper, I. Bloch, and N. Goldman, “Measuring the Chern number of Hofstadter bands with ultracold bosonic atoms”, *Nature Physics* **11**, 162–166 (2014) (cit. on pp. 4, 5, 95, 102).

- 
- [57] B. K. Stuhl, H.-I. Lu, L. M. Aycock, D. Genkina, and I. B. Spielman, “Visualizing edge states with an atomic bose gas in the quantum hall regime”, *Science* **349**, 1514–1518 (2015) (cit. on pp. 4, 5, 95).
- [58] M. Mancini, G. Pagano, G. Cappellini, L. Livi, M. Rider, J. Catani, C. Sias, P. Zoller, M. Inguscio, M. Dalmonte, and L. Fallani, “Observation of chiral edge states with neutral fermions in synthetic hall ribbons”, *Science* **349**, 1510–1513 (2015) (cit. on pp. 4, 95).
- [59] Y.-J. Lin, K. Jimenez-Garcia, and I. B. Spielman, “Spin-orbit-coupled Bose-Einstein condensates”, *Nature* **471**, 83–86 (2011) (cit. on p. 4).
- [60] Y.-J. Lin, A. R. Perry, R. L. Compton, I. B. Spielman, and J. V. Porto, “Rapid production of  $^{87}\text{Rb}$  Bose-Einstein condensates in a combined magnetic and optical potential”, *Phys. Rev. A* **79**, 063631 (2009) (cit. on p. 4).
- [61] D Jaksch and P Zoller, “Creation of effective magnetic fields in optical lattices: the Hofstadter butterfly for cold neutral atoms”, *New Journal of Physics* **5**, 56 (2003) (cit. on p. 4).
- [62] M. Aidelsburger, M. Atala, S. Nascimbène, S. Trotzky, Y.-A. Chen, and I. Bloch, “Experimental Realization of Strong Effective Magnetic Fields in an Optical Lattice”, *Phys. Rev. Lett.* **107**, 255301 (2011) (cit. on pp. 4, 102, 103).
- [63] M. Aidelsburger, M. Atala, M. Lohse, J. T. Barreiro, B. Paredes, and I. Bloch, “Realization of the Hofstadter Hamiltonian with Ultracold Atoms in Optical Lattices”, *Phys. Rev. Lett.* **111**, 185301 (2013) (cit. on pp. 4, 102).
- [64] D. R. Hofstadter, “Energy levels and wave functions of bloch electrons in rational and irrational magnetic fields”, *Phys. Rev. B* **14**, 2239–2249 (1976) (cit. on p. 4).
- [65] T. Kitagawa, E. Berg, M. Rudner, and E. Demler, “Topological characterization of periodically driven quantum systems”, *Phys. Rev. B* **82**, 235114 (2010) (cit. on pp. 4, 102).
- [66] T. Oka and H. Aoki, “Photovoltaic hall effect in graphene”, *Phys. Rev. B* **79**, 081406 (2009) (cit. on p. 4).
- [67] N. H. Lindner, G. Refael, and V. Galitski, “Floquet topological insulator in semiconductor quantum wells”, *Nat. Phys.* **7**, 490–495 (2011) (cit. on pp. 4, 102).
- [68] C. V. Parker, L.-C. Ha, and C. Chin, “Direct observation of effective ferromagnetic domains of cold atoms in a shaken optical lattice”, *Nat. Phys.* **9**, Letter, 769–774 (2013) (cit. on pp. 4, 99).
- [69] F. D. M. Haldane, “Model for a Quantum Hall Effect without Landau Levels: Condensed-Matter Realization of the "Parity Anomaly"”, *Phys. Rev. Lett.* **61**, 2015–2018 (1988) (cit. on p. 4).

- [70] M.-C. Chang and Q. Niu, “Berry phase, hyperorbits, and the Hofstadter spectrum: Semiclassical dynamics in magnetic Bloch bands”, *Phys. Rev. B* **53**, 7010–7023 (1996) (cit. on p. 5).
- [71] E. Alba, X. Fernandez-Gonzalvo, J. Mur-Petit, J. K. Pachos, and J. J. Garcia-Ripoll, “Seeing topological order in time-of-flight measurements”, *Phys. Rev. Lett.* **107**, 235301 (2011) (cit. on pp. 5, 76, 95).
- [72] P. Hauke, M. Lewenstein, and A. Eckardt, “Tomography of band insulators from quench dynamics”, *Phys. Rev. Lett.* **113**, 045303 (2014) (cit. on pp. 5, 76, 95).
- [73] N. Fläschner, B. S. Rem, M. Tarnowski, D. Vogel, D.-S. Lühmann, K. Sengstock, and C. Weitenberg, “Experimental reconstruction of the Berry curvature in a topological Bloch band”, ArXiv e-prints (2015) (cit. on p. 5).
- [74] T. Li, L. Duca, M. Reitter, F. Grusdt, E. Demler, M. Endres, M. Schleier-Smith, I. Bloch, and U. Schneider, “Bloch state tomography using Wilson lines”, ArXiv e-prints (2015) (cit. on p. 5).
- [75] A. H. Castro Neto, F. Guinea, N. M. R. Peres, K. S. Novoselov, and A. K. Geim, “The electronic properties of graphene”, *Rev. Mod. Phys.* **81**, 109–162 (2009) (cit. on pp. 5, 25, 69).
- [76] F. Wilczek and A. Zee, “Appearance of gauge structure in simple dynamical systems”, *Phys. Rev. Lett.* **52**, 2111–2114 (1984) (cit. on pp. 5, 7, 9).
- [77] R. Yu, X. L. Qi, A. Bernevig, Z. Fang, and X. Dai, “Equivalent expression of  $\mathbb{Z}_2$  topological invariant for band insulators using the non-Abelian Berry connection”, *Phys. Rev. B* **84**, 075119 (2011) (cit. on pp. 5, 73, 74, 89).
- [78] L. Duca, “Probing topological properties of Bloch bands with ultracold atoms in a honeycomb optical lattice”, PhD thesis (Ludwig-Maximilian-Universität München, 2015) (cit. on pp. 6, 41, 42, 59, 60, 64, 69, 105, 114).
- [79] J. Anandan, “The geometric phase”, *Nature* **360**, 307–313 (1992) (cit. on pp. 7–9).
- [80] J. W. Zwanziger, M. Koenig, and A. Pines, “Berry’s phase”, *Annu. Rev. Phys. Chem.* **41**, 601–646 (1990) (cit. on pp. 7, 8, 10, 74).
- [81] D. J. Griffiths, *Introduction to Quantum Mechanics* (Dorling Kindersley (India) Pvt. Ltd., 2005) (cit. on pp. 7, 16, 34).
- [82] R. Shankar, *Principles of Quantum Mechanics* (Plenum Publishing Corporation, 1994) (cit. on pp. 7, 16).
- [83] A. Shapere and F. Wilczek, *Advanced Series in Mathematical Physics: Volume 5, Geometric Phases in Physics* (World Scientific, Singapore, 1989) (cit. on pp. 7–9).
- [84] H. Schey, *Div, grad, curl, and all that: an informal text on vector calculus* (W.W. Norton & Company, Inc., 2005) (cit. on pp. 9, 16).

- 
- [85] M. E. Peskin and D. V. Schroeder, *An Introduction to Quantum Field Theory (Frontiers in Physics)* (Westview Press, 1995) (cit. on pp. 9, 15).
- [86] A. A. Abdumalikov Jr, J. M. Fink, K. Juliusson, M. Pechal, S. Berger, A. Wallraff, and S. Filipp, “Experimental realization of non-abelian non-adiabatic geometric gates”, *Nature* **496**, Letter, 482–485 (2013) (cit. on p. 9).
- [87] C. Zu, W.-B. Wang, L. He, W.-G. Zhang, C.-Y. Dai, F. Wang, and L.-M. Duan, “Experimental realization of universal geometric quantum gates with solid-state spins”, *Nature* **514**, 72–75 (2014) (cit. on p. 9).
- [88] R. Shindou and K.-I. Imura, “Noncommutative geometry and non-abelian berry phase in the wave-packet dynamics of bloch electrons”, *Nuclear Physics B* **720**, 399–435 (2005) (cit. on p. 10).
- [89] M. Ben Dahan, E. Peik, J. Reichel, Y. Castin, and C. Salomon, “Bloch Oscillations of Atoms in an Optical Potential”, *Phys. Rev. Lett.* **76**, 4508–4511 (1996) (cit. on pp. 11, 45, 54, 75).
- [90] A Alexandradinata, X. Dai, and B. Bernevig, “Wilson-loop characterization of inversion-symmetric topological insulators”, *Phys. Rev. B* **89**, 155114 (2014) (cit. on pp. 15, 73–75, 90).
- [91] W. Kohn, “Analytic Properties of Bloch Waves and Wannier Functions”, *Phys. Rev.* **115**, 809–821 (1959) (cit. on pp. 17, 120).
- [92] J. Cayssol, “Introduction to dirac materials and topological insulators”, *C. R. Phys.* **14**, 760–778 (2013) (cit. on pp. 25, 74).
- [93] G. P. Mikitik and Y. V. Sharlai, “Manifestation of berry’s phase in metal physics”, *Phys. Rev. Lett.* **82**, 2147–2150 (1999) (cit. on pp. 26, 29).
- [94] D. L. Bergman, C. Wu, and L. Balents, “Band touching from real-space topology in frustrated hopping models”, *Phys. Rev. B* **78**, 125104 (2008) (cit. on pp. 26, 29, 101).
- [95] G. W. Semenoff, “Condensed-matter simulation of a three-dimensional anomaly”, *Phys. Rev. Lett.* **53**, 2449–2452 (1984) (cit. on p. 26).
- [96] K. I. Petsas, A. B. Coates, and G. Grynberg, “Crystallography of optical lattices”, *Phys. Rev. A* **50**, 5173–5189 (1994) (cit. on p. 32).
- [97] J. L. Mañes, F. Guinea, and M. A. H. Vozmediano, “Existence and topological stability of fermi points in multilayered graphene”, *Phys. Rev. B* **75**, 155424 (2007) (cit. on pp. 34, 69).
- [98] Y. Hasegawa, R. Konno, H. Nakano, and M. Kohmoto, “Zero modes of tight-binding electrons on the honeycomb lattice”, *Phys. Rev. B* **74**, 033413 (2006) (cit. on pp. 34, 69).

- [99] D. A. Steck, *Rubidium 87 D Line Data*, Available online at <http://steck.us/alkalidata/> (revision 2.1.5), 2015 (cit. on pp. 38, 105, 111).
- [100] S. Falke, E. Tiemann, C. Lisdat, H. Schnatz, and G. Grosche, “Transition frequencies of the *D* lines of  $^{39}\text{K}$ ,  $^{40}\text{K}$ , and  $^{41}\text{K}$  measured with a femtosecond laser frequency comb”, *Phys. Rev. A* **74**, 032503 (2006) (cit. on p. 38).
- [101] R. Grimm, M. Weidemüller, and Y. B. Ovchinnikov, “Optical dipole traps for neutral atoms”, *Adv. At. Mol. Opt. Phys.* **42**, edited by B. Bederson and H. Walther, 95–170 (2000) (cit. on p. 38).
- [102] K. L. Lee, B. Grémaud, R. Han, B.-G. Englert, and C. Miniatura, “Ultracold fermions in a graphene-type optical lattice”, *Phys. Rev. A* **80**, 043411 (2009) (cit. on p. 41).
- [103] P. Soltan-Panahi, J. Struck, P. Hauke, a. Bick, W. Plenkers, G. Meineke, C. Becker, P. Windpassinger, M. Lewenstein, and K. Sengstock, “Multi-component quantum gases in spin-dependent hexagonal lattices”, *Nature Physics* **7**, 434–440 (2011) (cit. on p. 41).
- [104] S. Ospelkaus-Schwarzer, “Quantum Degenerate Fermi-Bose Mixtures of  $^{40}\text{K}$  and  $^{87}\text{Rb}$  in 3D Optical Lattices”, PhD thesis (Universität Hamburg, 2006) (cit. on p. 44).
- [105] S. Chaudhuri, S. Roy, and C. S. Unnikrishnan, “Realization of an intense cold Rb atomic beam based on a two-dimensional magneto-optical trap: Experiments and comparison with simulations”, *Phys. Rev. A* **74**, 023406 (2006) (cit. on pp. 44, 112).
- [106] T. G. Tiecke, S. D. Gensemer, A. Ludewig, and J. T. M. Walraven, “High-flux two-dimensional magneto-optical-trap source for cold lithium atoms”, *Phys. Rev. A* **80**, 013409 (2009) (cit. on pp. 44, 112).
- [107] J. Schoser, A. Batär, R. Löw, V. Schweikhard, A. Grabowski, Y. B. Ovchinnikov, and T. Pfau, “Intense source of cold Rb atoms from a pure two-dimensional magneto-optical trap”, *Phys. Rev. A* **66**, 023410 (2002) (cit. on pp. 44, 112).
- [108] V. Gokhroo, G. Rajalakshmi, R. K. Easwaran, and C. S. Unnikrishnan, “Sub-Doppler deep-cooled bosonic and fermionic isotopes of potassium in a compact  $2\text{D}^+$ -3D MOT set-up”, *J. Phys. B. At. Mol. Opt. Phys.* **44**, 115307 (2011) (cit. on pp. 44, 112).
- [109] J. Catani, P. Maioli, L. De Sarlo, F. Minardi, and M. Inguscio, “Intense slow beams of bosonic potassium isotopes”, *Phys. Rev. A* **73**, 033415 (2006) (cit. on p. 44).
- [110] K. Dieckmann, R. J. C. Spreeuw, M. Weidemüller, and J. T. M. Walraven, “Two-dimensional magneto-optical trap as a source of slow atoms”, *Phys. Rev. A* **58**, 3891–3895 (1998) (cit. on pp. 44, 112).

- 
- [111] H. J. Metcalf and P. van der Straten, *Laser Cooling and Trapping* (Springer-Verlag New York, Inc., 1999) (cit. on pp. 44, 105, 112, 116).
- [112] M. Greiner, I. Bloch, T. W. Hänsch, and T. Esslinger, “Magnetic transport of trapped cold atoms over a large distance”, *Phys. Rev. A* **63**, 031401 (2001) (cit. on pp. 44, 107, 113).
- [113] D. M. Brink and C. V. Sukumar, “Majorana spin-flip transitions in a magnetic trap”, *Phys. Rev. A* **74**, 035401 (2006) (cit. on pp. 44, 114).
- [114] D. S. Naik and C. Raman, “Optically plugged quadrupole trap for Bose-Einstein condensates”, *Phys. Rev. A* **71**, 033617 (2005) (cit. on pp. 44, 114).
- [115] E. Majorana, “Teoria Relativistica di Particelle Con Momento Intrinseco Arbitrario”, *Il Nuovo Cimento* (1924-1942) **9**, 335–344 (2008) (cit. on p. 44).
- [116] L. De Sarlo, P. Maioli, G. Barontini, J. Catani, F. Minardi, and M. Inguscio, “Collisional properties of sympathetically cooled  $^{39}\text{K}$ ”, *Phys. Rev. A* **75**, 022715 (2007) (cit. on p. 45).
- [117] F. Ferlaino, C. D’Errico, G. Roati, M. Zaccanti, M. Inguscio, G. Modugno, and A. Simoni, “Feshbach spectroscopy of a K-Rb atomic mixture”, *Phys. Rev. A* **73**, 040702 (2006) (cit. on pp. 45, 117).
- [118] C. D’Errico, M. Zaccanti, M. Fattori, G. Roati, M. Inguscio, G. Modugno, and A. Simoni, “Feshbach resonances in ultracold 39 K”, *New Journal of Physics* **9**, 223 (2007) (cit. on pp. 45, 117).
- [119] W. Ketterle and M. Zwierlein, “Making, probing and understanding ultracold Fermi gases”, *Nuovo Cimento Rivista Serie* **31**, 247–422 (2008) (cit. on pp. 48, 116).
- [120] P. Törmä and K. Sengstock, *Quantum Gas Experiments: Exploring Many-Body States* (World Scientific Publishing Co, 2015) (cit. on p. 49).
- [121] M. Greiner, “Ultracold quantum gases in three-dimensional optical lattice potentials”, PhD thesis (Ludwig-Maximilians-Universität München, 2003) (cit. on pp. 50, 51, 107, 113).
- [122] F. Gerbier, A. Widera, S. Fölling, O. Mandel, T. Gericke, and I. Bloch, “Interference pattern and visibility of a Mott insulator”, *Phys. Rev. A* **72**, 053606 (2005) (cit. on pp. 50, 51).
- [123] M. Greiner, O. Mandel, T. Esslinger, T. W. Hansch, and I. Bloch, “Quantum phase transition from a superfluid to a Mott insulator in a gas of ultracold atoms”, *Nature* **415**, 39–44 (2002) (cit. on p. 51).
- [124] F. Gerbier, A. Widera, S. Fölling, O. Mandel, T. Gericke, and I. Bloch, “Phase Coherence of an Atomic Mott Insulator”, *Phys. Rev. Lett.* **95**, 050404 (2005) (cit. on p. 51).

- [125] M. Greiner, I. Bloch, O. Mandel, T. W. Hänsch, and T. Esslinger, “Exploring Phase Coherence in a 2D Lattice of Bose-Einstein Condensates”, *Phys. Rev. Lett.* **87**, 160405 (2001) (cit. on p. 51).
- [126] A. Kastberg, W. D. Phillips, S. L. Rolston, R. J. C. Spreeuw, and P. S. Jessen, “Adiabatic Cooling of Cesium to 700 nK in an Optical Lattice”, *Phys. Rev. Lett.* **74**, 1542–1545 (1995) (cit. on p. 51).
- [127] E. Peik, M. Ben Dahan, I. Bouchoule, Y. Castin, and C. Salomon, “Bloch oscillations of atoms, adiabatic rapid passage, and monokinetic atomic beams”, *Phys. Rev. A* **55**, 2989–3001 (1997) (cit. on p. 54).
- [128] M. Atala, “Measuring Topological Invariants and Chiral Meissner Currents with Ultracold Bosonic Atoms”, PhD thesis (Ludwig-Maximilian-Universität München, 2014) (cit. on p. 54).
- [129] A. Zenesini, D. Ciampini, O. Morsch, and E. Arimondo, “Observation of Stückelberg oscillations in accelerated optical lattices”, *Phys. Rev. A* **82**, 065601 (2010) (cit. on p. 56).
- [130] S. Kling, T. Salger, C. Grossert, and M. Weitz, “Atomic Bloch-Zener Oscillations and Stückelberg Interferometry in Optical Lattices”, *Phys. Rev. Lett.* **105**, 215301 (2010) (cit. on p. 56).
- [131] M. Cristiani, O. Morsch, N. Malossi, M. Jona-Lasinio, M. Anderlini, E. Courtade, and E. Arimondo, “Instabilities of a Bose-Einstein condensate in a periodic potential: an experimental investigation”, *Opt. Express* **12**, 4–10 (2004) (cit. on p. 58).
- [132] B. Wu and Q. Niu, “Landau and dynamical instabilities of the superflow of Bose-Einstein condensates in optical lattices”, *Phys. Rev. A* **64**, 061603 (2001) (cit. on p. 58).
- [133] M. Modugno, C. Tozzo, and F. Dalfovo, “Role of transverse excitations in the instability of Bose-Einstein condensates moving in optical lattices”, *Phys. Rev. A* **70**, 043625 (2004) (cit. on p. 58).
- [134] Y. Aharonov and D. Bohm, “Significance of Electromagnetic Potentials in the Quantum Theory”, *Phys. Rev.* **115**, 485–491 (1959) (cit. on p. 59).
- [135] F. Wilczek and A. Shapere, *Geometric Phases in Physics*, Advanced series in mathematical physics (World Scientific, 1989) (cit. on p. 59).
- [136] M. Atala, M. Aidelsburger, J. T. Barreiro, D. Abanin, T. Kitagawa, E. Demler, and I. Bloch, “Direct measurement of the Zak phase in topological Bloch bands”, *Nat. Phys.* **9**, 795–800 (2013) (cit. on pp. 61, 95).
- [137] F. Grusdt, D. Abanin, and E. Demler, “Measuring  $\mathbb{Z}_2$  topological invariants in optical lattices using interferometry”, *Phys. Rev. A* **89**, 043621 (2014) (cit. on pp. 73, 74, 89, 95).

- 
- [138] M. Fruchart and D. Carpentier, “An introduction to topological insulators”, *C. R. Phys.* **14**, 779–815 (2013) (cit. on p. 74).
- [139] J. Zak, “Berry’s phase for energy bands in solids”, *Phys. Rev. Lett.* **62**, 2747–2750 (1989) (cit. on p. 74).
- [140] A. Alexandradinata and B. A. Bernevig, “Berry-phase description of Topological Crystalline Insulators”, ArXiv e-prints (2014) (cit. on p. 74).
- [141] S. Shevchenko, S. Ashhab, and F. Nori, “Landau-Zener-Stückelberg interferometry”, *Phys. Rep.* **492**, 1–30 (2010) (cit. on p. 82).
- [142] L. Fallani, L. De Sarlo, J. E. Lye, M. Modugno, R. Saers, C. Fort, and M. Inguscio, “Observation of Dynamical Instability for a Bose-Einstein Condensate in a Moving 1D Optical Lattice”, *Phys. Rev. Lett.* **93**, 140406 (2004) (cit. on p. 84).
- [143] S. Kivelson, “Wannier functions in one-dimensional disordered systems: application to fractionally charged solitons”, *Phys. Rev. B* **26**, 4269–4277 (1982) (cit. on pp. 87, 93).
- [144] K. von Klitzing, “The quantized Hall effect”, *Rev. Mod. Phys.* **58**, 519–531 (1986) (cit. on p. 90).
- [145] Y. Makeenko, *Methods of Contemporary Gauge Theory* (Cambridge University Press, 2005) (cit. on p. 91).
- [146] N. Goldman, J. Beugnon, and F. Gerbier, “Detecting Chiral Edge States in the Hofstadter Optical Lattice”, *Phys. Rev. Lett.* **108**, 255303 (2012) (cit. on p. 95).
- [147] N. Goldman, J. Dalibard, A. Dauphin, F. Gerbier, M. Lewenstein, P. Zoller, and I. B. Spielman, “Direct imaging of topological edge states in cold-atom systems”, *Proceedings of the National Academy of Sciences* **110**, 6736–6741 (2013) (cit. on p. 95).
- [148] A. Dauphin and N. Goldman, “Extracting the Chern Number from the Dynamics of a Fermi Gas: Implementing a Quantum Hall Bar for Cold Atoms”, *Phys. Rev. Lett.* **111**, 135302 (2013) (cit. on p. 95).
- [149] X.-J. Liu, K. T. Law, T. K. Ng, and P. A. Lee, “Detecting Topological Phases in Cold Atoms”, *Phys. Rev. Lett.* **111**, 120402 (2013) (cit. on p. 95).
- [150] M. Buchhold, D. Cocks, and W. Hofstetter, “Effects of smooth boundaries on topological edge modes in optical lattices”, *Phys. Rev. A* **85**, 063614 (2012) (cit. on p. 95).
- [151] H. Price and N. Cooper, “Mapping the Berry curvature from semiclassical dynamics in optical lattices”, *Phys. Rev. A* **85**, 1–12 (2012) (cit. on p. 95).
- [152] E. Zhao, N. Bray-Ali, C. J. Williams, I. B. Spielman, and I. I. Satija, “Chern numbers hiding in time-of-flight images”, *Phys. Rev. A* **84**, 063629 (2011) (cit. on p. 95).

- [153] L. Wang, A. A. Soluyanov, and M. Troyer, “Proposal for Direct Measurement of Topological Invariants in Optical Lattices”, *Phys. Rev. Lett.* **110**, 166802 (2013) (cit. on p. 95).
- [154] T. D. Stanescu, V. Galitski, and S. Das Sarma, “Topological states in two-dimensional optical lattices”, *Phys. Rev. A* **82**, 013608 (2010) (cit. on p. 95).
- [155] X.-J. Liu, X. Liu, C. Wu, and J. Sinova, “Quantum anomalous Hall effect with cold atoms trapped in a square lattice”, *Phys. Rev. A* **81**, 033622 (2010) (cit. on p. 95).
- [156] M. Killi, S. Trotzky, and A. Paramekanti, “Anisotropic quantum quench in the presence of frustration or background gauge fields: a probe of bulk currents and topological chiral edge modes”, *Phys. Rev. A* **86**, 063632 (2012) (cit. on p. 95).
- [157] M. Killi and A. Paramekanti, “Use of quantum quenches to probe the equilibrium current patterns of ultracold atoms in an optical lattice”, *Phys. Rev. A* **85**, 061606 (2012) (cit. on p. 95).
- [158] D. A. Abanin, T. Kitagawa, I. Bloch, and E. Demler, “Interferometric Approach to Measuring Band Topology in 2D Optical Lattices”, *Phys. Rev. Lett.* **110**, 165304 (2013) (cit. on p. 95).
- [159] W. Beugeling, J. C. Everts, and C. Morais Smith, “Topological phase transitions driven by next-nearest-neighbor hopping in two-dimensional lattices”, *Phys. Rev. B* **86**, 195129 (2012) (cit. on p. 96).
- [160] D. A. Steck, *Quantum and Atom Optics*, Available online at <http://steck.us/teaching>, 2006 (cit. on p. 97).
- [161] S. Will, “Interacting bosons and fermions in three-dimensional optical lattice potentials”, PhD thesis (Johannes Gutenberg-Universität Mainz, 2011) (cit. on pp. 101, 105).
- [162] K.-J. Boller, A. Imamoglu, and S. E. Harris, “Observation of electromagnetically induced transparency”, *Phys. Rev. Lett.* **66**, 2593–2596 (1991) (cit. on p. 101).
- [163] G. Wirth, M. Olschlager, and A. Hemmerich, “Evidence for orbital superfluidity in the p-band of a bipartite optical square lattice”, *Nat. Phys.* **7**, 147–153 (2011) (cit. on p. 101).
- [164] D. Green, L. Santos, and C. Chamon, “Isolated flat bands and spin-1 conical bands in two-dimensional lattices”, *Phys. Rev. B* **82**, 075104 (2010) (cit. on p. 101).
- [165] V. Apaja, M. Hyrkäs, and M. Manninen, “Flat bands, Dirac cones, and atom dynamics in an optical lattice”, *Phys. Rev. A* **82**, 041402 (2010) (cit. on p. 101).
- [166] C. Wu and S. Das Sarma, “ $p_{x,y}$ -orbital counterpart of graphene: Cold atoms in the honeycomb optical lattice”, *Phys. Rev. B* **77**, 235107 (2008) (cit. on p. 101).

- 
- [167] C. Wu, D. Bergman, L. Balents, and S. Das Sarma, “Flat Bands and Wigner Crystallization in the Honeycomb Optical Lattice”, *Phys. Rev. Lett.* **99**, 070401 (2007) (cit. on p. 101).
- [168] J. Cayssol, B. Dòra, F. Simon, and R. Moessner, “Floquet topological insulators”, *Phys. Status Solidi Rapid Res. Lett.* **7**, 101–108 (2013) (cit. on p. 102).
- [169] M. Aidelsburger, “Artificial gauge fields with ultracold atoms in optical lattices”, PhD thesis (Ludwig-Maximilian-Universität München, 2015) (cit. on p. 102).
- [170] H. Miyake, G. A. Siviloglou, C. J. Kennedy, W. C. Burton, and W. Ketterle, “Realizing the Harper Hamiltonian with Laser-Assisted Tunneling in Optical Lattices”, *Phys. Rev. Lett.* **111**, 185302 (2013) (cit. on p. 102).
- [171] D. C. Tsui, H. L. Stormer, and A. C. Gossard, “Two-Dimensional Magnetotransport in the Extreme Quantum Limit”, *Phys. Rev. Lett.* **48**, 1559–1562 (1982) (cit. on p. 102).
- [172] R. Willett, J. P. Eisenstein, H. L. Störmer, D. C. Tsui, A. C. Gossard, and J. H. English, “Observation of an even-denominator quantum number in the fractional quantum Hall effect”, *Phys. Rev. Lett.* **59**, 1776–1779 (1987) (cit. on p. 102).
- [173] H. L. Stormer, “Nobel Lecture: The fractional quantum Hall effect”, *Rev. Mod. Phys.* **71**, 875–889 (1999) (cit. on p. 102).
- [174] R. B. Laughlin, “Anomalous quantum hall effect: an incompressible quantum fluid with fractionally charged excitations”, *Phys. Rev. Lett.* **50**, 1395–1398 (1983) (cit. on p. 102).
- [175] X.-G. Wen, “Topological orders and edge excitations in fractional quantum Hall states”, *Adv. Phys.* **44**, 405–473 (1995) (cit. on p. 102).
- [176] C. Nayak, S. H. Simon, A. Stern, M. Freedman, and S. Das Sarma, “Non-abelian anyons and topological quantum computation”, *Rev. Mod. Phys.* **80**, 1083–1159 (2008) (cit. on p. 102).
- [177] S. A. Parameswaran, R. Roy, and S. L. Sondhi, “Fractional quantum hall physics in topological flat bands”, *C. R. Phys.* **14**, 816–839 (2013) (cit. on p. 102).
- [178] E. J. Bergholtz and Z. Liu, “Topological flat band models and fractional Chern insulators”, *Int. J. of Mod. Phys. B* **27**, 1330017 (2013) (cit. on p. 102).
- [179] S. Raghu, X.-L. Qi, C. Honerkamp, and S.-C. Zhang, “Topological Mott Insulators”, *Phys. Rev. Lett.* **100**, 156401 (2008) (cit. on p. 102).
- [180] C. J. Kennedy, W. C. Burton, W. C. Chung, and W. Ketterle, “Observation of Bose-Einstein condensation in a strong synthetic magnetic field”, *Nat. Phys.* **11**, Article, 859–864 (2015) (cit. on p. 103).
- [181] M. Bukov, L. D’Alessio, and A. Polkovnikov, “Universal high-frequency behavior of periodically driven systems: from dynamical stabilization to Floquet engineering”, *Adv. Phys.* **64**, 139–226 (2015) (cit. on p. 103).

- [182] T. Bilitewski and N. R. Cooper, “Scattering theory for Floquet-Bloch states”, *Phys. Rev. A* **91**, 033601 (2015) (cit. on p. 103).
- [183] C. E. Creffield, “Instability and control of a periodically driven Bose-Einstein condensate”, *Phys. Rev. A* **79**, 063612 (2009) (cit. on p. 103).
- [184] M. Genske and A. Rosch, “Floquet-Boltzmann equation for periodically driven Fermi systems”, *Phys. Rev. A* **92**, 062108 (2015) (cit. on p. 103).
- [185] S. Choudhury and E. J. Mueller, “Transverse collisional instabilities of a Bose-Einstein condensate in a driven one-dimensional lattice”, *Phys. Rev. A* **91**, 023624 (2015) (cit. on p. 103).
- [186] S. Choudhury and E. J. Mueller, “Stability of a Floquet Bose-Einstein condensate in a one-dimensional optical lattice”, *Phys. Rev. A* **90**, 013621 (2014) (cit. on p. 103).
- [187] M. Bukov, S. Gopalakrishnan, M. Knap, and E. Demler, “Prethermal Floquet Steady States and Instabilities in the Periodically Driven, Weakly Interacting Bose-Hubbard Model”, *Phys. Rev. Lett.* **115**, 205301 (2015) (cit. on p. 103).
- [188] M. Bukov, M. Heyl, D. A. Huse, and A. Polkovnikov, “Heating and Many-Body Resonances in a Periodically-Driven Two-Band System”, *ArXiv e-prints* (2015) (cit. on p. 103).
- [189] C. Sträter and A. Eckardt, “Orbital-driven melting of a bosonic Mott insulator in a shaken optical lattice”, *Phys. Rev. A* **91**, 053602 (2015) (cit. on p. 103).
- [190] M. Weinberg, C. Ölschläger, C. Sträter, S. Prella, A. Eckardt, K. Sengstock, and J. Simonet, “Multiphoton interband excitations of quantum gases in driven optical lattices”, *Phys. Rev. A* **92**, 043621 (2015) (cit. on p. 103).
- [191] W. Ketterle, D. S. Durfee, and D. M. Stamper-Kurn, “Making, probing and understanding Bose-Einstein condensates”, in *Proceedings of the International School of Physics Enrico Fermi Course CXL*, edited by M. Inguscio, S. Stringari, and C. Wieman (IOS Press, 1994), pp. 67–176 (cit. on p. 105).
- [192] C. J. Pethick and H. Smith, *Bose Einstein Condensation in Dilute Gases* (Cambridge University Press, Cambridge, 2001) (cit. on p. 105).
- [193] T. Rom, “Bosonische und fermionische Quantengase in dreidimensionalen optischen Gittern: Präparation, Manipulation und Analyse”, PhD thesis (Ludwig-Maximilian-Universität München, 2009) (cit. on pp. 105, 111).
- [194] J. P. Ronzheimer, “Non-Equilibrium Dynamics of Ultracold Atoms in Optical Lattices”, PhD thesis (Ludwig-Maximilian-Universität München, 2013) (cit. on pp. 105, 112).
- [195] T. Best, “Interacting Bose-Fermi mixtures in optical lattices”, PhD thesis (Johannes Gutenberg-Universität Mainz, 2011) (cit. on p. 105).

- 
- [196] T. Li, “An Apparatus for Probing Fermions in a Quasi-Two-Dimensional Geometry”, Master’s thesis (Ludwig-Maximilians-Universität München, 2011) (cit. on pp. 105, 107, 113).
- [197] M. Boll, “A 2D+ -3D MOT system for producing laser-cooled K-Rb mixtures”, Master’s thesis (Ludwig-Maximilians-Universität München, Johannes Gutenberg Universität Mainz, 2011) (cit. on p. 105).
- [198] M. Reitter, “Ultracold Fermions in a novel 2D setup”, Master’s thesis (Ludwig-Maximilians-Universität München, 2012) (cit. on p. 105).
- [199] T. G. Tiecke, “Feshbach resonances in ultracold mixtures of the fermionic quantum gases  ${}^6\text{Li}$  and  ${}^{40}\text{K}$ ”, PhD thesis (University of Amsterdam, 2009) (cit. on p. 111).
- [200] W. D. Phillips, “Nobel lecture: laser cooling and trapping of neutral atoms”, *Rev. Mod. Phys.* **70**, 721–741 (1998) (cit. on p. 112).
- [201] C. Adams and E. Riis, “Laser cooling and trapping of neutral atoms”, *Prog. Quant. Electr.* **21**, 1–79 (1997) (cit. on p. 112).
- [202] A. Ridinger, S. Chaudhuri, T. Salez, U. Eismann, D. R. Fernandes, K. Magalhães, D. Wilkowski, C. Salomon, and F. Chevy, “Large atom number dual-species magneto-optical trap for fermionic  ${}^6\text{Li}$  and  ${}^{40}\text{K}$  atoms”, *The European Physical Journal D* **65**, 223–242 (2011) (cit. on p. 112).
- [203] W. Petrich, M. H. Anderson, J. R. Ensher, and E. A. Cornell, “Behavior of atoms in a compressed magneto-optical trap”, *J. Opt. Soc. Am. B* **11**, 1332–1335 (1994) (cit. on p. 112).
- [204] I. Geisel, K. Cordes, J. Mahnke, S. Jöllenbeck, J. Ostermann, J. Arlt, W. Ertmer, and C. Klempt, “Evolutionary optimization of an experimental apparatus”, *Appl. Phys. Lett.* **102**, 214105 (2013) (cit. on p. 112).
- [205] F. Draxler, “Evolutionäre Optimierung einer Kühlsequenz zur Erzeugung ultrakalter Atome”, B.Sc thesis (Ludwig-Maximilians-Universität München, 2014) (cit. on p. 112).
- [206] M. Landini, S. Roy, L. Carcagní, D. Trypogeorgos, M. Fattori, M. Inguscio, and G. Modugno, “Sub-Doppler laser cooling of Potassium atoms”, *Phys. Rev. A* **84**, 043432 (2011) (cit. on p. 112).
- [207] A. L. Migdall, J. V. Prodan, W. D. Phillips, T. H. Bergeman, and H. J. Metcalf, “First Observation of Magnetically Trapped Neutral Atoms”, *Phys. Rev. Lett.* **54**, 2596–2599 (1985) (cit. on p. 114).
- [208] E. Majorana and M. Inguscio, “Oriented atoms in a variable magnetic field”, in *Ettore Majorana Scientific Papers*, edited by G. F. Bassani (Springer Berlin Heidelberg, 2006), pp. 113–136 (cit. on p. 114).

- [209] G. Modugno, G. Ferrari, G. Roati, R. J. Brecha, A. Simoni, and M. Inguscio, “Bose-Einstein Condensation of Potassium Atoms by Sympathetic Cooling”, *Science* **294**, 1320–1322 (2001) (cit. on p. 115).
- [210] K. B. Davis, M.-O. Mewes, M. A. Joffe, M. R. Andrews, and W. Ketterle, “Evaporative Cooling of Sodium Atoms”, *Phys. Rev. Lett.* **74**, 5202–5205 (1995) (cit. on p. 115).
- [211] M. H. Anderson, J. R. Ensher, M. R. Matthews, C. E. Wieman, and E. A. Cornell, “Observation of Bose-Einstein Condensation in a Dilute Atomic Vapor”, *Science* **269**, 198–201 (1995) (cit. on p. 115).
- [212] W. Ketterle and N. V. Druten, “Evaporative cooling of trapped atoms”, *Adv. At. Mol. Opt. Phys.* **37**, edited by B. Bederson and H. Walther, 181–236 (1996) (cit. on p. 116).
- [213] E. G. M. van Kempen, S. J. J. M. F. Kokkelmans, D. J. Heinzen, and B. J. Verhaar, “Interisotope Determination of Ultracold Rubidium Interactions from Three High-Precision Experiments”, *Phys. Rev. Lett.* **88**, 093201 (2002) (cit. on p. 117).
- [214] A. Marte, T. Volz, J. Schuster, S. Dürr, G. Rempe, E. G. M. van Kempen, and B. J. Verhaar, “Feshbach Resonances in Rubidium 87: Precision Measurement and Analysis”, *Phys. Rev. Lett.* **89**, 283202 (2002) (cit. on p. 117).
- [215] P. F. Bedaque, E. Braaten, and H.-W. Hammer, “Three-body Recombination in Bose Gases with Large Scattering Length”, *Phys. Rev. Lett.* **85**, 908–911 (2000) (cit. on p. 117).

# Acknowledgements

I would like to begin by thanking Lucia Duca and Martin Reitter, the two people with whom I worked most closely. Lucia has been there since the beginning. She was my comrade in the trenches as we labored through the practicalities of building a lab and confronted the more mundane aspects of experimental physics. Those early days would have been far more taxing without her. Martin joined about a year and a half later. He readily participated in the gluing and cabling and winding, quickly learned how to run the machine, and brought essential German skills (language and otherwise). Together, we built up a functioning experiment. Even though there were the inevitable setbacks, the hard times were less hard because we shared them. Similarly, the excellent company made the good times even better. I feel very fortunate to have had such dedicated and reliable teammates who are both great physicists and great people.

Near the end of my PhD, we were joined by Jakob Näger and Karen Wintersperger. Jakob and Karen are already fully contributing to the lab work, and I trust the experiment will produce exciting results in their capable hands.

Most great teams have great leaders, and ours is no exception. I have tremendously benefited from the guidance of Monika Schleier-Smith, Ulrich Schneider, and Immanuel Bloch. I have the utmost respect for Monika, whose deep knowledge of physics and incredible work ethic are constant sources of inspiration. I learned a great deal from her in the two years she was our post-doc and thank her for cultivating an atmosphere of openness, where I always felt comfortable asking many questions, even the same ones multiple times. I could not have asked for a better mentor and look forward to working with her in the future.

Even from the beginning, Uli trusted us enough to leave us alone in the lab. At the same time, he was always there to help when we were stuck, and I am continuously impressed by his breadth of knowledge on both physics and technical issues. Moreover, although his success as group leader was certainly tied to mine as a PhD student, Uli was never overbearing and patiently allowed me to learn from my mistakes. I am deeply grateful to him for giving me both support and the freedom to develop my own ideas.

Immanuel is an exceptional physicist, whose high standards are balanced by a healthy dose of practicality. I strive to emulate his ability to form an intuitive physical understanding from a mess of formalism and greatly admire how he maintains a clear view on the big picture while simultaneously paying careful attention to the details (e.g., in figure design). Despite his busy schedule, Immanuel stayed fully involved

in our experiments and always took the time to deeply discuss physics, listen to my concerns, and offer advice. I thank Immanuel for providing an excellent research environment and giving me the opportunity to learn from him.

In addition to my experimentalist colleagues, there are a few theorists who have been instrumental to the work in this thesis. Fabian Grusdt and Eugene Demler offered important insights into the Wilson line experiment. I greatly value my continued correspondence with Fabian, who has an abundance of clever ideas and is incredibly patient and kind in answering my experimentalist questions.

The work on selection rules in the outlook of this thesis grew out of a collaboration with Aris Alexandradinata and Judith Höller. They, too, have been patient. As true condensed matter theorists, I imagine it must have been sometimes perplexing to communicate with me. We understand each other much better now, and I have high hopes for our nascent projects.

The diversity of experiments in the Bloch group meant that the answer to many of my questions was usually just next door, down the stairs, or a phone call away. I would particularly like to thank current and former members of the Boson team, Monika Aidelsburger, Marcos Atala, Michael Lohse, and Christian Schweizer. Their experiments are most closely related to ours, and they have always been very accommodating whenever I burst in for an impromptu discussion. Our neighboring lab, the Fermi I team, have kindly tolerated our equipment raids. I thank Pranjal Bordia, Henrik Lüschen, and Michael Schreiber for their generosity and good will.

Bodo Hecker, our electronics engineer, has been crucial to the success of our experiments. His thorough help in all our electronics woes is greatly appreciated. I have enjoyed the many group retreats and events organized by our secretaries, Zohra Hauck, Ildiko Kecskesi, Marianne Kargl, and Kristina Schuldt. I am especially grateful to Ildiko for her help in so many things. From smoothing out my residence permit issues to finding a doctor, I always felt more emboldened to face German bureaucracy with Ildiko at my side.

I was initially encouraged to come to Munich by Vladan Vuletić. My time in his lab was very formative, and I thank him for giving me the opportunity early on to meet and learn from so many excellent physicists. Having now been a graduate student myself, I appreciate even more the patient guidance I received from Haruka Tanji-Suzuki. She was wonderful teacher, and I owe very much to her indeed.

Outside of lab, but not apart from it, friends provided community and welcomed distractions. Here, I find myself thanking many of the same people again. I've had thought-provoking discussions about physics and other things with Pranjal, my almost-neighbor, and Ahmed Omran, my fellow cat-enthusiast. I met Zhenkai Lu during my undergraduate days and am glad we could also share our PhD years.

Somewhat remarkably, I have never tired of seeing Lucia and Martin. I thank them for many memories, some clearer than others, many made on nights that bled into mornings. On multiple occasions, we were accompanied by Friedrich Hönig and Florian Röttich. I thank Fritz for broadening my knowledge of things sci-fi and Flo for

improving my communication skills.

Scattered on different countries are others that I hold dear. I am fortunate to have spent most of my life now knowing Enikő Horváth. I thank her for keeping close despite the distance. My parents have gifted me with the opportunity to choose my own path. I am especially grateful to my mother, who, for my sake, has traveled so far and sacrificed so much. Finally, I thank Manuel Endres, who shared the weight of my blue days and was unwavering in his encouragement and support. I look forward to ending our time apart.